Critical Collapse of Newtonian Fluids

by

Silvestre Aguilar-Martinez

B.Sc., California State University, Fresno, 2002
M.Sc., The University of British Columbia, 2008

A THESIS SUBMITTED IN PARTIAL FULFILLMENT OF
THE REQUIREMENTS FOR THE DEGREE OF

DOCTOR OF PHILOSOPHY

in

The Faculty of Graduate and Postdoctoral Studies

(Physics)

THE UNIVERSITY OF BRITISH COLUMBIA

(Vancouver)

August 2015

Abstract

This thesis constitutes a numerical study concerning the dynamics of an inviscid fluid subject to Newtonian gravity. Type-II critical phenomena has been previously measured in gravitational collapse simulations of isothermal-gas-spheres in Newtonian gravity. Our first objective was to extend this work by applying the more general polytropic-gas equation-of-state to the spherically symmetric fluid. We showed that under generic conditions of critical collapse, the polytropic gas allows for scale-invariant solutions. These solutions display self-similarity of the first kind with non-linear scaling between the space and time variables. One of these solutions was identified as the critical solution in critical collapse simulations. Such solution was found to have a single unstable mode with a Lyapunov exponent whose value depends on the polytropic index (Γ) from the equation of state. We argued that this behavior constitutes evidence of type-II critical phenomena with a transition from type-II to type-I behavior occurring at $\Gamma \geq 6/5$. Thus, the polytropic gas exhibits both types of critical behavior. These phenomena was investigated dynamically and also from perturbation analysis.

In the second phase of the project we extended the hydrodynamic model to treat axi-symmetric gravitational collapse. This allowed us to study the effect of angular momentum on the critical solution. As previously predicted, infinitesimal initial rotation introduces a non-spherical, unstable axial mode into the dynamics. The measured scaling behavior of the specific angular momentum of the collapsed core agrees with the predicted growth rate (Lyapunov exponent) of the axial perturbation. This two-mode linear regime modifies the scaling laws via the introduction of universal functions that depend on the two-parameter family of initial data. The predicted universality of these functions was confirmed through careful measurements of the collapsed mass and its angular momentum near the collapse threshold. A two-parameter space survey reveals a universal behavior of the order-parameters, with no mass-gap even in the presence of finite initial rotation. The behavior changes slightly beyond some initial rotation threshold. The results then, can be interpreted as an intermediate convergence to a non-spherical self-similar critical solution with a single unstable mode.

Preface

The work presented in this manuscript contains original research conducted by the author in collaboration with the research supervisor, Professor Matthew W. Choptuik. This contribution is summarized and highlighted in Chap. 4 and Chap. 5. Only the discussion of the spin-up mode in Sec. 5.1 had previously been published. It should be pointed out that in the exposition of the formalism displayed in Chap. 2 certain equations had to be rederived to tailor therefor the purposes of this investigation. In particular, the discussion on type-II critical phenomena Sec. 2.8.1 was revised from what was done in *Phys. Rev. D*, 65(064019):1-10, (2002) to treat the polytropic gas in Newtonian gravity. We repeated Gundlach's perturbation analysis and derived the Newtonian-specific scaling laws for the collapsed mass and specific angular momentum of the collapsed core namely, Eqs. (2.118) and (2.120). These previously unpublished equations are analogous to the scaling laws for the black hole mass and its specific angular momentum derived in *Phys. Rev. D*, 65(064019):1-10, (2002).

Table of Contents

Appendices

List of Tables

List of Figures

Notation Conventions

During the writing of this thesis we tried to be as consistent as possible with the notation and definitions previously used in related works. In particular, the employed notation and convention follows from the work of the most repeatedly cited authors. As it will be made clear, this practice will assist in the comparison of the physical results. We provide a partial list of the symbols which we anticipate could potentially generate confusion while reading this thesis.

G	Newton's constant, set to unity in all numerical calculations.
x	Similarity variable, r/t^n
n	Scaling exponent, $2-\Gamma$
τ	Zooming time coordinate,$-\ln(1-t/t_0)$
Q	Convergence factor
Q_0	Similarity variable related to central density, $\ln(4\pi G\rho_c(t_0-t)^2)$
$\mathbf{q}$	$1\times\mathcal{N}$ array of conservative variables (continuum case), denotes $(q_1,\,\ldots,\,q_{\mathcal{N}})^{\intercal}$. All bold-faced symbols represent 1-dimensional arrays.
$\mathbf{p}$	$1\times\mathcal{N}$ array of primitive variables (continuum case), denotes $(p_1,\,\ldots,\,p_{\mathcal{N}})^{\intercal}$
$\mathbf{Q}$	Array of conservative variables (discrete case)
$\mathbf{P}$	Array of primitive variables (discrete case)
$\vec{x}$	Position vector $(x_1,\,x_2,\,x_3)$. All quantities with $\vec{\cdot}$ denote spatial vectors.

q	Magnitude of vector factor on the azimuthal velocity used in setting initial angular momentum $\|\vec{q}\|$
δ	Magnitude of small vector quantity $\|\vec{\delta}\|$ related to the initial angular momentum
a	Magnitude of the specific angular momentum of the collapsed core, $\|\vec{a}\|$
M	Mass of the collapsed core
$F(\vec{\delta})$	Universal function related to the mass of the collapsed core
$\vec{G}(\vec{\delta})$	Universal function related to the specific angular momentum of the collapsed core. In axisymmetry $\vec{G}(\vec{\delta}) = G(\delta)\hat{z}$

Acknowledgements

I would like to express my sincere gratitude to my research advisor Professor Matthew Choptuik. I am truly indebted to him for the guidance he provided throughout this research project. I specially appreciate his highly rigorous and critical style of teaching while granting his students a great degree of freedom in the pursuit of research ideas. I feel truly honored for being a part of his research group during these years. I also would like to extend special thanks to the members of my research committee Professors, Jeremy Heyl, William Unruh and Hirohisa Tanaka.

I am obliged to professor Frans Pretorius; the programs PAMR and AMRD that he developed, played a significant role in expediting our code development and calculations. I also owe many thanks to Scott Noble; many of the ideas used in the development of our spherically symmetric hydrodynamic code were inspired by and built upon his work of the subject. He [Scott] was also very generous with his time in answering many of my hydro questions via email. I also owe a great deal to Professor Carsten Gundlach; much of our work is motivated by his studies on critical phenomena. I would like to specially thank him for our Skype conversation which help me clarify important concepts pertaining to this research.

Moreover, I would like to take this opportunity to thank my friends and colleagues at UBC: Daoyan Wang, Arman Akbarian, Graham Reid, Jason Penner, Bruno Mundim, and Ben Gutierrez. Great gratitude is extended to Lynn Baglole and Shanda Walters. I thank them for their encouragement and for reading part of this manuscript. I also want to use this chance to thank my high school counselor Dennis Conner and my friend, Robert Bergen. Their support and generosity

arrived at a critical time in my life and help set into motion the events which have culminated with the writing of the dissertation. Furthermore, I would like to thank my family for their patience and unwavering support.

I am profoundly grateful to The Natural Sciences and Engineering Research Council of Canada (NSERC) which provided the financial support that made this work possible.

Dedication

Este trabajo está dedicado con gran afecto a mi padre, Alvaro y a la memoria de mi madre, Delfina.

Chapter 1

Introduction

Einstein's theory of General Relativity (GR) as well as Newton's law of gravity provide a mathematical framework that successfully model the effect of gravitation where matter-energy act as a source. An important consequence of both theories is the production of compact states of matter through the mechanism of gravitational collapse [51, 70, 104]. Some of the most exciting areas of research in astronomy and astrophysics involve just such a scenario. Examples of these are neutron stars, black holes, active galactic nuclei, supernovae, collapsars, etc. Much effort has been allocated towards the investigation of these systems using facilities such as γ-ray and X-ray telescopes [86, 110]. Parallel to this development a more theoretical approach has emerged with the goal of solving the dynamical equations (GR/Newtonian) using numerical techniques in an attempt to simulate/model these phenomena. The literature on the subject is too immense to list, therefore, we direct the reader to a short compendium of reviews and applications of the methods to various physical systems, [7, 20, 23, 25, 26, 29, 67, 92, 100, 107]. Numerical methods have proven to be instrumental in advancing our understanding of the process of gravitational collapse.

The *perfect fluid* model is a subclass of the matter models often used in numerical simulations of astrophysical and cosmological phenomena. This model ignores non-adiabatic effects such as viscosity and radiative transfer [3, 25, 26, 67]. In inflationary cosmology the perfect fluid is used to model the contribution of radiation energy to the stress-energy tensor, see [62, 79, 106] and references therein. It also serves as a basic model of stellar structure, see discussion on barotropic fluids in

[58, 80]. The perfect fluid is also widely used in investigations of a more fundamental nature associated with the interaction of gravity and matter. Its ramifications are far reaching in fields such as critical phenomena, naked singularity formation, cosmic censorship, and quantum gravity. The project presented herein is of the latter theoretical orientation. Our aim was to consider an idealized fluid model coupled to gravity in order to investigate critical gravitational collapse using numerical techniques. This was done in an attempt to shed more light on the surprising critical phenomena which is known to emerge at the collapse threshold [10].

1.1 Overview

In numerical calculations of the collapse of a massless real scalar field in GR, Choptuik (1993) discovered intricate, small-scaled, periodic structures on the scalar field profile that developed at the threshold of gravitational collapse [15]. This behavior would later be called *Critical Phenomena in Gravitational Collapse*. To date, a myriad of other matter models have been studied, with some showing a similar critical behavior. An up to date list of these can be found in Gundlach's review of the subject [10]. Following Choptuik's discovery, Evans and Coleman (1994) identified similar behavior in spherically symmetric critical collapse of a photon gas [22]. The Evans and Coleman critical solution, like Choptuik's counterpart was found to be scale-invariant (self-similar). This however, displayed a continuous symmetry, unlike the "periodic echoing", discrete symmetry found in Choptuik's solution. In spite of these differences, a general description of critical phenomena can be made in a model independent way. In what follows, we provide a brief description of critical phenomena in gravitational collapse, focusing on the perfect fluid model. The more complete formalism is given in Sec. 2.8.

Initial conditions are imposed on the matter fields via a set of parameters *e.g.* temperature, width of matter distribution, amplitude of the energy density, etc. Numerical integration of Einstein's equations and the equations of motion for the matter fields yield the following empirical facts; the matter-energy initially "implodes" under the influence of gravity–the spatial profile of the energy distribution narrows effectively strengthening the gravitational interaction, which in some cases will lead to singularity formation, *e.g.* a black hole in General Relativity [104]. If we allow control of the initial data through a single control parameter p, *i.e.* a 1-parameter family of data, one discovers that the outcome of the evolution can be divided into two, sometimes three qualitatively different states.

1. For a certain range of the parameter p the initial implosion is followed by an "explosion", an effect that leads to the dispersion of the matter-energy away from the center. We call these data *subcritical*.
2. If the implosion continues leading to singularity/black hole formation; we call this the *supercritical* regime.
3. After some time the evolution settles into a static configuration, a star-like state.

If generic choices of p yield end-states described only by 1 or 2 (collapse/dispersal) for a particular matter type under investigation then, we find that these results are associated with two regimes in the domain of p. For example, if $p > p^\star$ where $p^\star$ is some threshold, then the end-state corresponds to complete collapse (black hole formation) regardless of the difference $p - p^\star$. Similarly, for $p < p^\star$ the evolution leads unambiguously to dispersal of the matter. We can the tune the initial data to the threshold of singularity formation, by setting $p = p^\star$. The spacetime and matter fields resulting from this fine-tuning is known as the critical solution. This solution has been found to possess qualities which are reminiscent of phase transitions in statistical mechanics [10, 34].

In analogy with phase transitions in statistical mechanics the critical solution is said to belong to two distinct types. Type-I critical behavior refers to static metastable configurations of the matter-energy. The solution is time-translation symmetric. This symmetry can be continuous, that is the solutions to the equations of motions $Z(r,t)$ is invariant under $Z(r,t) \to Z(r,t+\Delta t)$ for any $\Delta t \in \mathbb{R}$, or discrete *i.e.* invariant under $Z(r,t) \to Z(r,t+\nu\Delta t')$ where $\Delta t'$ is a specific period characteristic of the solution, and $\nu \in \mathbb{Z}$. However, this is only true if we have fine-tuned the, initial condition to precisely the threshold parameter $p^\star$. Experimentally, it is impossible to fine tune the initial state to $p = p^\star$ due to limitations in numerical precision. The critical solution is extrapolated from the behavior near the collapse threshold. In particular, the time the computed solution converges to the critical solution as a result of fine tuning p to $p^\star$ follows the scaling law

$$t \sim -\sigma \ln |p - p^\star|, \tag{1.1}$$

where t is the life-time of an almost static state which resembles the critical solution and σ, called the scaling exponent, is a constant whose significance is discussed in Sec. 2.8. Furthermore, if we explore the supercritical regime (p close to $p^\star$ for which singularity formation is the outcome) the mass of the black hole ($M_{\rm BH}$) has a minimum, finite value, thus there exists a "mass-gap" in the size of the possible black holes. This is the reason for the label Type-I critical phenomenon. $M_{\rm BH}$, playing the role of the order parameter, changes discontinuously at the critical value $p = p^\star$, and thus reminds us of first-order phase transitions in statistical mechanics. See top plot in Fig. 1.1 for a typical example.

For the case of Type-II critical phenomena, arguably the more interesting case, the solution is scale symmetric (self-similar), where again, the symmetry can be either continuous or discrete. The scaling law now involves the order parameter, $M_{\rm BH}$ such that,

$$\ln M_{\rm BH} \sim \gamma \ln |p - p^\star|, \tag{1.2}$$

for values of p in the supercritical regime, γ is again called the scaling exponent discussed in Sec. 2.8. In this case there is no mass gap in the spectrum of $M_{\rm BH}$, see bottom plot in Fig. 1.1. The transition between flat (dispersal) and singular final spacetimes can be made continuously via the critical solution, and hence it is analogous to second-order phase transitions in statistical mechanics [10, 34].

Another property of the critical solution is *universality.* It can be verified (by numerical integration of the governing equations) that the critical solution and the scaling exponent (γ), are independent of the details of, and choice of 1-parameter initial data family. Evidence of universality has been found in many models that display type-II critical behavior [9, 15, 22, 52, 55, 73, 103]. This property of the critical solution can be understood in terms of linear perturbation theory as outlined by [99]. The single-unstable-mode structure of the critical solution makes it an intermediate attractor of the critical evolution. The unstable mode grows according to $1/(t_0 - t)^{Re(\lambda_0)}$, where t_0 is the time of singularity formation and λ_0 is the Lyapunov exponent of the perturbation mode. It can be shown that $\gamma = 1/\lambda_0$. This formalism will be discussed in more detail in Sec. 2.8.

1.1.1 Historical Context

This brief historical review is focused on those studies involving the perfect fluid model. Its presentation is aimed at establishing the relevance of our project. Type-II critical phenomena was observed in critical collapse simulations of a perfect fluid that obeys an ultrarelativistic equation of state (EoS),

$$P = k\rho, \tag{1.3}$$

where the variables P and ρ represent the pressure and energy density, respectively, with k being a constant of proportionality [22, 47, 73, 74, 96]. Evans and Coleman found the critical solution for $k = 1/3$ (photon gas). Calculation of the black hole mass resulting from supercritical evolutions of the radiation fluid found that the mass followed a power-law similar to that of Choptuik's scalar field. The black hole mass was shown to obey Eq. (1.2), with scaling exponent $\gamma \approx 0.36$. Koike *et al.* (1994)

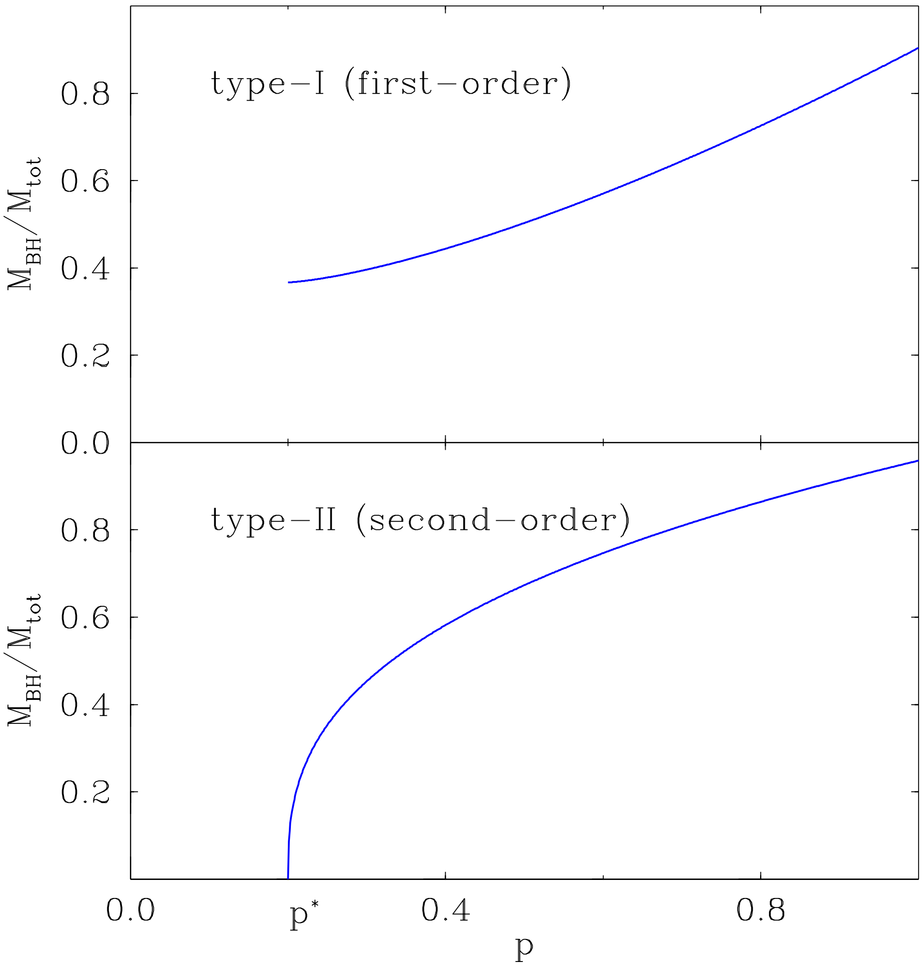

Figure 1.1: Behavior of the order-parameter M_{BH} near the threshold of gravitational collapse. This plot illustrates the typical behavior of M_{BH} in the vicinity of the critical parameter ($p = p^{\star}$). A gap exists in the possible values of M_{BH} (top) across the collapse threshold parameter $p^{\star}$ whereas for type-II transitions M_{BH} "turns on" at arbitrarily small values (bottom) as $p \to p^{\star -}$ (p approaches $p^{\star}$ from the left in the given example).

studied linear perturbations about the Evans-Coleman solution and discovered it had a single growing mode. From their result, a more precise calculation of the scaling exponent was possible. They found, $\gamma \equiv 1/\lambda_0 \approx 0.3558019$. It was soon established that universality did not extend to including different values of k from Eq. (1.3) [66]. Nielsen and Choptuik (2000) [73, 74] found continuously self-similar critical solutions for selected values of $k \in (0,\, 1]$. They measured, for instance, mass-scaling exponents $\gamma \approx 0.15$ at $k = 0.05$ and $\gamma \approx 1.0$ at $k = 1$. Their work included spherically symmetric collapse simulations and solutions to the autonomous system of equations obtained by assuming a self-similar ansatz.

This work was extended by Noble (2008) [75] in his studies of the *ideal gas* EoS,

$$P = k\rho_0\epsilon. \tag{1.4}$$

The variables ρ_0 and ϵ are respectively the rest-mass energy density and specific internal energy, and k is again a constant parameter. Noble (2008) carried out simulations of critical collapse of an ideal gas in spherical symmetry [75]. It was revealed that the critical solution was identical to that previously found by Nielsen *et. al.* [73, 74] using the simpler ultrarelativistic EoS (1.3). These results were interpreted heuristically as the tendency of the collapsing ideal gas towards an ultrarelativistic limit, modeled by $P = k\rho$. This follows from the fact that for rapidly collapsing matter, $\rho = \rho_0 + \epsilon\rho_0 \approx \epsilon\rho_0$.

Ori and Piran (1990) studied self-similar solutions of a spherically symmetric perfect fluid with EoS (1.3) in GR. They showed that the limit $k \to 0$ (Eq. (1.3)) yields the weak-field approximation—the solutions reduce to those describing, isothermal self-similar flows in Newtonian gravity [77]. This Newtonian system will be discussed in detail in Sec. 2.3. Investigations involving the Newtonian isothermal self-similar fluid model date back the work of Larson (1969)[60] and independently Penston (1969) [81]. The regular (analytic) self-similar solution found simultaneously by Larson and Penston, later named the Larson-Penston (LP) solution, was proposed as a candidate solution to describe the early stages of gravitational collapse of molecular clouds. Shu (1977) [95] found a static self-similar solution which is singular at the origin and used it as initial data in collapse simulations. The work of Hunter (1977) [56] provided a more complete picture of the spectrum of analytic self-similar solutions to the isothermal gas model. He [Hunter] applied a graphical technique which allowed him to determine in principle all of the regular self-similar solutions to the isothermal gas. He found the solution spectrum to be discrete and infinite. This technique was also applied in this work, details of its application are given in Sec. 4.1.1. The solutions were shown to form a hierarchical structure Sec. 2.6.2. The first member in the hierarchy is the previously known Larson-Penston solution, with subsequent solutions labeled Hunter-A,B,C,... Extrapolation of this Hunter-spectrum hints at a convergence to the static singular solution found by Shu [95]. More details of these solution are provided in Sec. 2.6.2 and Chap. 4.

Similar to the work done by Nielsen and Choptuik [73, 74], Harada *et al.* performed spherically-symmetric dynamical simulations of critical collapse of a perfect fluid in GR with a focus on the near-Newtonian regime, specifically $k \in (0,\ 0.036]$ in Eq. (1.3) [47]. They showed that the type-II critical phenomena previously measured continued to $k \to 0$ (the Newtonian limit). The results of the numerical experiments were interpreted as follows. The dynamical solution of generic initial data was shown to have late time ($t_0 - t \to 0$) convergence to a general relativistic self-similar solution. This solution had been previously studied by Ori and Piran by solving the autonomous system (one obtained by assuming a self-similar ansatz for the metric and fluid fields in spherically-symmetric, Schwarzschild-like spacetime) [77]. We refer to this as the Ori-Piran solution. Fined-tuned initial data (critical solution) showed intermediate convergence to a different self-similar solution. This critical solution had similar properties to the critical solution found by Evans and Coleman [22] for the radiation fluid. Here, we use the label Evans-Coleman solution to refer to the critical solution for arbitrary $k \in (0,\ 1]$. Like Koike *et. al.*'s stability analysis of the radiation gas [99], Harada (2001) [44] carried out a similar linear stability work on the Ori-Piran and Evans-Coleman similarity solutions for $k \in (0, 0.036]$. Their results failed to find any unstable modes for the Ori-Piran solution, thus provided further support towards its role as a "global attractor solution" during gravitational collapse. This was clearly in agreement with the dynamical calculations and the late time behavior of the solution. On the other hand, the Evans-Coleman solution (the critical collapse solution for the General Relativistic perfect fluid calculated in [22]), according to Harada *et. al.*'s analysis [44] indicated the presence of a single unstable mode. The Lyapunov exponent of this mode was related to the scaling laws of the order parameters *e.g.* the black hole mass (M_{BH}). From these results a value of the scaling exponent $\gamma \equiv 1/\lambda_0$ was computed for different values of k near $k = 0$. The value of the unstable mode at $k = 0$ was extrapolated to be $1/\lambda_0 \sim 0.11$ [44]. Based on these results Harada *et. al.* [44, 47] predicted that a similar type-II critical phenomena would emerge for a strictly Newtonian calculation with appropriate re-definition of the order-parameter given that there are no black holes of the Newtonian gravity. This analogous quantity is the collapsed mass M(collapsed), which like the black hole mass, M_{BH} is proportional to a length scale. Thus, the collapsed mass, is the order-parameter to be measured in Newtonian critical collapse. The definition of M(collapsed) or simply M and further details are given in Sec. 1.2.1.

Linear stability analysis of the Newtonian isothermal gas system conducted in [64] confirmed that the first member of the Hunter series [56], namely, the Hunter-A solution contained a single unstable mode. The reciprocal of the growth rate for the unstable mode was calculated to be $1/\lambda_0 \approx 0.10567$, in agreement with the estimated value of 0.11, [44, 47]. Given the single growing mode property of the Hunter-A solution Maeda *et. al.* (2001) [64] predicted its role as a critical solution in Newtonian critical collapse of isothermal spheres. In contrast, calculations related to the stability of the Larson-Penston solution indicated an absence of any unstable modes, suggesting its potential role as a universal attractor during the evolution of collapsing isothermal gas spheres [64]. Dynamical simulation of critical collapse of an isothermal gas in Newtonian gravity confirmed the Hunter-A solution as the Newtonian analogue of the Evans-Coleman solution [48]. Harada and Maeda (2003) also showed that the Larson-Penston solution is a universal attractor and thus is the Newtonian analogue of the Ori-Piran solution [48]. The meaning of "critical phenomena in Newtonian collapse" is made more concrete in Secs. 1.2 and 1.2.1. The connection with the GR self-similar solutions from the perspective of dynamical simulations in the Newtonian limit ($k \to 0$ in Eq. (1.3)) was made clear thanks to the work of Snajdr (2006) [96]. Quadruple precision numerics were used to calculate spherically symmetric critical collapse evolutions of a perfect ultra-relativistic fluid in GR. The high level of precision in the calculation of the numerical solution resolved the convergence to the Newtonian solutions as $k \to 0$, in accordance with the initial predictions of Ori and Piran [77]. The numerical calculation of the scaling laws showed convergence to the Newtonian results of [44, 47, 48, 64].

Beyond spherical symmetry Gundlach has argued that the critical collapse solution of a perfect fluid that behaves in accordance with EoS (1.3) and is endowed with initial infinitesimal angular momentum contains a second unstable mode in the vanishing k regime [10, 24, 30–34]. The second, non-spherical[1] growing mode is attributed to an $\ell = 1$ axial perturbation. Gundlach (2002) [32] calculates modifications to the scaling laws (*e.g.* M_{BH}) taking into account a non-spherical, unstable axial perturbation mode using the formalism of Koike *et. al.* Specifically, he calculated the effect that the axial mode would have on the scaling of the BH mass (M_{BH}) and its angular momentum ($\vec{L}_{\mathrm{BH}}$). These calculations constitute predictions for the critical behavior of the perfect fluid (with EoS (1.3)) near the collapse threshold. Thus, the modified scaling laws are a test for the presence of this extra unstable mode. A discussion of the non-spherical perturbations related to our system is found in Sec. 2.5. The consequences of any non-spherical unstable mode(s) in our model

---

[1] The second mode can only come via non-spherical perturbations, since by definition of the critical solution there can only be one unstable spherical mode

are examined in Sec. 2.8.1.

Similar non-spherical linear perturbation analyses about the Larson-Penston solution has been carried out in Newtonian fluids [38–42]. Simulations of gravitational collapse of an isothermal gas in Newtonian gravity have identified the growth of axial and polar (the bar-mode) non-spherical perturbations [68, 69]. The bar-mode perturbation (polar perturbations with $\ell = 2$, Appx. B) is believed to be responsible for the process of fragmentation and formation of binary star systems [68]. The spectrum of all axial perturbations can be computed explicitly for the isothermal ideal gas [41], where it is clear that all self-similar solutions are subject to axial instabilities (Sec. 2.5). Axisymmetric evolutions of the Newtonian fluid would repress any $\ell = 2$, $m \neq 0$ bar mode instabilities since these are ϕ-dependent functions, (ϕ is the azimuthal coordinate in polar spherical coordinates (r, θ, ϕ)) and axisymmetry requires that all of the fields are independent of ϕ. The only potentially observable $\ell = 2$ polar perturbation corresponds to $m = 0$, however, for reasons discussed in Sec. 2.7 this mode is also eliminated given the symmetry restrictions imposed on the initial data. Therefore, it is expected that axisymmetric evolutions of critical collapse in Newtonian gravity have two unstable perturbation modes, the known spherical one found in [64] and the axial mode [40, 41]. The effect of this non-spherical axial perturbation on the critical phenomena measured in [48, 64], we argue, is analogous to that predicted by Gundlach in [32]. A major part of this project involves this investigation.

1.2 Critical Phenomena in Newtonian Collapse

Before we can properly discuss critical phenomena in Newtonian collapse some concepts must be clarified. We considered the system described by a spherically symmetric isothermal gas. For concreteness, it is assumed that Temperature T (equivalently the internal energy) is the control parameter as was done in [48]. Known empirically from numerical calculations performed by Harada *et. al.* [48] that for

$T < T^\star$ the end result is a singular solution (the supercritical regime). This is characterized by an exponential growth of the density and pressure at the origin. The parameter $T^\star$ represents a critical temperature. Close examination of this singular solution reveals a tendency towards self-similarity. It becomes apparent that this self-similar end-state is described by the Larson-Penston solution. Such end-states are analogous to the General Relativistic self-similar black hole solution. More is said about this association throughout Sec. 2.6. The quantity analogous to the black hole mass in Newtonian gravity is the collapsed mass M. The mass of the collapsed region in Newtonian gravity is defined in Sec. 1.2.1. In the case of dispersion, *i.e* evolutions for which $T > T^\star$, (the subcritical regime) after the initial implosion the gas then disperses out to infinity, leaving a rarefied region at the origin where the density and pressure tend to zero. This solution is analogous to flat spacetime in GR. The critical case ($T \approx T^\star$), as described in the previous section the solution tends towards the one-mode unstable Hunter-A solution at intermediate times, later it either converges to the LP solution, or disperses. This is interpreted as a consequence of the growth of the unstable mode just as in the general relativistic case. The properties of the critical solution give rise to the features of the system which are characteristic of type-II critical phenomena, *e.g.* scaling laws and universality.

1.2.1 Newtonian Analogue of the Black Hole Mass

Particular singular solutions in Newtonian gravity play an analogous role to the black hole solution of General Relativity. In the specific case of an isothermal gas an example of these singular solutions is the self-similar Larson-Penston solution. Similar to General Relativity, certain regions of the parameter space of initial conditions will lead to gravitational collapse in purely Newtonian gravity. The fields describing the fluid diverge exponentially at the origin. Like black hole formation in GR, the Newtonian collapse results in the formation of collapsed cores or compact objects. Naturally, just like the black hole mass, we should be able to associate a mass quantity to these objects. Borrowing the definition used in Harada (2003) [48], the mass of the core is defined as the integral of fluid elements over the innermost region with "in-falling" radial velocity. In spherical coordinates, with the origin set at the center of collapse, the fluid elements in the collapsing region have negative radial velocity. The radius at which the velocity field changes sign defines the bounds for the integration, and the physical size of the collapsing core. This is illustrated is Fig. 1.2(a). This innermost region of negative radial fluid velocity forms at the early stages of collapse, its evolution can be tracked over time as shown in Fig.4.13(a). The core's mass stops evolving as the collapsing fluid approaches the time of singularity formation t_0 (Fig. 4.13(a)). The mass of the core approaches a fixed value that depends on the initial conditions, this is what we called the collapsed mass M the quantity which is analogous to the black hole mass M_{BH}. More is said about this tendency to a fixed value of the collapsed mass as $t \to t_0$ in Sec. 4.2.1.

This situation is similar in axisymmetry except that the velocity in the core's region is not purely radial, however, the core can still be defined by a negative radial component of the velocity field. In cylindrical coordinates $(s,\, \phi,\, z)$ where, s is the distance from the axis of symmetry (the z-axis), the fluid velocity is given by $\vec{v}(t, s, \phi, z) = (v_s,\, v_\phi,\, v_z)$. Explicitly in terms of the coordinates, $v_s \equiv \dot{s}$, $v_\phi \equiv s\dot{\phi}$ and $v_z \equiv \dot{z}$, where $\dot{} \equiv \frac{d}{dt}$. The radial velocity in these coordinates is then,

$$v_r(s,z) = \frac{s v_s + z v_z}{\sqrt{s^2 + z^2}}. \tag{1.5}$$

So, the sign of v_s and the coordinate z determine whether or not the velocity is "in-falling". Once we have defined the core the measurement of the mass M and specific angular momentum $\vec{a}$ follows by integrating over the core's region.

1.3 Goals/Objectives

The general goal of this research project was to generate numerical solutions of the Euler equations of fluid dynamics (Chap. 2) coupled to Newtonian gravity in spherical and axial symmetry. The purpose of this undertaking is to study critical gravitational collapse. The first objective that we set out to achieve was to extend the spherically-symmetric-fluid work in [48, 64] to accommodate for a more generic/realistic EoS *i.e.* the polytropic ideal gas law (2.18). This was done by numerical computation of the solutions to the dynamical equations in spherical symmetry under conditions of critical collapse. Furthermore, assuming a self-similar ansatz and the simpler barotropic EoS (2.22) the fluid equations can be transformed into a system of ordinary differential equations (ODEs). We also looked for analytic self-similar solutions of this system, and studied their linear stability. The relation, between the dynamical and self-similar solutions was analyzed. The role of the adiabatic index (Γ) in both the dynamical solutions and the spectrum of similarity solutions was also investigated.

The second phase of the project involved extending our project to treat axisymmetric fluids. Given the significant increase in computation, very little work has been done in the form of dynamical simulations of critical collapse beyond spherical symmetry. One notable exception is the critical collapse of gravity waves in axisymmetry [1]. To date, there are no calculations of critical collapse involving a fluid dynamical model beyond spherical symmetry. Our goal was to provide the first such calculations, albeit in Newtonian gravity. We investigated non-spherical effects *i.e.* rotation (initial angular momentum) on the critical phenomena in Newtonian collapse first measured in [48, 64]. Given the analogy between the critical behaviors of the isothermal gas in Newton's gravity and the ultrarelativistic perfect fluid in GR, we argue that this analogy extends to the addition of angular momentum. Both systems are affected by the presence of an additional unstable but non-spherical mode. We measured this effect in the Newtonian system and tested the predicted behavior using the modified scaling laws derived in [34], and discussed in Sec. 2.8.1. These results allow us to reflect on the parallels with the GR perfect fluid system. In particular, we considered the implications that can be drawn from our Newtonian calculation to the full GR+fluid model in the limit where $k \to 0$ with EoS (1.3). Furthermore, the presence of a second growing mode in the critical collapse solution permits an extension of the analogy with statistical mechanics. This is discussed in Chap. 5. We also briefly discussed the effect of the adiabatic index Γ on the critical behavior.

1.3.1 Layout of the Rest of Thesis

The equations of motion are presented in Chap. 2, along with the theoretical basis for our numerical experiments. Following a presentation of the general fluid model, we imposed symmetry restrictions that lead us to the spherically symmetric Euler fluid equations. Two sets of such systems are presented, one pertaining to the more generic polytropic gas and the other to a constant entropy barotropic EoS. Strictly speaking only the latter simpler system, as discussed in Sec. 2.1.2, allows for scale-invariant solutions. The axisymmetric fluid equations are also introduced followed by a discussion of the spherically symmetric linear perturbation to the isentropic fluid equations. A brief discussion of the non-spherical linear perturbations relevant to the axisymmetric evolution is introduced. Lastly, in Chap. 2, the modified, rotation inclusive formalism for type-I and type-II “Newtonian” critical phenomena observed in the numerical experiments is presented.

In Chapter 3 we provide a brief overview of all the numerical techniques used in this project. This begins with presentation of finite difference techniques, followed by a derivation of the finite volume equations necessary for proper treatment of hydrodynamics and conservation laws. We included a brief discussion of the type of *shock-capturing* methods that were used. We then listed the structure of the discrete equations in both spherical and axial symmetry, time-integration technique, regularity and boundary conditions. Finally, code-validation data is given that include the *independent residual* test, and evidence of the code's compliance with the conservation of mass, angular momentum and total energy.

Chapter 4 contains all of our the spherically symmetric calculations. The dynamical solutions obtained using the spherically symmetric code are listed and discussed here. First, we presented the calculation of the self-similar solutions to the isentropic fluid equations, followed by the calculation of their unstable linear perturbations modes. We analyzed the dependence of the results on the chosen value of the so-called adiabatic index Γ in the EoS. Notice that both, the polytropic ideal gas, $P = (\Gamma - 1)\rho\epsilon$ and the isentropic EoS $P = K\rho^{\Gamma}$ (with K being constant) have dependencies on the adiabatic index Γ. This is followed by calculation of the explicit time-dependent equations. These are used to simulate critical gravitational collapse. These results are compared and with the calculated self-similar solutions. Again, the role of Γ is documented.

Chapter 5 is devoted to the presentation of the axisymmetric calculations. It begins with the presentation of the relevant non-spherical perturbation mode, *i.e.* the axial mode. Its dependence on Γ is also noted. Calculations of the evolution of critical collapse data with rotation are given. The results are compared the those obtained in spherical symmetry by turning "off" the angular momentum at the initial state as a check for consistency. The axisymmetric code is used to investigate the effect of angular momentum on the critical solution by calculation of the order parameter *e.g.* the collapsed mass. The connection of these results with GR and statistical mechanics is also discussed.

Finally in Chapter 6 we include some concluding remarks regarding the importance and significance of the accomplished work. We mentioned possible extensions of the current project and further related work.

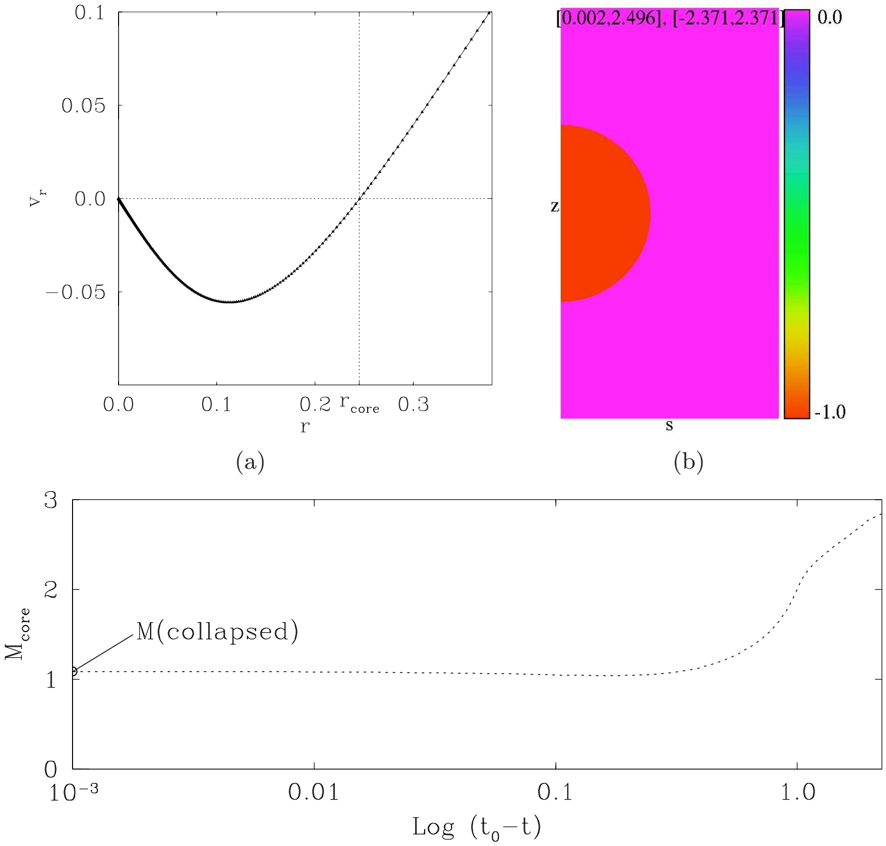

(a)

(b)

(c)

Figure 1.2: The Newtonian analogue of the black hole mass is defined in terms of the total mass contained in the inner-most region of the density distribution with negative radial fluid velocity measured at t near t_0, the time of singularity formation. Panel (a) sketches this situation in spherical symmetry. Early in the evolution such a region is formed, the radial distance measured from the origin ($r = 0$) to the first point where the radial velocity changes sign (from negative to positive) defines the size of the collapsing core r_{core} as seen in (a). Such a region can similarly be defined in axial symmetry be calculating the radial fluid velocity according to Eq. (1.5). Panel (b) sketches this region for a typical axisymmetric evolution, here we highlighted the region where $v_r(t, s, z) < 0$. The core's region corresponds to the area in (b) depicted in red. Again, this region can be unambiguously defined even at the early in the evolution. Once this region is defined, calculation of its mass and angular momentum is straightforward. Panel (c) shows the evolution of the core's mass. Notice that the core's size and mass changes with time but as its evolution nears t_0 it approaches a fixed value. This value is what is referred to as the collapsed mass M(collapsed) or simply M. This is the quantity that is analogous to the black hole mass M_{BH}.

Chapter 2

Formalism and Equations of Motion

This project involves a particular fluid dynamical model. The equations governing the dynamics of fluid flows belong to a class of time-dependent partial differential equations (PDEs) known as *conservation laws*. In their most general representation they constitute a non-linear, vector-valued, multi-dimensional system of hyperbolic equations. In a coordinate system given by $\{\vec{x},\, t\}$ such system in index notation can be written as,

$$\frac{\partial q_k(\vec{x},t)}{\partial t} + \sum_{j=1}^{3} \frac{\partial f_k^j(\mathbf{q})}{\partial x^j} = \psi_k(\mathbf{q};\vec{x},t), \tag{2.1}$$

where $\mathbf{q} = (q_1, \ldots,\, q_k,\, \ldots, q_{\mathcal{N}})^{\intercal}$ is an $\mathcal{N} \times 1$ matrix of so-called *conservative variables*, $\mathcal{N}$ denotes the dimension, *i.e* the number of equations. The function $\mathbf{f}^j(\mathbf{q})$ is also a $\mathcal{N} \times 1$ matrix referred to as the physical flux along the j^{th} direction; in the general case this is a non-linear function of the conservative variables. Finally, $\boldsymbol{\psi}(\mathbf{q};\vec{x},t)$ is the source function.

A specially simple example of a conservation law is given by the advection equation in one spatial dimension,

$$\frac{\partial q_0}{\partial t} + \frac{\partial}{\partial y}(\nu q_0) = 0. \tag{2.2}$$

In its simplest form q_0 is a scalar, thus Eq. (2.2) is a scalar conservation law, and ν is a constant. Note that we used the variable y to denote a generic spatial dimension in order to reserve x for the definition of the similarity variable given by Eq. 2.44. Equation (2.2) describes the 'advection' of quantity q_0 with constant speed ν. The Burger's equation,

$$\frac{\partial q_0}{\partial t} + \frac{\partial}{\partial y}\left(\frac{q_0^2}{2}\right) = 0, \tag{2.3}$$

provides a less trivial example of a scalar conservation law, it has applications in many areas including fluid dynamics *e.g.* [61]. In this case, the flux is a non-linear function of q_0; this leads to nonuniform characteristic flow speed equivalent to q_0 since,

$$\frac{\partial q_0}{\partial t} + q_0 \frac{\partial q_0}{\partial y} = 0, \tag{2.4}$$

this in turn can lead to discontinuities in the profile of q_0 even if it is initially smooth. This arises from the non-linearity of the flux function, a fact that complicates the search for solutions to conservation laws. However, given the ubiquity of these types of systems in many areas of physics and engineering, much effort has been devoted to solving them. This effort consists of developing adequate numerical methods to deal with possibly discontinuous solutions. The numerical approach used in this project is discussed in Chap. 3. In this chapter we present the particular system of conservation laws which comprises our physical model. The particular geometry underlying our symmetry assumptions is also presented here.

2.1 Fluid Dynamics in Newtonian Gravity

We considered the non-relativistic, self-gravitating, inviscid fluid model given by *Euler's equations* of fluid dynamics coupled to Newtonian gravity. They correspond to the inviscid form of the more general *Navier-Stokes* equations. The literature contains many derivations of the Euler equations, one approach being the application of Newtons laws, principles of conservation and thermodynamics, the other, the slow flow, weak-field limit of general relativistic conservation laws. We will not provide an extra derivation here, instead we refer the reader to the [28, 57] for these details. The Euler equations constitute a vector-value system of inhomogeneous conservation laws for the mass, momentum and energy of infinitesimal fluid elements. The gravitational interaction enters the formalism as a source-term in Euler's equations. Newton's law of gravity is described by Poisson's equation. The differential, coordinate independent form of these is given by,

$$\begin{aligned} \frac{\partial \rho}{\partial t} + \nabla \cdot (\rho \vec{v}) &= 0, && (2.5)\\ \frac{\partial \rho \vec{v}}{\partial t} + \nabla \cdot (\rho \vec{v} \otimes \vec{v}) &= -\nabla P - \rho \nabla \varphi, && (2.6)\\ \frac{\partial E}{\partial t} + \nabla \cdot ((E+P)\vec{v}) &= -\rho \vec{v} \cdot \nabla \varphi, && (2.7) \end{aligned}$$

with,

$$\nabla^2 \varphi = 4\pi G \rho. \tag{2.8}$$

The variables $\rho(\vec{x},t)$, $\vec{v}(\vec{x},t)$, $P(\vec{x},t)$, represent the density, velocity and pressure respectively, at location $\vec{x}$ and time t. These are sometimes referred to as the *primitive variables*. The set formed by $\{\rho,\ \rho\vec{v},\ E\}$ are the *conservative variables*. The quantity $\rho\vec{v}$ is the momentum per unit mass, and $E(\vec{x},t)$, defined by

$$E = \rho\epsilon + \frac{1}{2}\rho v^2, \tag{2.9}$$

is the internal and kinetic contributions to the total energy density of the fluid; the variable, $\epsilon(\vec{x},t)$ represents the internal energy per unit mass. This function is related to the other state variables, ρ and P via an equation of state such as,

$$\epsilon = \epsilon(\rho, P). \tag{2.10}$$

Finally, the system is coupled to Newton's law of gravity, equation (2.8), where $\varphi(\vec{x},t)$ is the Newtonian potential. The contribution to the energy missing in Eq. (2.9) is the gravitational potential energy $-\frac{1}{2}\rho\varphi$. Note that we can incorporate this term into Eq. (2.9) leading to an alternative expression for Eq. (2.7), namely,

$$\frac{\partial E_T}{\partial t} + \nabla \cdot ((E_T + P)\vec{v}) = -\rho \frac{\partial \varphi}{\partial t}, \tag{2.11}$$

where, $E_T = \rho\epsilon + \frac{1}{2}\rho v^2 + \frac{1}{2}\rho\varphi$.

2.1.1 Equation of State

The fluid model under consideration is comprised by the six equations (2.5)–(2.8) that relate a total of seven unknown quantities, namely ρ, $\vec{v}$ (three components), P, and ϵ. Clearly, an extra condition is necessary in order to uniquely specify the state of the system. This necessary condition is supplied by the equation of state. It gives a relationship among the thermodynamic quantities, bulk properties of the system. In this project we considered the equations of state (EoS) corresponding to an *ideal gas*. For such EoS the pressure P in the gas is related to the density (ρ) and the temperature (T) according to,

$$P = \frac{k_B}{m}\rho T. \tag{2.12}$$

Where k_B is the Boltzmann constant and m is the mass of the constituent particles. The ideal gas law can be derived from first principles from the kinetic theory of gases [91].

We further restrict our attention to *polytropic gases*, in which the internal energy in a fixed volume is proportional to its temperature, and,

$$\epsilon = c_v T, \tag{2.13}$$

the constant of proportionality c_v is known as the specific heat at constant volume. A process involving a small change in temperature (dT) leads to a corresponding change in internal energy ($d\epsilon$),

$$d\epsilon = c_v dT. \tag{2.14}$$

For a process that includes expansion or contraction but is held at constant pressure, the change is internal energy contributes to the change in temperature of the gas and the work done according to the first law of thermodynamics,

$$d\epsilon = c_p dT - P d(1/\rho). \tag{2.15}$$

The constant c_p is called the specific heat at constant pressure. Note that the change in volume per unit mass is written as $d(1/\rho)$. If we define,

$$h \equiv \epsilon + \frac{P}{\rho}, \tag{2.16}$$

where h is known as the *enthalpy* and since the process is held at constant pressure we can integrate Eq. (2.15) to obtain,

$$h = c_p T. \tag{2.17}$$

Solving for the temperature in Eq. (2.13) and Eq. (2.17) then combining these results using the ideal gas law (2.12) yields,

$$(c_p - c_v)\epsilon = c_v \frac{P}{\rho}.$$

With the definition $\Gamma \equiv c_p/c_v$ we obtain the familiar

$$P = (\Gamma - 1)\rho\epsilon, \tag{2.18}$$

EoS for a polytropic ideal gas.

During a thermodynamic process a quantity of typical interest is the entropy. Often it is more convenient to speak of the entropy per unit mass (*specific entropy*);

this is commonly denoted by s. Roughly speaking s is a measure of the degree of "disorder" in a physical system. From the first law of thermodynamics, a small change in entropy ds is related to the other thermodynamics quantities according to,

$$Tds = d\epsilon + Pd(1/\rho). \tag{2.19}$$

Using the polytropic EoS (2.18) we can eliminate ϵ and obtain,

$$\frac{ds}{c_v} = \frac{dP}{P} - \Gamma\frac{d\rho}{\rho}. \tag{2.20}$$

Integrating this equation and solving for the pressure leads to,

$$P = K_0 e^{s/c_v} \rho^{\Gamma}, \tag{2.21}$$

where K_0 is a constant of integration[2]. Eq. (2.21) is an alternative expression for the polytropic EoS, where the specific entropy is included instead of the internal energy. If the evolution of the fluid takes place at constant entropy, these type of fluid solutions are referred to as *isentropic flows*. Under these conditions ($s = s_0 =$ constant) it is clear that the EoS is simply,

$$P = K\rho^{\Gamma}, \tag{2.22}$$

where $K = K_0 e^{s_0/c_v}$ is also a constant. Thus the pressure is solely a function of the density; the EoS in this case is said to be *barotropic*. Therefore, constant entropy conditions for a polytropic gas lead to a barotropic EoS. As we will see in the next section isentropic flows provide a significant simplification to the dynamical model. A further special circumstance is obtained by setting $\Gamma = 1$ in the barotropic EoS

---

[2] Physically, $K_0 = P_0 \rho_0^{-\Gamma} e^{-s/c_v}$ represents a reference point from which the changes in the state of the gas are measured. P_0, ρ_0 and s_0 are the reference values of pressure, density and entropy.

(2.22). Doing this we get,

$$P = K\rho, \tag{2.23}$$

which is the EoS for an *isothermal gas*.

2.1.2 Restriction to Spherical Symmetry

For spherically symmetric flows, the coordinate free system (2.5)-(2.8), when written in spherical polar coordinates (r, θ, ϕ) becomes,

$$\begin{aligned}
\frac{\partial \rho}{\partial t} + \frac{1}{r^2}\frac{\partial}{\partial r}(r^2 \rho v) &= 0, && (2.24)\\
\frac{\partial \rho v}{\partial t} + \frac{1}{r^2}\frac{\partial}{\partial r}(r^2(\rho v^2 + P)) &= \frac{2P}{r} - \rho\frac{\partial \varphi}{\partial r}, && (2.25)\\
\frac{\partial E}{\partial t} + \frac{1}{r^2}\frac{\partial}{\partial r}(r^2(E+P)v) &= -\rho v\frac{\partial \varphi}{\partial r}, && (2.26)\\
\frac{1}{r^2}\frac{\partial}{\partial r}(r^2\frac{\partial \varphi}{\partial r}) &= 4\pi G\rho. && (2.27)
\end{aligned}$$

Here, the fields $\rho(r,t)$, $v(r,t)$, $P(r,t)$, and $\varphi(r,t)$ have no angular dependence. Therefore, this system is essentially one dimensional. Nonetheless, we would like to eliminate the factors of $1/r^2$ on the radial derivatives and turn Eqs. (2.24)–(2.26) into a Cartesian-like conservation law with sources similar to Eq. (2.1). This is done so that the application of the numerical methods discussed in Chap. 3 is straightforward. The system can be cast into the form of Eq. (2.1) in at least two ways:

- Variable substitution $r \rightarrow r^3$
- Expansion, *i.e.* $\frac{1}{r^2}\frac{\partial}{\partial r}(r^2 f) \rightarrow \frac{2f}{r} + \frac{\partial f}{\partial r}$

The variable substitutions $r \rightarrow r^3$ effectively, regularizes the gradient operator,

$$\frac{1}{r^2}\frac{\partial}{\partial r} \quad \text{by} \quad 3\frac{\partial}{\partial r^3}$$

which follows from application of the chain rule. Under this transformation, the system now has the form,

$$\frac{\partial}{\partial t}\begin{pmatrix}\rho\\ \rho v\\ E\end{pmatrix}+3\frac{\partial}{\partial r^3}\begin{pmatrix}r^2\rho v\\ r^2(\rho v^2+P)\\ r^2(E+P)v\end{pmatrix}=\begin{pmatrix}0\\ \frac{2P}{r}-\rho\frac{\partial\varphi}{\partial r}\\ -\rho v\frac{\partial\varphi}{\partial r}\end{pmatrix}, \tag{2.28}$$

which is that of Eq. (2.1) with the qualification that now the spacial derivative of the flux is with respect to r^3. The so-called expansion of the gradient operator generates a term that appears to be singular at $r = 0$, namely $2f/r$. It should be noted that $f \sim r$ near the origin, so the term $2f/r$ is regular at $r = 0$. This term is collected as a geometric source term in the right-hand-side. Note that the mass conservation Eq. (2.24) acquires a source term. Explicitly, the system then becomes,

$$\frac{\partial}{\partial t}\begin{pmatrix}\rho\\ \rho v\\ E\end{pmatrix}+\frac{\partial}{\partial r}\begin{pmatrix}\rho v\\ (\rho v^2+P)\\ (E+P)v\end{pmatrix}=\begin{pmatrix}-\frac{2\rho v}{r}\\ -\frac{2\rho v^2}{r}-\rho\frac{\partial\varphi}{\partial r}\\ -\frac{2(E+P)v}{r}-\rho v\frac{\partial\varphi}{\partial r}\end{pmatrix}. \tag{2.29}$$

Again, this model has the Cartesian-like form of Eq. (2.1). Since finite difference methods (Chap. 3) were used to solve Poisson's Equation (2.27) we are not concerned with the particular form of this operator in spherical symmetry. In our studies restricted to spherical symmetry both expressions Eq. (2.28) and Eq. (2.29) were solved numerically. We found no discernible difference in the results of the numerical experiments (Chap. 4), following the use of either Eq. (2.28) or Eq. (2.29). This system is supplemented with the polytropic ideal gas EoS (2.18).

Fluid Equation for Isentropic Flows

Further simplification of the equations of motion can be achieved by assuming isentropic conditions. In such a case the ideal gas law EoS reduces to the barotropic form given by Eq. (2.22). This assumption reduces the number of equations needed to describe the flow dynamics. It can be easily checked that the energy equation (2.7) becomes redundant. In addition, given spherical symmetry we can use Gauss' law to integrate Poisson's equation and introduced the variable $M(r,t)$ to denote the total mass contained within a sphere of radius r, thus we arrive at the system,

$$\begin{aligned} \frac{\partial M}{\partial t} + 4\pi r^2 \rho v &= 0, && (2.30)\\ \frac{\partial \rho v}{\partial t} + \frac{1}{r^2}\frac{\partial}{\partial r}(r^2(\rho v^2 + P)) &= \frac{2P}{r} - \frac{GM\rho}{r^2}, && (2.31)\\ \frac{\partial M}{\partial r} &= 4\pi r^2 \rho. && (2.32) \end{aligned}$$

Notice that we have chosen to work with the variable $M(r,t)$ instead of the Newtonian potential $\varphi(r,t)$. This was done in order to ease comparison with previous work where the gravitational interaction in the isentropic fluid model is given in terms of $M(r,t)$. In particular, our notation matches that used in [98]. The Newtonian potential however, can it be easily computed from,

$$\frac{\partial \varphi}{\partial r} = \frac{GM}{r^2}. \tag{2.33}$$

As it will be explicitly evident in Sec. 2.2 the system of fluid equations (2.30)–(2.32) which is only valid for a barotropic EoS, *i.e.* (2.22) allows for particular scale-invariant (self-similar) solutions.

2.1.3 Restriction to Axial Symmetry

Using a cylindrical coordinate system $(s,\ \phi,\ z)$ and assuming axial symmetry, Euler+Poisson equations take the form,

$$\begin{aligned}
\frac{\partial \rho}{\partial t} + \frac{1}{s}\frac{\partial}{\partial s} s(\rho v_s) + \frac{\partial}{\partial z}(\rho v_z) &= 0, & (2.34)\\
\frac{\partial}{\partial t}(\rho v_s) + \frac{1}{s}\frac{\partial}{\partial s} s(\rho v_s^2 + P) + \frac{\partial}{\partial z}(\rho v_s v_z) &= \frac{\rho v_\phi^2 + P}{s} - \rho\frac{\partial \varphi}{\partial s}, & (2.35)\\
\frac{\partial}{\partial t}(\rho v_\phi) + \frac{1}{s}\frac{\partial}{\partial s} s(\rho v_s v_\phi) + \frac{\partial}{\partial z}(\rho v_\phi v_z) &= -\frac{\rho v_s v_\phi}{s}, & (2.36)\\
\frac{\partial}{\partial t}(\rho v_z) + \frac{1}{s}\frac{\partial}{\partial s} s(\rho v_s v_z) + \frac{\partial}{\partial z}(\rho v_z^2 + P) &= -\rho\frac{\partial \varphi}{\partial z}, & (2.37)\\
\frac{\partial E}{\partial t} + \frac{1}{s}\frac{\partial}{\partial s} s(E + P)v_s + \frac{\partial}{\partial z}(E + P)v_z &= -\rho\left(v_s\frac{\partial \varphi}{\partial s} + v_z\frac{\partial \varphi}{\partial z}\right), & (2.38)\\
\frac{1}{s}\frac{\partial}{\partial s} s\frac{\partial}{\partial s}\varphi + \frac{\partial \varphi}{\partial z^2} &= 4\pi\rho. & (2.39)
\end{aligned}$$

All of the fields are functions of s, z and t. Here, we use the variable s to represent the distance from the axis of symmetry, namely the z-axis. Normally, ρ is used, but in our case that variable is reserved for the fluid density. Similar to the spherically symmetric case we proceed to write the axisymmetric system in the Cartesian-like form of Eq. (2.1) with sources. The left-hand-side has the form of a generic two-dimensional conservation law in Cartesian coordinates while geometric terms generated by expanding $\partial_s(s\mathbf{f})$ are collected on the right-hand-side as source terms.

In vector notation, the axisymmetric fluid equations are,

$$\frac{\partial}{\partial t}\begin{pmatrix}\rho\\ \rho v_s\\ \rho v_\phi\\ \rho v_z\\ E\end{pmatrix}+\frac{\partial}{\partial s}\begin{pmatrix}\rho v_s\\ \rho v_s^2+P\\ \rho v_s v_\phi\\ \rho v_s v_z\\ (E+P)v_s\end{pmatrix}+\frac{\partial}{\partial z}\begin{pmatrix}\rho v_z\\ \rho v_z v_s\\ \rho v_z v_\phi\\ \rho v_z^2+P\\ (E+P)v_z\end{pmatrix}=$$

$$\begin{pmatrix}-\frac{\rho v_s}{s}\\ -\frac{\rho(v_s^2-v_\phi^2)}{s}-\rho\frac{\partial\varphi}{\partial s}\\ -\frac{2\rho v_s v_\phi}{s}\\ -\frac{\rho v_s v_z}{s}-\rho\frac{\partial\varphi}{\partial z}\\ -\frac{(E+P)v_s}{s}-\rho(v_s\frac{\partial\varphi}{\partial s}+v_z\frac{\partial\varphi}{\partial z})\end{pmatrix}. \tag{2.40}$$

Finite volume, and multigrid numerical methods were used to obtain approximate solutions to the above axisymmetric system, Eq. (2.40), and Poisson's Eq. (2.39). Just as was done in spherical symmetry the polytropic EoS (2.18) was used to complement this fluid-dynamical model.

2.2 Self-similarity

The property of *self-similarity* can often be found in physical systems that extend across different space and time scales. The concept has a well defined mathematical meaning (see Buckingham's π theorem [4]). Heuristically, the property of self-similarity refers to a system (physical, mathematical *e.g.* geometrical [3]) that resembles itself at different scales. In mathematics, solutions to time-dependent partial differential equations may display self-similarity. This is understood as a consequence of the scale invariance of the dynamical equations, *i.e.* the system is

---

[3] Examples of geometrical self-similarity are fractal objects such as the Sierpinski triangle or the Koch snowflake.

invariant under a rescaling transformation. Two important examples of systems which accept scale-invariant solutions are the Euler's equations of gas dynamics in Newtonian gravity and the general relativistic perfect fluid. We must qualify that in both cases only with an appropriate choice of EoS for the fluid can the solutions to be rendered scale-invariant. In the case of the General Relativistic perfect fluid, only the barotropic EoS (1.3) admits self-similar solutions [65].

We focused on the type of self-similarity that is involved in the solutions to a hydrodynamic system coupled to Newtonian gravity. Under certain circumstances the solution to the dynamical equations (*e.g.* the density field) can be written as a product of a dimensionless variable, a function of time and some combination of other invariant parameters and constants of the physical system. Furthermore, if the functional dependence of the dimensionless variable is given by $r/l(t)$, r being the spatial coordinate and $l(t)$ some time-dependent length scale, the solution is then said to be self-similar. Considering only one spatial dimension (*e.g.* spherical symmetry) this can be written as,

$$p_j(r,t) = c_j(t)\theta_j(x), \tag{2.41}$$

where $x = r/c_0(t)$. The explicit time dependence is completely contained in the functions $c_j(t)$, along with all other parameters and constants; these have been suppressed in the writing of Eq. (2.41). The index j denotes the j-th field variable. If the form of $\{c_j(t)\}$ can be obtained directly from dimensional analysis then this is referred to as a self-similar solution of the *first kind* [5]. Alternatively, if this cannot be obtained from dimensional considerations alone, but requires solving an eigenvalue problem, then it is called incomplete self-similarity, or self-similarity of the *second kind* [5]. This type of self-similar solutions are not relevant in our project, thus they will not be discussed any further.

Self-similar solutions of the first kind have been identified in the spherically symmetric fluid-dynamic+Newtonian gravity models [56, 60, 81, 98, 108]. For some models the dimensionless variable is $x \propto r/t$. This implies a linear scaling between the space and time variable *i.e.* the dimensionless functions $\{\theta_j(x)\}$ remain invariant under $(r,\, t) \rightarrow (\eta r,\, \eta t)$, where $\eta \equiv$ constant. Other models [98, 108], the scaling between the space and time variables is non-linear, $r \propto t^{\sigma}$, where σ is a function of the model parameters. All of these concepts can be formalized by introducing the machinery of group theory. This is done specifically in the context of Galilean "spacetime" in [14].

Even though this project is strictly Newtonian, important parallels exist between self-similarity in Newtonian and General Relativistic hydrodynamic systems. For simplicity, we only consider self-similarity in spherical symmetry. Self-similarity of the first kind in General Relativity implies the existence of a *homothetic* vector field $\boldsymbol{\xi}$ such that the solution (metric ($g_{\mu\nu}$), and matter fields) in the appropriate coordinates ($\tau \equiv -\ln t$, $\zeta \equiv r/t$) is re-scaled under Lie differentiation along $\boldsymbol{\xi} = -\partial/\partial\tau$, *e.g.* $\mathcal{L}_{\boldsymbol{\xi}} g_{\mu\nu} = 2 g_{\mu\nu}$, since $g_{\mu\nu}(\tau, \zeta) = e^{-2\tau} \tilde{g}_{\mu\nu}(\zeta)$, where $\tilde{g}_{\mu\nu}(\zeta)$ is scale invariant. Note that the solution's spatial dependence enters only through the ratio $\zeta = r/t$. These solutions were first studied in the pioneering work of Cahill and Taub [11]. The connection between this homothetic solution and its Newtonian counterpart is discussed in Sec. 2.6. A generalization of self-similarity of the second kind exists in General Relativity, called *kinematic self-similarity* [12, 13]. At the present time kinematic self-similarity does not seem to occur in critical phenomena in gravitational collapse in GR and for this reason it will not be discussed here.

2.3 Self-similar Ansatz

A spherically symmetric ideal gas at constant entropy is modeled by Eqs. (2.30)–(2.32). This system admits a self-similar solution. Our interest in this isentropic model is to investigate the self-similar solutions that might describe the fluid evolution in the 'epoch' prior to gravitational collapse. If we define the time variable t such that this event (collapse) happens at $t = 0$, implies we are concerned with the interval $\infty < t < 0$. Borrowing from the approach and notation used by Suto and Silk (1988) [98], the transformation

$$t \to -t, \quad v \to -v, \quad \rho \to \rho \quad P \to P, \quad \text{and} \quad M \to M, \tag{2.42}$$

leaves the system of Eqs. (2.30)–(2.32) invariant. Following this transformation we considered only $0 < t < \infty$. In some parts of this thesis we have used another shift of the time coordinate, namely, $t \to (t_0 - t)$ where t_0 denotes the time of collapse. However, unless otherwise specified we use t and the event of interest happens at $t = 0$.

The nature of the self-similar solution can be determined by dimensional analysis. We began by assuming a factorization of the time dependence in all of the dynamical fields according to,

$$\begin{aligned} r &= c_0(t)x, \\ \rho(r,t) &= c_1(t)\alpha(x),\ v(r,t) = c_2(t)u(x), \\ P(r,t) &= c_3(t)\beta(x),\ M(r,t) = c_4(t)m(x). \end{aligned} \tag{2.43}$$

The fields $u(x)$, $\alpha(x)$, $\beta(x)$, $m(x)$ are the scale-invariant variables related to v, ρ, P and M, respectively. Assuming a power-law scaling $c_0(t) \propto t^n$ the other coefficients $c_1(t)$, $c_2(t)$, $c_3(t)$, and $c_4(t)$ can be computed following substitution into Eqs. (2.30)–(2.32). With the correct coefficients (2.43) becomes,

$$x = \frac{r}{\sqrt{\kappa} t^n}, \tag{2.44}$$

$$v(r,t) = \sqrt{\kappa} t^{n-1} u(x), \tag{2.45}$$

$$\rho(r,t) = \frac{\alpha(x)}{4\pi G t^2}, \tag{2.46}$$

$$P(r,t) = \frac{\kappa t^{2n-4}}{4\pi G} (\alpha(x))^\Gamma, \tag{2.47}$$

$$M(r,t) = \frac{\kappa^{3/2} t^{3n-2}}{(3n-2)G} m(x). \tag{2.48}$$

As expected the coefficients involve the parameters and constants G, K (through $\kappa = K(4\pi G)^{1-\Gamma}$) and Γ. The exponent, $n = 2 - \Gamma$ [98]. If suitable solutions for the similarity variables $u(x)$, $\alpha(x)$, $\beta(x)$, $m(x)$ can be found, the general case $\Gamma \neq 1$ corresponds to self-similar solutions of the first kind with non-linear scaling $r \propto t^{2-\Gamma}$. The case where $\Gamma = 1\,(n = 1)$ corresponds to an isothermal gas, and linear scaling $r \propto t$.

The autonomous system that results from applying this self-similar ansatz, Eqs. (2.44)–(2.48) into the isentropic gas model, Eqs. (2.30)–(2.32) is,

$$(nx-u)\frac{d\alpha}{dx} - \alpha\frac{du}{dx} = -\frac{2\alpha}{x}(x-u) \tag{2.49}$$

$$\Gamma\alpha^{\Gamma-2}\frac{d\alpha}{dx} - (nx-u)\frac{du}{dx} = -\frac{nx-u}{3n-2}\alpha - (n-1)u, \tag{2.50}$$

$$\frac{dm}{dx} = (3n-2)x^2\alpha. \tag{2.51}$$

After some algebraic manipulations we arrive at,

$$\frac{d\alpha}{dx} = \frac{\alpha}{(nx-u)^2 - \Gamma\alpha^{\Gamma-1}}\left[(n-1)u + \frac{nx-u}{3n-2}\alpha - 2\frac{(x-u)(nx-u)}{x}\right], \tag{2.52}$$

$$\frac{du}{dx} = \frac{1}{(nx-u)^2 - \Gamma\alpha^{\Gamma-1}}\left[(nx-u)(n-1)u + \frac{(nx-u)^2}{3n-2}\alpha - 2\Gamma\frac{x-u}{x}\alpha^{\Gamma-1}\right], \tag{2.53}$$

together with the algebraic relation,

$$m(x) = \alpha x^2(nx-u). \tag{2.54}$$

Thus solving equations (2.52) and (2.53) for the similarity variables $\alpha(x)$ and $u(x)$ with appropriate boundary conditions plus the algebraic condition (2.54) completely determines the self-similar flow.

2.3.1 Boundary Conditions

In considering solutions to Eq. (2.52), and Eq. (2.53) we restricted our attention to those which are regular (analytic) at $x = 0$. This condition is imposed by assuming a Taylor series expansion of $\alpha(x)$ and $u(x)$ in x near the origin. The expansions are inserted into Eq. (2.52) and Eq. (2.53) in order to determine the expansion coefficients. Up to $\mathcal{O}(x^4)$ the asymptotic solutions are given by,

$$\begin{aligned} u(x) &= \frac{2}{3}x - \frac{\alpha_*^{1-\Gamma}}{15\Gamma}\Big(\alpha_* - \frac{2}{3}\Big)\Big(n - \frac{2}{3}\Big)x^3 + \ldots, && (2.55)\\ \alpha(x) &= \alpha_* - \frac{\alpha_*^{2-\Gamma}}{6\Gamma}\Big(\alpha_* - \frac{2}{3}\Big)x^2 + \ldots && (2.56)\end{aligned}$$

where $\alpha_* \equiv \alpha(x = 0)$. Here, as was done in [48, 64] we will refer to the parameter $Q_0 = \ln \alpha_*$ when specifying the above boundary conditions. Studies involving other asymptotic solutions which are not regular at at $x = 0$ exist in the literature. However, they were not considered in this project. These are discussed in [63, 98, 105]. Furthermore, we seek solutions to Eq. (2.52) and Eq. (2.53) that exists over an arbitrary range in x *i.e.*, $x \in (0, \infty)$. In doing so we must be cautious near the singular point,

$$nx - u = \sqrt{\Gamma}\alpha^{(\Gamma-1)/2}, \qquad (2.57)$$

where the denominator of equations (2.52) and (2.53) vanishes. Known also as the sonic curve, this set of points consists of the all points for which the flow speed $v(r, t)$ relative to the curve r/t equals the local sound speed, $c_s = \sqrt{\kappa}t^{n-1}(\Gamma\alpha^{\Gamma-1})^{1/2}$. In our treatment we required that α and u be analytic everywhere including across the sonic critical curve. Thus, in the vicinity of the sonic point $x = x_s + \delta x$ it is assumed that the solution can be Taylor expanded,

$$\begin{aligned} \alpha(x) &= \alpha_0 + \alpha_1(x - x_s) + \alpha_2(x - x_s)^2 + \ldots, && (2.58)\\ u(x) &= u_0 + u_1(x - x_s) + u_2(x - x_s)^2 + \ldots. && (2.59)\end{aligned}$$

The parameter x_s labels the sonic point and becomes a new parameter in the problem whose value is yet to be determined. As a necessary condition for continuity is that the numerator of Eq. (2.52) must vanish at the sonic point;

$$0 = (n-1)u_0 + \frac{nx_s - u_0}{3n-2}\alpha_0 - 2\frac{(x_s - u_0)(nx_s - u_0)}{x_s}. \tag{2.60}$$

This, together with Eq. (2.57) allows us to find the coefficients $\{\alpha_0, u_0\}$ in terms of x_s. If $n = 1$ (isothermal gas), the solution for α_0 and u_0 can be obtained in closed form in terms of x_s. However, if $n \neq 1$ then $\{\alpha_0, u_0\}$ can only be computed numerically by first determining a numerical value for x_s. We can generate conditions for the higher order coefficients namely, α_1, u_1, α_2, u_2, $\ldots$ by examining the analytic behavior of Eqs. (2.53), (2.52) near the sonic point x_s. This is accomplished through the substitution of the expansions (2.58), (2.59) into Eqs. (2.53), (2.52). Keeping terms up to linear order in $x - x_s$ yields,

$$F_1 + F_2(x - x_s) + \mathcal{O}((x - x_s)^2) = 0, \tag{2.61}$$

$$G_1 + G_2(x - x_s) + \mathcal{O}((x - x_s)^2) = 0, \tag{2.62}$$

where, F_1, G_1, F_2, G_2 are complicated expressions involving the coefficients, α_1, u_1, α_2, u_2 and x_s. Clearly, from the linear independence $(x - x_s)^k$ where $k \in \mathbb{Z}$, the coefficients F_1, G_1, F_2, G_2 must all vanish, and this gives a set of equations that allows us to determine the coefficients α_1, u_1, α_2, u_2. One important feature which aids computation of the solution is the fact that each set of conditions involves only coefficients of the corresponding and lower orders. The nonlinear set of conditions has the following general form,

$$F_0(\alpha_0, u_0, \Gamma, x_s) = 0, \tag{2.63}$$

$$G_0(\alpha_0, u_0, \Gamma, x_s) = 0, \tag{2.64}$$

$$F_1(\alpha_0, u_0, \alpha_1, u_1, \Gamma, x_s) = 0, \tag{2.65}$$

$$G_1(\alpha_0, u_0, \alpha_1, u_1, \Gamma, x_s) = 0, \tag{2.66}$$

$$F_2(\alpha_0, u_0, \alpha_1, u_1, \alpha_2, u_2, \Gamma, x_s) = 0, \tag{2.67}$$

$$G_2(\alpha_0, u_0, \alpha_1, u_1, \alpha_2, u_2, \Gamma, x_s) = 0. \tag{2.68}$$

Clearly,

$$F_0 = n x_s - u_0 - \sqrt{\Gamma}\alpha_0^{(\Gamma-1)/2}, \tag{2.69}$$

$$G_0 = (n-1)u_0 + \frac{n x_s - u_0}{3n-2}\alpha_0 - 2\frac{(x_s - u_0)(n x_s - u_0)}{x_s}. \tag{2.70}$$

We solved Eqs. (2.63)–(2.68) in sequence (via an iterative method such as Newton's method), obtaining the lowest order solution(s) α_0, u_0 and using them in the higher order ones. A consistency check can be performed on equations Eqs. (2.63)–(2.68), where setting $n = 1$ (isothermal case) should yield a system that is soluble in closed form. In this case, the solutions for the coefficients given in terms of x_s should match those obtained in [47, 56, 60, 81, 95]. These expressions are also included in Appx. A.

2.4 Spherically Symmetric Linear Perturbations

Included with our study of spherically symmetric self-similar solutions to Eq. (2.52), and Eq. (2.53) is an investigation of their linear stability. We considered spherically symmetric linear perturbations about the self-similar solutions, $\bar{\alpha}(x)$, $\bar{u}(x)$, $\bar{m}(x)$.

These can be introduced in the following form,

$$\begin{aligned} \alpha(r,t) &= \bar{\alpha}(x) + \varepsilon\alpha_1(x,t), \\ u(r,t) &= \bar{u}(x) + \varepsilon u_1(x,t), \\ m(r,t) &= \bar{m}(x) + \varepsilon m_1(x,t), \end{aligned} \tag{2.71}$$

for $\varepsilon << 1$. The explicit time dependence is contained in the quantities $\alpha_1(x,t)$, $u_1(x,t)$ and $m_1(x,t)$. Plugging the above ansatz, (2.71)–(2.72) into the dynamical system governing isentropic flows, *i.e.* Eqs. (2.30)-(2.32) will yield, up to linear order in ε the system,

$$0 = m_1' - (3n-2)x^2\alpha_1, \tag{2.72}$$

$$0 = (nx-\bar{u})x^2\alpha_1 - x^2\bar{\alpha}u_1 - m_1 - \frac{\dot{m}_1 t}{3n-2}, \tag{2.73}$$

$$\begin{aligned} 0 = &- \frac{t\dot{m}_1{}'}{3n-2} + (nx-\bar{u})x^2\alpha_1' - (\bar{u}'-2)x^2\alpha_1 - (\bar{\alpha}'u_1 + \bar{\alpha}u_1')x^2 \\ &- 2x(\bar{\alpha}u_1 + \alpha_1\bar{u}), \end{aligned} \tag{2.74}$$

$$\begin{aligned} 0 = &- \frac{t\dot{m}_1}{(3n-2)^2x^2} - \frac{\bar{\alpha}u_1}{3n-2} - (nx-\bar{u})u_1' + (n-1)u_1 \\ &- (\alpha_1\bar{\alpha}' - \bar{\alpha}\alpha_1')\Gamma\bar{\alpha}^{\Gamma-3} + u_1\bar{u}' + t\dot{u}_1 + \frac{(nx-\bar{u})\alpha_1}{3n-2}. \end{aligned} \tag{2.75}$$

The notation "prime" and/or "dot" ($'$ and/or $\dot{}$) indicate partial differentiation with respect to x and/or t. The time dependence of the perturbations is assumed to follow,

$$\begin{aligned} \alpha_1(x,t) &= \delta\alpha(x)e^{\lambda\tau(t)}, \\ u_1(x,t) &= \delta u(x)e^{\lambda\tau(t)}, \\ m_1(x,t) &= \delta m(x)e^{\lambda\tau(t)}, \end{aligned} \tag{2.76}$$

where,

$$\tau = -\ln t. \tag{2.77}$$

Using these ansatz in Eqs. (2.72)–(2.75) and dropping the “bar” notation on the self-similar solutions by simply writing α and u together with some algebraic manipulations, we obtained a system of ODEs for the perturbations functions $\delta\alpha(x)$ and $\delta u(x)$. These are,

$$\begin{aligned}
\delta\alpha' =& \frac{1}{(nx-u)^2 - \Gamma\alpha^{\Gamma-1}} \Bigg\{ \Big[-\Gamma\alpha^{\Gamma-2}\alpha' + \frac{2u(nx-u)}{x} + \frac{(nx-u)\alpha}{3n-2-\lambda} \\
& + (u'-2-\lambda)(nx-u)\Big]\delta\alpha + \Big[(u'+3n-\lambda-1)\alpha + \\
& (nx-u)\alpha' - \frac{2u\alpha}{x} - \frac{\alpha^2}{3n-2-\lambda}\Big]\delta u\Bigg\}, \qquad (2.78)\\
\delta u' =& \frac{1}{\alpha((nx-u)^2 - \Gamma\alpha^{\Gamma-1})} \Bigg\{ \Big[(u'-\lambda-2)\Gamma\alpha^{\Gamma-1} - \frac{2u}{x}\Gamma\alpha^{\Gamma-1} - \\
& (nx-u)\Gamma\alpha^{\Gamma-2} - (nx-u)\Gamma\alpha^{\Gamma-2}\alpha' + \frac{(nx-u)^2\alpha}{3n-2-\lambda}\Big]\delta\alpha + \\
& \Big[\frac{2}{x}\Gamma\alpha^{\Gamma} + \Gamma\alpha^{\Gamma-1}\alpha' + (nx-u)(u'+n-\lambda-1)\alpha - \\
& \frac{(nx-u)\alpha^2}{3n-2-\lambda}\Big]\delta u\Bigg\}, \qquad (2.79)\\
\delta m' =& -(3n-2)x^2\delta\alpha, \qquad (2.80)\\
\delta m =& \frac{(3n-2)(nx-u)x^2}{3n-2-\lambda}\delta\alpha - \frac{(3n-2)x^2\alpha}{3n-2-\lambda}\delta u. \qquad (2.81)
\end{aligned}$$

Again, we required that the perturbations also be analytic everywhere. In particular, we impose regularity at $x = 0$ and at the sonic point ($x = x_s$). Previously we demanded analyticity of the self similar solutions α and u at $x = 0$ leading us to the Eqs. (2.55) and (2.56). Applying these asymptotic solutions to the perturbation equations we find that their leading order behavior near the origin ($x << 1$) is given by,

$$\begin{aligned} \delta\alpha &= \frac{3e^{Q_0}}{\lambda}\delta u_0, && (2.82) \\ \delta u &= x\delta u_0. && (2.83) \end{aligned}$$

Where δu_0 is a free parameter which can be used to normalize the perturbation mode. At the sonic point a necessary condition for analyticity is that the numerator in Eq. (2.78) vanishes, *i.e.*

$$\begin{aligned} &(nx-u)\Big[-(nx-u)\frac{\alpha'}{\alpha}+\frac{2u}{x}+u'-2-\lambda+\frac{\alpha}{3n-2-\lambda}\Big]\delta\alpha+ \\ &\qquad\Big[u'+3n-\lambda-1+(nx-u)\frac{\alpha'}{\alpha}-\frac{2u}{x}-\frac{\alpha}{3n-2-\lambda}\Big]\alpha\delta u=0. \qquad (2.84) \end{aligned}$$

Given the above condition (2.84) it can be easily checked that the numerator in Eq. (2.79) also vanishes. Once the expansions (2.58) and (2.59) have been inserted into Eq. (2.84) we have a boundary condition at the sonic point. Note that since we only have one condition the perturbations can only be determined up to a constant factor, again, this constant factor is a fundamental freedom that can use it to normalize the perturbation function. As it will be discussed in more detail later on, the boundary conditions (2.82)–(2.84) can only be satisfied for certain values of the Lyapunov exponent, λ. We will further restrict our search for growing perturbation modes $\lambda > 0$ which would tell us the stability of the solutions α and u. Our stability analysis is a generalization of the work of [47] for a polytropic EoS. Again, a consistency check can be performed in the limit $\Gamma \to 1$ where their results should be recovered.

2.5 Non-spherical Linear Perturbations

Clearly, a more complete study concerning the stability of the spherically symmetric self-similar solutions mentioned in Sec. 2.3 must include perturbations arising from small departures from spherical symmetry. Previously, several papers have been devoted to this topic, notably [38–41]. These investigations ware conducted considering general non-spherical perturbations in terms of scalar and vector spherical harmonics as outlined in [6]. These are most conveniently treated in spherical coordinates r, ϕ, θ, r is the radial distance from a fixed origin and ϕ and θ are the azimuthal and polar angles, respectively. Since the background solution is the spherically symmetric self-similar solution the formulation of the system of perturbation equations also includes the variables x and τ as defined in Eqs. (2.44) and (2.77). Non-spherical perturbations about the self-similar solutions for the scalar quantities in our model *e.g.* the dimensionless density variable α, generally have the form,

$$\alpha(\tau, x, \phi, \theta) = \bar{\alpha}(x) + \sum_{\ell,m} \delta\alpha_\ell^m(x) Y_\ell^m(\phi, \theta) e^{\lambda_\ell^m \tau}. \tag{2.85}$$

$\delta\alpha_\ell^m$ is a small radial functions, λ_ℓ^m are the corresponding growth rates and $Y_\ell^m(\phi, \theta)$ are the spherical harmonics. The linear independence and completeness properties of the spherical harmonics allows for the representation of any angular dependent functions in terms of their sum. Similar deviations from spherical symmetry can be considered for the other scalar quantities such as $m(\tau, x, \phi, \theta)$.

General perturbations for the vector-valued quantities have a more complicated representation. Fortunately, such general representations are possible through vector-spherical-harmonics. As explained in [6] the general vector perturbation can be done by taking sums of the vector quantities,

$$\vec{Y}_\ell^m(\phi, \theta) \equiv Y_\ell^m(\phi, \theta)\hat{r}, \tag{2.86}$$

$$\vec{\Psi}_\ell^m(\phi, \theta) \equiv \nabla Y_\ell^m(\phi, \theta), \tag{2.87}$$

$$\vec{\Phi}_\ell^m(\phi, \theta) \equiv \hat{r} \times \nabla Y_\ell^m(\phi, \theta). \tag{2.88}$$

Therefore, perturbations about the self-similar velocity field $\vec{u}(x) = (\bar{u}(x),\, 0,\, 0)$ have the form,

$$\vec{u}(\tau, x, \phi, \theta) = \vec{\bar{u}}(x) + \sum_{\ell,m} \delta u_\Psi(x) \vec{\Psi}_\ell^m(\phi, \theta) e^{\lambda\tau} + \sum_{\ell,m} \delta u_\Phi(x) \vec{\Phi}_\ell^m(\phi, \theta) e^{\lambda\tau} \tag{2.89}$$

Indices $\{\ell,\, m\}$ are implied on the Lyapunov exponent λ and the small quantities δu_Ψ, δu_Φ; they have been suppressed to keep the notation from getting too cluttered. Terms which are proportional to $\vec{\Psi}_\ell^m$ are labeled as "polar" perturbations, whereas those proportional to $\vec{\Phi}_\ell^m$ are called "axial" perturbations. This naming convention is also used in [30, 33].

Linear perturbations in the small δ-quantities for the Euler+Poisson system with EoS (2.22) decouple into either, purely polar or, purely axial perturbations. This means that to linear order, the equations resulting from considering small perturbations proportional to Eqs. (2.86)–(2.88) of the spherically symmetric fields do not have a coupled mixtures of $\vec{\Psi}_\ell^m$ and $\vec{\Phi}_\ell^m$ terms, but an independent sum of the two. According to the work done in [39] the lowest-order polar perturbation of any possible self-similar solutions of the polytropic gas is given by an $\ell = 2$ mode. This is called the bar-mode instability. With our choice of initial data (Sec. 2.7) this mode can only be observed in full three dimensional simulations, see [38]. Due to its limited relevance in our dynamical axisymmetric model, and the fact that no evidence of unstable polar modes were detected in our simulations (Chap. 5) we did not include further analysis of polar perturbations. Nevertheless, explicit calculation of all possible unstable polar modes about the spherically-symmetric self-similar solutions for the polytropic gas is left as extension to this thesis. Other reasons for our omission of these polar modes are discussed in Sec. 2.6. Nevertheless, the polar perturbation equations about the self-similar solutions for the polytropic gas are provided in Appx. B. The axial perturbations about the self-similar velocity field $\vec{\bar{u}}(x)$ are given by,

$$\begin{pmatrix} u_r \\ \delta u_\theta \\ \delta u_\phi \end{pmatrix} = \begin{pmatrix} \bar{u}(x) \\ \dfrac{\delta u_\Phi(x)}{x\sin\theta}\dfrac{\partial}{\partial\phi}Y_\ell^m(\theta,\phi)e^{\lambda\tau} \\ -\dfrac{\delta u_\Phi(x)}{x}\dfrac{\partial}{\partial\theta}Y_\ell^m(\theta,\phi)e^{\lambda\tau} \end{pmatrix}. \tag{2.90}$$

Note that the dimensionful fluid velocity is obtained through

$$\vec{v}(r,\phi,\theta) = \sqrt{\kappa}t^{n-1}\begin{pmatrix} u_r \\ \delta u_\theta \\ \delta u_\phi \end{pmatrix} \tag{2.91}$$

from Eq. (2.45) and recalling that $\kappa = K(4\pi G)^{1-\Gamma}$ and $n = 2-\Gamma$. Inserting this expression for the velocity into the continuity Eq. (2.5) and keeping only the linear-order terms in the perturbations it is easy to show that

$$\delta\alpha_\ell^m(x) = 0. \tag{2.92}$$

Recall that $\delta\alpha_\ell^m(x)$ represent non-spherical perturbations about the spherically symmetric dimensionless density variable $\bar{\alpha}(x)$. From this and Poisson's equation follows that

$$\delta\varphi_\ell^m(x) = 0 \tag{2.93}$$

for the perturbations of the Newtonian potential. We have already mentioned that the energy Eq. (2.7) becomes redundant for a barotropic EoS, therefore, the axial perturbations in this case are completely governed by the momentum equation (2.6).

When this is written in spherical coordinates we get,

$$\begin{aligned}\frac{\partial \rho v_r}{\partial t} + \frac{1}{r^2}\frac{\partial}{\partial r}(r^2 \rho v_r^2) + \frac{1}{r\sin\theta}\frac{\partial}{\partial\theta}(\sin\theta \rho v_r v_\theta) + \frac{1}{r\sin\theta}\frac{\partial}{\partial\phi}(\rho v_r v_\phi)\\ -\frac{\rho(v_\theta^2 + v_\phi^2)}{r} = -\frac{\partial P}{\partial r} - \rho\frac{\partial\varphi}{\partial r},\end{aligned} \tag{2.94}$$

$$\begin{aligned}\frac{\partial \rho v_\theta}{\partial t} + \frac{1}{r^2}\frac{\partial}{\partial r}(r^2 \rho v_r v_\theta) + \frac{1}{r\sin\theta}\frac{\partial}{\partial\theta}(\sin\theta \rho v_\theta^2) + \frac{1}{r\sin\theta}\frac{\partial}{\partial\phi}(\rho v_\theta v_\phi)\\ +\frac{\rho v_r v_\theta}{r} - \cot\theta\frac{\rho v_\phi^2}{r} = -\frac{1}{r}\frac{\partial P}{\partial\theta} - \frac{\rho}{r}\frac{\partial\varphi}{\partial\theta},\end{aligned} \tag{2.95}$$

$$\begin{aligned}\frac{\partial \rho v_\phi}{\partial t} + \frac{1}{r^2}\frac{\partial}{\partial r}(r^2 \rho v_r v_\phi) + \frac{1}{r\sin\theta}\frac{\partial}{\partial\theta}(\sin\theta \rho v_\theta v_\phi) + \frac{1}{r\sin\theta}\frac{\partial}{\partial\phi}(\rho v_\phi^2)\\ +\frac{\rho v_r v_\phi}{r} + \cot\theta\frac{\rho v_\theta v_\phi}{r} = -\frac{1}{r\sin\theta}\frac{\partial P}{\partial\phi} - \frac{\rho}{r\sin\theta}\frac{\partial\varphi}{\partial\phi}.\end{aligned} \tag{2.96}$$

The linear perturbations are obtained by inserting equations (2.90), (2.92), and (2.93) into the above system; we find that,

$$\frac{\partial}{\partial t}(\rho\delta v_\theta) + \frac{1}{r^2}\frac{\partial}{\partial r}(r^2\rho v_r \delta v_\theta) = 0, \tag{2.97}$$

$$\frac{\partial}{\partial t}(\rho\delta v_\phi) + \frac{1}{r^2}\frac{\partial}{\partial r}(r^2\rho v_r \delta v_\phi) = -\frac{\rho v_r \delta v_\phi}{r}. \tag{2.98}$$

In term of the similarity variables this becomes,

$$(\lambda + 3 - n)\frac{\alpha\delta u_\Phi}{x} + nx\frac{d}{dx}\left(\frac{\alpha\delta u_\Phi}{x}\right) - \frac{1}{x^2}\frac{d}{dx}(x\alpha u\delta u_\Phi) = \frac{\alpha u \delta u_\Phi}{x^2} \tag{2.99}$$

Combining this equation with relation (2.49) and some algebraic manipulations we get the following simple equation for the axial perturbations,

$$(\lambda - 2n + 1)\delta u_\Phi + (nx - u)\frac{d\delta u_\Phi}{dx} = 0. \tag{2.100}$$

Using the fact that near the origin $u \approx 2x/3$ we can solve for λ,

$$\begin{aligned}\lambda &= 3 - 2\Gamma + \left(\Gamma - \frac{4}{3}\right) \lim_{x\to 0} \left(\frac{x\dfrac{d\delta u_\Phi}{dx}}{\delta u_\Phi} \right) \\ &= \frac{1}{3} + \left(\Gamma - \frac{4}{3}\right) \left(\lim_{x\to 0} \left(\frac{x\dfrac{d\delta u_\Phi}{dx}}{\delta u_\Phi} \right) - 2 \right). \end{aligned} \tag{2.101}$$

We only consider perturbations which are regular at the origin, in particular $v_\phi \sim r$ near $r = 0$. This implies that $\delta u_\Phi(x)$ can be Taylor expanded in powers or x thus,

$$\delta u_\Phi(x) = \sum_{\nu=0}^{\infty} x^{\ell+1} a_{\ell\nu} x^{2\nu} \quad \text{where,} \quad x \ll 1, \quad \ell = 1,\, 2,\, \ldots \tag{2.102}$$

and $a_{\ell\nu}$ are scalar coefficients. The above expression Eq. (2.102) ensures regularity of the v_ϕ near the origin. Inserting expression (2.102) into Eq. (2.101) we get,

$$\lambda_{\ell,\nu} = \frac{1}{3} + \left(\Gamma - \frac{4}{3}\right)(\ell - 1 + 2\nu)\,. \tag{2.103}$$

In the case where the overall perturbation grows linearly in x the fastest growing mode corresponds to ($\ell = 1$, $\nu = 0$) with growth rate $\lambda = 1/3$, provided $\Gamma < 4/3$. Therefore, all regular self-similar solutions of the polytropic gas have an ($\ell = 1$) unstable axial mode. For the an isothermal gas ($\Gamma = 1$) only the $\ell = 1$ mode is unstable. If we consider $\Gamma \in [1,\, 4/3)$ higher ℓ-values can be unstable, however, their growth rates are always less than 1/3, see Fig. 2.1. For example, in the case where $1 < \Gamma \lessapprox 1.17$ the polytropic gas contains two unstable axial modes, namely $\ell = 1$ an $\ell = 2$. However, if we restrict our attention to axial symmetry, along with equatorial symmetry of the initial data (Sec. 2.7), the $\ell = 2$ mode is suppressed. The $\ell = 1$ axial perturbation mode is often called the *spin-up* mode, [38, 41]. A formal solution for the spin-up mode can be obtained by direct integration of Eq. (2.100)

$$\delta u_\Phi(x) = \delta u_{\Phi 0} \exp\left(-\int \frac{\lambda - 2n + 1}{nx - u} dx\right). \tag{2.104}$$

$\delta u_{\Phi 0}$ is a constant of integration. From this expression it is clear that all regular self-similar solutions are unstable against the spin-up mode.

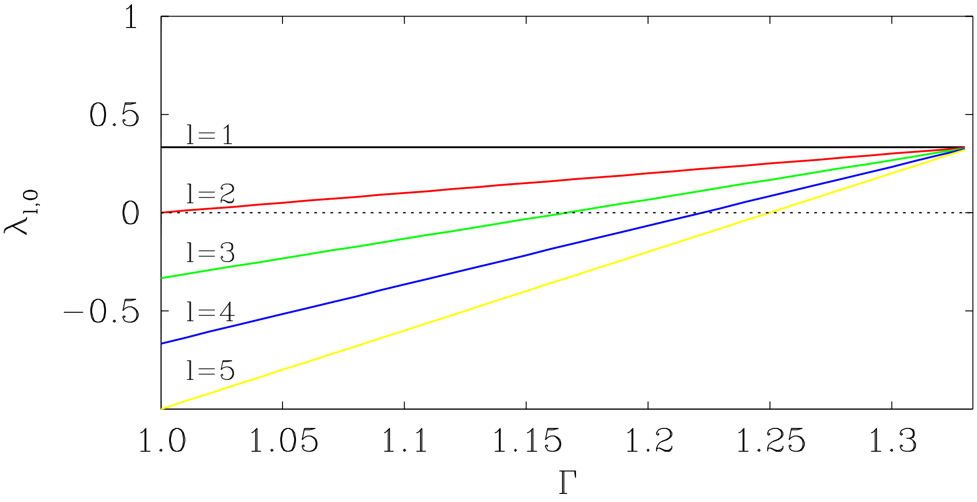

Figure 2.1: This plot illustrates the spectrum of axial perturbation modes and its dependence on Γ. For the isothermal gas ($\Gamma = 1$) only the $\ell = 1$ perturbation mode is unstable with growth rate $\lambda_{1,0} = 1/3$. The $\ell = 1$ mode has the same growth rate ($\lambda_{1,0} = 1/3$) independent of the value of Γ, thus all self-similar solutions of the polytropic gas are unstable against this axial perturbation. Known as the spin-up mode, it is the fastest growing axial mode for $1 \le \Gamma < 4/3$. Values of $\Gamma > 1$ lead to higher unstable ℓ modes, from these, the $\ell = 2$ mode is first to "turns on" (becomes unstable) at $\Gamma > 1$ but its growth rate is less than that of the spin-up mode for the values of Γ that were considered. Given, axial symmetry and the symmetry of the initial data (Sec. 2.7), this $\ell = 2$ mode is not observable. The $\ell = 3$ mode becomes unstable at $\Gamma \gtrapprox 1.17$.

2.6 Correspondence with General Relativity

This investigation was initially motivated by previous studies involving spherically symmetric self-similar solutions of a perfect fluid in General relativity (GR) [10, 11, 22, 45–47, 73, 74, 77, 96]. All these studies considered a barotropic EoS (1.3), which describes an isothermal gas. However, in GR the interpretation typically given to Eq. (1.3) is that of an ultra-relativistic perfect fluid. This can be derived from the ideal gas law $P = k\rho_0\epsilon$, where ϵ is the specific energy density, and ρ_0 is the density measured in the rest frame of the fluid element. The product $\rho_0 c^2$ (where c is the speed of light) is the rest-mass energy density of the fluid. The total energy density of the fluid element is given by $\rho c^2 = \rho_0 c^2(\epsilon/c^2 + 1)$ (internal plus rest-mass energy density). In the ultrarelativistic limit, $\rho_0\epsilon \gg \rho_0 c^2$, so $\rho \approx \rho_0\epsilon$ and we get Eq. (1.3). To distinguish the ultrarelativistic EoS from the isothermal gas, Eq. (2.23) we use a lower-case k in the former case.

All the calculations we have performed were strictly Newtonian. The relevant results from GR will simply be reported without repeating any of the calculations. The interested reader will be provided with the appropriate references for complete details and discussions. Ori and Piran calculated general relativistic self-similar solutions of a perfect fluid with EoS (1.3) in spherical symmetry [77]. They showed that by taking a particular limit of $k \to 0$ (from the EoS) the self-similar solutions of the general relativistic autonomous system reduced to the Newtonian isothermal-gas self-similar solutions. Therefore, the limit $k \to 0$ in EoS (1.3) can be considered the Newtonian limit of the general relativistic perfect fluid. Through this transition the Newtonian solutions inherit the properties of their general relativistic counterparts as discovered by [44, 47, 77, 96]. The Newtonian solutions are briefly discussed in section 2.6.2.

2.6.1 Regular Newtonian Self-similar Solutions

Regular Newtonian self-similar solutions for an isothermal gas were first studied in [56, 60, 81]. One of these solutions simultaneously discovered by Larson and Penston (called the Larson-Penston (LP) solution) is regular in the similarity variable but singular at the origin in the dimensionful variables such as the fluid density $\rho(r, t)$.

The blow-up[4] occurs at a finite time, and has finite mass. The solution can also be studied after the formation of the singularity [64, 77]. After collapse, the core continues to grow by accreting mass thus this solution is analogous to black hole solutions in GR, see [77]. Hunter (1977) [56] reported an infinite branch of self-similar solutions to the Newtonian-isothermal-gas-system different from the Larson-Penston solution. These solutions, again, contained a singularity in the regular coordinates (r, t) at a finite future time t_0. However, in this case the "collapsing core" shirks to zero as $t \to t_0$ and thus has zero mass. After collapse, the fluid expands outward, and the central density tends to zero as $t \to \infty$ [64, 77]. When expressed in terms of the similarity variable $x \propto r/t$ all these solutions are finite and regular at the center $(x = 0)$. Their properties at the origin $(x = 0)$ can be used to order the solutions into a hierarchy. In the literature the solutions are labeled as Hunter-A, Hunter-B, Hunter-C, etc, with Hunter-A (HA) having the lowest amplitude in the dimensionless density similarity variable, $\alpha(x)$ in our notation. A sketch of these solutions for $t_0 - t > 0$ is provided in Fig. 2.2, the hierarchical structure formed by the amplitude of $\alpha(x)$ can be appreciated in Fig. 2.2(a). The Hunter-solutions for the self-similar fluid velocity $u(x)$ as seen in Fig. 2.2(b) all contain oscillations which also follow a hierarchical paradigm. The Larson-Penston does not contain oscillations in the profile of $u(x)$, thus it is a pure collapse solution. A third type of self-similar-solution reported by Maeda *et. al.* (2001) is the so-called *homogeneous solution.* This solution is particularly simple and it can be obtained in closed form, see Table 4.1. It represents either an expanding or a collapsing solution. The latter corresponds to a "big crunch" singularity; the collapse happens everywhere at t_0. This solution may have some relevance in Newtonian cosmology [82]. This solution is also plotted in Fig. 2.2.

Spherical linear perturbations of the Newtonian isothermal gas self-similar solutions were studied in [64]. The calculations reveal that the LP solution has no

---

[4] Mathematicians often call the singular behavior in the governing PDEs as a "blow-up".

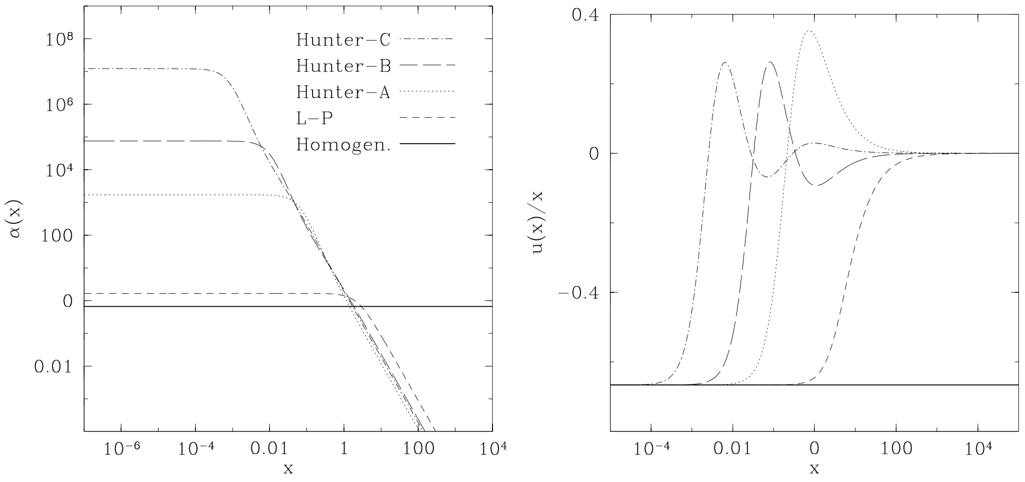

(a)

(b)

Figure 2.2: Sketch of the regular self-similar solutions for the isothermal gas ($\Gamma = 1$). Plots of the dimensionless density $\alpha(x)$ are provided in panel (a). Aside from the homogeneous solution, the Larson-Penston solution has the lowest amplitude with $\alpha(0) \approx 1.6658$ (a). Members of the Hunter-family have increasingly higher amplitudes arranged in hierarchical order. As seen in panel (b), the Hunter-solutions contains oscillations in the self-similar velocity profile ($u(x)$). The number of these oscillations also follows the same hierarchical structure, with the Larson-Penston and homogeneous solutions having 0 oscillations, Hunter-A 1, Hunter-B 2, Hunter-C 3, and so on. The absence of any oscillation in the profile of the Larson-Penston solution means it describes homologous collapse of the core; the homogeneous solutions describes simultaneous collapse. All of these plots correspond to the regime where $t < t_0$, (t_0 being the time of collapse) thus they illustrate the behavior of the fields prior to the time of singularity formation. These solutions are also calculated and discussed in [64].

unstable spherically symmetric linear perturbations modes. In contrast, the Hunter solutions contain growing (unstable) perturbation modes. The Hunter-A solution has a single unstable mode. The Hunter-B solution has two unstable modes, Hunter-C has three and so on. All the Hunter solutions investigated in [64] follow this pattern. The homogeneous solution was found to be unstable against fluctuations emanating from the sonic point. The fluctuations grow into a shock thus destroying the regularity of the solution. This is known as “kink”-mode instability.

2.6.2 Regular GR Self-similar Solutions

The pioneering work of Cahill and Taub (1971) [11] on spherical similarity solutions of Einstein's equations for a perfect fluid promoted interest in the investigation of gravitational collapse. This is due to the fact that self-similar solutions provide a simpler avenue for the analysis of the gravitational collapse process. An example of this was the work Ori and Piran (1990) [77]; they studied and classified the multiple similarity solutions of the GR+perfect fluid system. A summary of their classification and description is given below.

(1) *Black-hole solutions:* Singular solutions with finite mass. The singularity (Black hole) forms at a finite proper time. The collapse happens homologously. After black hole formation, the mass continues to grow by accretion. These solutions are the general relativistic versions of the Larson-Penston blow-up solution. Some authors refer to this as the GRLP (general relativistic Larson-Penston) others called it the Ori-Piran solution(s) [46].

(2) *Repulsive solutions:* These solutions contain oscillations in their velocity profiles. Again, the singularity forms at a finite proper time t_0 but immediately vanishes. The central density tends to zero for $t \gg t_0$, the gas expands outwardly. These solutions are analogous to the Newtonian Hunter solutions. The first member of this family is the general relativistic Hunter-A solution (GRHA). This is also known as the Evans-Coleman[5]solution [22, 46].

(3) *Asymptotically Friedmann solutions* This solutions describe a "big crunch" singularity. The entire spacetime collapses at t_0. This is the general relativistic version of Newtonian homogeneous solutions previously described.

The spectrum of similarity solutions which are analytic everywhere is discrete just as its Newtonian counterpart.

---

[5] In most cases, the Evans-Coleman solutions refers to the 1-mode unstable self-similar solution for the radiation gas $k = 1/3$.

Linear stability analysis of the Ori-Piran (GRLP) solution reveal an absence of spherically symmetric growing mode perturbations [45, 59]. The Evans-Coleman (GRHA) solution was shown to contain a single such perturbation mode [22, 66, 99]. The specific value of the Lyapunov exponent (growing mode) has been found to depend on the parameter k of the EoS (1.3). This single analytic mode structure of the Evans-Coleman solution persists over the entire range $k \in [0, 1]$ [73, 74]. Solving the general relativistic spherical-linear-perturbation equations reveal that as $k \to 0$ the value of the unstable mode (Lyapunov exponent) converges to the known value for the Hunter-A solution [45]. Further evidence of this convergence can also be found in dynamical simulations of critical collapse of an ultrarelativistic perfect fluid in the limit ($k \to 0$) [96]. We will talk more about this result in our discussion of critical phenomena, Chap. 4.

Table 2.1: Newtonian-GR similarity solutions.

Newtonian	General Relativity
Larson-Penston	Ori-Piran (GRLP)
Hunter-A	Evans-Coleman (GRHA)
Hunter-B	GRHB
Homogeneous solution $\alpha(x) = 2/3$, $u(x) = -2x/3$	Friedmann Solution†
Static Singular Solution $\alpha(x) = 2/x^2$, $u(x) = 0$	Static Singular Solution†

† Their explicit form can be found in Ref. [77]

2.6.3 Non-spherical Perturbations

Gundlach (2002) calculated non-spherical linear perturbations about the similarity solutions for the perfect fluid in GR with EoS (1.3) [32, 33]. Similar to the Newtonian system the linear-order axial and polar perturbations are decoupled. The growth rate spectrum of all axial perturbations can be computed in closed form, this is given by,

$$\lambda_\ell^n(k) = \frac{2(1-3k) - (1+3k)(\ell + 2n)}{3(1+k)}, \tag{2.105}$$

where k is the EoS proportionality constant in Eq. (1.3). The parameter $n \in \{0, 1, 2, \dots\}$, it denotes a particular solution of the radial equations. Naturally, Eq. (2.105) is the General Relativistic version of Eq. (2.103). Clearly, setting, $n = 0$ in Eq. (2.105) yields the least negative, slowest decaying perturbation for any k and ℓ. For $k \in [0, 1]$ with $n = 0$, all $\ell \geq 2$ are negative and thus decaying, but for $\ell = 1$ within $0 < k \leq 1/9$ there is exactly one growing ($\lambda_1^0 > 0$) axial perturbation, namely,

$$\lambda_1^0 = \frac{1-9k}{3(1+k)}. \tag{2.106}$$

Similar to the Newtonian fluid the axial mode is common to all similarity solutions. In particular, the Evans-Coleman solution, which we know has an unstable spherical mode is also unstable against the axial mode. Gundlach showed that in the range $0 < k \leq 1/9$ the Evans-Coleman solution is stable against all polar perturbations. This was shown by numerical analysis of the perturbations equations [33]. We must point out that the k-range over which no unstable polar perturbations were found includes the Newtonian limit ($k \to 0$), hence, the Newtonian equivalent to the Evans-Coleman solution *i.e.* the Hunter-A solution is predicted to be absent of any unstable polar modes. Note that in the Newtonian limit the growth rate of the unstable axial mode $\lambda_1^0 = 1/3$ which is the known spin-up mode discussed in Sec. 2.5. The stability structure of the Evan-Coleman solution is exactly analogous to the Newtonian Hunter-A solution, at least for the range where $k \in [0, 1/9]$. This is a key property of this unstable solution that motivated this project. Both the Evans-Coleman solution (also known as GRHA) and the Hunter-A solutions have the same mode structure. Therefore, we expect that their role as critical collapse solutions result in very similar type-II critical phenomena. This has already been shown in spherical symmetry. Our goal here is to test this in axisymmetry with the addition of rotation.

2.7 Initial Data

A large portion of our research involve investigating the role of angular momentum in gravitational collapse beginning with generic initial data in axial symmetry. In the case of initial infinitesimal rotation, it is expected that the angular momentum of the final compact object be related to the initial axial perturbations [32]. These axial perturbations in general can be described by a vector-value (three functions) function of the spatial coordinates *i.e.* $\vec{g}(r,\theta,\phi)$. Following Gundlach's suggestions we can explore this 3∞-dimensional parameter space by means of vector-value factor $\vec{q}$ [32]. The initially rotating data, or more specifically the v_ϕ (in cylindrical coordinates $(s,\ \phi,\ z)$) velocity field is specified by the product $\vec{q}g_0(r,\theta,\phi)$. The rest of the initial data is constructed such that $\vec{q}=0$ reduces to the spherical symmetry. In addition to the three parameters (components) of $\vec{q}$, there is an extra control parameter labeled as p which controls other spherically symmetric aspect of the initial conditions *e.g.* the amplitude of the initial density profile. Thus, the initial condition is controlled by a 4-family of initial data.

The quantities of interest during the evolution of the fluid are the mass of the compact object (M) and its specific angular momentum ($\vec{a}$). Symmetry requires that these quantities be related to the parameters p and $\vec{q}$ by way of,

$$M(p,-\vec{q}) = M(p,\vec{q}), \qquad \vec{a}(p,-\vec{q}) = -\vec{a}(p,\vec{q}). \tag{2.107}$$

Various forms for the profiles $g_0(r,\theta,\phi)$ which physically specify differential rotation were tested, all with the reflection symmetry about the equatorial plane.

2.8 Critical Phenomena

Numerical calculations of the evolution of a spherically symmetric real scalar field in General Relativity at the threshold of black hole formation led to the discovery of critical phenomena in gravitational collapse [15]. The numerical experiments revealed that the final fate of this data belonged to one of two categories. One, characterized by complete collapse of the matter-energy, *i.e.* black hole formation, *i.e.* the supercritical regime. Two, the subcritical regime is characterized by complete dispersal of the matter-energy out to infinity leaving behind flat, Minkowski space. A bisection search was carried out between these two regimes to locate the threshold, critical value of a control parameter p, this parameter is labeled $p^\star$. The mass of the black hole that formed during supercritical evolutions was shown to depend of on the "distance" from the critical parameter $p^\star$ according the following power-law,

$$M_{\mathrm{BH}} \propto |p - p^\star|^\gamma. \tag{2.108}$$

This is the now famous scaling-law for the black hole mass. The black hole masses resulting from evolutions across the critical parameter $p^\star$ appear to "turns-on" at arbitrarily small values. The exponent γ is independent of the particular choice of 1-parameter family of initial data, thus it is universal. Furthermore, the critical solution (scalar field and metric functions) display discrete self-similarity, see [15] for more details. This solution is also described in [76, 85]. The self-similarity of the critical solution, power-law scaling and universality are reminiscent of 2^{th} order phase-transition in statistical mechanics. This is the reason for the label *type*-II critical phenomena.

Type-II critical phenomena was also identified in critical collapse simulations of a radiation fluid by Evans and Coleman [22]. The critical solution is continuously self-similar–it is the single-unstable-mode Evans-Coleman solution previously known. The reciprocal of the scaling exponent γ is the Lyapunov exponent (growth rate) of the unstable mode. The work Koike *et. al.* [99] and Maison [66] based on the renormalization group provided a coherent framework which associates the salient features of critical phenomena *i.e.* universality and power-law scaling with the single-mode instability property of the critical solution.

2.8.1 Type II Critical Behavior and Scaling Laws

The formalism provided Koike *et. al.* applies to any autonomous system of equations whose solution under linear spherically symmetric perturbations has a single growing mode. Here, we would like to summarize and generalize their analysis for the case of a spherically symmetric self-similar solution containing two unstable modes. One of these modes is spherically symmetric, while the other is a non-spherical axial mode. We borrow from Gundlach's analysis [32], where he describes an intermediate linear regime governed by two unstable modes. Finally, we will apply this formalism to the Newtonian fluid model to derive scaling laws for the collapsed mass and maximum density.

Let $Z(\tau, x, \theta, \phi)$ represent a solution to the dynamical system (PDEs) in spherical coordinates. The variables,

$$\begin{aligned} x &= \frac{r}{l(t)}, \\ \tau &= -\ln t, \end{aligned} \tag{2.109}$$

where $l(t)$ is some time dependent length scale. If the solution is solely a function x *i.e.* $Z(x)$ clearly then, the solution is spherically symmetric and self-similar. Furthermore, if $Z(x)$ has a single spherically symmetric unstable mode we label this solution by $Z^{\star}(x)$. In addition, we assume that $Z^{\star}(x)$ solution also has an axial non-spherical unstable mode. Our aim is to construct the 4-parameter initial data, controlled by p and $\vec{q}$ as described in Sec. 2.7 that goes through the "intermediate linear regime". This is the region in phase space parametrized by $(p, \vec{q})$ that yields solutions that are well approximated by $Z^\star(x)$ plus the two unstable modes (spherical and axial-non-spherical). This is represented by,

$$Z(\tau, x, \theta, \phi; p, \vec{q}) \simeq Z^\star(x) + A(p, \vec{q}) Z_0(x) e^{\lambda_0 \tau} + \vec{B}(p, \vec{q}) \cdot \vec{Z}_1(x, \theta, \phi) e^{\lambda_1 \tau}. \qquad (2.110)$$

$Z_0(x)$ and $\vec{Z}_1(x, \theta, \phi)$ are the spherical and non-spherical mode functions respectively. Their corresponding growth rates are λ_0 and λ_1. We have explicitly included the dependence on the initial data parameters p and $\vec{q}$ through the constant $A(p, \vec{q})$, and constant vector $\vec{B}(p, \vec{q})$. Recall that we also require that $\vec{q} = 0$ reduces to spherical symmetry. This implies $\vec{B}(p, 0) = 0$. The solution then only has one unstable mode. In order to properly inherit the spherically symmetric results discussed in [10, 99] we must require the existence of initial critical value parameter $p = p^\star$ such that $A(p^\star, 0) = 0$. We refer to $(p = p^\star, \vec{q} = 0)$ as the critical point since both A and $\vec{B}$ vanish there.

For simplicity, we assumed the functions $A(p, \vec{q})$, and $\vec{B}(p, \vec{q})$ are analytic at the critical point as in [10, 32]. Their leading order behavior around the critical point is given by,

$$\begin{aligned} A(p, \vec{q}) &\simeq \frac{\partial A(p^\star, 0)}{\partial p}(p - p^\star) + \text{second order}, &(2.111)\\ \vec{B}(p, \vec{q}) &\simeq \frac{\partial \vec{B}(p^\star, 0)}{\partial \vec{q}}\vec{q} + \text{second order}. &(2.112)\end{aligned}$$

By definition of a critical solution $A(p^\star, 0) = 0 = \vec{B}(p^\star, 0)$. With this more explicit form of the constants, the intermediate linear regime is now given by,

$$Z(\tau, x, \theta, \phi; p, \vec{q}) \simeq Z^\star(x) + C_0(p - p^\star) Z_0(x) e^{\lambda_0 \tau} + \vec{q} C_1 \cdot \vec{Z}_1(x, \theta, \phi) e^{\lambda_1 \tau}. \qquad (2.113)$$

where the scalar $C_0 \equiv \partial_p A(p^\star, 0)$ and the 3×3 matrix $C_1 \equiv \partial_{\vec{q}} \vec{B}(p^\star, 0)$.

At some intermediate time (τ_*) our solution is well approximated by (2.113).

We can relabel the small deviations from $Z^\star(x)$ by introducing,

$$\begin{aligned} \epsilon &\equiv C_0(p-p^\star)e^{\lambda_0\tau_*}, &(2.114)\\ \vec{\delta} &\equiv \vec{q}C_1 e^{\lambda_1\tau_*}, &(2.115)\end{aligned}$$

where ϵ and $\vec{\delta}$ are now the small fixed quantities. Solving for τ_* in (2.114) and replacing it in (2.115) yields,

$$\vec{\delta} = \frac{\vec{q}C_1}{(C_0\epsilon^{-1})^{\lambda_1/\lambda_0}(p-p^\star)^{\lambda_1/\lambda_0}}. \tag{2.116}$$

Following Gundlach's argument [32] we take

$$Z(\tau_*, x, \theta, \phi; p, \vec{q}) \simeq Z^\star(x) + \epsilon Z_0(x) + \vec{\delta}\cdot\vec{Z}_1(x,\theta,\phi). \tag{2.117}$$

as Cauchy data. Later on, when the perturbation(s) have grown sufficiently large, $\epsilon \sim \mathcal{O}(1)$, the solution will either disperse or collapse. Nevertheless, the only scale in our system is set by $e^{-\tau_*}$ [99], which from Eq. (2.114) we get that, $e^{-\tau_*} = (C_0\epsilon^{-1}|p-p^\star|)^{1/\lambda_0}$.

At this point, we would like to apply this formalism to the our Newtonian the axi-symmetric polytropic gas, Eqs. (2.34)–(2.39). We assume that dynamical solution to this Newtonian model with the "appropriate initial conditions" controlled by p and $\vec{q}$ is able to approach a 2-mode unstable spherically symmetric self-similar solution. So, the solution at some intermediate time is described by the linear regime given by Eq. (2.117). The total mass enclosed inside radius r, at time t for any similarity solution is given by Eq. (2.48). Its dimensions are given by the explicit time dependent part *i.e.* $M(r,t) \propto t^{3n-2}$. Therefore, the mass of the compact object that may form following the solution's departure from the linear regime scales as t_*^{3n-2}, where $t_* = e^{-\tau_*}$, by definition. The remaining dependence can only be on the dimensionless parameter $\vec{\delta}$ and the sign of $(p - p^\star)$. We then have,

$$M(p, \vec{q}) = (\bar{C}_0 |p - p^\star|)^{(4-3\Gamma)/\lambda_0} F(\vec{\delta}) \tag{2.118}$$

We have set $C_0 \epsilon^{-1} \equiv \bar{C}_0$, and substituted $n = 2 - \Gamma$. The function $F(\vec{\delta})$, along with λ_0 are universal as stipulated in [32]. Similarly, the scale of the specific angular momentum, denoted by $\vec{a}$ is set by t_*^{2n-1}. This is determined from dimensional analysis since the units of $\vec{a}$ are related the units of $M(r,t)$ (mass) and $\vec{v}(r,t)$ (velocity) according to

$$[\vec{a}] = \frac{[G][M]}{[\vec{v}]}, \tag{2.119}$$

where [ ] means "units of" and G is the Gravitational constant. Therefore,

$$\vec{a}(p, \vec{q}) = (\bar{C}_0 |p - p^\star|)^{(3-2\Gamma)/\lambda_0} \vec{G}(\vec{\delta}). \tag{2.120}$$

The vector function $\vec{G}(\vec{\delta})$ is also universal. The scaling laws for an isothermal gas are obtained by setting $\Gamma = 1$, the solutions have self-similarity of the first kind. In this case Eq. (2.118) and Eq. (2.120) are formally identical to equations (17) and (19) derived in [32].

In the limit $\vec{q} \to 0$ we should recover the spherically symmetric results. From Eq. (2.107) we conclude that $F(\vec{\delta})$ must be even in $\vec{\delta}$, whereas $\vec{G}(\vec{\delta})$ must be odd. Thus, in the limit $\vec{q} \to 0$ the scaling law for the mass is,

$$\begin{aligned} M =& [\bar{C}_0 (p - p^\star)]^{(4-3\Gamma)/\lambda_0} F(0) \\ =& [\bar{C}_0 (p - p^\star)]^{(4-3\Gamma)/\lambda_0}, \end{aligned} \tag{2.121}$$

where we have recovered Choptuik's scaling law for the mass of the compact object as a function of the collapse threshold [15]. The self-similar critical solution $(Z^\star(x \propto r/t^{2-\Gamma}))$ in this case yields a scaling exponent that depends explicitly on the adiabatic index Γ, as well as λ_0 due to the non-linear scaling $r \propto t^{2-\Gamma}$. From

Eq. (2.107) we conclude that the leading order behavior of $\vec{G}(\vec{\delta})$ in the limit $\vec{q} \to 0$ is proportional to $\vec{\delta}$. Then, the scaling law for $\vec{a}$ follows,

$$\begin{aligned}\vec{a} =& [\bar{C}_0(p - p^\star)]^{(3-2\Gamma)/\lambda_0}\vec{\delta} \\ =& C_1\vec{q}[\bar{C}_0(p - p^\star)]^{(3-2\Gamma-\lambda_1)/\lambda_0}.\end{aligned} \tag{2.122}$$

Since $\lambda_1 = 1/3$ and ignoring all the family-dependent constants we can write,

$$M \propto (p - p^\star)^{(4-3\Gamma)/\lambda_0} \quad \text{as} \quad \vec{q} \to 0, \tag{2.123}$$

$$\vec{a} \propto \vec{q}(p - p^\star)^{(2/3)(4-3\Gamma)/\lambda_0} \quad \text{as} \quad \vec{q} \to 0. \tag{2.124}$$

In axial symmetry, the vector quantities can be treated as scalars once the axis of symmetry is aligned with the z-axis. With these conditions and using cylindrical coordinates (s, ϕ, z) we have,

$$\vec{a} = a\hat{z}, \quad \vec{\delta} = \delta\hat{z}, \quad \vec{G}(\vec{\delta}) = G(\delta)\hat{z}. \tag{2.125}$$

$\hat{z}$ is the unit-vector along the z-axis. The above discussion is a summary of [32]. Notice that the scaling laws for M and $\vec{a}$ highlight the importance of $\Gamma = 4/3$, $(n = 2/3)$, at this value, the autonomous system given by Eq. (2.52) and Eq. (2.53) becomes singular and no self-similar solutions exists.

In a similar way we can generate the scaling law for the maximum central density attained during subcritical evolutions $\rho(0,t) \equiv \rho_{\max}$. Since $\rho_{\max} \propto t_*^{-2}$ we find that

$$\rho_{\max} \propto |p - p^\star|^{-2/\lambda_0} \quad \text{as} \quad \vec{q} \to 0. \tag{2.126}$$

If critical collapse initial data of the ideal gas model in Newtonian gravity reaches a Hunter-A-type similarity solutions then we expect the characteristic variables such as the mass and specific angular momentum obey the scaling laws just described. They represent the key predictions to be tested against dynamical evolutions of critical collapse. These tests are presented in Chap. 4 and Chap. 5.

2.8.2 Type I Critical Behavior

A possible result for the evolution of our fluid+gravity model endowed with critical initial data is a static, star-like solution, $Z^\star(r)$ instead of a Hunter-A-type of scale-invariant solution. Similar to type-II critical behavior, this solution is only observed following the fine tuning of a 1-parameter family of initial data to the brink of gravitational collapse. Again, this solution is by definition a critical solution. Here, were discuss the general properties of this solution. The formalism of Koike *et. al.* [99] applies equally to the static critical solution. The only difference is that the static case requires the use of regular coordinates (r, t) as oppose to zooming coordinates $(\ln(x), \tau)$. The formalism is nearly identical to the self-similar case, so we will not repeat it here. This is done in detail in [72, 76]. In this case, the mass of static solution does not change; proximity to the threshold value $p^\star$ does not lead to smaller black holes but instead, a mass-gap exists set by the length scale of the static solution. Nevertheless, a scaling law for the lifetime T_0 of the critical solution can be deduced. As before, this is a result of the solution being funneled through the linear regime. This is given by,

$$T_0 \propto -\frac{1}{\lambda_0} \ln |p - p^\star|. \tag{2.127}$$

Here, λ_0 is the growth rate of the spherically symmetric unstable mode. This kind of behavior is called type-I critical phenomena

At the current time there is no formalism that introduces slow rotation of the static critical solution as non-spherical linear perturbations in a way that is analogous to what is done for the similarity solutions, Sec. 2.8.1. Heuristically, one possibility is to incorporate the effect of rotation on the critical solution by adding a non-spherical function, *i.e.*

$$Z(t,r,\theta,\phi;p,\vec{q}) \simeq Z^{\star}(r) + A(p,\vec{q})Z_0(r)e^{\lambda_0 t} + f(t,r,\theta,\phi;p,\vec{q}). \tag{2.128}$$

Clearly, we should require that $f(t,r,\theta,\phi;p,\vec{q}=0) \equiv 0$. Then, at $\vec{q}=0$ an expansion of $A(p,\vec{q})$ near $p = p^{\star}$ yields the scaling law (2.127), recovering the spherically symmetric result. We could write the function $f(t,r,\theta,\phi;p,\vec{q})$ in terms of the linear non-spherical modes of the critical solution $Z^{\star}(r)$. However, as discussed at the end of Chap. 4 we do not have access to the solution $Z^{\star}(r)$ nor to its linear spherical perturbations making it impossible to check Eq. (2.128) directly. This is a result of not having enough equations to solve the hydrostatic system, see Sec. 4.2.4. Therefore, we will not say much more about the linear regime in the case of type-I critical phenomena. The only available tool for checking whether the quasi-static solutions encountered in this project exhibit type-I critical behavior is Eq. (2.127). Due to the lack of a theoretical basis for treating rotation in critical collapse of our Newtonian model the topic is only marginally explored in this project. It is left for future work.

Chapter 3

Numerical Methods

This chapter contains a brief presentation of the methods and techniques used in the numerical analysis of the equations of motion introduced in Chap. 2. The main objective of these methods is to provide approximate solutions to the time-dependent nonlinear system of partial differential equations (PDEs). Due to the nature of this project a combination of numerical techniques were used to simultaneously provide solutions to the gravitational field determined by the Newtonian potential $\varphi(\vec{x}, t)$, and the dynamical fluid variables $\rho(\vec{x}, t)$, $\vec{v}(\vec{x}, t)$ and $P(\vec{x}, t)$ (density, velocity and pressure). Considerably more effort was allocated to finding solutions to the hydrodynamic component which is given by a system of conservation laws. The nonlinear nature of these system is known to give rise to discontinuities (shocks) even from smooth initial conditions.

3.1 Finite Differences

Arguably the most common of all numerical techniques used in the production of approximate solutions to PDEs are finite differencing algorithms. These approaches hinge on generating a finite-difference representation of a system of PDEs. This is done by Taylor expansions of the continuum solution at nearby points in order to approximate the derivatives in the equations through finite differences. The result of the procedure is a system of equations that relates the solution at various points on a discrete domain. The finite-difference equations comprise an algebraic system of equations whose solutions represent approximations to the continuum system (PDEs). The finite difference approximation can in general be made arbitrary though some control parameter, *e.g.* h, the grid spacing, at the cost of a greater number of algebraic manipulations. We provide a brief introduction to the method, a more complete discussion can be found in [16, 35, 71, 83]. Here, we borrow the notation used in [16].

A system of PDEs can be written in the following abstract notation,

$$Lu = f, \tag{3.1}$$

the solution u, can be a scalar or vector-valued function. The function f is sometimes called the "source", and L is a type of differential operator. For what follows it is assumed that both u and f are continuous and smooth. In general $u = u(\vec{y}, t)$, and $f = f(u; \vec{y}, t)$ where $\vec{y}$ denotes the position vector in some coordinate system and t is the time. For simplicity we assume that u is a scalar function and is dependent upon time and only one spatial variable *i.e.* (y, t). Similarly, we assume that $f = f(u, y, t)$ and consequently it is also a scalar function. A commonly given example is the linear wave equation,

$$(\partial_{tt} - \partial_{yy})u(y, t) = 0, \tag{3.2}$$

clearly in this case, $L = \partial_{tt} - \partial_{yy}$, and $f(u, y, t) = 0$.

As previously stated, the process of approximating the continuum solution $u(y, t)$ follows from the construction of a discrete system analogous to (3.1). First, we consider a discrete domain, a subset of points selected from the continuum. To simplify the discussion a set of N uniformly spaced points is selected $\{y_1,\, y_2,\, \ldots, y_j,\, \ldots, y_N\}$, where $y_{j+1} - y_j = h$. Thus, h is the fundamental control parameter of the discretization. Again, adopting the notation used in [16], the discrete system has the form,

$$L^h u^h = f^h. \tag{3.3}$$

Where now, u^h represents the solution of the discrete system, the other quantities with superscript h are the discrete version of the quantities in (3.1). Equation (3.3) is called the finite difference approximation (FDA) of the PDE, Eq. (3.1). If our construction of the difference operator, L^h, is correct then the discrete solution u^h should approximate u. As we said before, the degree of the approximation is determined by the grid spacing parameter h. By design, the FDA (3.3) should reduce to Eq. (3.1) as $h \to 0$.

Our goal is to find the discrete solution u^h by inverting the difference operator L^h. For nonlinear algebraic equations a close-form discrete solution is in general unattainable. Nevertheless, an approximate solution to the algebraic system, $\tilde{u}^h$, can still be provided through an iterative process such as Newton's method. This leads to the introduction of a *residual* function, defined as

$$r^h = L^h \tilde{u}^h - f^h. \tag{3.4}$$

It measures the degree to which the difference equation (3.3) is satisfied.

Now, we address the method for generating discrete representation(s) of the differential operator L. This can be done by way of multiple Taylor series expansions of the continuum system. This allows us to represent any combination of derivatives, or higher derivatives as combinations of finite differences between neighboring points. The operator can be approximated to the desired order in the power of the distance between points, *i.e.* $\mathcal{O}(h^p)$. The number of terms we choose to keep in the Taylor series expansion of L determines the order of our finite difference approximation. Naturally, this truncation of the series introduces another source of error. A Taylor series expansion of the original PDE has the form,

$$\tau^h = L^h u - f^h. \tag{3.5}$$

The quantity τ^h is called the *truncation error*, it contains higher order terms not included in the definition of L^h. Note that u is the solution to the continuum system.

The solution to the difference equation u^h is said to *converge* if it satisfies, $u^h \to u$ as $h \to 0$. For *consistency* we must add,

$$\lim_{h \to 0} \tau^h = 0, \tag{3.6}$$

This ensures that the finite difference approximation reduces to the continuum equation (PDE).

Now that the basics concepts have been laid out, we discuss how we quantify the *solution error* involved in the numerical approximation. Naturally, this is defined as,

$$e^h = u - u^h. \tag{3.7}$$

Similar to the other error quantities, r^h and τ^h we would like to express e^h as a function of h. More specifically, we want to express e^h as a sum of linear powers of h. This will allow us to specify the order of approximation of the numerical algorithm. However, the definition of the solution error involves the exact solution u, which is what we want to determine in the first place. Fortunately, the difference $u - u^h \equiv e^h$ should be a smooth function and thus expressible as an infinite series in powers of h. Then,

$$e^h = u - u^h = \sum_{l=1}^{\infty} h^l e_l. \tag{3.8}$$

This is known as the *Richardson's expansion* [87]. The coefficients $e_l = e_l(y, t)$.

Let us assume that the truncation error for some discretization scheme is $\mathcal{O}(h^2)$. Therefore

$$L^h u - f^h = \tau^h = \tau_2(x, t) h^2 + \mathcal{O}(h^3).$$

Furthermore, let us assume that we could solve the FDA equation exactly *i.e.* $L^h u^h -$

$f^h = 0$. Then,

$$L^h(u - u^h) = \sum_{l=1}^{\infty} h^l (L^h e_l) = \tau_2(x,t)h^2 + \mathcal{O}(h^3).$$

The following ansatz for e^h trivially satisfies the above condition.

$$e^h = \sum_{l=1}^{\infty} h^{l+1} e_{l+1}. \tag{3.9}$$

Note that the leading term in the series has a factor of h^2. We use the leading order term to define the order of the solution error, which for this discretization scheme is $\mathcal{O}(h^2)$. Assuming linearity of the operator L the truncation and solution errors are related via,

$$\begin{aligned} L^h u - f^h = \tau^h &= L^h(u^h + e^h) - f^h \\ &= L^h e^h. \end{aligned} \tag{3.10}$$

We can analyze the principle of convergence using the Richardson's expansion. Suppose a numerical solution u^h has been obtained for a difference equation of the type given by Eq. (3.3). If a second-order discretization scheme has been employed, the truncation error is given by,

$$\tau^h = \tau_2 h^2 + \tau_3 h^3 + \ldots. \tag{3.11}$$

Based on Richardson's analysis the solution error in such a case should follow,

$$u^h = u + e_2 h^2 + e_3 h^3 + \ldots. \tag{3.12}$$

At two higher levels of resolution, namely $2h$ and $4h$ the solution errors are,

$$u^{2h} = u + e_2(2h)^2 + e_3(2h)^3 + \ldots, \tag{3.13}$$

$$u^{4h} = u + e_2(4h)^2 + e_3(4h)^3 + \ldots. \tag{3.14}$$

For what follows it is crucial that we assumed the error calculation is performed at the same point (y, t) in all three cases. The difference between two levels *e.g.* h and $2h$ to leading order is,

$$u^{2h} - u^h \approx (2^2 - 1)e_2h^2. \tag{3.15}$$

Similarly, for levels $2h$ and $4h$

$$u^{4h} - u^{2h} \approx 2^2(2^2 - 1)e_2h^2. \tag{3.16}$$

The ratio of these two results defines a quantity called the *convergence factor*

$$Q(y, t) = \frac{u^{4h} - u^{2h}}{u^{2h} - u^h}. \tag{3.17}$$

Clearly, in this case $Q(y, t) = 4$. This defines the order of convergence of the numerical scheme, for the present example a convergence factor $(Q(y, t))$ of 4 denotes 2^{nd}-order convergence. For illustration purposes it often useful to synthesize the information contained in $Q(y, t)$ by computing a spatial norm, typically the l_2-norm. The notation $\|\cdot\|_{l_2}$ denotes the l_2-norm, which is defined as,

$$\left\|u^h\right\|_2 = \left(\frac{1}{N}\sum_{j=1}^{N}(u_j^h)^2\right)^{\frac{1}{2}}. \tag{3.18}$$

Applying this to the convergence factor, we obtain a time series,

$$Q(t) = \frac{\left\|u^{4h} - u^{2h}\right\|}{\left\|u^{2h} - u^h\right\|}. \tag{3.19}$$

If the solution converges *i.e.* $\lim_{h\to 0} u^h = u$ and it is properly described by the Richardson's expansion this quantity should remain constant. In the above case $Q(t) = 4$. Similarly, we could calculate convergence factors for other orders of the discretization. It is easy to show that for 1^{st}-order schemes $Q(t) = 2$.

3.1.1 Independent Residual

Even if the numerical algorithm passes the consistency and convergence tests outlined above, it does not guarantee that u^h is converging to the desired continuum solution u pertaining to system (3.1). Since the above tests only indicate a narrowing of the gap between u^h and some continuum function as $h \to 0$, it is possible that u^h approaches to the wrong continuum solution. The *independent residual* test is designed to avoid this pitfall.

To illustrate this point we consider the following. Suppose that a second-order scheme ($\tau^h \sim \mathcal{O}(h^2)$) has been successfully implemented such that a numerical solution u^h to the FDA (3.3) has been obtained. This implies,

- *consistency:* $\lim_{h\to 0}(L^h u - f^h) = 0$,
- *convergence:* $\lim_{h\to 0}(u - u^h) = 0$.

There is considerable freedom in the formulation of the FDA. This follows from the variety of ways that we can use Taylor series expansions to construct L^h. Therefore, we can easily generate an alternative difference operator $\tilde{L}^h$. Like L^h, this new operator must also satisfy the consistency requirement, $\lim_{h\to 0} \tilde{L}^h u - f^h = 0$. Therefore, a 2^{nd}-order approximation to L in terms of the mesh-spacing h follows,

$$\tilde{L}^h = L + E_2 h^2 + \mathrm{O}(h^3), \tag{3.20}$$

where the $E_2(y,t)$s are the coefficients generated by the Taylor series expansion.

Likewise, convergence to the continuum solution allows,

$$u^h = u + e_2 h^2 + \mathrm{O}(h^3). \tag{3.21}$$

Then,

$$\tilde{L}^h u^h = \left(L + E_2 h^2 + \dots\right)\left(u + e_2 h^2 + \dots\right) = Lu + (E_2 u + L e_2) h^2 + \mathcal{O}(h^3). \tag{3.22}$$

Thus, we see that the operator $\tilde{L}^h$ should follow the same quadratic convergence as L^h. Suppose that an error has been introduced in our representation of L^h, but we have correctly solved $L^h u^h - f^h = 0$, satisfying the consistency requirement. Therefore, we still should measured the desired convergence but the solution that is approached follows,

$$u^h = u + e_0 + \sum_{l=1}^{\infty} e_l h^l, \tag{3.23}$$

where, e_0 is an $\mathcal{O}(1)$ error in the solution introduced by not having implemented the correct/desired L^h operator. In the limit $h \to 0$, u^h approaches $u + e_0$ instead of u. The action of $\tilde{L}^h$ on this numerical solution is,

$$\tilde{L}^h u^h = Lu + \tilde{L}^h e_0 + \mathcal{O}(h^2). \tag{3.24}$$

The $\mathcal{O}(1)$ term, $\tilde{L}^h e_0$ clearly violates the consistency requirement, unless $\tilde{L}^h e_0 = 0$ which is highly unlikely. Obviously, errors could still creep in via the construction of $\tilde{L}^h$. However, since this operator is only used once after the numerical solutions has been obtained it is easier to ensure its correctness. Consequently, if u^h passes the independent residual test we can be highly confident that we have the numerical solution to the differential equation we set out to solve. This test was the primary diagnostic tool we used to establish the correctness of our numerical results. For more information, and other examples on the independent residual test see [37, 71, 76, 85].

3.2 Finite Volumes: Conservative Methods

The finite difference techniques described in Sec. 3.1 were used in order to calculate the Newtonian potential $\varphi(\vec{x},t)$ by solving Poisson's equation numerically. In this section we present the numerical methods used in solving the equations of fluid dynamics with sources. As previously mentioned, these equations are susceptible to the formation of shocks and discontinuities in the fluid variables even from smooth initial conditions. This issue leads to undefined gradients in the equations of motion. Nevertheless, this problem can be confronted by considering the integral form of the fluid equations. These can be obtained directly by integrating the differential form of these equations over a finite volume V_j. We apply this to a general vector-valued differential conservation law Eq. (2.1), more specifically to the k-th equation. Therefore,

$$\int_{V_j} \frac{\partial q_k}{\partial t} dV + \int_{V_j} \nabla \cdot \vec{f}_k(\mathbf{q}) dV = \int_{V_j} \psi_k(\mathbf{q},\vec{x},t) dV. \tag{3.25}$$

The quantities $q_k(\vec{x},t)$, $\vec{f}_k(\mathbf{q})$, $\psi_k(\mathbf{q},\vec{x},t)$ introduced in Chap. 2 represent the k-th conserved variable, flux and source functions respectively. Application of the divergence theorem yields,

$$\frac{\partial}{\partial t} \int_{V_j} q_k dV + \oint_{S_j} \vec{f}_k \cdot \hat{n} dS = \int_{V_j} \psi_k(\mathbf{q},\vec{x},t) dV. \tag{3.26}$$

S_j is the surface which encloses the volume V_j, and $\hat{n}$ is a vector normal to this surface. The derived integral equation (3.26) does not involve gradients of the dynamical variable q_k, and so discontinuities in q_k do not lead to ill-defined terms. The above equation (3.26) is a typical mathematical statement of conservation. The change in quantity q_k inside a cell of volume V_j equals the flux over the boundary of such cell S_j plus a source or sink of q_k inside V_j.

We can formally integrate equation (3.26) over a time interval $\Delta t = t^{n+1} - t^n$

to produce,

$$\int_{V_j} q_k(\vec{x}, t^{n+1})dV - \int_{V_j} q_k(\vec{x}, t^n)dV + \int_{t^n}^{t^{n+1}} \oint_{S_j} \vec{f_k} \cdot \hat{n} dS dt = \int_{t^n}^{t^{n+1}} \int_{V_j} \psi_k dV dt. \tag{3.27}$$

Dividing Eq. (3.27) by the volume element V_j allows us to identify the quantity,

$$Q_{k,j}(t) \equiv \frac{1}{V_j} \int_{V_j} q_k(\vec{x}, t) dV, \tag{3.28}$$

which is the average value of q_k over the finite cell V_j. To make this discussion more concrete in the following section we discuss the integral conservation law in a given coordinates system. This allows us to generate a discrete equation for the cell averages $Q_{k,j}$.

3.2.1 Spherical Coordinates: Spherical Symmetry

We considered writing Eq. (3.27) in spherical polar coordinates. For simplicity we assume spherical symmetry *i.e.* all the physical fields *e.g.* q_k are independent of the coordinates θ and ϕ. Under this assumption it is convenient to define the cell's volume as $V_j = 4\pi(r_{j+1/2}^3 - r_{j-1/2}^3)$. Which is a spherical shell of inner and outer boundaries given by $r_{j-1/2} \equiv r_j - \Delta r/2$ and $r_{j+1/2} \equiv r_j + \Delta r/2$, respectively. Note that Δr is considered small. For this geometry, the surface integral in Eq. (3.27) becomes,

$$\begin{aligned}\int_{t^n}^{t^{n+1}} \oint_{S_j} \vec{f_k} \cdot \hat{n} dS dt &= \int_{t^n}^{t^{n+1}} \left(\int_{S^i_{j+1/2}} f_k dS - \int_{S^i_{j-1/2}} f_k dS \right) dt. \\ &= \int_{t^n}^{t^{n+1}} 4\pi r_{j+1/2}^2 f_k(t, r_{j+1/2}) dt \\ &\quad - \int_{t^n}^{t^{n+1}} 4\pi r_{j-1/2}^2 f_k(t, r_{j-1/2}) dt, \end{aligned} \tag{3.29}$$

where $S_{j\pm1/2}$ denotes the outer/inner boundaries of the cell, and f_k is the radial component of the flux vector corresponding to the k^{th} conservation law. The notation can be simplified through the following definition,

$$F^{n+1/2}_{k,j+1/2} = \frac{1}{\Delta t}\int_{t^n}^{t^{n+1}} f_k(t, r_{j+1/2})dt. \tag{3.30}$$

This quantity is known as the *numerical flux.* With the additional definition

$$\Psi^{n+1/2}_j = \frac{1}{\Delta t V_j}\int_{t^n}^{t^{n+1}}\int_{V_j} \psi dV dt, \tag{3.31}$$

we finally arrive at a discrete equation for the conservation laws where the dynamical variables are the cell averages $Q(x,t)$,

$$\begin{aligned} Q^{n+1}_j - Q^n_j + \frac{3\Delta t}{r^3_{j+1/2} - r^3_{j-1/2}}\left(r^2_{j+1/2}F^{n+1/2}_{j+1/2} - r^2_{j-1/2}F^{n+1/2}_{j-1/2}\right) \\ = \Delta t \Psi^{n+1/2}_j. \end{aligned} \tag{3.32}$$

We have suppressed the index k to keep the notation from becoming unmanageable. It is implied that Eq. 3.32 represents the k^{th} component of a vector-valued nonlinear conservation law. The components are coupled through $F^{n+1/2}_{j+1/2}$ and $\Psi^{n+1/2}_j$.

3.2.2 Cylindrical Coordinates: Axial Symmetry

Due to its relevance to the calculations performed in this thesis we expressed the integral conservation law, Eq. (3.26) in cylindrical coordinates (s, ϕ, z). The physical system is assumed to be axisymmetric, so all the fields *e.g.* q_k are independent of the azimuthal angle ϕ (if the axis of symmetry coincides with the z-axis). In this situation there are two non-trivial flux vector components for the k^{th} equation, namely, f^s_k and f^z_k (the other component f^ϕ_k is trivial in the sense that it does not appear in the equations of motion since, $\partial f^\phi_k/\partial\phi = 0$).

The cell boundaries are given by $[s_{i-1/2}, s_{i+1/2}] \times [z_{j-1/2}, z_{j+1/2}]$, while its volume, $V_{ij} = 2\pi(s^2_{i+1/2} - s^2_{i-1/2})(z_{j+1/2} - z_{j-1/2})$. Once again, $s_{i\pm1/2} = s_i \pm \Delta s/2$, where Δs is a small parameter. The same holds for $z_{j\mp1/2} = z_i \pm \Delta z/2$ with Δz also being a small parameter, typically $\Delta s = \Delta z$. The surface integral in Eq. 3.26 becomes

$$\begin{aligned}\int_{t^n}^{t^{n+1}} \oint_S \vec{f}_k \cdot \hat{n} dS dt = &\int_{t^n}^{t^{n+1}} \left(\int_{z_{j-1/2}}^{z_{j+1/2}} 2\pi s_{i+1/2} f^s_k(t, s_{i+1/2}, z)dz - \right.\\ &\left. \int_{z_{j-1/2}}^{z_{j+1/2}} 2\pi s_{i-1/2} f^s_k(t, s_{i+1/2}, z)dz \right) dt +\\ &\int_{t^n}^{t^{n+1}} \left(\int_{s_{i-1/2}}^{s_{i+1/2}} 2\pi f^s_k(t, s, z_{j+1/2}) s ds - \right.\\ &\left. \int_{z_{i-1/2}}^{z_{i+1/2}} 2\pi f^s_k(t, s, z_{j-1/2}) s ds \right) dt. \qquad (3.33)\end{aligned}$$

Similarly, following the definitions of the numerical fluxes, we obtain

$$F^s_{i\pm1/2,j} = \frac{1}{\Delta t \Delta z} \int_{t^n}^{t^{n+1}} \int_{z_{j-1/2}}^{z_{j+1/2}} f^s(t, s_{i\pm1/2}, z) dz dt, \qquad (3.34)$$

$$F^z_{i,j\pm1/2} = \frac{2}{\Delta t (s^2_{i+1/2} - s^2_{i-1/2})} \int_{t^n}^{t^{n+1}} \int_{s_{i-1/2}}^{s_{i+1/2}} f^z(t, s, z_{j\pm1/2}) s ds dt. \qquad (3.35)$$

Notice, we have suppressed the superscript $n + 1/2$ which denotes a temporal average, as well as the index k which indicates our discussion applies to an arbitrary component of a vector of conservation laws. The average of the source function over the cell V_{ij} is,

$$\Psi^{n+1/2}_{ij} = \frac{1}{\Delta t V_{ij}} \int_{t^n}^{t^{n+1}} \int_{V_{ij}} \psi dV dt. \qquad (3.36)$$

Combining, Eqs. (3.33)–(3.36) along with Eq. (3.28), we arrive at equation,

$$\begin{aligned}Q^{n+1}_{ij} - Q^n_{ij} + \frac{2\Delta t}{(r^2_{i+1/2} - r^2_{i-1/2})} \left(s_{i+1/2} F^s_{i+1/2,j} - s_{i-1/2} F^s_{i-1/2,j} \right) +&\\ \frac{\Delta t}{\Delta z} \left(F^z_{i,j+1/2} - F^z_{i,j-1/2} \right) = \Delta t \Psi_{ij}.& \qquad (3.37)\end{aligned}$$

This is the discrete version of the conservation law, Eq. 2.1 subject to axial symmetry. The dynamical variables are the cell-averages Q_{ij}.

Eqs. 3.32 and 3.37 are *finite volume* discrete formulations of the conservation laws whose solutions are the cell-averages. A significant impediment in solving for the cell averages is the fact that the numerical fluxes *e.g.* $F_{j\pm1/2}$ are functions of the solutions to the continuous problem q_k, which are unknown. Effective numerical methods provide adequate representation of the numerical fluxes so that the finite volume equations can be used to solve for the cell averages. A brief description of these methods is given below, Sec. 3.3.

3.3 The Riemann Problem

The source-free, non-linear conservation-law,

$$\partial_t \mathbf{q} + \partial_x \mathbf{f}(\mathbf{q}) = 0, \tag{3.38}$$

where $\mathbf{q} = (q_1, \ldots, q_{\mathcal{N}})^\intercal$, $\mathbf{f} = (f_1, \ldots, f_{\mathcal{N}})^\intercal$, and the initial data,

$$\mathbf{q}(0, x) = \begin{cases} \mathbf{q}^L, & x < 0 \\ \mathbf{q}^R, & x > 0 \end{cases} \tag{3.39}$$

represents a general statement of the *Riemann problem.* By definition the Riemann problem is one-dimensional; it is extensively discussed in [61, 101]. Here we present only the features which have relevance to our hydrodynamical model. The conditions entailed by the Riemann problem are typical of certain problems in physics and engineering *i.e.* those involving fluid dynamics.

The solution to the Riemann problem clearly depends on the form of the flux function $\mathbf{f}(\mathbf{q})$. For the scalar case ($\mathbf{q} = q$) with initial data $q^L > q^R$ (Fig. 3.1) and $f(q^L)$, $f(q^R) > 0$, a formal solution can be provided. The *Rankine-Hugoniot jump* *condition*,

$$f(q^R) - f(q^L) = s \cdot (q^R - q^L), \tag{3.40}$$

gives the shock speed, s (see Ref. [61] for more details). At later times the solution is described by,

$$q(t,x) = \begin{cases} q^L, & x < st \\ q^R, & x > st. \end{cases} \tag{3.41}$$

Alternatively, if $q^L < q^R$ with $f(q^L)$, $f(q^R) > 0$ the solution to the scalar Riemann problem is given by,

$$q(t,x) = \begin{cases} q^L, & x < \dfrac{\partial f(q^L)}{\partial q} t \\ \hat{q}(x/t), & \dfrac{\partial f(q^L)}{\partial q} t < x < \dfrac{\partial f(q^R)}{\partial q} t \\ q^R, & x > \dfrac{\partial f(q^R)}{\partial q} t. \end{cases} \tag{3.42}$$

The discontinuity disappears after the initial time, the two state q^L and q^R are connected by a continuous self-similar state $\hat{q}(x/t)$. This is known as a *rarefaction fan* [101].

The problem of direct relevance to this project is the Riemann problem for a vector-valued, nonlinear, coupled system given by Eq. 3.38. Discontinuous initial data can be given through any combination of the components for the left and right vectors $\mathbf{q}^L$ and $\mathbf{q}^R$. The solution of the vector-valued Riemann problem can simultaneously yield shocks, and rarefaction waves, as well as *contact discontinuities*. A possible wave pattern for such initial data is given by Fig. 3.1 In general, the evolution gives rise to intermediate states $\mathbf{q}^{*L}$ and $\mathbf{q}^{*R}$. The specific values for these states as well as the characteristic waves (shocks, rarefaction fan, contact discontinuities) displayed in Fig. 3.1 together represents the solution to the vector Riemann problem.

Our numerical problem requires that we solve for the cell averages *e.g.* $\mathbf{Q}_j^{n+1}$

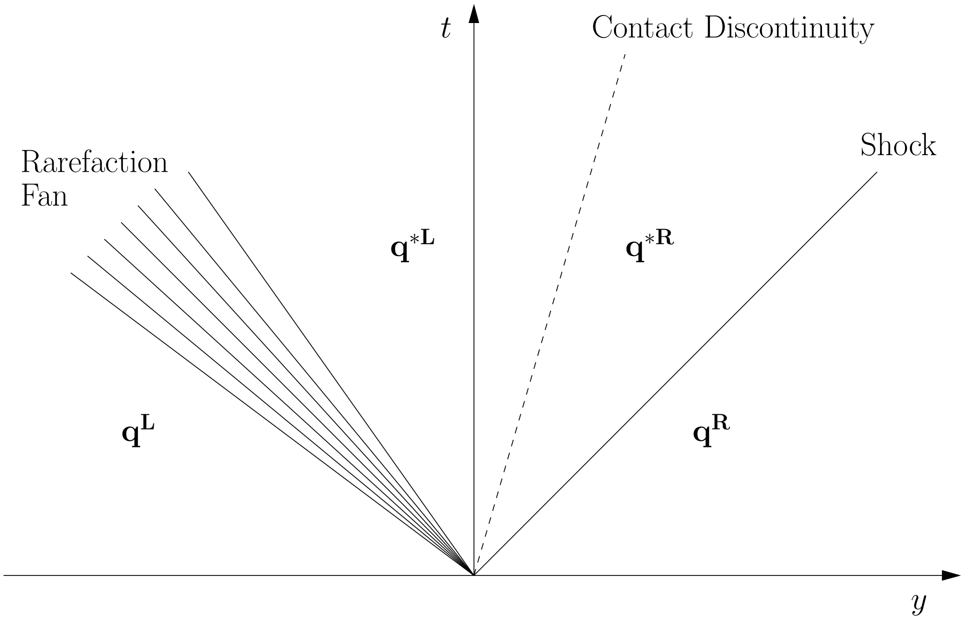

Figure 3.1: Typical wave pattern solution to the vector Riemann problem (this is the generic solution for a three-component vector Riemann problem, *i.e.* $\mathbf{q} = (q_1\ q_2\ q_3)^\intercal$ [101]). The straight lines represent the various waves *e.g.* shocks waves. They separate the different states; knowledge about these states constitute the complete solution to the Riemann problem.

[6]. Implicit in our finite-volume formulations given by Eqs. 3.32 and 3.37, is the requirement that the solution at the interfaces could be accessed in order to construct $\mathbf{F}_{j+1/2}$. In general, adjacent cell averages will not be equal *i.e.* $\mathbf{Q}_j \neq \mathbf{Q}_{j+1}$. A zeroth-order extrapolation at the boundary according to $\mathbf{Q}_j = \hat{\mathbf{Q}}^{\mathrm{L}}_{j+1/2}$, and $\mathbf{Q}_{j+1} = \hat{\mathbf{Q}}^{\mathrm{R}}_{j+1/2}$ leads to a situation that is identical to the Riemann problem with $\hat{\mathbf{Q}}^{\mathrm{L}}_{j+1/2}$ and $\hat{\mathbf{Q}}^{\mathrm{R}}_{j+1/2}$ playing the role of the discontinuous initial data. Thus the solution to the Riemann problem could be used to obtained the solution at the interface. Recall that this is a requirement for the construction of $\mathbf{F}_{j+1/2}$. Generating an approximation to the solution at the cell borders via this (zeroth-order) extrapolation procedure in conjunction with the Riemann problem solution is known as the *Godunov method*

---

[6] The bold-faced symbol represents vector notation. Alternatively, we could use index notation and refer to the k-th component $Q^{n+1}_{k,j}$ as was done in Sec. 3.2

[61]. With this procedure for computing $\mathbf{F}_{j+1/2}$ the cell averages can be integrated forward in time according to the finite volume formulas Eqs. 3.32 and 3.37. The specific way in which the Riemann solution is used to construct the numerical fluxes is discussed in the following sections. In this work, we have used two commonly used methods, *Roe's approximate Riemann solver* and the *Harten-Lax-Leer-contact* (HLLC) *approximate Riemann solver*. These are discussed extensively in [61, 88, 101] and reviewed below.

3.4 Approximate Riemann Solvers

Before we introduce the approximate Riemann solvers Roe and HLLC, we should address the use of the qualifier "approximate" attached to their name. This follows from the fact that the numerical fluxes, $\mathbf{F}_{j+1/2}$ are constructed by solving the Riemann problem corresponding to a "linearized" conservation law. The discontinuous data at the cell boundary is applied to a linear set of conservation laws obtained through a linearization procedure of the original equations of motion.

For concreteness, let us write the general one-dimensional vector conservation law in quasi-linear form. Starting with Eq. (2.1) in index notation we can get,

$$\frac{\partial q_k}{\partial t} + \sum_{m=1}^{\mathcal{N}} \frac{\partial f_k}{\partial q_m} \frac{\partial q_m}{\partial y} = \psi_k. \tag{3.43}$$

The quantities involved are defined at the start of Chap. 2. Defining the components of the Jacobian matrix is the expression,

$$A_{k,m} \equiv \frac{\partial f_k(\mathbf{q})}{\partial q_m}. \tag{3.44}$$

So that,

$$\frac{\partial q_k}{\partial t} + \sum_{m=1}^{\mathcal{N}} A_{k,m} \frac{\partial q_m}{\partial y} = \psi_k. \tag{3.45}$$

In vector notation this equation becomes,

$$\frac{\partial \mathbf{q}}{\partial t} + \mathbf{A}\frac{\partial \mathbf{q}}{\partial y} = \boldsymbol{\psi}. \tag{3.46}$$

Clearly the matrix $\mathbf{A}$ is a function of the vector of conservative variables $\mathbf{q}$. However, over very small changes in time, *e.g.* $t^{n+1} - t^n = \Delta t$ we may assume that $\mathbf{q}$ is approximately constant which implies that $\mathbf{A}$ is also approximately constant. If Δt is sufficiently small we may approximate the solution to the non-linear problem by the solving the linear Riemann problem (Eq. (3.46) with constant $\mathbf{A}$). This solution, or more specifically the characteristic structure of Jacobian matrix ($\mathbf{A}(\mathbf{q} = \text{constant})$) is then used to reconstruct the flux function at the cell borders via the HLLC algorithm (described in Sec. 3.4.1). In this sense the HLLC and Roe are approximate Riemann solvers.

In order to solve the linear Riemann problem posed by Eq. (3.46) an appropriate representation of $\mathbf{A}$ from the states $\mathbf{q}^L$, $\mathbf{q}^R$ is required. This representation is denoted by $\hat{\mathbf{A}}(\mathbf{q}^L, \mathbf{q}^R)$. The following conditions must be satisfied by $\hat{\mathbf{A}}(\mathbf{q}^L, \mathbf{q}^R)$ [61],

1. All the eigenvalues of $\hat{\mathbf{A}}$ are real *i.e.* $\hat{\mathbf{A}}$ is non-singular (diagonalizable).
2. $\hat{\mathbf{A}}(\mathbf{q}^L, \mathbf{q}^R) \longrightarrow \mathbf{A}(\mathbf{q})$ in the limit $\mathbf{q}^L$, $\mathbf{q}^R \rightarrow \mathbf{q}$
3. $\hat{\mathbf{A}}(\mathbf{q}^L, \mathbf{q}^R)(\mathbf{q}^L - \mathbf{q}^R) = \mathbf{f}(\mathbf{q}^L) - \mathbf{f}(\mathbf{q}^R)$

The first condition ensures that the system of linear equations is hyperbolic, *i.e.* finite, real characteristics speeds. The second condition guarantees consistency with the nonlinear conservation law. Finally, the third condition states that the shock speed is given by the Rankine-Hugoniot condition, Eq. (3.40). These requirements are discussed in [61] in extensive detail.

3.4.1 The HLLC Approximate Riemann Solver

The HLLC solver was proposed by Harten, Lax and van Leer [50]. One begins by assuming a three-wave pattern solution of the vector Riemann problem similar to that displayed in Fig. 3.1. These waves-speeds are labeled as $\{S^L, S^R, S^*\}$. After some short time period Δt the initial two-state system given by Eq. (3.39) may in general evolve into a four-state solution such as $\{\mathbf{q}^L, \mathbf{q}^{*L}, \mathbf{q}^{*R}, \mathbf{q}^R\}$. The speeds S^L and S^R are eigenvalues of the Jacobian $\hat{\mathbf{A}}$ and correspond to the fastest characteristics speeds emanating from the discontinuity. Toro *et. al.* [102], in order to restore the full characteristic structure of the Euler equations, introduced the third speed S^* (another eigenvalue of $\hat{\mathbf{A}}$), which is the speed of propagation of the contact discontinuity separating states $\mathbf{q}^{*L}$ and $\mathbf{q}^{*R}$ (Fig. 3.1). States separated by a contact discontinuity have characteristic speeds that run parallel the $\mathbf{q}^{*L}$–$\mathbf{q}^{*R}$ boundary. See [102].

For the specific case of the source-free Euler equations of fluid dynamics, the initial data for the Riemann problem is given by, $\mathbf{q}^L(\mathbf{p}^L)$ and $\mathbf{q}^R(\mathbf{p}^R)$ where the states $\mathbf{p}^L = (\rho^L, v^L, P^L)^\intercal$ and $\mathbf{p}^R = (\rho^R, v^R, P^R)^\intercal$ are the vectors of primitive variables. In this case the fastest speeds can be defined according to,

$$S^L = \hat{v} - \hat{c}_s, \quad S^R = \hat{v} + \hat{c}_s. \tag{3.47}$$

The variables, $\hat{v}$ and $\hat{c}_s$ are the *Roe-average*[7] velocity, and local sound speed defined by,

$$\hat{v} = \frac{\sqrt{\rho^L} v^L + \sqrt{\rho^R} v^R}{\sqrt{\rho^L} + \sqrt{\rho^R}}, \tag{3.48}$$

$$\hat{c}_s = \left((\Gamma - 1)(\hat{H} - \frac{1}{2}\hat{v}^2) \right)^{1/2}, \tag{3.49}$$

---

[7] This particular average ensures condition 2 is satisfied *i.e.* $\hat{\mathbf{A}}$ as $\mathbf{q}^L, \mathbf{q}^R \to \mathbf{q}$ for the Euler equations

where $H = (E + P)/\rho$ is the enthalpy, with its Roe-average given by,

$$\hat{H} = \frac{\sqrt{\rho^L} H^L + \sqrt{\rho^R} H^R}{\sqrt{\rho^L} + \sqrt{\rho^R}}. \tag{3.50}$$

Next, the speed of propagation of the contact discontinuity S_* is given by,

$$S_* = \frac{P^R - P^L + \rho^L v^L (S^L - v^L) - \rho^R v^R (S^R - v^R)}{\rho^L (S^L - v^L) - \rho^R (S^R - v^R)}. \tag{3.51}$$

With these definitions the numerical flux vector at the interface between cells j and $j+1$ is constructed according to,

$$\mathbf{F}^{\mathrm{HLLC}}_{j+1/2} = \begin{cases} \mathbf{F}^L & \text{if } 0 \le S^L, \\ \mathbf{F}^L_* & \text{if } S^L \le 0 \le S_*, \\ \mathbf{F}^R_* & \text{if } S_* \le 0 \le S^R, \\ \mathbf{F}^R & \text{if } 0 \ge S^R, \end{cases} \tag{3.52}$$

Where,

$$\mathbf{F}^X_* = F^X + S^X (\mathbf{q}^X_* - \mathbf{q}^X), \tag{3.53}$$

and $X \in \{L,\, R\}$. Finally, the intermediate $*$ states are given by the formula,

$$\mathbf{q}^X_* = \rho^X \left(\frac{S^X - v^X}{S^X - S_*} \right) \begin{bmatrix} 1 \\ S_* \\ \dfrac{E^X}{\rho^X} + (S_* - v^X) \left(S_* + \dfrac{P^X}{\rho^X (S^X - v^X)} \right) \end{bmatrix}. \tag{3.54}$$

The generalization to more than one spatial dimension is easily done by solving the linearized Riemann problem along each direction independently. Thus, expressions (3.47)–(3.54) apply for all the independent directions. For more details on the HLLC solver see [101].

3.4.2 The Roe Solver

The Roe solver relies on a full decomposition of the linearized Riemann problem into its characteristic structure. Again, for the special case of the Euler equations in one dimension this is done through diagonalization of the Jacobian matrix $\hat{\mathbf{A}}$ evaluated at the Roe averages *e.g.* Eqs. (3.48)– (3.50). The characteristic structure is then used to construct the numerical flux according to,

$$\mathbf{F}^{\mathrm{Roe}}_{j+1/2} = \frac{1}{2}\left(\mathbf{f}(\mathbf{q}^{L}_{j+1/2}) + \mathbf{f}(\mathbf{q}^{R}_{j+1/2}) - \sum_{k} |\lambda_k| \omega_k \boldsymbol{\chi}_k\right), \tag{3.55}$$

where, $\boldsymbol{\chi}_k$ and λ_k are k^{th} eigenvectors and eigenvalues of the Jacobian. The quantities ω_ks are the solutions to equation,

$$\mathbf{q}^R - \mathbf{q}^L = \sum_k \omega_k \boldsymbol{\chi}_k, \tag{3.56}$$

and are called the “jumps”. They are the coefficients involved in the decomposition of the discontinuity $\mathbf{q}^R - \mathbf{q}^L$ into the linear characteristic waves, $\boldsymbol{\chi}_k$. Lastly, $\mathbf{f}(\mathbf{q}^X_{j+1/2})$ is the physical flux evaluated at the L/R initial state. In the case of the Euler equations this is,

$$\mathbf{f}(\mathbf{q}) = \begin{bmatrix} \rho v \\ \rho v^2 + P \\ (E+P)v \end{bmatrix}. \tag{3.57}$$

The extension to higher dimensions is again straightforward. Complete information on the Roe solver can be found in [61]. It is easy to note that the Roe solver is computationally more expensive than the HLLC solver since it involves complete diagonalization of the Jacobian matrix $\hat{\mathbf{A}}$ at every cell interface.

3.4.3 Cell Boundary Variable Reconstruction

The Godunov method is 1^{st}-order accurate in the local grid spacing. This is due to the fact that the L/R-states involved in setting up the Riemann problem are obtained through a zero-order extrapolation of the cell averages $\{\mathbf{Q}_j\}$. For example, in the interface between the j^{th} and the $(j+1)^{\mathrm{th}}$ cells, the L/R states which define the Riemann problem are $\mathbf{Q}_j$ and $\mathbf{Q}_{j+1}$ respectively. A higher level of accuracy can be achieved by providing a better approximation to the L/R states from the cell averages. The goal of high resolution methods is to accomplish this through a special extrapolation procedure. Such procedure should take into account the discontinuous nature of the data *i.e.* the presence of shocks, and avoid the introduction of spurious oscillations.

A linear piece-wise reconstruction of the fluid variables at the cell boundaries leads to a 2^{nd} order accurate (in the spatial grid spacing) computational scheme. In order to avoid spurious oscillation near shocks the scheme is only 1^{st}-order accurate at such points, and also at local extrema. These techniques are known as *essentially-non-oscillatory* (ENO) methods [94]. We should clarify that in practice the extrapolation is performed on the cell-averaged primitive variables ($\{\mathbf{P}_j\}$). From these we then compute the L/R conservative variables of the Riemann problem. This process can be written symbolically as follows,

$$\mathbf{P}^{L}_{j+1/2} = \quad \mathbf{P}_j + \boldsymbol{\sigma}_j (y_{j+1/2} - y_j), \tag{3.58}$$

$$\mathbf{P}^{R}_{j+1/2} = \quad \mathbf{P}_j + \boldsymbol{\sigma}_j (y_{j+1/2} - y_{j+1}). \tag{3.59}$$

Here, $\mathbf{P}_j$[8] are the cell-averaged primitive variables, with y_j being its coordinate location in the one-dimensional discrete domain, and $\boldsymbol{\sigma}_j$ is called the slope limiter,

---

[8] Whenever we speak of the discrete conservation laws we use the symbols $\mathbf{P}_j$ and $\mathbf{Q}_j$ to refer to the primitive and conservative variables. Lower-case variables $\mathbf{p}$ and $\mathbf{q}$ are their corresponding continuum representation. We also use the lower-case symbols when referring to the generic solution of the Riemann problem.

It is chosen from the slopes,

$$\mathbf{s}_{j-1/2} \equiv \frac{\mathbf{P}_j - \mathbf{P}_{j-1}}{y_j - y_{j-1}}, \quad \mathbf{s}_{j+1/2} \equiv \frac{\mathbf{P}_{j+1} - \mathbf{P}_j}{y_{j+1} - y_j}, \tag{3.60}$$

according to,

$$\boldsymbol{\sigma}_j = \mathrm{minmod}(\mathbf{s}_{j-1/2}, \mathbf{s}_{j+1/2}), \tag{3.61}$$

where, applied to each component separately,

$$\mathrm{minmod}(a,b) = \begin{cases} 0 & \text{if} \quad ab < 0 \\ a & \text{if} \quad |a| < |b| \quad ab > 0 \\ b & \text{if} \quad |b| < |a| \quad ab > 0. \end{cases} \tag{3.62}$$

The above, Eq. (3.62) defines the "minmod" slope limiter. Other ENO such limiters exists, see [72, 76]. Throughout, this project we have exclusively used the minmod limiter to perform the variable reconstruction. Finally, the conservative variables $\mathbf{Q}^L_{j+1/2}$, $\mathbf{Q}^R_{j+1/2}$ can be computed from $\mathbf{P}^L_{j+1/2}$, $\mathbf{P}^R_{j+1/2}$ via the definition, $\mathbf{Q}(\mathbf{P})$. From the definition of the minmod limiter it follows that at shocks and extrema $\boldsymbol{\sigma}_j = 0$, thus the extrapolation is piece-wise constant and locally the scheme is 1^{st}-order accurate.

3.5 Time Integration

The time integration of the equations of motion (Euler+Poisson equations) was done through a two-step explicit method. This procedure is called *Huen's method* and it is 2^{nd}-order accurate in the time step Δt. In one spatial dimension, *e.g.* spherical symmetry, it can be simply stated as,

$$\tilde{\mathbf{Q}}_j = \mathbf{Q}^n_j + \Delta t \hat{L}(\mathbf{Q}^n), \tag{3.63}$$

$$\mathbf{Q}^{n+1}_j = \frac{1}{2}\Big(\tilde{\mathbf{Q}}_j + \mathbf{Q}^n_j + \Delta t \hat{L}(\tilde{\mathbf{Q}})\Big), \tag{3.64}$$

where we have lumped together all the complicated operation involved in the spatial integration and source terms into the operator $\hat{L}(\mathbf{Q}^n)$.

Since we also performed calculations in axial symmetry, the methods we needed to apply are effectively two-dimensional. In this case the time integration through Huen's two step predictor-corrector method becomes,

$$\tilde{\mathbf{Q}}_{ij} = \mathbf{Q}^n_{ij} + \Delta t L_s(\mathbf{Q}^n) + \Delta t L_z(\mathbf{Q}^n), \tag{3.65}$$

$$\mathbf{Q}^{n+1}_{ij} = \frac{1}{2}\Big(\tilde{\mathbf{Q}}_{ij} + \mathbf{Q}^n_{ij} + \Delta t L_s(\tilde{\mathbf{Q}}) + \Delta t L_z(\tilde{\mathbf{Q}})\Big), \tag{3.66}$$

where $L_s(\mathbf{Q}^n)$, $L_z(\mathbf{Q}^n)$ are the spatial integration *i.e.* solution to the linearized Riemann problem along the two independent directions s and z (in cylindrical coordinates $(s,\, \phi,\, z)$). The indices i and j refer to the location $(s_i,\, z_j)$. The source terms are included in either or both of the terms $L_s(\mathbf{Q}^n)$ and $L_z(\mathbf{Q}^n)$.

An important property of Huen's two-step method is that it is known to be *Total-Variation-Diminishing* (TVD). It is a statement regarding the stability of the algorithm. The concept was first introduced by Harten [49], with the total variation being defined as,

$$\mathrm{TV}(\mathbf{Q}^n_j) = \sum_j |\mathbf{Q}^n_{j+1} - \mathbf{Q}^n_j|. \tag{3.67}$$

or in two-dimensions[9] [27, 61],

$$\mathrm{TV}(\mathbf{Q}^n_{ij}) = \sum_{i,j} \Delta s|\mathbf{Q}^n_{i+1,j} - \mathbf{Q}^n_{i,j}| + \Delta z|\mathbf{Q}^n_{i,j+1} - \mathbf{Q}^n_{i,j}|. \tag{3.68}$$

The method is said to be TVD if $\mathrm{TV}(\mathbf{Q}^{n+1}_{ij}) \leq \mathrm{TV}(\mathbf{Q}^n_{ij})$ and $\mathrm{TV}(\mathbf{Q}^n_{ij})$ is monotonically decreasing in time.

---

[9] Again, we assume axial symmetry and we use cylindrical coordinates $(s,\, \phi,\, z)$.

3.6 The Grid Structure

Here, we present the grid structure used in approximating the solution to Eqs. (2.5)–(2.8) in spherical and axial symmetry. The spherically symmetric grid along with its adaptive-mesh-refinement (AMR) facility closely follows the algorithm used in [76], where a single dynamical, non-uniform grid was used. We provide a brief summary of this algorithm in Sec. 3.6.1. For the calculations in axial symmetry we used a multitude of uniform grids. The dynamically chosen grids ensure uniform truncation error over the entire computational domain. This AMR algorithm was developed by Berger and Collela [8].

3.6.1 Spherical Symmetry Non-uniform Grid

A nonuniform grid structure was used to discretized the spherically symmetric computational domain. This algorithm was developed and previously used in [76], therefore we will not describe it here in great detail. The grid domain (distance r from the origin) is divided into three regions, Ω_a, Ω_b, Ω_c. The innermost region $\Omega_a : 0 < r \leq r_a$ consists of a uniform grid of N_a points and uniform spacing $r_{i+1} - r_i = \Delta r_a$. There are N_b points in $\Omega_b : r_a < r \leq r_b$ spaced according to $\ln(r_{i+1}) - \ln(r_i) = \Delta R$, with uniform ΔR. The transition from the uniform region to the logarithmic, nonuniform region can be made smooth by choosing

$$e^{R_a + \Delta R} - e^{R_a} = \Delta r_a, \tag{3.69}$$

where $R_a = \ln(r_a)$. This is required so that we can use the same routines, *e.g.* cell-boundary variable reconstruction (Sec. 3.4.3) across the $\Omega_a - \Omega_b$ domain interface. Lastly, $\Omega_c : r_b \leq r \leq r_c$ is again a uniform grid of N_c points and uniform spacing $r_{i+1} - r_i = \Delta r_c$. The transition between the nonuniform (logarithmic) grid and the uniform grid is again smooth provided we impose,

$$e^{R_b} - e^{R_b - \Delta R} = \Delta r_c, \tag{3.70}$$

where, $R_c = \ln(r_c)$.

To completely specify the grid it is sufficient to provide the parameters $\{N_a, N_b, N_c, \Delta r_a\}$. While the other grid parameters are given by,

$$\Delta R = \ln\left(\frac{N_a+1}{N_a}\right), \quad \Delta r_c = \Delta r_a \left(\frac{N_a+1}{N_a}\right)^{N_b-1}. \tag{3.71}$$

These follow from conditions (3.69) and (3.70). Trivially,

$$r_a = N_a \Delta r_a, \quad r_b = (N_a+1)\Delta r_c, \quad r_c = N_c \Delta r_c + r_b. \tag{3.72}$$

The AMR procedure

During gravitational collapse of an ideal gas, the solution, as characterized by the fields ρ, $\vec{v}$ and P evolves over a wide range of spatial and temporal scales. Proper resolution of these requires dynamical refinement of the mesh-spacing. For the spherically symmetric code, this requirement was accomplished by utilizing essentially non-oscillatory (ENO) methods in order to construct a 3rd order interpolating polynomial that was used to add points in regions of high gradients, see [93] for more details regarding ENO-methods.

During the evolution, if the normalized gradient *i.e.* $\frac{1}{||\rho||_{l_2}}\frac{\partial \rho}{\partial r}$, ($||\rho||_{l_2}$ is the l-2 norm of the density field) exceeded a certain threshold, then the AMR procedure was applied, otherwise the evolution was continued. The application of the technique can be outlined as follows:

- Reduce the grid spacing by a factor of 1/2 in the uniform grid such that $r_a \to r_a/2$, keeping the number of grid points in this region constant, but reducing $\Delta r_a \to \Delta r_a/2$. The new points are interpolated using the 3rd order

ENO polynomial.

- The region left behind in the reduction $r_a \to r_a/2$ is interpolated and incorporated into the logarithmic grid. Therefore, $N_b \to N_b + N_b'$, where $N_b' = \mathrm{NINT}(\ln(2)/\Delta R)$. The function NINT() operates on a real number to provide the nearest integer. The interpolation in this region is also done via the 3^{rd} order ENO interpolant.
- Repeat process after a set number of evolution time steps.

This process doubles the resolution over a collapsing volume near the origin in order to adequately resolve the form the fields ρ, v, P and φ. This AMR algorithm is very similar to the one used in [76].

3.6.2 Axial Symmetry Grid

We used cylindrical coordinates (s, ϕ, z) in computing the evolution of the axisymmetric fluid. The axis of symmetry was chosen to coincide with the z-axis. The domain is defined by $[0, s_{\mathrm{max}}] \times [-z_{\mathrm{max}}, z_{\mathrm{max}}]$. This is known as the *base grid*. The total number of points in the base grid is given by, $N_{0s} \times N_{0z}$. These integer parameters define the uniform base grid spacing through,

$$\Delta s_0 = \frac{s_{\mathrm{max}}}{N_{0s}}, \quad \Delta z_0 = \frac{2z_{\mathrm{max}}}{N_{0z}} \tag{3.73}$$

The physical boundaries are set by s_{max} and z_{max}, these are chosen such that

$$\varphi \sim \frac{1}{\sqrt{s_{\mathrm{max}}^2 + z_{\mathrm{max}}^2}} << 1. \tag{3.74}$$

Recall that $\varphi(s, z)$ is the Newtonian potential in axisymmetry.

The AMR in this case is accomplished through application of Berger-Collela's algorithm [8]. Unlike the single grid used in the spherically symmetric calculations, here, a nested hierarchy of grids is used in order to resolve the high gradient regions.

The hierarchy of grids is evolved. At the highest level of resolution, a new grid can be added or deleted based on a prescribed truncation error criterion. We will not explain the algorithm here, instead we refer the reader to the original work of Berger and Collela, [8].

Given the large dynamical range involved in simulations of gravitational collapse and the localized nature of the phenomena, the use of AMR greatly expedites the computations. For example, the density amplitude evolves through the range $\sim$ 1–10^7, for a typical critical collapse simulation. Nevertheless, the search for a critical solution requires dozens of runs, each taking longer as the critical solution is approached. On a single CPU the computation time would be an insurmountable obstacle even with the use of AMR. As a result, we were also required to carry out our calculations in parallel. We used a computational infrastructure called *PAMR* (Parallel Adaptive Mesh Refinement) developed by Frans Pretorius [21, 84]. This facility allows for each grid in the hierarchy to be partitioned into smaller rectangular grids and distributed among a set number of processing units on a computer cluster. Synchronization and interpolation of the boundary points after every step in the evolution is handled by the PAMR program [84].

3.7 Solution to Poisson's Equation

It is simple to show that a 2^{nd}-order discretization of the spherically symmetric Poisson's equation, Eq. (2.27) can be put into the linear form,

$$\mathbf{M}\boldsymbol{\Phi} = 4\pi\boldsymbol{\varrho}, \tag{3.75}$$

where $\mathbf{M}$ turns out to be a tridiagonal matrix, and the vectors $\boldsymbol{\Phi} = (\varphi_1, \ldots, \varphi_j, \ldots, \varphi_N)$, $\boldsymbol{\varrho} = (\rho_1, \ldots, \rho_j, \ldots, \rho_N)$ store the discrete value of the Newtonian potential and the fluid density respectively. Note that $N \equiv N_a + N_b + N_c$. Solution to Eq. (3.75) is easily obtained by inverting the matrix $\mathbf{M}$. This was done using the standard

Linear-Algebra package (LAPACK) routines.

The boundary and regularity conditions are incorporated into the tridiagonal structure of $\mathbf{M}$. We require that $\varphi(t,r)$ be an even function of r, *i.e.* $\partial\varphi(t,0)/\partial r = 0$. The discrete form of the 2$^{\text{nd}}$ derivative which shows up in $\mathbf{M}$ at the $r=0$ becomes,

$$\frac{1}{r^2}\frac{\partial}{\partial r}r^2\frac{\partial\varphi}{\partial r}\bigg|_{r=0} \rightarrow \frac{6(\varphi_2-\varphi_1)}{\Delta r^2}, \tag{3.76}$$

with $\varphi_1 \equiv \varphi(0,t)$ and $\varphi_2 \equiv \varphi(\Delta r, t)$. At the outer boundary we impose the condition that the potential should fall as

$$r\varphi \rightarrow \text{constant} \quad \text{at large } r.$$

In terms of the discrete system we get that,

$$r_N\varphi_N = r_{N-1}\varphi_{N-1}. \tag{3.77}$$

Where $N \equiv N_a + N_b + N_c$. The boundary conditions on the fluid variables *e.g.* ρ are discussed in the Sec. 3.8.

The 2-dimensional axisymmetric Poisson's equation (2.39) was solved using the *multigrid* method. This methods employs a hierarchy of fine and coarse grids. The elliptic equations are thereby solved on every grid using *Gauss-Seidel* relaxation. The solution is either injected from the fine grid to the coarse grid or interpolated from the coarse to the fine grid. The advantage of the methods over straightforward relaxation is expediency in acquisition of the numerical solution. Shifting between different grid levels turns out to reduces the number of relaxation sweeps needed for solution convergence. The method and its convergence properties are discussed in [16].

We required evenness of the axisymmetric Newtonian potential with respect to the axis of symmetry, coordinate s. This means that the discrete approximation to the 2^{nd} derivative with respect to s at $s = 0$ follows,

$$\frac{1}{s}\frac{\partial}{\partial s} s \frac{\partial \varphi}{\partial s}\bigg|_{s=0} \to \frac{4(\varphi_{2,j} - \varphi_{1,j})}{\Delta s^2}. \tag{3.78}$$

Once again, at the outer boundary we assume the Newtonian potential follows

$$\sqrt{s^2 + z^2}\varphi(t, s, z) = \text{constant} \quad \text{at large } \sqrt{s^2 + z^2}.$$

In terms of the discrete rectangular domain we have three outer boundaries, so we used the conditions,

$$\sqrt{s_{N_s-1}^2 + z_j^2}\varphi_{N_s-1,j} = \sqrt{s_{N_s}^2 + z_j^2}\varphi_{N_s,j}, \tag{3.79}$$

$$\sqrt{s_i^2 + z_{N_z-1}^2}\varphi_{i,N_z-1} = \sqrt{s_i^2 + z_{N_z}^2}\varphi_{i,N_z}, \tag{3.80}$$

$$\sqrt{s_i^2 + z_2^2}\varphi_{i,2} = \sqrt{s_i^2 + z_1^2}\varphi_{i,1} \tag{3.81}$$

In all of the discrete expressions we have suppressed the time dependence.

3.8 Fluid Boundary Conditions

The numerical solution for the fluid variables correspond to the cell-averaged values. Naturally, these averages are located at the cell centers of the discretized domain. Notice that given either spherical or axisymmetric geometry the origin, $r = 0$ or ($s = 0$, $z = 0$) cannot correspond to a cell center. Thus, the regularity conditions for the fluid variables which are valid at the origin must be somehow extrapolated to a distance that is half of cell away from the origin ($\Delta r/2$ in spherical symmetry), *i.e.* the location of the first cell average.

3.8.1 Fluid Regularity Conditions in Spherical Symmetry

So-called conservative regularity conditions for this type of cell-centered data were proposed by [76]. In spherical symmetry this is done by first assuming the full solution (not the cell-averages) follows a Taylor series expansion near the origin. The solution is thus approximated by a polynomial expansion of degree $\mathcal{M}-1$ in accordance with,

$$\mathbf{q}_j(r) = \sum_{m=0}^{\mathcal{M}-1} \mathbf{a}_m (r-r_j)^m. \tag{3.82}$$

The j index denotes the discrete cell locations near r, and $\mathbf{a}_m$ is the vector or undetermined coefficients. There are $\mathcal{M}$ such vectors given Eq. (3.82). However, since we are concerned with extrapolating cell-averages, these are obtained by integration, via,

$$\begin{aligned}\mathbf{Q}_j(r_i) =& \frac{1}{V_i}\int_{V_i} \mathbf{q}_j dV \\ =& \frac{3}{r_{i+1/2}^3 - r_{i-1/2}^3} \sum_{m=0}^{\mathcal{M}-1} \mathbf{a}_m \left(\int_{r_{i-1/2}}^{r_{i+1/2}} (r-r_j)^m r^2 dr \right).\end{aligned} \tag{3.83}$$

The index-j denotes the point at which the solution is Taylor expanded, whereas the index-i is the location of the cell-average being extrapolated. We demand that these averages obey (in a local sense) the conservation properties of the numerical solution. Therefore, the cell-averages calculated via expansion (3.83) must equal the numerical solution obtained by solving the finite volume equations *e.g.* Eq. (3.32). These equivalence allows us to determine the vector coefficients $\mathbf{a}_m$. If the expansion is done about the origin, *i.e.* $r_j = 0$, and we keep terms in the expansion up to order $\mathcal{M} = 4$ then determining the $\mathbf{a}_m$s lead to the following relationships among the cell averages.

$$\text{Even:}\quad \mathbf{Q}_i = \frac{1}{1627}(3311\mathbf{Q}_{i+1} - 2413\mathbf{Q}_{i+2} + 851\mathbf{Q}_{i+3} - 122\mathbf{Q}_{i+4}), \tag{3.84}$$

$$\text{Odd:}\quad \mathbf{Q}_i = \frac{1}{36883}(35819\mathbf{Q}_{i+1} - 16777\mathbf{Q}_{i+2} + 4329\mathbf{Q}_{i+3} - 488\mathbf{Q}_{i+4}). \tag{3.85}$$

The above relations are obtained following the behavior of the fields near the origin. Even fields such as the fluid density ρ are finite at $r = 0$ and have vanishing first derivatives *i.e.* $\partial\rho(t,0)/\partial r$. Whereas odd fields such as the fluid velocity v vanish at the origin but have finite spatial first derivative. Relations (3.84) and (3.85) were used to extrapolate the cell-averages for the even and odd fields near $r = 0$. Note that i^{th} cell-average is the one being extrapolated, thus it corresponds to the first physical cell in the domain; in general, there could be additional ghost cells to the interior of r_i. In our numerical work $i = 1$ and so there are no additional ghost cells. Therefore special care is taken in the computation of the numerical fluxes at $1 + 1/2$-interface [10]. These techniques were first used in [76].

3.8.2 Fluid Regularity Conditions in Axial Symmetry

Equivalent conservative regularity conditions were applied to the axisymmetric fluid. To our knowledge this constitutes the first time this is done for a 2-dimensional axisymmetric fluid code. The condition of regularity of the fluid fields in this case extends along the axis of symmetry, the z-axis in cylindrical coordinates (s, ϕ, z). Again, we assume a series expansion in s such as,

$$\mathbf{q}_j(s,z) = \sum_{m=0}^{\mathcal{M}-1} \mathbf{a}_m(z)(s - s_j)^m. \tag{3.86}$$

---

[10] The minmod limiter requires 2 cells to the left and right of the cell border. In the case of $1 + 1/2$ in spherical symmetry the assumptions of evenness or oddness of the fluid variable are directly incorporated into the cell-border reconstruction and thus into the numerical flux

Clearly, the solution depends now on the z-axis. This dependence is included in the undetermined coefficients $\mathbf{a}_m(z)$s. The corresponding cell-averages for this expansion can be computed through the integral,

$$\begin{aligned}\mathbf{Q}_j(s_i, z_k) =&\frac{1}{V_{i,k}}\int_{V_{i,k}}\mathbf{q}_j dV\\ =&\frac{2}{s^2_{i+1/2}-s^2_{i-1/2}}\sum_{m=0}^{\mathcal{M}-1}\mathbf{a}_m(z_k)\left(\int_{i-1/2}^{i+1/2}(s-s_j)^m r dr\right).\end{aligned} \tag{3.87}$$

We clarify that Eq. (3.87) computes the i-k^{th} cell average (located at $(s_j,\, z_k)$) from expansion of the solution at $(s_j,\, z_k)$.

Similarly, we impose local fluid conservation of the extrapolated values. Consistency requires an equivalence between these cell averages computed using Eq. (3.87) and the numerical solution of the axisymmetric finite volume Eqs. (3.37). If the expansion is performed on the axis of symmetry ($s_j = 0$) then calculation of the coefficients $\mathbf{a}_m$s yield the following relationships between the cell averages near the z-axis,

$$\text{Even:}\quad \mathbf{Q}_{i,k} =2\mathbf{Q}_{i+1,k}-\frac{10}{7}\mathbf{Q}_{i+2,k}+\frac{1}{2}\mathbf{Q}_{i+3,k}-\frac{1}{14}\mathbf{Q}_{i+4,k}, \tag{3.88}$$

$$\text{Odd:}\quad \mathbf{Q}_{i,k} =\frac{1}{1627}(1419\mathbf{Q}_{i+1,k}-635\mathbf{Q}_{i+2,k}+161\mathbf{Q}_{i+3,k}-18\mathbf{Q}_{i+4,k}). \tag{3.89}$$

The set of cell averages closest to the z-axis corresponds to index $i = 1$, this is the first physical cell. Note that we can then use the next four cell centers to extrapolate the value of the $i = 1$ cell average from Eqs. (3.88) and (3.89). Eq. (3.88) imposes the $s = 0$ regularity condition for the even variables such as $\rho(t, s, z)$, $P(t, s, z)$ and $v_z(t, s, z)$, whereas Eq. (3.89) is used for the odd fields, $v_s(t, s, z)$ and $v_\phi(t, s, z)$. All of the mathematical expression involved in the discussion of regularity conditions, namely, Eqs. (3.82)–(3.89) are time dependent, this however, was suppressed in the above equations.

Lastly, at the outer boundary we used "outflow" boundary conditions. These are simple to implement and are non-reflective [19, 36, 54, 78, 89, 90]. Following the update of the interior cells through the prescribed Godunov-type method described in secs. 3.4 and 3.5 the cell(s) at the outer boundary are updated (copied) using the value of the last (outermost) physical cell. In spherical symmetry this is easily represented by,

$$\mathbf{Q}_N \equiv \mathbf{Q}_{N-1}, \tag{3.90}$$

where N denotes the number of cells such that $r_N = r_{\max}$. The above condition, Eq. (3.90) can be thought of as an approximation to,

$$\left.\frac{\partial \mathbf{q}(r,t)}{\partial r}\right|_{r=r_N} = 0, \tag{3.91}$$

where $\mathbf{q}(r,t)$ is the continuous fluid variable. It is easy see that the solution at the boundary satisfying Eq. (3.91) is $\mathbf{q}(r - vt)$; if the radial fluid velocity is always positive, then, $\mathbf{q}(r - vt)$ describes a function which is advected in the positive r-direction. In all of our simulations the radial velocity is always positive or zero at the boundary, thus corresponding to outflow (it is always set to zero at the initial time). In practice, the boundary is set far away from the center, so, the dynamics there do not have enough time to significantly disturb the fluid at the boundary. This minimizes fluid loss due to outflow, maintaining approximate conservation of mass. For the axisymmetric code these condition is given by,

$$\begin{aligned}
\mathbf{Q}_{N_x,k} \equiv& \mathbf{Q}_{N_x-1,k} \quad \text{for} \quad k = 1,\, 2,\, \ldots,\, N_z, \\
\mathbf{Q}_{i,1} \equiv& \mathbf{Q}_{i,2} \quad \text{for} \quad i = 1,\, 2,\, \ldots,\, N_x - 1, \\
\mathbf{Q}_{i,N_z} \equiv& \mathbf{Q}_{i,N_z-1} \quad \text{for} \quad i = 1,\, 2,\, \ldots,\, N_x - 1,
\end{aligned} \tag{3.92}$$

with the identification that $[s_1,\, s_{N_x}] \equiv [s_{\min},\, s_{\max}]$, and $[z_1,\, z_{N_z}] \equiv [z_{\min},\, z_{\max}]$.

3.9 Conserved Quantities and Error Diagnostics

To ascertain the correctness of the numerical solutions we applied the independent residual test, compliance with conservation laws as well as various consistency checks between the spherically symmetric and axisymmetric calculations. First, we checked that our numerical algorithm conserves total energy E_{total}, total mass M_{total}, and total angular momentum L_{total}. The results of our calculation involving critical collapse are also checked for consistency with previous, related calculations. These are discussed in more detail in Chaps. 4 and 5.

3.9.1 Code Validation: Spherical Symmetry

We first checked that our spherically symmetric fluid model conserves total mass and energy. In spherical symmetry, these quantities are defined by the integrals,

$$M_{\text{total}}(t) = 4\pi \int_0^{r_{\max}} \rho(r,t) r^2 dr, \tag{3.93}$$

$$E_{\text{total}}(t) = 4\pi \int_0^{r_{\max}} E(r,t) r^2 dr, \tag{3.94}$$

where,

$$E(r,t) = \frac{P}{\Gamma - 1} + \frac{1}{2}\rho v^2 + \frac{1}{2}\rho\varphi, \tag{3.95}$$

is the total energy density of the fluid element. These integrals were approximated numerically at every time step. Fig. 3.2 illustrates the conservation property of the solution. This is shown via convergence of the measured quantities M_{total} and E_{total} at four resolution levels. As the resolution is incremented, the conserved quantities converged to a constant value. More specifically, the deviation from the measured time averages, $\langle M_{\text{total}} \rangle$ and $\langle E_{\text{total}} \rangle$ tends to zero as the resolution increases, Fig 3.2. The resolution is adjusted and monitored according to the following procedure.

At the lowest resolution level L_0 we start with an initial spacing Δr_{a0} over the uniform grid Ω_a. Higher levels L_1, L_2, L_3, … are initialized according to

$\Delta r_{a0}/2$, $\Delta r_{a0}/4$, $\Delta r_{a0}/8$. During the evolution this relative resolution is maintained over the Ω_a domain by scripting/recording the times and locations the AMR procedure is activated at L_0. Then, this script is read off at levels L_1, L_2, L_3, ... to appropriately double the resolution in both Δr_a and Δt at the correct r_a and t values. Therefore, over the uniform mesh $r \in (0, r_a]$ the resolution is precisely double at each higher level. However, over the logarithmic region ($r \in [r_a, r_b]$) the resolution cannot be precisely doubled while satisfying condition (3.69). This is the reason for stating that the resolution in the entire domain is only approximately doubled. Nevertheless, in simulations involving gravitational collapse most of the interesting dynamics occur over region covered by the uniform grid (Ω_a) where the resolution is most easily monitored.

To clinch the correctness of the numerical solution we checked for convergence of the independent residual introduced in Sec. 3.1.1. If the solution obtained is correct then applying an alternative discretization of the dynamical model to this solution defines the independent residual. The independent residuals for the Euler+Poisson Eqs. (2.29) and (2.27) in spherical symmetry, are labeled by, I_ρ, $I_{\rho v}$, I_E and I_φ are expected to converge to zero as the resolution is incremented. Note that here we refer to the Cartesian-like, vector form of Euler's equation in order use the more compact matrix notation in our definition of the independent residual given by,

$$\mathbf{I} = \frac{\mathbf{Q}_i^{n+1} - \mathbf{Q}_i^n}{\Delta t} + \frac{\mathbf{f}(\mathbf{Q}_{i+1}^n) - \mathbf{f}(\mathbf{Q}_{i-1}^n)}{4\Delta r} + \frac{\mathbf{f}(\mathbf{Q}_{i+1}^{n+1}) - \mathbf{f}(\mathbf{Q}_{i-1}^{n+1})}{4\Delta r} + - \frac{\mathbf{S}_i^n + \mathbf{S}_i^{n+1}}{2}, \tag{3.96}$$

where $\mathbf{I} \equiv (I_\rho, I_{\rho v}, I_E)^\intercal$ and $\mathbf{f}(\mathbf{Q}_i^n)$ are the physical fluxes computed from the numerical solution *i.e.* the cell-averages $\mathbf{Q}_i^n$ at time t^n and position r_i. The above Eq. (3.96), is a 2^{nd}-order finite difference approximation to the Euler equations and is independent of the methods used calculate the numerical solutions (finite volume and Godunov-type methods) therefore, it comprises an adequate definition of the in-

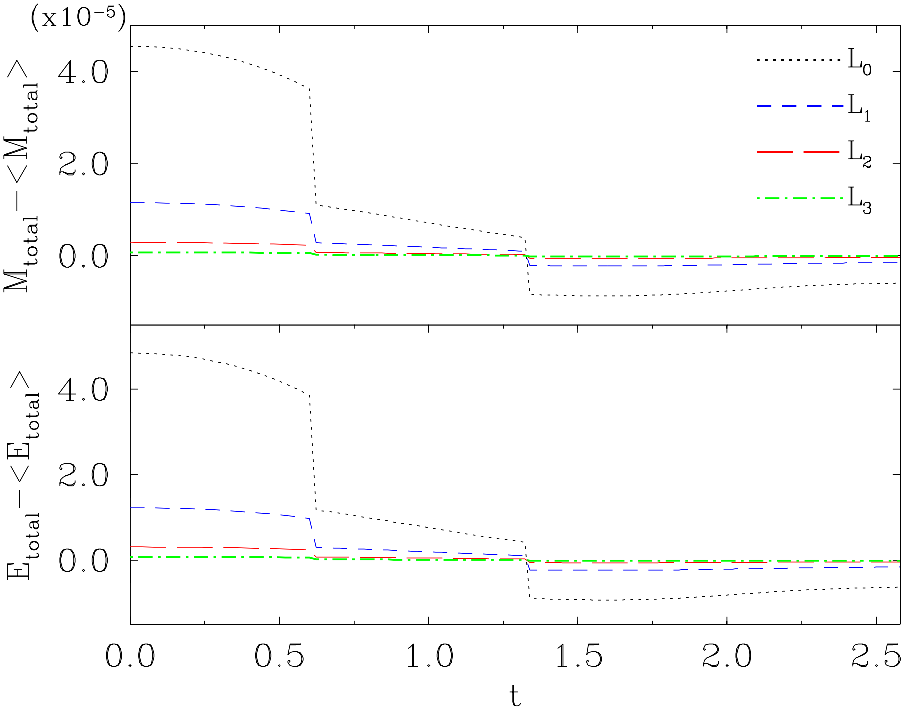

Figure 3.2: Plots illustrating the convergence of total mass (M_{total}) and energy (E_{total}) towards a constant value as the resolution is increased. Therefore, indicating the conservation of total mass and energy for the spherically symmetric hydrodynamic model. Plotted here are the deviation from the mass and energy time averages, $\langle M_{\text{total}}\rangle$ and $\langle E_{\text{total}}\rangle$ respectively. These are given at four levels of resolution, L_0, L_1, L_2, L_3, each successive level has approximately doubled the resolution of the previous one. These levels correspond to initial ($t = 0$) resolution over the uniform interior grid (Ω_a) of Δr_{a0}, $\Delta r_{a0}/2$, $\Delta r_{a0}/4$, $\Delta r_{a0}/8$, where our control parameter is Δr_{a0}. The approximate doubling of resolution (the resolution can only be exactly doubled over interior domain Ω_a) was achieved by scripting the regridding process, so that at each level L_j, the mesh refinement is performed at the same locations and at the same time. This accounts for the coincidence in the 'step' structure of the plotted data

dependent residual. The independent residual for Poisson's equation (2.27) is given by the following 1$^{\text{st}}$-order discretization,

$$I_\varphi = \frac{\varphi^n_{i+2} - 2\varphi^n_{i+1} + \varphi^n_i}{\Delta r^2} + \frac{2}{r_i}\frac{\varphi^n_{i+1} - \varphi^n_i}{\Delta r} - 4\pi\rho^n_i. \tag{3.97}$$

These residuals were evaluated at many resolutions levels.

The resolution levels L_ns are again set by scripting *i.e.* recording the times and locations the AMR facility is activated on the lowest level, L_0 during the evolution. This script is then read-off on L_1 to ensure that the resolution is always approximately doubled that of L_0, on L_2 it is quadrupled, and so on. For our applied HRSC method, the expected convergence of the independent residuals' l_2-norm is 2^{nd}-order except at shocks and extrema. At these locations only 1^{st}-order convergence is expected. If we scale the l_2-norms at levels L_1, L_2, $L_3 \ldots$ by a factor of $2, 4, 8, \ldots$ respectively, then the l_2-norms should overlap if the convergence is of order 1. For 2^{nd}-order the scaling factors should be $4, 16, 64, \ldots$. Since our dynamical model does involve shocks and extrema we expect less than 2^{nd}-order convergence. We scaled the l_2-norms of the independent residuals according to order 1 and plotted the results in Fig. 3.3. We clearly see higher than 1^{st} order convergence. The initial data corresponding to these convergence test is discussed in Table 4.4, Model-A.

3.9.2 Code Validation: Axial Symmetry

In the absence of any external torques the axially symmetric fluid conserves total angular momentum $\vec{L}_{\text{total}}$, in addition to total mass (M_{total}) and energy (E_{total}). In cylindrical coordinates these conserved quantities are given by the following integrals,

$$M_{\text{total}}(t) = 2\pi \int_{-z_{\max}}^{z_{\max}} \int_0^{s_{\max}} \rho(t,s,z) s ds dz, \tag{3.98}$$

$$|\vec{L}_{\text{total}}(t)| = L_z = 2\pi \int_{-z_{\max}}^{z_{\max}} \int_0^{s_{\max}} \rho(t,s,z) v_\phi(t,s,z) s^2 ds dz, \tag{3.99}$$

$$E_{\text{total}}(t) = 2\pi \int_{-z_{\max}}^{z_{\max}} \int_0^{s_{\max}} E(t,s,z) s ds dz. \tag{3.100}$$

These integrals were numerically approximated at every time step, this served to confirm the conservation of mass, angular momentum and energy. The plots provided in Fig. 3.4 clearly illustrate this for a sample run corresponding to $\Gamma = 1.00001$. The measured deviation from the time average quantities, *i.e.* $|M_{\text{total}} - \langle M_{\text{total}} \rangle|$,

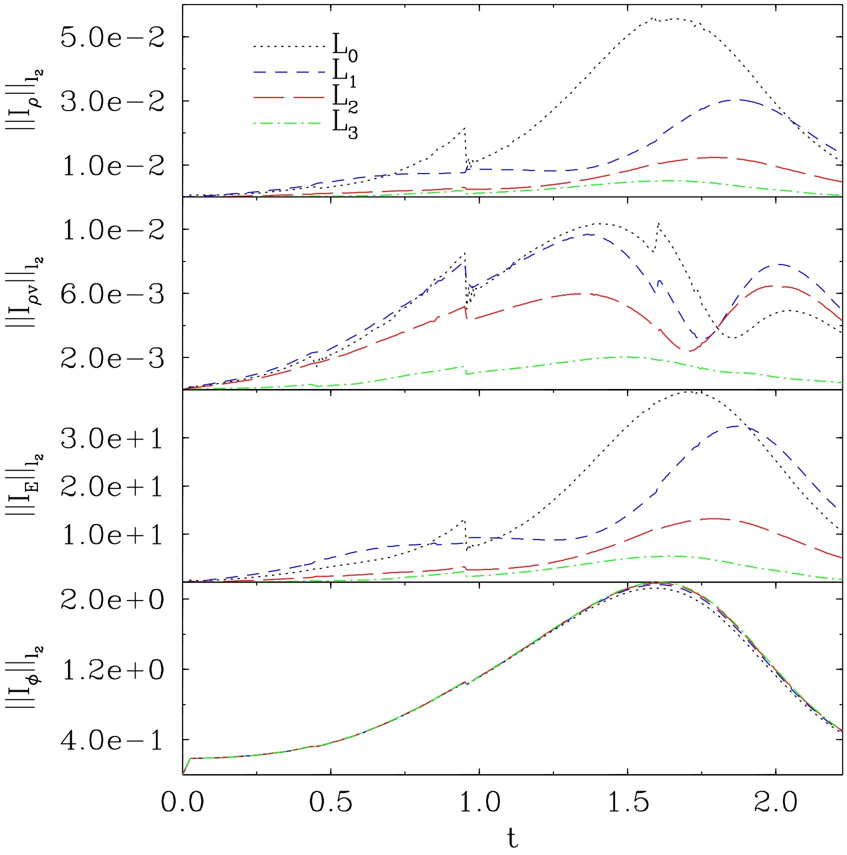

Figure 3.3: The independent residual convergence test for the spherically symmetric fluid. The l_2-norms of the independent residuals corresponding to the three conservation laws (fluid model) and Poisson's equation (Newtonian gravity) are presented here at four levels of resolution L_0, L_1, L_2, L_3. At each subsequent level the resolution is doubled. These panels illustrate the l_2-norms of the independent residuals I_ρ, $I_{\rho v}$, I_E and I_φ. These l_2-norms at levels L_0, L_1, L_2, L_3 were scaled by their respective factors 1, 2, 4, 8, such that 1^{st}-order convergence of the solution would make the scaled l_2-norm data were overlap. Since the HRSC methods we used are spatially 1^{st}-order at shocks and extrema and 2^{nd}-order everywhere else, we expect that the l_2-norms to indicate higher than 1^{st}-order convergence but less than second order. This fact is shown in the above panels

$|\vec{L}_{\text{total}} - \left\langle |\vec{L}_{\text{total}} \right\rangle|$, and $|E_{\text{total}} - \langle E_{\text{total}} \rangle|$ converges to zero with increasing resolution. These quantities are plotted in Fig. 3.4 at four levels of resolution (L_0, L_1, L_2, L_3). The mesh spacing (Δx, Δz) and time step (Δt) is multiplied by a factor of 1/2 at each successive higher level.

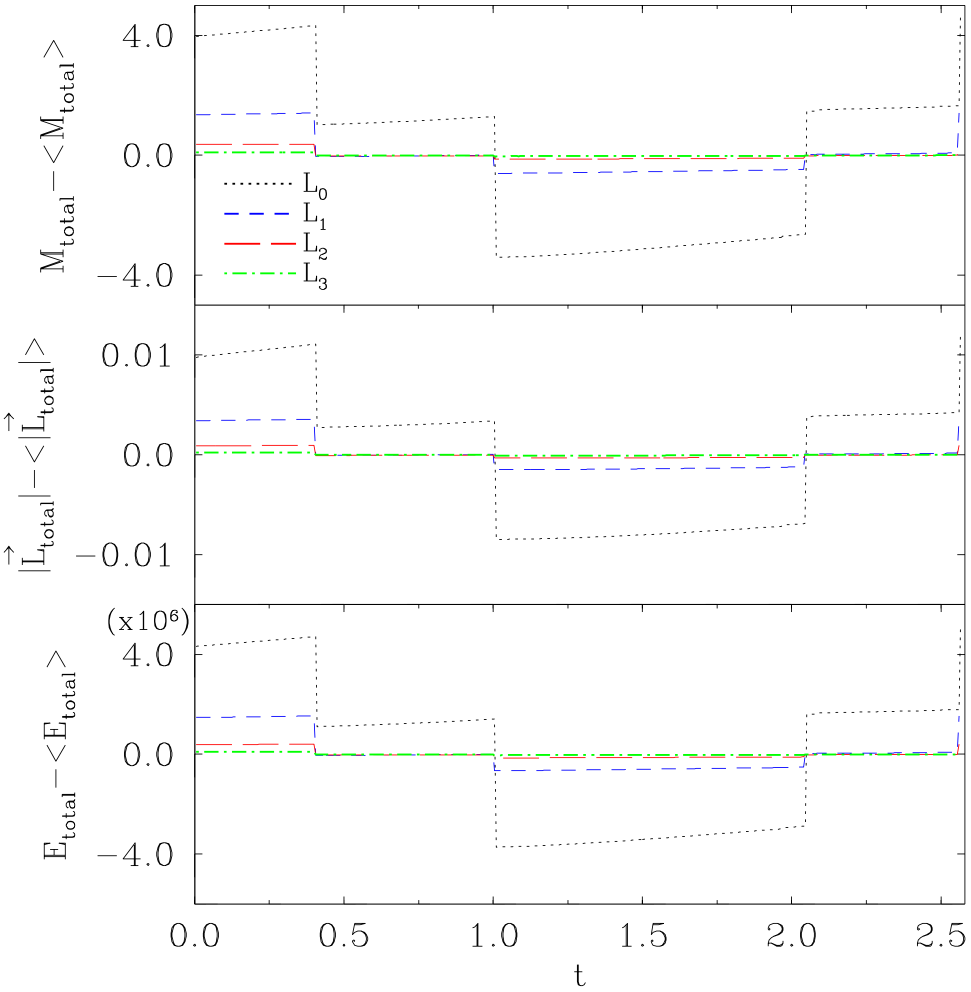

Figure 3.4: Plots of convergence of the conserved quantities for the axi-symmetric fluid. These plots indicate conservation of total mass ($M_{\rm total}$), angular momentum ($\vec{L}_{\rm total}$) and energy ($E_{\rm total}$). Once again, the deviation from their respective averages, $\langle M_{\rm total}\rangle$, $\left\langle |\vec{L}_{\rm total}| \right\rangle$, and $\langle E_{\rm total}\rangle$ converge to zero as resolution improves. Four resolution levels, labeled by L_0, L_1, L_2, L_3 were tested where level L_j has twice the resolution of level L_{j-1}. Again, the regridding procedure was scripted so that the AMR activation is coincident in both space and time in all the refinement levels tested. This accounts for the observed ‘step’ structure in the data.

As was done for the spherically symmetric fluid, the independent residual test was applied to the axisymmetric fluid dynamical equations. If applied correctly, the test allows us to claim, with very high degree of certainly that the employed numerical algorithm has indeed provided a solution to the equations of motion [16]. The corresponding 2^{nd}-order discretization used to define the independent residual for the axi-symmetric Euler equations (2.40) is

$$\begin{aligned}\mathbf{I} = \frac{\mathbf{Q}^{n+1}_{i,k} - \mathbf{Q}^{n}_{i,k}}{\Delta t} &+ \frac{\mathbf{f}^s(\mathbf{Q}^{n}_{i+1,k}) - \mathbf{f}^s(\mathbf{Q}^{n}_{i-1,k})}{4\Delta s} + \frac{\mathbf{f}^s(\mathbf{Q}^{n+1}_{i+1,k}) - \mathbf{f}^s(\mathbf{Q}^{n+1}_{i-1,k})}{4\Delta s} \\ &+ \frac{\mathbf{f}^z(\mathbf{Q}^{n}_{i,k+1}) - \mathbf{f}^z(\mathbf{Q}^{n}_{i,k-1})}{4\Delta z} + \frac{\mathbf{f}^z(\mathbf{Q}^{n+1}_{i,k+1}) - \mathbf{f}^z(\mathbf{Q}^{n+1}_{i,k-1})}{4\Delta z} \\ &- \frac{\mathbf{S}^{n}_{i,k} + \mathbf{S}^{n+1}_{i,k}}{2}. \end{aligned} \tag{3.101}$$

Similarly, $\mathbf{I} \equiv \left(I_\rho,\, I_{\rho v_s},\, I_{\rho v_\phi},\, I_{\rho v_z}\, I_E\right)^\intercal$. Note that $\mathbf{f}^s$ and $\mathbf{f}^z$ are the physical fluxes along the s and z directions, respectively. The independent residual for the axi-symmetric Poisson's equations is,

$$\begin{aligned}I_\varphi = \frac{\varphi^n_{i+2,k} - 2\varphi^n_{i+1,k} + \varphi^n_{i,k}}{\Delta s^2} &+ \frac{\varphi^n_{i,k+2} - 2\varphi^n_{i,k+1} + \varphi^n_{i,k}}{\Delta z^2} \\ &+ \frac{1}{s_i}\frac{\varphi^n_{i+1} - \varphi^n_{i}}{\Delta s} - 4\pi\rho^n_i. \end{aligned} \tag{3.102}$$

Measurements of the l_2-norms for the independent residuals of Euler's and Poisson's Eqs. (2.40) and (2.39) in axial symmetry are provided in Fig. 3.5. Again, we observed higher than 1^{st}-order convergence of the independent residual in accordance with HRSC methods. These sample convergence test pertain to octant-symmetric initial data, more specifically we used model-A in Table 5.1, with $\Gamma = 1.00001$.

Floor

To conclude the chapter on the numerical methods we mention briefly the treatment given to 'vacuum' regions in the computational domain. We used the minimum-atmosphere floor technique to ensure the fluid velocities are defined everywhere

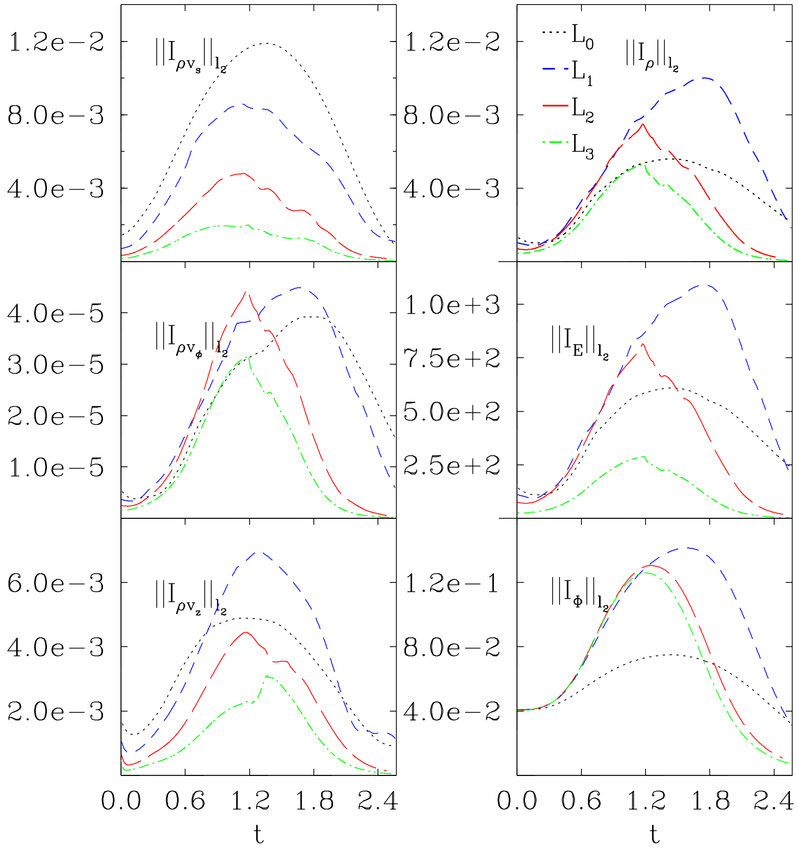

Figure 3.5: Independent residual convergence tests for the axi-symmetric fluid model. Plotted above are the l_2-norms of the independent residuals for the Euler equations (hydrodynamics) and Poisson's equation (Newtonian gravity) in axial symmetry. These residuals are labeled, $I_{\rho v_s}$, $I_{\rho v_\phi}$, $I_{\rho v_z}$, I_ρ, I_E and I_φ. The independent residual data is presented at four resolution levels, L_0, L_1, L_2, L_3. At each subsequent level the resolution is doubled. The l_2-norms at levels L_0, L_1, L_2, L_3 were scaled by their respective factors 1, 2, 4, 8, so if the convergence were 1st order everywhere and at all times the rescaled norms would approximately overlap. Since the methods used to solve the equation of hydrodynamics motion are spatially second-order except at shocks and extrema (HRSC methods) we expect less than second order convergence but higher than first order.

at all times. The underlying assumption is that these region(s) are dynamically insignificant due to their low energy content. In all of our simulations the minimum-atmosphere, or "floor" for the fluid density was set to $\rho_{\rm atm} = 10^{-12}$ and $P_{\rm atm} =$

10^{-12} for pressure. In the spherically symmetric model, the atmosphere has zero initial velocity. In axial-symmetry, only the axial component v_ϕ is initially non-zero in the rarefied (floor) regions. With these conditions, the fluid evolves without the generation of undefined, negative density or pressure regions, even after the atmosphere acquires a finite velocity.

Chapter 4

Results: Spherical Symmetry

In this chapter we present the results for all the calculations conducted in spherical symmetry. We begin with the spectrum of self-similar solutions for the polytropic gas. The nature of these solutions is discussed along with the role of the adiabatic index Γ. This discussion is followed by an analysis of the spherically symmetric linear perturbations, where again, the role of Γ is examined. We comment on the isothermal gas limit $\Gamma \to 1$ for which the results are well known [56, 60, 64, 81, 108].

4.1 Self-similar Solutions

Continuous self-similar solutions satisfying equations (2.52), and (2.53), along with regularity conditions (2.55)-(2.59) were determined via numerical integration. Recall that this model contains two undetermined parameter α^* and x_s, the amplitude of the dimensionless density and location of the sonic point respectively. We found that analytic solutions are only possible for specific values of the parameter $\alpha^* = \exp(Q_0)$ and x_s, thus, the spectrum of self-similar solutions is discrete. The correct values for Q_0 and x_s were found using a graphical technique initially used in [56] to find the analytic self-similar solution for an isothermal gas. This technique consists in integrating Eqs. (2.52), and (2.53) forward *i.e.* from $x \approx 0$ up to a 'matching point' $x_M < x_s$, as well as backwards from x_s to x_M. Since Q_0 is associated with the boundary conditions of $\alpha(x)$ and $u(x)$ at the origin it is reasonable that the forward integrations should be parametrized by different choices of Q_0. Similarly x_s determines the analytic behavior of the fields at the sonic point therefore, the backward integrations were parametrized by x_s. An example of these integrations in terms of the dimensionless velocity over the similarity variable x $(u(x)/x)$ is given in Fig. 4.1. Curves represented by blue-long-dashed lines correspond to forward integration at different values of Q_0. The red-short-dashed lines are the backwards integrations. Note that these solutions have different values at the matching point x_M (terminating point for both integrations). For a specific choice of Q_0 and x_s the solutions obtained by the forwards and backwards integrations join smoothly at x_M, as shown by the black dotted curve in Fig. 4.1. A systematic method to determine all possible smooth matchings of the solution at a prescribed x_M is described bellow.

The solutions at the matching point are stored in the arrays $f_{Q_0} \equiv \{\alpha(x_M),$ $u(x_M)\ Q_0\}$, $b_{x_s} \equiv \{\alpha(x_M),\, u(x_M),\, x_s\}$, where clearly f_{Q_0} and b_{x_s} contain the forward and backward integration data respectively. For purposes of illustration we consider $\Gamma = 1.12$ (non-isothermal gas) in our model. For this case, we integrated Eqs. (2.52) and (2.53) forwards with choices of Q_0 ranging from 0 to about 50, whereas for the backwards integrations x_s was varied over an interval ranging from x_M to about $4x_M$. Hundreds of runs were carried out for each case, the results/solutions at x_M $(\alpha(x_M), u(x_M))$ were plotted on a phase diagram given by Fig. 4.2. The intersections between the curves f_{Q_0} and b_{x_s} correspond to smooth matchings of the solutions at $x = x_M = 0.4$. These determine the correct choices of parameters Q_0 and x_s that yields regular (analytic) solutions. The same analysis was applied for other values of Γ.

The spectrum of solutions can be ordered according to the value of the parameter Q_0 (from here onward we refer to Q_0 instead of α^* to specify the value α at the origin). We labeled the solution with the lowest allowed value of Q_0 as the "Larson-Penston-type" solution. This solution has some relevance in astrophysical scenarios involving core collapse, and has been discussed in [63, 98, 105, 108]. Subsequent matchings occur at higher values of Q_0. This is referred to as the "Hunter-type" branch of solutions, see Fig. 4.2. The limiting $(Q_0 \to \infty)$ case is a singular, static

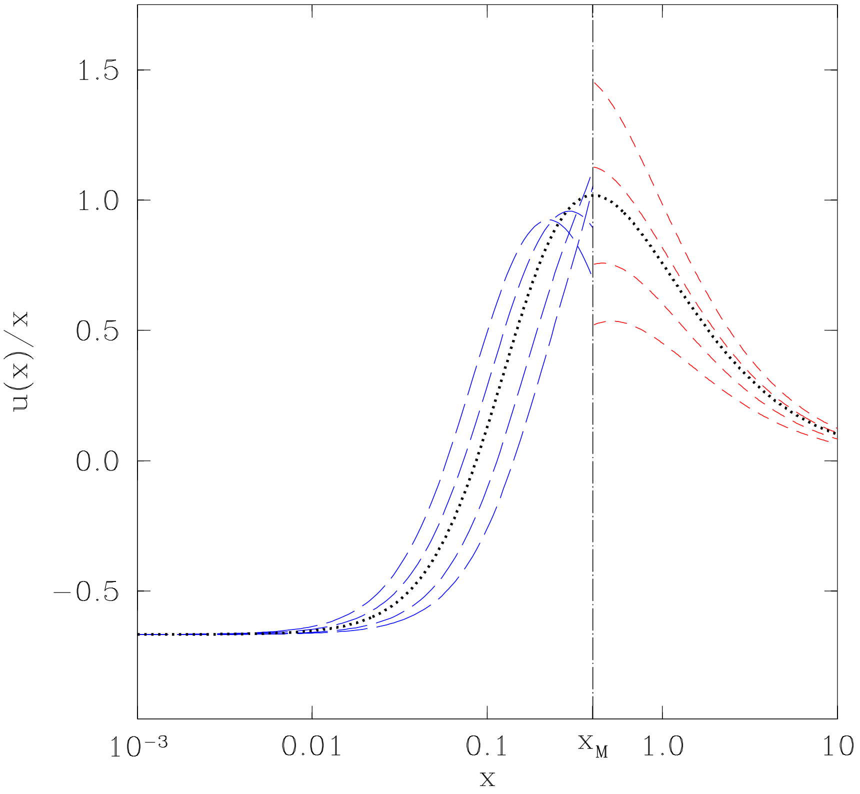

Figure 4.1: Plot of $u(x)/x$ for various choices of integration parameters Q_0 and x_s. The blue-long-dashed line represents the numerical solution from $x = 0$ to a so-called matching point x_M ($x_M = 0.4$ in this case). The matching point is chosen so that the autonomous system (Eqs. (2.52) and (2.53)) is well-behaved over the interval $[0,\, x_M]$. Specifically, the denominator in Eq. (2.52) is non-zero. It is noted that different choices of Q_0 yield different solutions at x_M. Similarly, the red-short-dashed curves represent the solutions obtained from integrating these equations for different choices of x_s (the choice for x_s represents a guess for the location of the sonic point). These integrations start at the chosen value of x_s and terminate at x_M. Note that $x_M < x_s$ and so the integrations from x_s are x_M are done in the reverse direction. Again, the solutions at x_M vary with x_s. Nevertheless, for a specific choice of Q_0 and x_s the solutions obtained by the forwards and backwards integrations match smoothly at x_M, a fact that is illustrated by the black-dotted line. This particular choice of parameters represent an analytic solution to the autonomous system.

($u = 0$) solution. The structure of the spectrum is essentially identical to that of the isothermal gas [56]. These solutions were labeled "Hunter-type-A, B, C, D, …" in

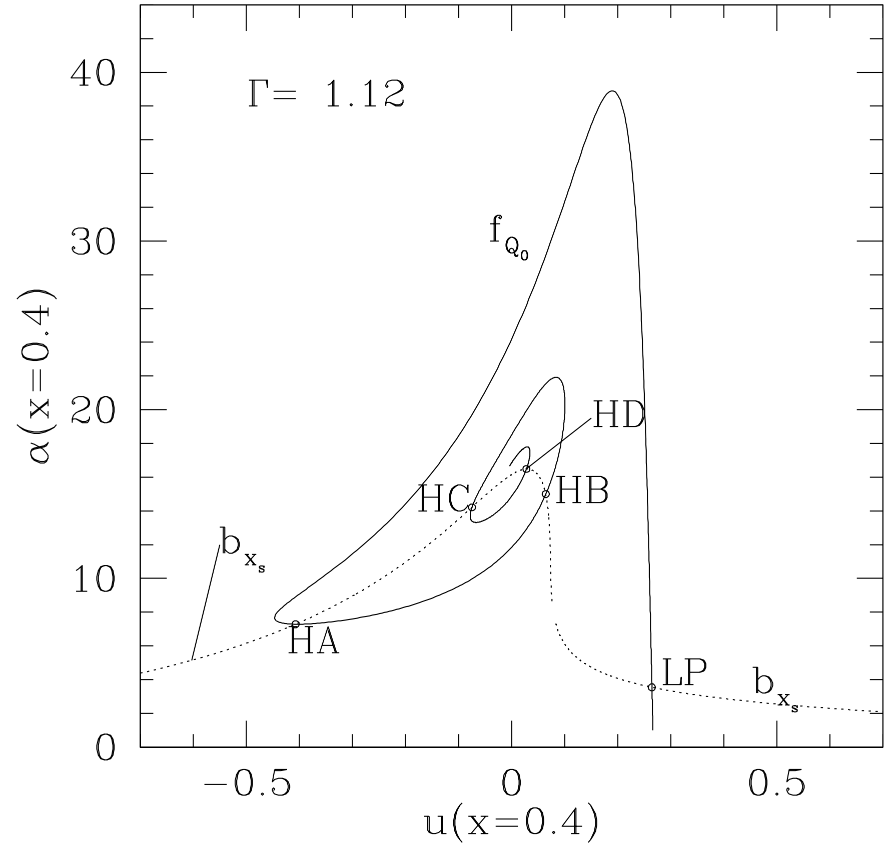

Figure 4.2: Phase space plot for the computed solutions $\alpha(x)$ and $u(x)$ at $x = 0.4$, where the adiabatic index $\Gamma = 1.12$. The curve f_{Q_0} are the results of the forward integrations of equations (2.52), and (2.53) from $x \simeq 0$ to $x = x_M = 0.4$ parametrized by Q_0; whereas the curve b_{x_s} are the results of backward integrations parametrized by x_s starting from the sonic point x_s to $x = x_M = 0.4$. The points where the curves cross correspond to the correct preregistration of the solutions. Only a discrete set of parameters $\{Q_0, x_s\}$ results in allowed solutions. The Larson-Penston (LP) solution has the lowest value for the parameter Q_0. As shown the Hunter solutions (HA-HD) are generated as the f_{Q_0} begins to spiral around a common point in the b_{x_s} curve. This graphical technique was used in [56].

accordance with their increasing central value parametrized by Q_0. To our knowledge this is the first time these Hunter-type solutions are explicitly determined for $\Gamma > 1$. Since the spectrum structure for higher values of Γ is essentially identical to the isothermal case from here onward we shall call these set of regular solutions as simply the Larson-Penston (LP), and Hunter-A, B, C, D, ...

The specific values of Q_0 and x_s for the LP solution and the first four Hunter solutions are found in Table 4.1. Notice that the Hunter solutions have much higher central values since $\alpha(0) = \exp(Q_0)$. The profiles for the self-similar density variable $\alpha(x)$, corresponding to these solutions are plotted in Figure 4.3. The velocity variable $u(x)$ is plotted in Figure 4.4. A distinguishing feature of the Hunter solutions are the oscillations in the velocity profiles. The number of nodes in their profiles follows from their placement in the spectrum hierarchy, just as was found in [64] for $\Gamma = 1$. The Larson-Penston solutions lacks any of these oscillations which implies the fluid is collapsing into the origin for all times, *i.e.* this solution describes coherent core collapse. In contrast, the Hunter-A solutions contains a region adjacent to the collapsing core where the fluid is not in-falling. Since these plots represent self-similar solutions, this rarefied region "chases" the collapsing core evacuating fluid away from the origin. Higher order Hunter solutions contain more of these increasingly compact regions where the fluid velocity changes direction. All of these however, contain a rarefaction wave adjacent to a collapsing core as shown in Fig. 4.4.

Table 4.1: Values of the parameters Q_0 and x_s for the similarity solutions corresponding to $\Gamma = 1.12$.

Solution	Q_0	x_s
Larson-Penston	1.32732279	2.713336217
Hunter-A	10.62019209	6.110589148×10^{-1}
Hunter-B	14.63542969	1.649524387×10^{-1}
Hunter-C	21.75502169	1.012505889
Hunter-D	27.18143020	1.343169706

4.1.1 Solutions, $1 \leq \Gamma < 6/5$

In what follows we considered the effect of changing the polytropic index Γ on the Hunter and LP solutions. We found that the solutions' central value parameter Q_0 becomes larger as Γ is increased. The entire spectrum of analytic solutions shifts to

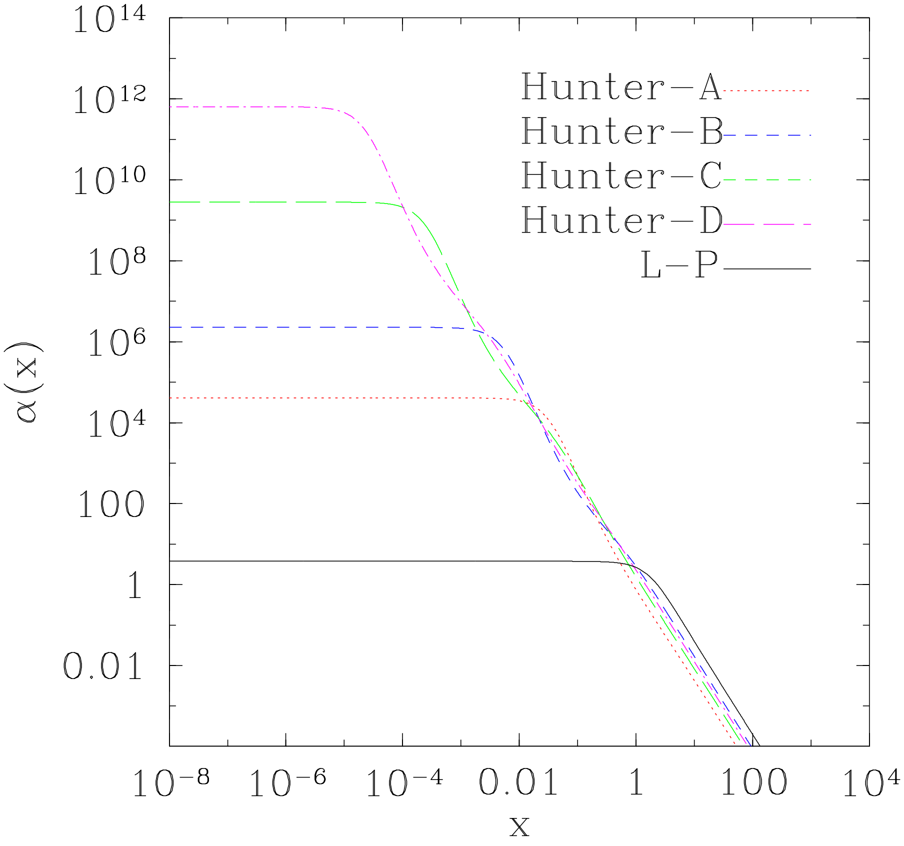

Figure 4.3: Plot of self-similar solutions $\alpha(x)$ corresponding to $\Gamma = 1.12$. These solutions plotted here on a logarithmic scale are the first four Hunter solutions $(A - D)$ as well as the Larson-Penston solution which has the lowest central value $(x = 0)$. The Hunter family appears to have an infinite and discrete structure with its members having ever-increasing central values. This is similar to the results presented in [64] for the isothermal gas.

higher Q_0 values, whereas the sonic point x_s migrates towards the origin. This fact make computation of the solutions increasingly more difficult. The matching point, x_M for the Hunter solutions is "squeezed" into a narrow region where the gradients in Eqs. (2.52), (2.53) are very high.

Aside from the LP solution, the Hunter-A solution has the lowest Q_0 among the Hunter family, so it is the least expensive to integrate since the gradients are less steep than the other family members Fig. 4.2. We computed the parameters

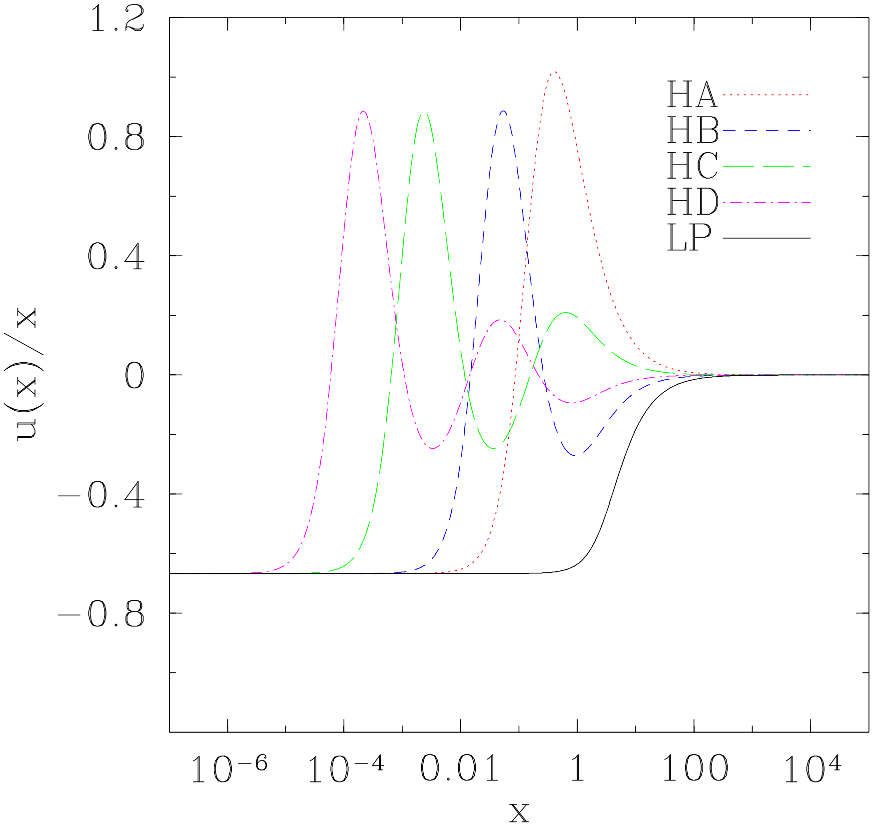

Figure 4.4: Plot of self-similar solutions $u(x)/x$ corresponding to $\Gamma = 1.12$ An oscillatory patterns is revealed near the origin for the Hunter solutions. Such oscillations are absent in the Larson-Penston solution. Furthermore, the number of nodes in their profiles is ordered. This is similar to the ordering of allowed central density parameter Q_0. This means that the Hunter-A solution has the lowest parameter Q_0 of the Hunter-family and displays one node, whereas the Hunter-D solution contains four nodes and has the fourth largest Q_0 value. The results shown here are very similar to those found in [64] Fig. (2) for $\Gamma = 1$.

Q_0, x_s for the Hunter-A solution for various values of Γ starting at the known $\Gamma = 1$ (the isothermal gas). We found that the center of the dimensionless density variable $\alpha(x)$ increases nonlinearly with linear increments in Γ. The results of the numerical integration are tabulated in 4.2. The density and velocity profiles for the Hunter-A solutions are presented in Fig. 4.5 and Fig. 4.6. We noticed that the node in the velocity field also changes non-linearly. This behavior is not shared by the LP

Table 4.2: The Hunter-A parameters Q_0 and x_s for some choices of $\Gamma \in [1,\ 6/5)$.

Γ	Q_0	x_s
1.0	7.45615862	7.390727573×10^{-1}
1.00001	7.45631897	7.390753939×10^{-1}
1.04	8.18305221	7.385798698×10^{-1}
1.12	10.62019209	6.110589148×10^{-1}
1.16	13.42242634	3.953918340×10^{-1}
1.18	16.67083350	2.067449815×10^{-1}
1.19	20.36959616	9.053763430×10^{-2}

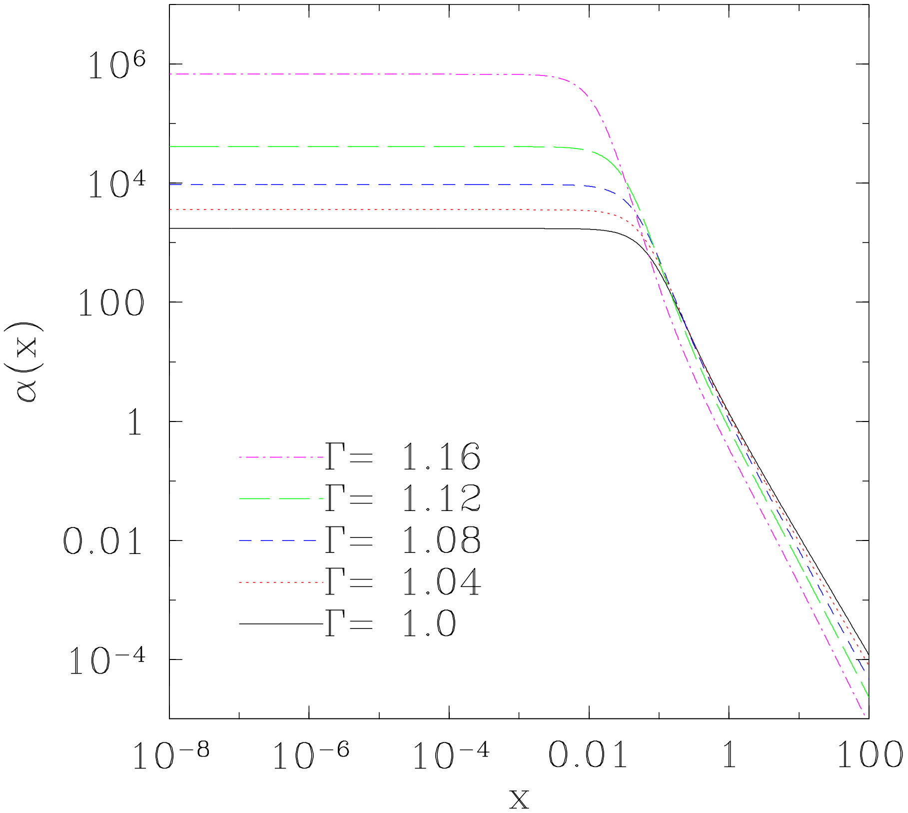

Figure 4.5: Hunter-A solution for $\alpha(x)$ in the range $1 \leq \Gamma < 6/5$. In contrast to the Larson-Penston solution, the Hunter-A solution does not behave linearly with respect to linear changes in Γ. As illustrated in this plot. This solution (Hunter-A) does not seem to exists for $\Gamma \geq 6/5$, its behavior near this critical value is displayed separately, Fig. 4.8.

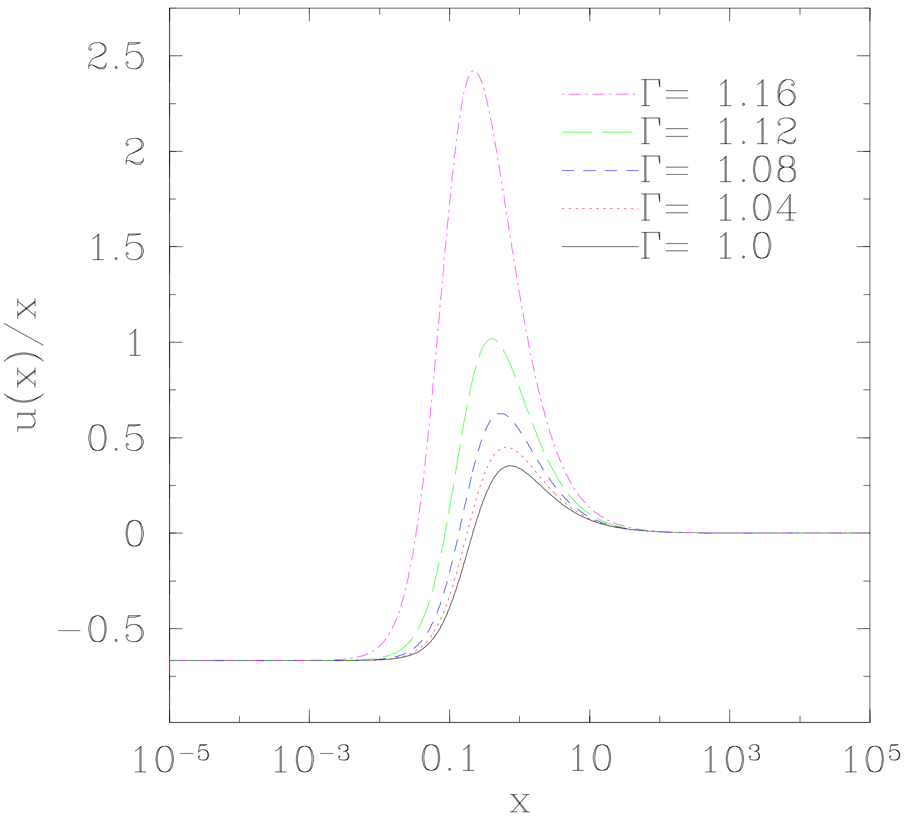

Figure 4.6: Hunter-A solution for $u(x)/x$ in the range $1 \leq \Gamma < 6/5$. The plotted $u(x)/x$ profiles are the Hunter-A solutions chosen at uniformly distributed Γ values over this range. We observed the single node which characterizes this solution grows nonuniformly as Γ is varied from 1 to 6/5.

solution which as seen in Fig. 4.7 changes linearly over the range $1 \leq \Gamma < 6/5$. We discovered that as we approach $\Gamma = 6/5$, the central value pertaining to the Hunter-A solution diverges. This limit was calculated by choosing Γ according to,

$$\Gamma(i+1) = \frac{6}{5} - \frac{6/5 - \Gamma(i)}{2^i}, \quad \text{for} \quad i = 0, 1, 2, \ldots, \infty. \tag{4.1}$$

Where $\Gamma(i)$ was used in the i^{th} integration, *i.e.* Γ is chosen such that interval $6/5 - \Gamma(i)$ is reduced by one half at every trial, as a result each new increment gets exponentially smaller. The results of the integrations were plotted in Fig. 4.8. This plot exhibits the exponential growth of the density profiles ($\alpha(x)$) for the Hunter-A solution in this limit. We concluded that Hunter-A disappears at $\Gamma = 6/5$, and given that it has the lowest central value, the entire Hunter family vanishes at this point. Our results also indicate that the Hunter solutions do not reappear in the range $6/5 < \Gamma < 4/3$. Our investigation looked for matchings in f_{Q_0} and b_{x_s} (Fig. 4.2) in the latter range but failed to find any. A single matching corresponding to the LP solution persists in the range $6/5 \le \Gamma < 4/3$.

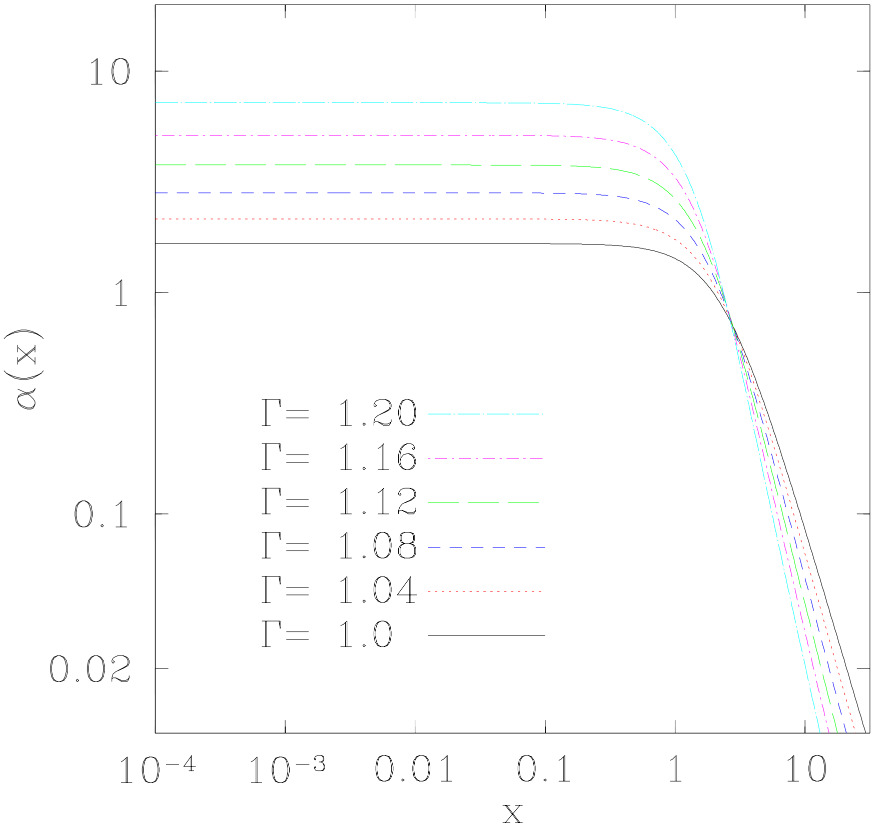

Figure 4.7: Larson-Penston solution for $\alpha(x)$ in the range $1 \le \Gamma \le 6/5$. The Larson-Penston solutions was calculated at uniformly spaced values of Γ in this interval. Notice that the dimensionless density profile ($\alpha(x)$) near the center increases linearly with respect of a linear increase in Γ. Notice also that we are able to compute this solution (LP) across the seemingly special value of $\Gamma = 6/5$.

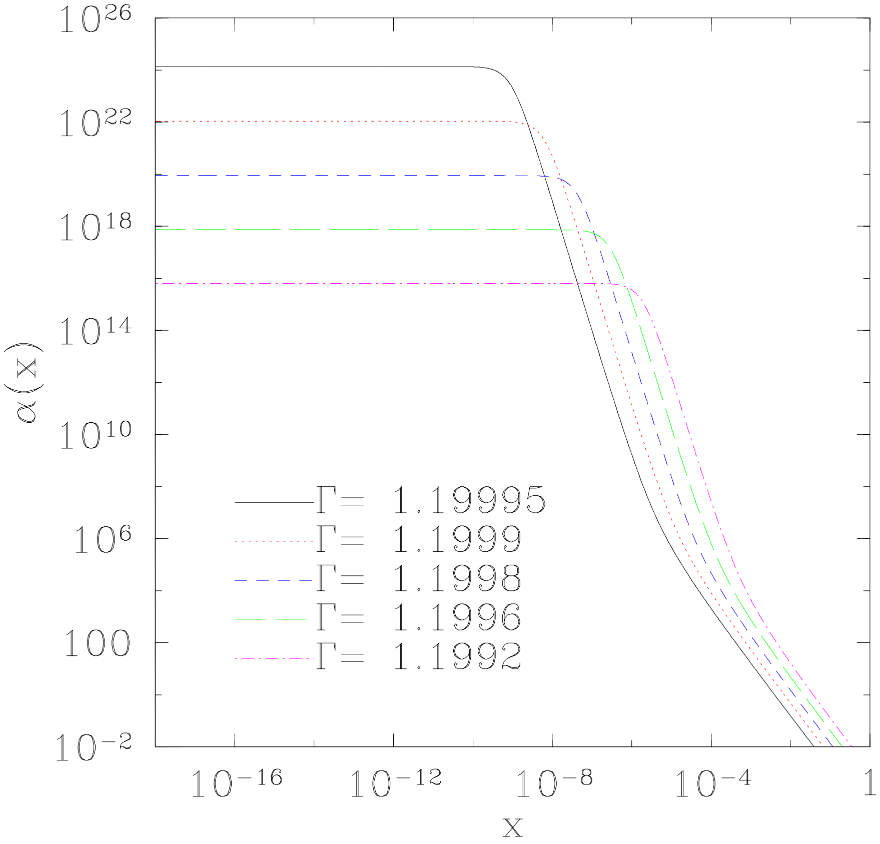

Figure 4.8: Multiple plots of the Hunter-A solutions at various values of Γ close to the critical value of $\Gamma = 6/5$. Γ is chosen at every trial such that the interval Γ-6/5 of the previous trial is reduced by a factor of 1/2. The amplitude of the Hunter-A solution as shown here increases exponentially.

4.1.2 Growing Modes

We looked exclusively for growing mode solutions ($\lambda > 0$) to Eqs. (2.78)–(2.84). This was done systematically by subjecting the spectrum of regular self-similar solutions for a given Γ to a linear stability analysis. Equations (2.78)–(2.80) were integrated using the *LSODE* facility in *Maple*-12. The relative tolerances were set to a maximum of 10^{-18} for all of our calculations, and we use equation (2.81) to check for consistency. The correct values for λ were determined by the shooting method-technique. First, the equations were integrated "outward" from $x \sim 0$ towards the sonic point x_s. Near x_s, the solutions $\delta\alpha(x)$ and $\delta u(x)$ go to $\pm\infty$ for some non-negative choice of λ. Since regularity implies that the solution is finite at the sonic point, we looked for $\lambda > 0$ such that $\delta\alpha(x)$ and $\delta u(x)$ are finite and satisfy Eq. (2.84) for $x \approx x_s$.

As was expected the possible non-negative solutions for λ depend on the specific self-similar solution being tested. There were no analytic growing modes found for the Larson-Penston solution at any Γ in the interval $[1, 4/3)$. Varying the growth rate, λ, from 0 to a vary large value ($\sim 10^{32}$) did not change the blow-up behavior of $\delta\alpha$, δu near the sonic point for the LP solution. This implies that there are no non-negative values of λ that can satisfy Eq. (2.84) and thus no unstable modes. The Hunter-A solution has precisely one growing mode for $\Gamma \in [1, 6/5)$, where the Hunter-A exists. The Hunter-B,C,D,... solutions have 2, 3, 4, ... growing modes respectively. In the limit $\Gamma \to 1$ the growth rate, λ, reduces to that computed in [64] for the isothermal gas. We discovered that the overall effect of Γ on the stability of the Hunter solutions is to render them more unstable, *i.e.* the growth rates becomes larger as Γ increases. Nevertheless, the overall mode structure and hierarchy of the solutions remains unchanged, until we reach $\Gamma = 6/5$.

Table 4.3 provides a list of the computed numerical values of the unstable modes for selected self-similar solutions. Notice that the unstable mode for the Hunter-A solution also seem to diverge at the special value of $\Gamma = 6/5$.

Table 4.3: Results of the stability analysis performed particularly on the Hunter-A solution for the range $1 \leq \Gamma < 6/5$.

Γ	Solution	Mode	λ
1.0	Hunter-A	1	9.4637
1.00001	Hunter-A	1	9.4643
1.001	Hunter-A	1	9.5247
1.04	Hunter-A	1	1.2729×10^{1}
1.12	Hunter-A	1	3.6734×10^{1}
	Hunter-B	1	1.0337×10^{1}
		2	2.6841×10^{2}
	Hunter-C	1	2.1588×10^{1}
		2	3.3496×10^{2}
		3	9.4086×10^{3}
1.16	Hunter-A	1	1.3456×10^{2}
1.18	Hunter-A	1	6.4143×10^{2}
1.19	Hunter-A	1	3.9349×10^{3}
1.1996	Hunter-A	1	1.228×10^{8}
1.1998	Hunter-A	1	1.344×10^{9}
1.1999	Hunter-A	1	1.49×10^{10}
1.19995	Hunter-A	1	1.67×10^{11}

The solution profile, and specifically its amplitude has a similar dependence on Γ, becoming singular at the origin as Γ approaches 6/5 (we fixed the free parameter $\delta u_0 = 1$ in Eqs. (2.82) and (2.83) in all our calculations). This behavior is expected since the self-similar solutions themselves, as was argued in Sec. 4.1.1 are singular there. A plot of the calculated perturbation functions, $\delta\alpha$ and δu for the Hunter-A solutions are presented in Fig. 4.9 in the extreme case where $\Gamma = 1.1999$. Again, we performed a consistency check by setting $\Gamma = 1$ and confirming that our solution profiles reduce to those provided in [64].

At this point we would like to summarize the results presented thus far. We found the spectrum of analytic similarity solutions for the polytropic gas model by integrating (numerically) the autonomous system Eqs. (2.52)–(2.54) and imposing regularity (analyticity) at the origin and the sonic point. The spectrum of solutions is discrete; it follows a hierarchical structure identical to the regular self-similar

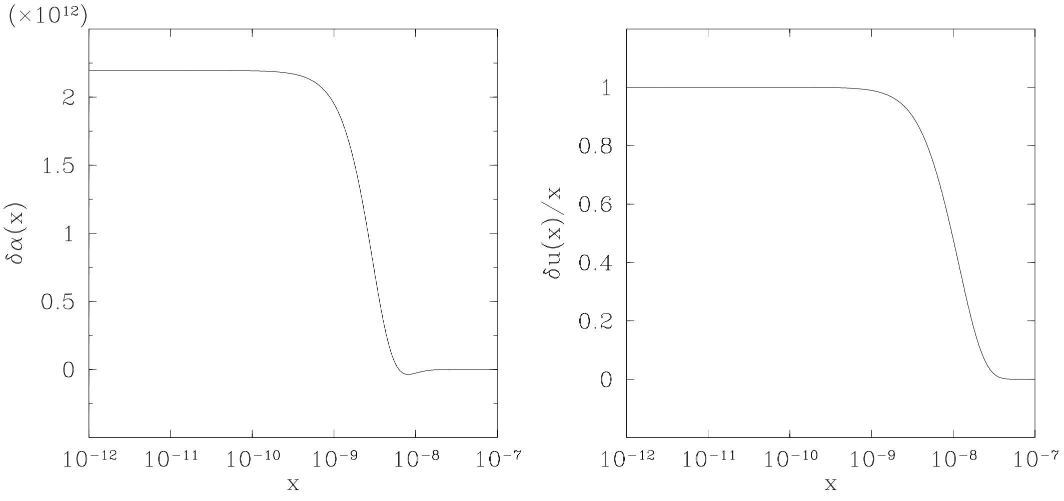

(a) (b)

Figure 4.9: Linear perturbation functions $\delta\alpha(x)$ and $\delta u(x)/x$ for the Hunter-A solution where $\Gamma = 1.1999$. The amplitude of $\delta\alpha(x)$ provided in panel (a) diverges as $\Gamma \to 6/5$. However, for $\Gamma < 6/5$ this amplitude can be rescaled (normalized), this freedom is entailed by the parameter δu_0 in Eqs (2.82) and (2.83). Panel (b) presents the profile for $\delta u(x)/x$. The features of mode functions are "squeezed" near the origin

solutions for an isothermal gas found previously in [56, 64]. In the limit $\Gamma \to 1$ our solutions reduce to the isothermal spectrum. This structure persists for $\Gamma \in [1,\, 6/5)$. In this range the first member of the Hunter-branch of solutions (Hunter-A) contains a single unstable mode, suggesting its potential role as a critical solution [64, 66, 99]. We found that the Lyapunov exponent corresponding to the unstable mode(s) of the all the Hunter solutions increases with increasing Γ. Interestingly, the entire Hunter-branch of self-similar solutions disappears for $\Gamma \geq 6/5$, hinting of a possible change in critical behavior of the polytropic gas at this value of Γ. This was investigated from dynamical simulations; the results are presented in the next section.

4.2 Numerical Simulations

In this section we present the numerical solutions of the spherically symmetric dynamical model given by Eqs. (2.24)–(2.27) for $1 \leq \Gamma < 4/3$. Previously, type-II critical phenomena had been identified in dynamical simulations of Newtonian gravitational collapse of an isothermal gas [48]. The work of Harada *et. al.* begins by considering an isentropic hydrodynamic model (equivalent to equations (2.30)–(2.32), with $\Gamma = 1$) from the outset. We begin with a more general approach by including the energy density conservation law Eq. (2.26) (Euler equations) and adopting the more generic polytropic ideal gas law, given by EoS (2.18).

Initial Data

In most of our calculations, the density and pressure profiles were initialized according to a Gaussian function. Nevertheless, a second 1-parameter family of initial data was used in some cases. We labeled these sets as, Models A and B. Their functional forms are provided in Table 4.4. In both cases, the radial velocity field of the initial data was set to zero. Note that the control parameter p, modulates the amplitude of the pressure profile.

For dynamical evolutions of Eqs (2.24)–(2.27) involving larger values of the parameter Γ, it was necessary to select initial data that "resembled" the corresponding Hunter-A solution. The reason for this selection is made explicit later on. The general form of this initial data is then given by,

$$Z(0, x) = Z^{\star}(x) + f_p(x). \tag{4.2}$$

Where $Z^{\star}(x)$ is the Hunter-A solution, and $f_p(x)$ is a function that describes the deviation from Hunter-A. We allow the parameter p to control one aspect of this function, *e.g.* the amplitude of a Gaussian profile. Our specific choice for $f_p(x)$ was,

$$f_p(x) \equiv \begin{pmatrix} pe^{-r^2} + \varepsilon_\rho(r) \\ \varepsilon_v(r) \\ \varepsilon_P(r) \end{pmatrix}. \tag{4.3}$$

The entries in Eq. (4.3) expresses the deviation from Hunter-A for the primitive variables $\rho(0,r)$, $v(0,r)$ and $P(0,r)$. The variables ε_ρ, ε_v, and ε_P are unknown functions, representing all other numerical errors associated with approximating the Hunter-A solution. These functions are small compared to the manually introduced Gaussian perturbation.

Table 4.4: Spherically symmetric initial data.

Model A	Model B
$\rho(0,r) = e^{-r^2}$	$\rho(0,r) = \begin{cases} \dfrac{1}{(1+r^2)^2} & \text{if } r < 1 \\ 10^{-12} & \text{if } r \geq 1 \end{cases}$
$v(0,r) = 0$	$v(0,r) = 0$
$P(0,r) = pe^{-r^2}$	$P(0,r) = \begin{cases} \dfrac{p}{(1+r^2)^2} & \text{if } r < 1 \\ 10^{-12} & \text{if } r \geq 1 \end{cases}$

4.2.1 Simulations $\Gamma \approx 1$

The numerical experiment consisted of evolving 1-parameter families of initial data of the type given in Table 4.4, until we could unambiguously, identify its final state. The observed initial stages of the evolution, regardless of its final fate are very similar. Qualitatively, we observed a deepening of the Newtonian potential well ($\varphi(r,t)$) with subsequent contraction of the matter at the origin. The central density increases as a core of collapsing matter forms around the center. Following this transient behavior, we found that for values of our control parameter p less than some threshold $p^\star$, the central density continues to grow; the central core collapses

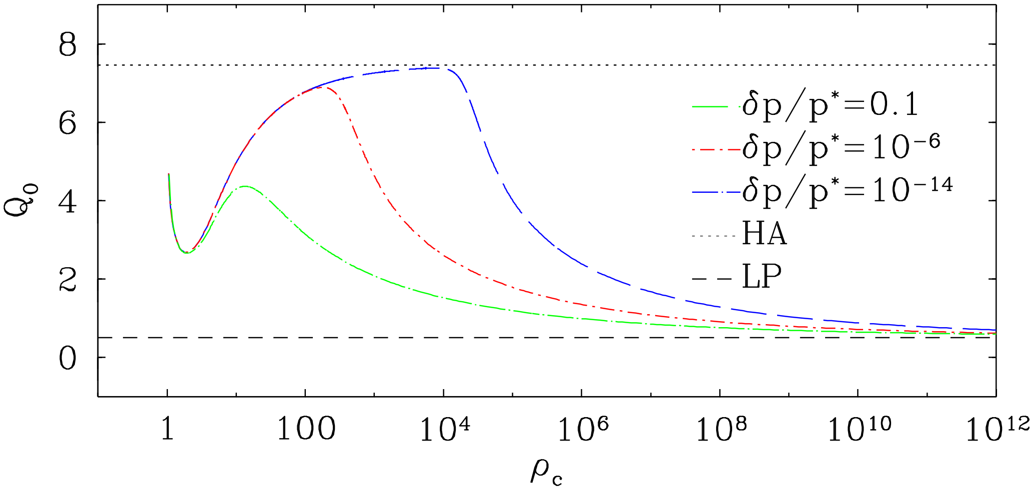

Figure 4.10: Plot of the similarity parameter Q_0 versus central density $\rho(t, 0)$ for varying degrees of fine-tuning. This plot shows the effect of fine tuning the control parameter p to the critical value $p^\star$, for $\Gamma = 1.00001$. Note that $|p - p^\star| \equiv \delta p$. The value of Q_0 characterizes the self-similar solutions (Table 4.1). $Q_0 = 4\pi G \rho_c t^2$ (with G set to 1 and $\rho_c \equiv \rho(0, t)$) computed from the dynamical solutions evolves towards the self-similar Larson-Penston (LP) value, irrespective of the fine tuning. The fine-tuned evolution approaches the numerical value of Q_0 corresponding to the Hunter-A (HA) solution at intermediate times. At late times, the spherical unstable perturbation mode interrupts this convergence, and the dynamically computed value of Q_0 again approaches the Larson-Penston value.

homologously. The central density grows exponentially, and over exponentially decreasing time scales. We followed this evolution until the central density had grown over 14 orders of magnitude; at which point the simulation is halted, and we declare this final state as the Newtonian analogue of black hole (BH) formation. In contrast, the subcritical regime, $p > p^\star$ the central density ceases to grow at some maximum value ρ_{max}, this is followed by a gradual decrease in the central density leading, ultimately to complete evacuation of the matter in the central region. We call this case, “dispersal”. Once these two regimes have been identified we focused on the behavior of the solution as we fine tuned our initial data to the threshold of singularity “BH” formation, *i.e.* we fine tune $p \to p^\star$. We call the solution at $p = p^\star$ the critical solution.

We first studied the near isothermal gas $\Gamma = 1.00001$, choosing this value of Γ allows us to compare our results with those obtained in [48, 64] where an strictly isothermal gas was considered. A bisection search which partitions the interval separating "collapse" and "dispersal" solutions was utilized to zero-in on the critical value $p^\star$. The search was performed until $|p - p^\star|/p^\star \to 10^{-14}$. We investigated the nature of the collapse at the origin ($r = 0$) by computing the dimensionless density $\alpha(x = 0)$ from the dynamical solution. For comparison purposes it is more convenient to work with $Q_0 = e^{\alpha(0)}$. Based on Eq. (2.43) we can compute

$$Q_0(t) = \ln(4\pi G\rho(t, 0)(t_0 - t)^2). \tag{4.4}$$

This requires that we know the time of singularity formation t_0. In order to identify this parameter in our simulations we applied a similar procedure to that used by Harada *et. al.* [48]. First, we assumed the center $\rho(t, 0)$ is at all times collapsing in a self-similar fashion such that $\rho(t, 0)(t_0 - t)^2$ is a constant. From this assumption we can compute t_0^n, the t^n-prediction for the time of collapse. Assuming the solution is self-similar, Q_0 is a constant and we have the relation,

$$\rho_c^{n+1}(t_0^n - t^{n+1})^2 = \rho_c^n(t_0^n - t^n)^2, \tag{4.5}$$

where $\rho_c^n \equiv \rho(t^n, 0)$. Then, t_0^n is used in Eq. (4.4) to determine Q_0. If this assumption is correct, Q_0 should be constant or approaching a constant value. More importantly, since Q_0 parametrizes the hierarchy of self-similar solutions as discussed in 4.1.1 we can monitor its possible convergence to any of these values. Another approach to compute t_0 also used in [48] involved directly measuring the time required for the fluid to effectively collapse. Numerically, this was accomplished by measuring the elapsed time during which the initial central density increases over 14 orders of magnitude.

By fine tuning p in our initial data close to the critical value of $p^\star$ we found that the computed quantity of $Q_0(t)$ converges to the value corresponding to the Hunter-A solution. In fact, the Hunter-A solution is the critical solution as suggested by its characteristic single-unstable-mode. Evidence for this is seen in Fig. 4.10, where we have plotted our computed value of $Q_0(t)$ against the central density, $\rho(t, 0)$, along with the known values of Q_0 for the Hunter-A and LP solutions. As the central density increases during critical collapse, the Hunter-A solution becomes an "intermediate attractor" of the evolution. As the density increases the growing mode eventually disrupts this convergence. The growing perturbation effectively "pushes" the intermediate state away from Hunter-A and towards the stable LP similarity solution. The LP solution as revealed by our mode analysis in Sec. 4.1.2 lacks any growing modes, so it is expected that any set of collapsing data will converge to it. This prediction is corroborated by Fig. 4.10. This result is essentially identical the one presented by Harada *et. al.* in [48]. However, we obtained this result via a more general EoS (2.18).

So far the presented results apply only to the central density. The convergence to the self-similar Hunter-A solutions extends over a region surrounding the center. A series of snapshots for critical evolution are presented in Fig. 4.11. The plots pertain to the dimensionless density variable $\alpha(x)$ defined in Eq. (2.43). Generic initial data convergences to the Hunter-A solution at intermediate times $(t_1 - t_5)$ in Fig. 4.11 (blue curve). We expect the same local convergence of the other dimensionless variables defined in Eq. (2.43). We also looked at the velocity profile $u(x)$ for critical evolution and found that in fact at intermediate times it matches the profile of the Hunter-A solution. A rarefaction wave envelopes the collapsing core, thus its size diminishes. This feature of the Hunter-A solution is replicated by the critical solution as seen in Fig. 4.12 panels $t_1 - t_5$. Over time the unstable mode begins to dominate the evolution and the solution deviates from Hunter-A. This is again verified by continuing the evolution of critical data past its intermediate convergence to the 1-mode unstable solution in Fig. 4.11 and Fig. 4.12 $(t_6 - t_9)$, the profiles of both $\alpha(x)$ and $u(x)$ are described by the LP solution. This late-time behavior is observed in supercritical evolutions irrespective of fine-tuning.

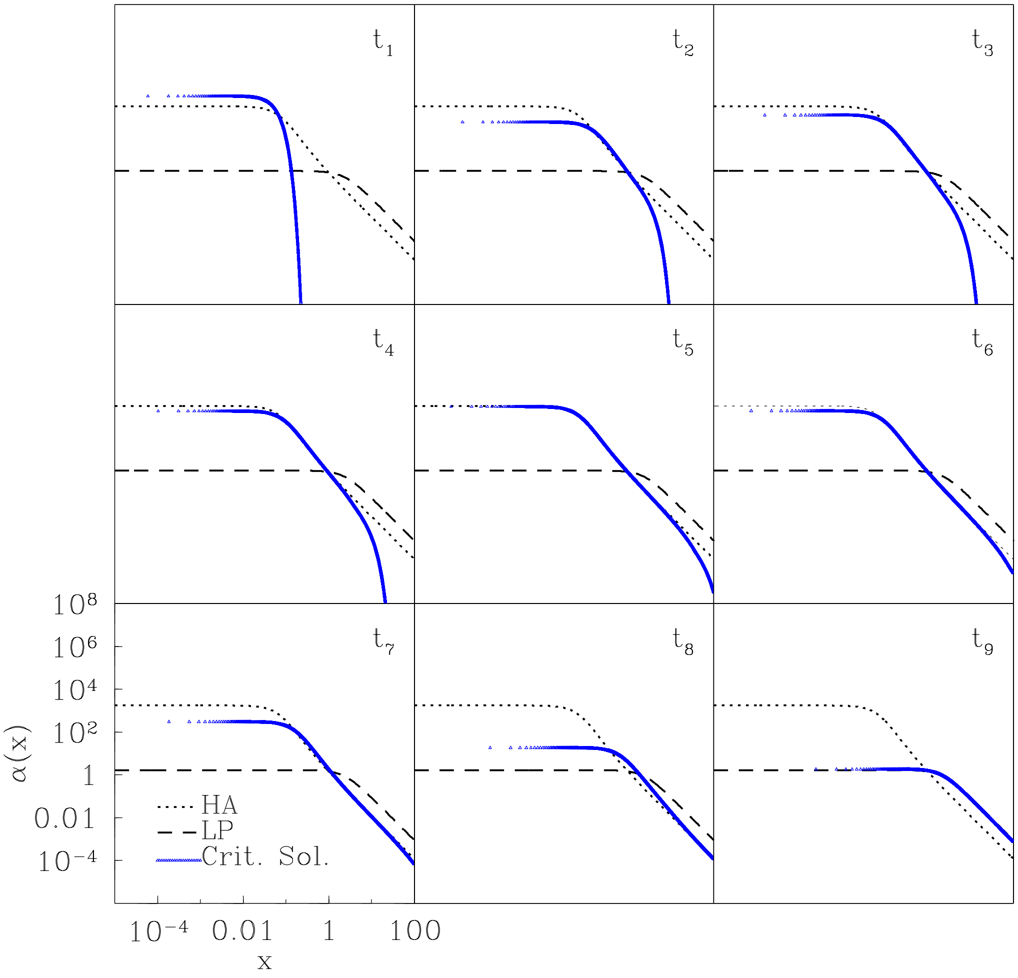

Figure 4.11: Snapshots of the evolution of $\alpha(x)$ for critical initial data using model-A, at $\Gamma = 1.00001$. This plot presents the evolution of the dimensionless density variable computed from the numerical solution $\rho(r,t)$ according to Eq. (2.46) for critical initial data ($|p-p^\star|/p^\star \to 10^{-14}$). The evolution data is represented by the blue curve. The top-left plot t_1 represents the initial data whereas the bottom-right t_9 represents the final state. Maximum approach to the 1-mode unstable Hunter-A solution (dotted line), is observed at intermediate times (t_5 in the above panel) As we expected as the unstable mode grows the solution finally settles into a profile that matches the LP solution (dashed plotted), t_9.

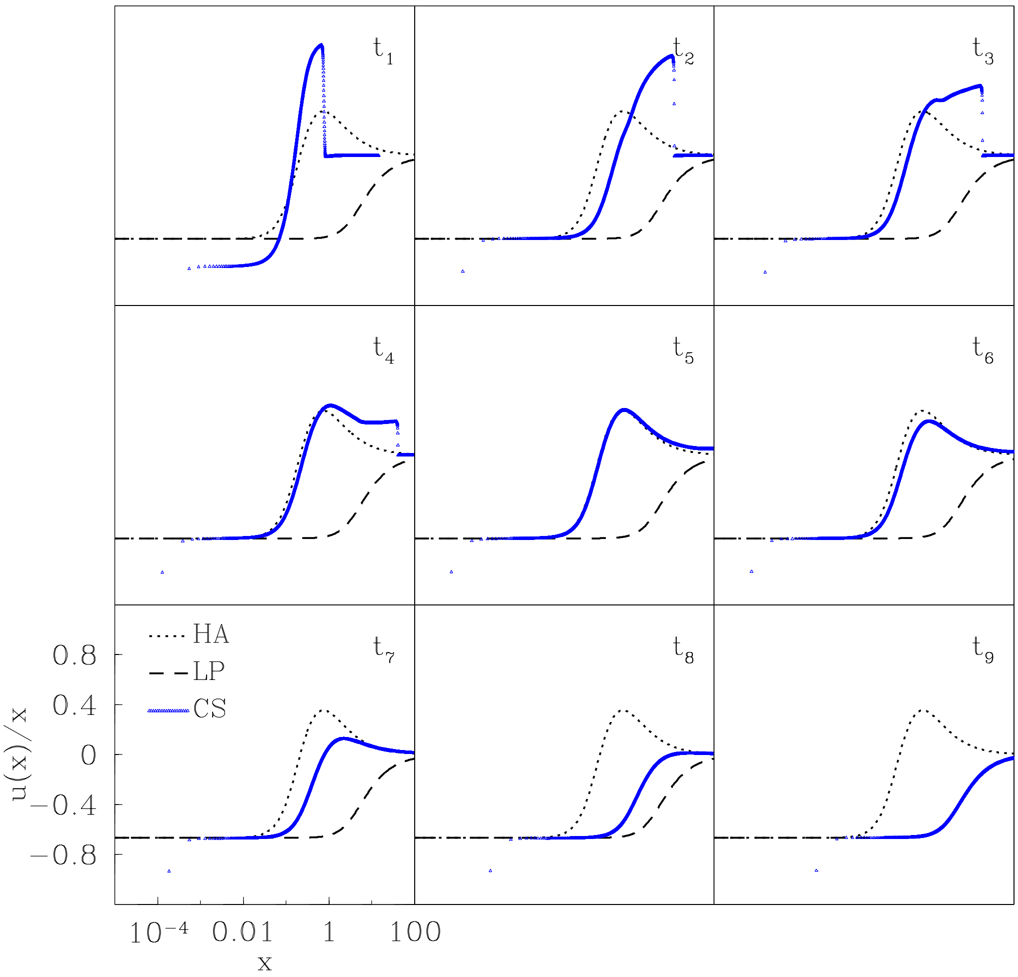

Figure 4.12: Snapshots of the evolution of $u(x)/x$ for critical initial data using model-A, at $\Gamma = 1.00001$. The plotted $u(x)$ profiles which correspond the critical solution ($|p - p^\star|/p^\star \to 10^{-14}$) are calculated from Eq. (2.45) at each time step. The flow near the origin replicates the features of the Hunter-A solution after some time (dotted line). In particular the node in the velocity profile which is responsible for the shrinking of collapsing core. Again the top-left plot is a snapshot of evolution an instant after the initial time (at $t = 0$ $u(x) = 0$), the central panel (t_5) corresponds to the maximum attained convergence to Hunter-A solution. Again, we see that at the final stage (t_9) $u(t, r)$ converges to the profile of the LP solution (dashed line).

Physical Interpretation of the Results

The Hunter-A solutions contains a rarefaction wave that travels towards the origin. This is entailed by the node on the profile of $u(x)$. This wave "catches" up with the collapsing center precisely at the time of singularity formation t_0. Loosely speaking the collapsing region (core) becomes infinitely small, even though the density diverges at this time ($t = t_0$). The fine tuning of initial data to the critical value $p^\star$ is not ideal due to numerical limitations. The data can be above or below the true threshold value. For subcritical data the rarefaction reaches the center before the singularity forms leading to dispersal of the gas away from the origin. Under supercritical conditions the rarefaction wave never reaches the center and the core ceases to shrink as the core collapses coherently.

The critical data goes through the linear regime discussed in Sec. 2.8.1 (without rotation, $\vec{q} = 0$). The final fate of the data is sealed by the sign of $\epsilon \equiv (p - p^\star)\exp(\lambda_0 \tau)$. Collapsing data will have the form, $Z(x,\tau) = Z^\star(x) + \epsilon\delta Z_0(x)$ at the linear regime (intermediate times). This occurs late enough in the evolution that the stable perturbations have died out, but early enough that ϵ is still small. The dispersal situation has the opposite sign, *i.e.* $Z(x,\tau) = Z^\star(x) - \epsilon\delta Z_0(x)$. For collapsed data, the time of departure from the critical solution sets the mass of the collapsed core. The longer the initial data converges to the Hunter-A solution, the smaller the core. If our formalism is correct, the scaling of the collapsed mass should follow Eq. (2.121). We selected a series of supercritical initial data evolutions and measured the mass of the collapsed core. This was done by simply integrating over the spherical shells which have in-falling velocity, over the innermost region of the cloud. The point at which velocity changes direction defines the radius of the core. The integration is performed at late times, once the solution has began its convergence to the LP solution and the core is collapsing coherently. At this point, neither the mass of the core nor its radius change prior to the blow up of the central density. This property of the LP solution is what allowed us to define the collapsed core. This is the same method used by Harada *et. al.* in their simulations of spherically symmetric isothermal gas collapsed [48].

A similar test can be conducted for the subcritical regime by measuring the maximum central density attained by the fluid before it began to disperse. Again, perturbation analysis and convergence to the 1-mode unstable, Hunter-A solution predicts a scaling of the maximum central density according to Eq. (2.126). The results of these calculations are plotted in Fig. 4.13. These plots show the scaling of both the collapsed mass and maximum density. Both plots indicate convergence to the predicted scaling law based on the existence of a single unstable mode. The slopes of the lines on the log-log scale of Fig. 4.13 are related to the reciprocal of the Lyapunov exponent of the unstable mode and the adiabatic index Γ, as dictated by Eqs. (2.121) and (2.126).

The results presented so far are consistent with the existence of type-II critical phenomena in the gravitational collapse of a soft fluid ($\Gamma = 1.00001$). As we have stated before, our critical collapse simulations pertained to a a more general Newtonian hydrodynamic model than previously considered. This is entailed by the inclusion of the energy conservation law, Eq. (2.7) and non-barotropic EoS (2.18). This model allows for generic entropy distributions, however, only under uniform entropy conditions can the self-similar solutions discussed in Sec. 4.1.1 be realized. We found that since the critical solution has vanishingly small mass (a feature of type-II critical phenomena), then the critical solution originates from a vanishingly small region of the initial conditions. Over this region, the entropy is arbitrarily close to a constant, unless shocks develop. No shocks seem to arise in any of the initial conditions we considered. Therefore, the critical solution is isentropic, thus it is reasonable to expect that one to the self-similar solutions of the autonomous system Eqs. (2.52)–(2.53) is realized as the critical solutions (Hunter-A).

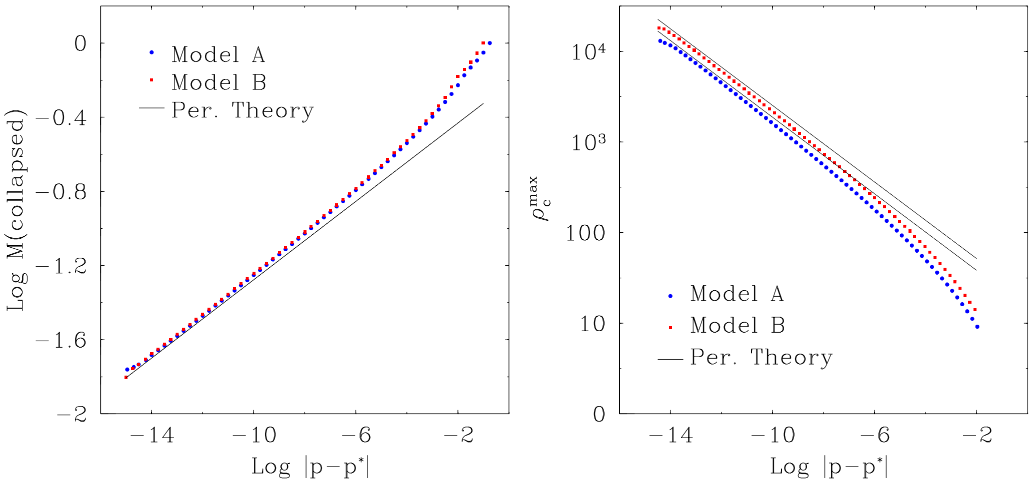

(a) (b)

Figure 4.13: Scaling behavior of the collapsed mass (M) and maximum central density $\rho_c^{\max}$ at $\Gamma = 1.00001$. The collapsed mass (a) and maximum density (b) were calculated from supercritical and subcritical evolutions, respectively. The solid line is the predicted scaling law behavior near the critical point ($|p - p^\star| \to 0$) derived from Eqs. (2.121) and (2.126). Agreement between the numerical simulation results (blue and red) and the results from perturbation theory (black) improve near the critical value $p^\star$, this is expected since the scaling laws only apply near criticality, where all other stable modes have died out. The bisection search ultimately fails as we approach the numerical precision limit (10^{-16}), and thus we are unable zero-in on the exact value of the critical parameter $p^\star$. At this point, we cannot reliably measure the difference $|p - p^\star|$. This failure begins to be evident in both sets of data as $|p - p^\star| \sim 10^{-14}$.

4.2.2 Connection with General Relativity

So far our studies of critical collapse of an ideal gas in Newtonian gravity have revealed the existence of type-II critical phenomena. This was made evident by the convergence to a 1-mode unstable critical solutions (Hunter-A) and the particular scaling properties of the collapsed mass and maximum density. The results presented so far pertain to the nearly isothermal gas, $\Gamma = 1.00001$. It is clear that our results are in agreement to those of presented in [48, 64] for the isothermal gas model. Previously, Snajdr and Choptuik [96] obtained these results from a General

Relativistic critical collapse of a perfect fluid with an ultra-relativistic EoS (1.3). This was done by considering the limit $k \to 0$, which, according to the work of Ori and Piran (1990) [77], certain regular similarity solutions of the GR perfect fluid with EoS (1.3) reduce to the weak-field (Newtonian limit) self-similar solutions of the isothermal gas. Snajdr and Choptuik found that the critical solution resembled the Newtonian Hunter-A solution as k tended to zero. Their normal mode analysis confirmed that the value of the growing mode also converged to that of Hunter-A. This was previously estimated in [45]. Further confirmation was obtained through calculations of the scaling behavior of the black hole mass. Again, the scaling exponent agree with our purely Newtonian calculations and those of [48, 64]. We noticed that the "transition" into the Newtonian regime maintains the solution's structure but leads to larger values of the unstable modes. This is evident in the data collected in [96]. This trend continues as Γ becomes greater than one, the unstable mode increases as evident in Table 4.3. The Hunter-A solution becomes infinitely unstable at $\Gamma = 6/5$ where this solution structure seems to break down.

4.2.3 Simulations $1 < \Gamma < 6/5$

We proceeded with our investigations of critical collapse by considering a stiffer EoS ($\Gamma > 1$). We recall at this point the discovered absence of 1-mode unstable regular solutions for $\Gamma \geq 6/5$. In Sections 4.1.1 and 4.1.2 we found the Hunter-A, 1-mode unstable solutions exist in the range, $1 < \Gamma < 6/5$. The value of the unstable mode, like the amplitude of the Hunter-A solution was found to be dependent on Γ. Both, this amplitude and its unstable mode become singular as $\Gamma \to 6/5$ (see Table 4.3). The presence of this 1-mode unstable solution suggests that similar critical behavior found at $\Gamma \approx 1$, persists up to, but not including $\Gamma = 6/5$.

We found similar convergence to the corresponding Hunter-A solution at these larger Γs during critical collapse. As Γ becomes larger, however, convergence to the corresponding Hunter-A solution becomes more difficult to ascertain. We attribute this in part to numerical precision limitations which hindered our ability to sufficiently fine tune the initial data to the critical parameter [11]. More importantly, the value of the unstable mode grows significantly as we approach $\Gamma = 6/5$; which means much faster growth of the perturbation. For example, in the case of $\Gamma = 1.00001$ the unstable mode grows approximately as $1/(t_0 - t)^{9.46}$, compared to $1/(t_0 - t)^{36.7}$ for $\Gamma = 1.12$. Calculations of Q_0 for critical data were carried out at various values of Γ. These results are plotted in Fig. 4.14. We see that the initial stages of the evolution proceed with the convergence to the Hunter-A solutions. The higher the value of Γ, the higher its instability as implied by the growth rate (Lyapunov exponent) of the unstable mode. This means that generic initial data, fine-tuned as closely as our numerical precision permits ($|p - p^\star|/p^\star \sim 10^{-15}$) does not have enough time to "shed away" the stable mode dependence that defined the initial state. Therefore, we see only a partial convergence to its Hunter-A solution.

We computed the profiles for $\alpha(x)$ and $u(x)$ at various values of Γ from the

---

[11] Using double precision arithmetic, the minimum difference $(p - p^\star)$ which could be resolved is 10^{-15} for a control parameter p that is of order 1. If quadruple precision were employed we could resolve differences down to 10^{-31}.

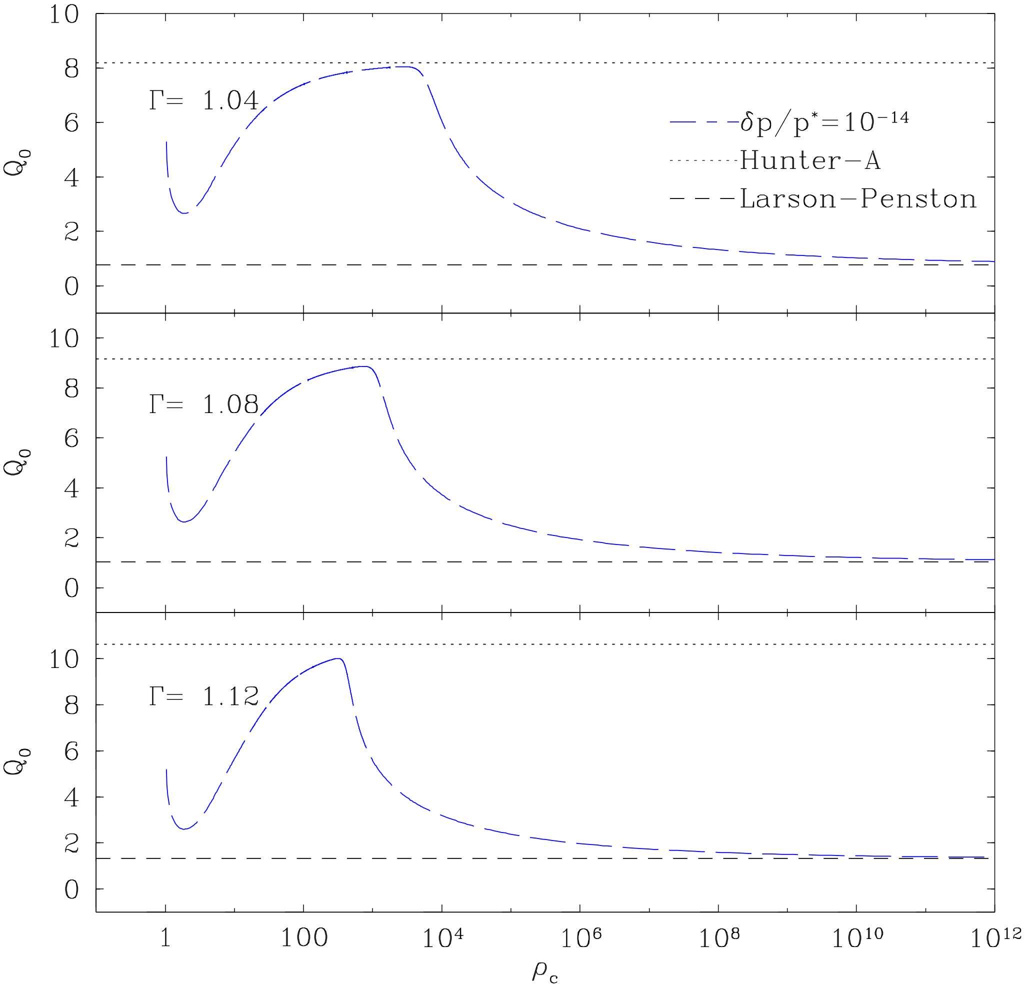

Figure 4.14: Evolution of Q_0 versus the central density ρ_c for critical collapse at multiple values of $\Gamma < 6/5$. All the presented evolutions in this plot correspond to critically collapsing data ($|p - p^\star|/p^\star \to 10^{-14}$). As Γ is increased towards the value of 6/5 the Hunter-A critical solutions becomes more unstable due to the growth of its unstable mode. The calculations are in agreement with this prediction. Of the presented cases $\Gamma \in \{1.04,\ 1.08,\ 1.12\}$, $\Gamma = 1.12$ shows the least amount of convergence to the Hunter-A solution (dotted line). All cases show convergence to the value of Q_0 corresponding the Larson-Penston (dashed line) solution at the later stages of the evolution.

numerical solutions, $\rho(r,t)$ and $v(r,t)$. We present the results of the solutions' maximum approach to the Hunter-A solution as indicated by plots of the variable $\alpha(x)$ in Fig. 4.15. Again, we observed a decrease in the degree of convergence at higher Γ values. As already suggested by our calculations of $Q_0(t)$ presented in Fig. 4.14 the late stages of critical-initial-data evolution are well described by their corresponding LP solutions. This fact is also evident in Fig. 4.16 where we observed that the evolution data for $\alpha(x)$ closely matches the profile of the LP solution. Late time convergence to the LP solution is unaffected at $\Gamma = 6/5$, this is expected since it continues to be stable until Γ reaches $4/3$.

The scaling exponent for the collapsed mass is predicted to be $((4-3\Gamma)/\lambda_0)$ as derived in Eq. (2.121). As Γ approaches $6/5$, we know that λ_0 grows nonlinearly, leading eventually to the vanishing of the scaling exponent. We measured the collapsed masses for $\Gamma \in (1, 6/5]$ near their respective collapsed threshold ($p^\star$). The mass scaling is consistent with the expected behavior of the 1-mode unstable critical solution, Fig. 4.17. However, as we mentioned, the large value of the growth rate λ_0, along with our precision limitation prevents the critical solution from a close approach to the Hunter-A solution. This however, does not change the fact that it is an intermediate attractor of the evolution. The larger value of the Lyapunov exponent means the solution does not have sufficient time to drive away the stable modes and the solution only marginally enters the linear regime.

We can manually remove the stable modes by choosing initial data close to the Hunter-A solution. In this case, the initial data is represented by the Hunter-A solution plus some generic background perturbation. Again, the perturbation is controlled by a single parameter (labeled, once again by p) which can be fine-tuned to the threshold of collapse (labeled by $p^\star$). Notice that this $p^\star$ is not equal to zero since that would mean we have provided the exact Hunter-A solution. Instead $p\star$ is a nontrivial value found as before through fine-tuning; therefore, there is still a generic aspect to the solutions deviations from the Hunter-A solution at the initial time. Under these circumstances, the initial data should be strongly attracted to the Hunter-A solution, which should be well described the linear regime, Eq. (2.113) (with $\vec{q} = 0$). This is particularly evident in the scaling of the collapsed mass when

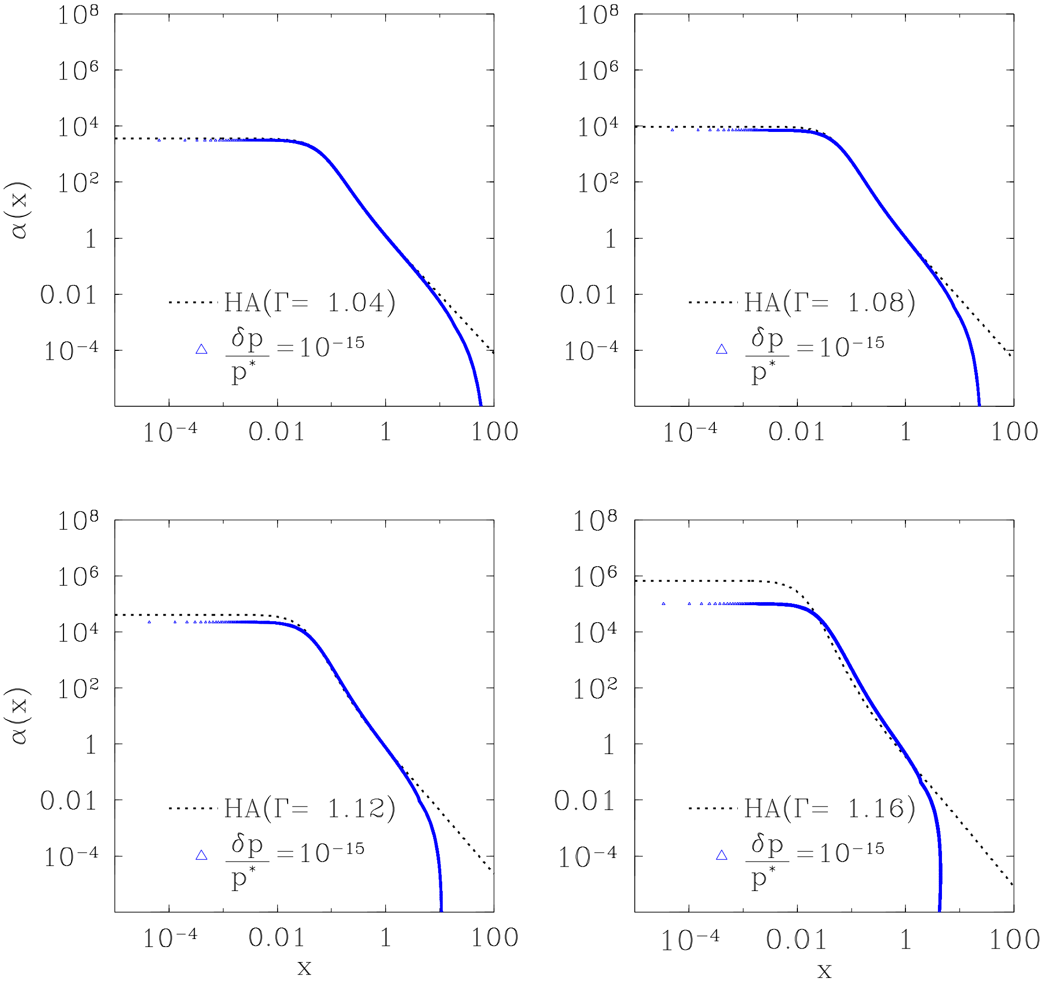

Figure 4.15: Plots of the dimensionless density variable $\alpha(x)$ emerging from critical initial data ($p \approx p^\star$) for $\Gamma = 1.04,\ 1.08,\ 1.12,\ 1.16$ taken at intermediate times. The dotted line represents the respective Hunter-A (HA) solutions obtained via integration of the autonomous system, Eqs. (2.52) and (2.53). While the blue cure is the dynamical solution for critical evolution *i.e.* $|p - p^\star|/p^\star \to 10^{-15}$. The evolution of $\alpha(x)$ approaches the Hunter-A solution, near the center, at intermediate times. The convergence becomes more tenuous at larger values of Γ.

subjected to this type of initial data. We performed experiments for the same values of Γ as previously studied and we found very good agreement with perturbation theory. These results are found in Fig. 4.18. The mass follows very closely the scaling law, given in Eq. 2.121 ($F(\vec{\delta} = 0) = 1$) derived by assuming the critical

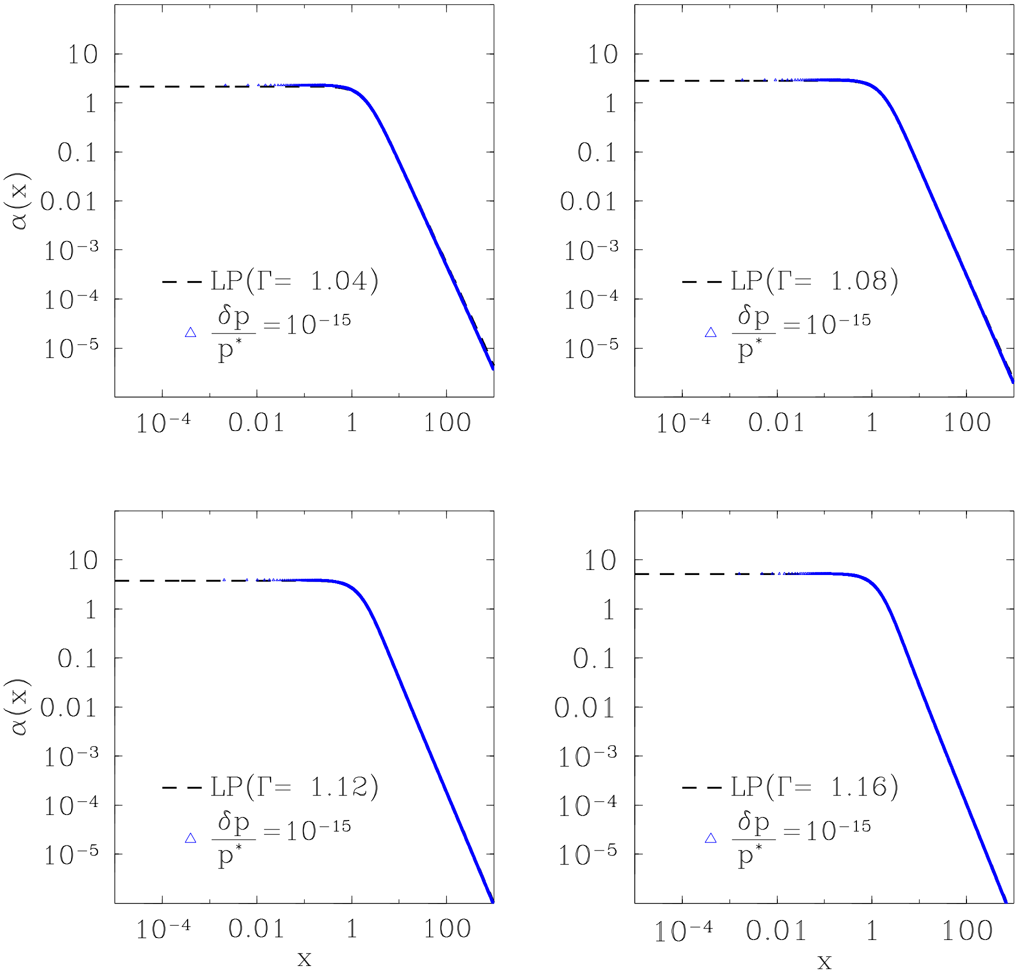

Figure 4.16: Plots of the dimensionless density variable $\alpha(x)$ emerging from critical initial data ($p \approx p^\star$) for $\Gamma = 1.04$, 1.08, 1.12, 1.16 taken at late times. The dashed and blue line represent the Larson-Penston (LP) and dynamical solutions respectively. The evolution data is taken late in the evolution when the unstable perturbation has grown and the solution has been driven away from the Hunter-A solution. We clearly see that in all cases the solution resembles the Γ-dependent Larson-Penston solution which lacks any spherically symmetric growing modes and therefore is stable.

solution reaches the linear regime.

At $\Gamma = 6/5$ supercritical evolutions of generic initial data (Model-A) near the threshold yielded approximately the same value of the collapsed mass, see Fig. 4.17. This indicates the development of a mass gap, a fact which is consistent with the scaling exponent going to zero. From this and the fact that there are no 1-mode unstable solutions for $\Gamma \geq 6/5$ we conclude that type-II critical behavior for this fluid model ends at this value of Γ. The transition into type-I behavior is discussed in the next section.

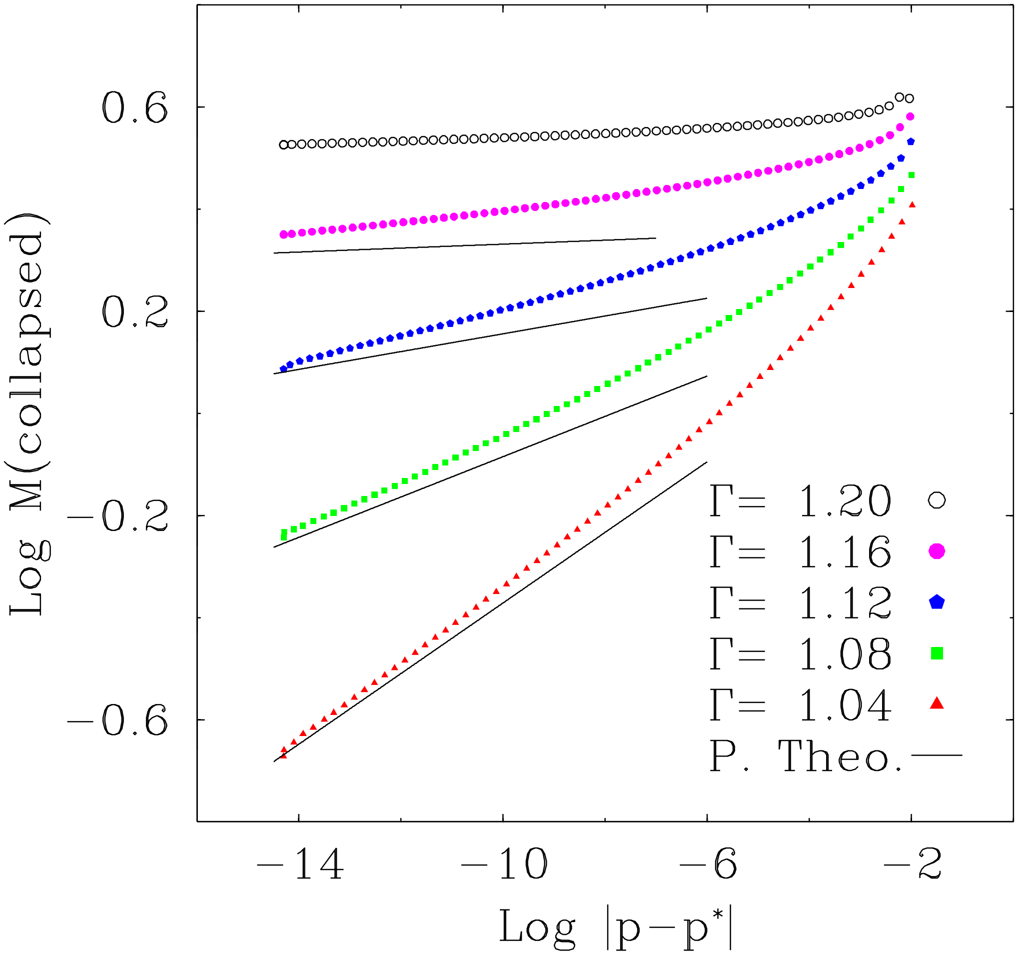

Figure 4.17: Scaling laws for the collapsed mass at $\Gamma = 1.04$, 1.08, 1.12, 1.16 and 1.2. The data is in agreement with the scaling law for the mass derived from the single unstable mode of the critical solution Eq. (2.121), also plotted. As the Γ approaches 6/5, greater precision is required to get close enough to the 1-mode unstable solution. The slope of the line is related to $\sim 1/\lambda_0$, the reciprocal of the unstable mode, thus as λ_0 diverges, the slope tends to zero. Consequently, a mass gap develops in the spectrum of possible collapsed mass for $\Gamma \geq 6/5$. The dynamical results agree with the prediction that this gap is generated at $\Gamma = 6/5$.

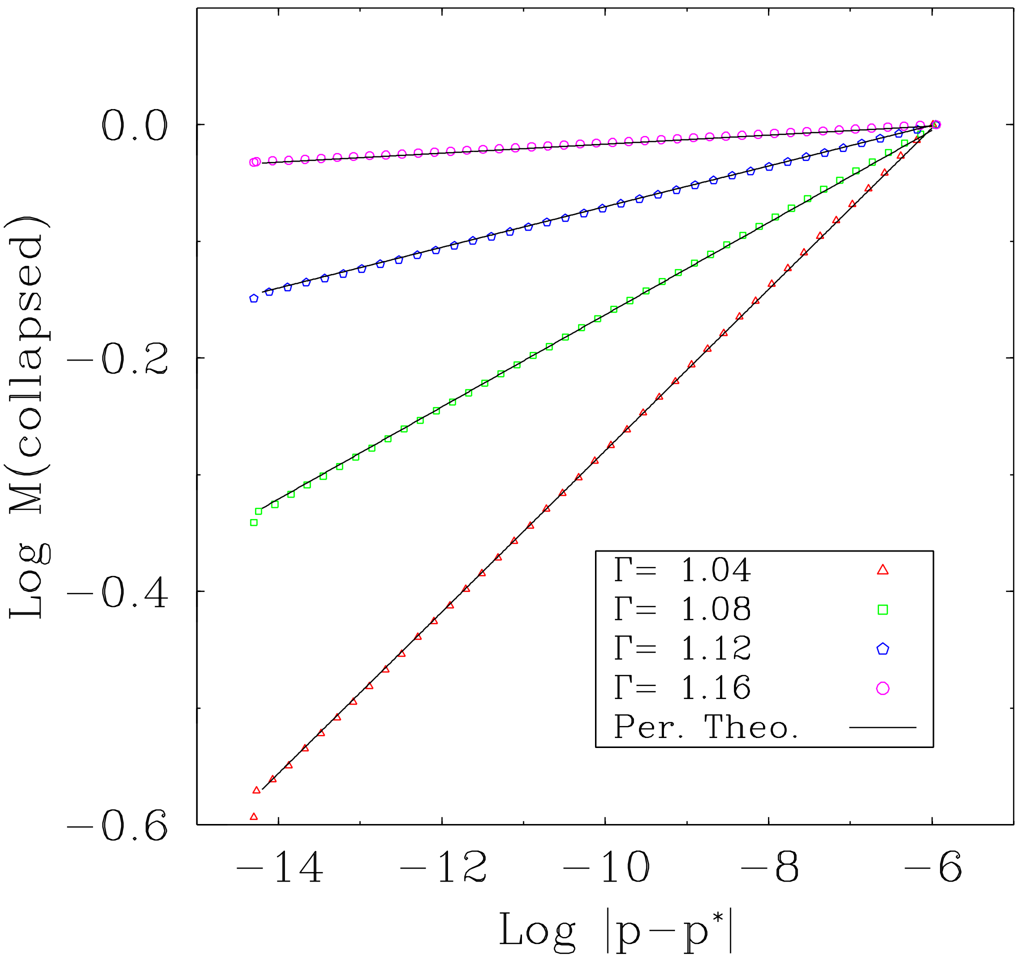

Figure 4.18: Plots of the collapsed mass M with initial data resembling the Hunter-A solutions at $\Gamma = 1.04$, 1.08, 1.12, 1.16, respectively. Additional fine-tuning of the initial data lead to the fading away of any deviations from Hunter-A. At late times the only the unstable mode grows, so the solutions is ensured to reach the linear regime where the scaling law for the mass of the core holds; this is evident in this plot. Calculations of the core mass are in close agreement with the predicted scaling law and the respective value of the unstable mode's growth rate. In this log-log plot, the slope formed by the series of collapsed cores becomes shallower at large Γ; this implies we need larger degree of fine-tuning to the critical parameter $p^\star$ to achieve infinitesimal "collapsed cores".

4.2.4 Simulations $6/5 \leq \Gamma < 4/3$

Calculations of critical collapse solutions were also carried out at $\Gamma \in [6/5, 4/3)$. The character of the critical collapse solution does in fact change for this range of the parameter Γ. Once more, we computed the quantity $Q_0(t)$ from the dynamical solutions. The late time evolution of this parameter indicates converge to its appropriate Larson-Penston value, irrespective of fine-tuning. This is shown in Fig. 4.19. For fine-tuned data at intermediate times, the central density stops growing and becomes static while Q_0 continues to vary according to $\sim (t_0 - t)^2$. The amount of time the central density hovers around this temporary maximum depends on how close the control parameter p in the initial data is a critical value $p^\star$. It is self-evident that in this case the central density is not describe by a self-similar solution *i.e.* one which "blows up" as $(t_0 - t)^2$ leading to a constant Q_0. Instead, the intermediate critical solutions seems to approach a static, star-like configuration, also shown in Fig. 4.19.

Snapshots of density, fluid velocity and specific entropy density provided in Fig. 4.20 illustrate a convergence to a static solution. The density is plotted on a log-log scale, the other two fields namely, v and $3s/c_v$ are on a linear-log graph. This evolution belongs to critical data ($|p - p^\star|/p^\star \sim 10^{-14}$). The density at the center quickly grows as a result of the initial implosion. Once it has reached a certain value, the fluid velocity tends to zero over a region near the origin. This configuration remains virtually unchanged for a long time relative to its initial transient behavior, the fluid then either collapses in a manner described by the LP solution (Fig. 4.19), or it disperses away from the center. The critical data presented in Fig. 4.20 also shows the presence of shocks. The first outgoing shock forms almost instantly at the start of the simulation. The second shock is generated following the initial compression of the fluid after which a shock wave is formed that travels radially outward. Notice that as the fluid crosses the shock front by falling into the compact object the specific entropy given in the form of $3s/c_v$ increases discontinuously. In regions where the flow is smooth the entropy field is simply advected (Fig. 4.20). This behavior is common to all critical initial data where $6/5 \leq \Gamma < 4/3$. Like the self-similar case the static solution is increasingly more difficult to resolve in the limit $\Gamma \to 6/5^{+}$. This parameter value implies a transition in the type of critical solution, a "boundary" separating static–similarity critical solutions.

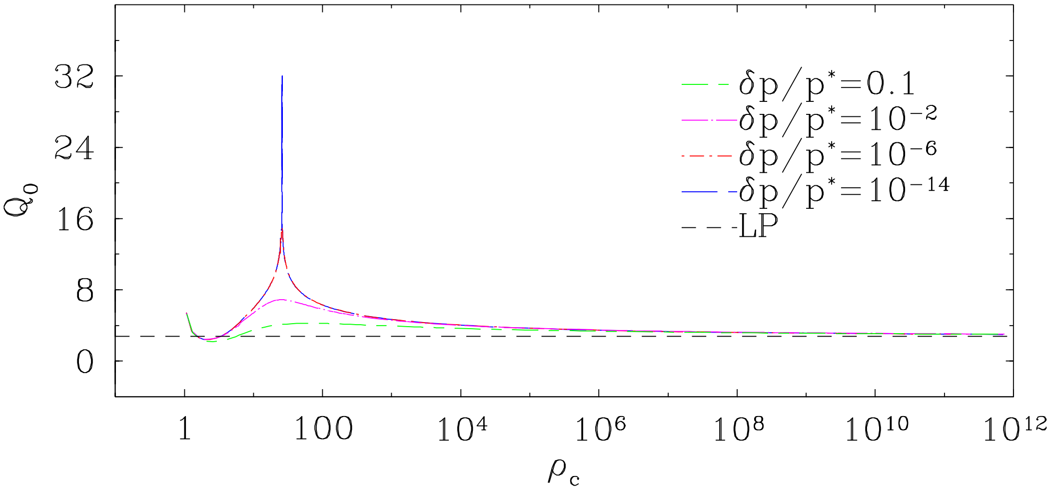

Figure 4.19: Plot of various measurements of Q_0 versus ρ_c for $\Gamma = 1.28$. The fine-tuning ($|p - p^\star|/p^\star \to 10^{-14}$) of the initial data do not yield in this case convergence of Q_0 to a constant value during intermediate times. Recall, Q_0 is computed from the dynamical data (Equations (4.4)). Instead Q_0 varies while the central density reaches an intermediate maximum. The fluid evolution becomes nearly static at this maximum density ($\rho(0,t) \sim 26$). In the case of supercritical data, this is followed by rapid collapse. At late times Q_0 converges to the value of the Larson-Penston self-similar solution, regardless of fine-tuning.

We cannot be certain that the static critical solution is characterized by a single unstable mode. In fact, the static solution cannot be determined from an autonomous system, that is by assuming a static, spherically symmetric ansatz. These type of static solutions must obey the spherically symmetric Euler+Poisson equa-

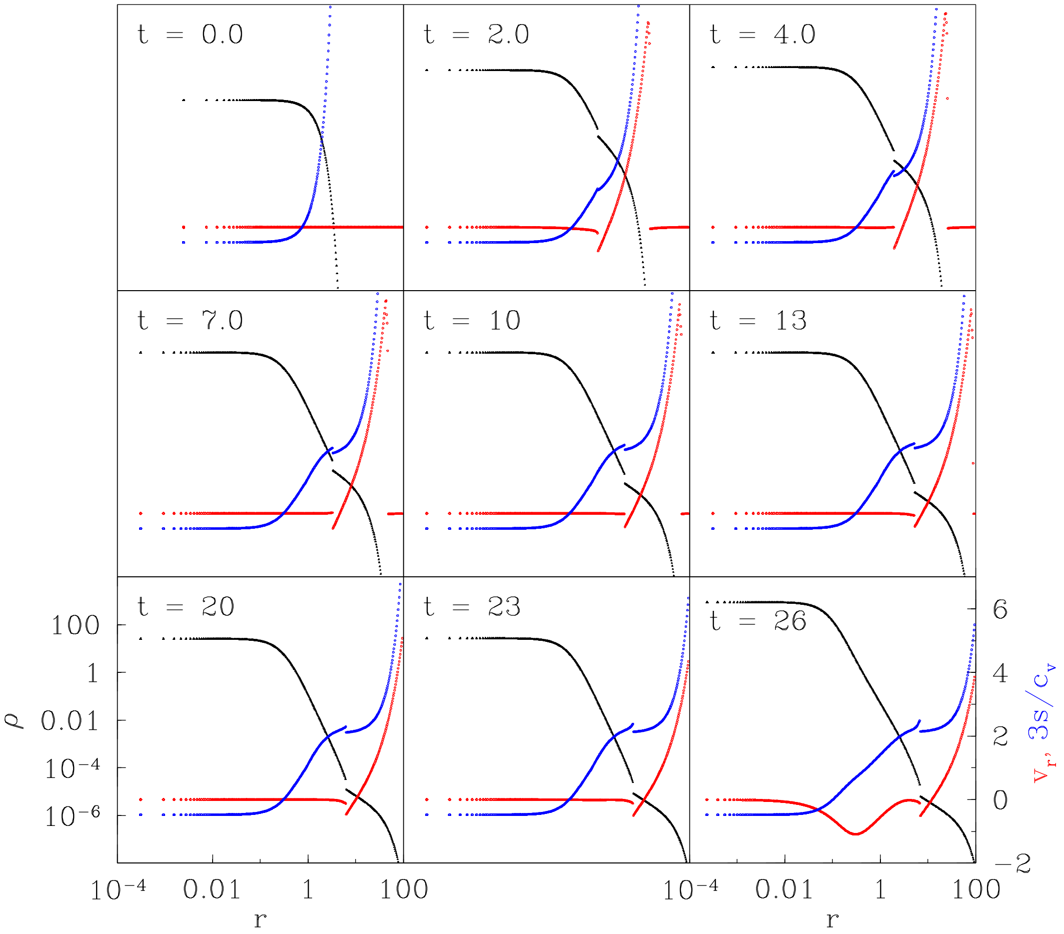

Figure 4.20: Snapshots of the critical evolution of model-A for $\Gamma = 1.28$. The profiles of density (ρ, black), fluid velocity (v, red) and entropy ($3s/c_v$, blue, c_v is the specific heat at constant volume) demonstrate convergence to a static intermediate state. The central density grows to a value of ~ 26 where it remains for some time before ultimately collapsing. Also evident in these plots is the presence of two outgoing shocks. The first shock develops almost instantly at the start of the evolution, while the second one forms following the contraction and subsequent expansion of the gas at the core's surface. Notice that the fluid which crosses the shock by falling onto the core acquires a jump in the entropy. In regions where the flow is smooth, the entropy is simply advected.

tions (2.24)–(2.27) with $v = 0$,

$$\frac{\partial P}{\partial r} = -\rho\frac{\partial \varphi}{\partial r}, \tag{4.6}$$

$$\frac{1}{r^2}\frac{\partial}{\partial r}(r^2\frac{\partial \varphi}{\partial r}) = 4\pi G\rho. \tag{4.7}$$

Together with the polytropic ideal gas-law Eq. (2.18) we have three equations and four unknowns, namely $\rho(r)$, $P(r)$, $\varphi(r)$ and $\epsilon(r)$. The static state of the fluid is the result of the nonlinear evolution of the equations of motion and it cannot be determined independently. This issue carries over to the linear perturbation analysis, whereby the solution to the eigenvalue problem requires that we know the time-independent solution of one of the field variables *e.g.* $\epsilon(r)$ and its perturbation.

Nevertheless, the stability properties of the critical solution can be inferred from the numerical simulations. In particular, the life-time of the critical solution must follow Eq. (2.127) if it in fact contains a single growing mode. We measured this life-time by calculating the elapsed time the central maximum hovers about a common value before collapse or dispersal. The results of these measurements are plotted against $p - p^\star$ in Fig. 4.21 for multiple values of Γ. We can clearly see the linear relationship, from which the value of the unstable mode can be estimated. We noted that the unstable mode decreases as we approach $\Gamma = 4/3$. Furthermore, in contrast to the self-similar critical solution, no evidence of universality was found in this case ($\Gamma \in [6/5,\, 4/3)$). The value of the unstable mode as well as the critical solutions showed dependence on the particular 1-parameter family being used. Initial data models A and B from Table 4.4 with $\Gamma = 1.28$ were tested. The results, plotted in Fig. 4.22(b) support the absence of universality. The slope of the linear relationship stated in Eq. (2.127) equals the reciprocal of the unstable mode λ_0, so a difference in the slopes imply different Lyapunov exponents (λ_0). Also plotted in Fig. 4.22(a) are the collapsed masses of the critical solutions. As stated earlier the critical solution associated with type-I critical phenomena is a finite, scale dependent solution (the scale set by the static solution). This scale is determine by the initial data and the collapsed mass is proportional to this scale. As evident in Fig. 4.22(a), both sets of data exhibit a mass gap in the profile of the core's mass that is clearly not universal.

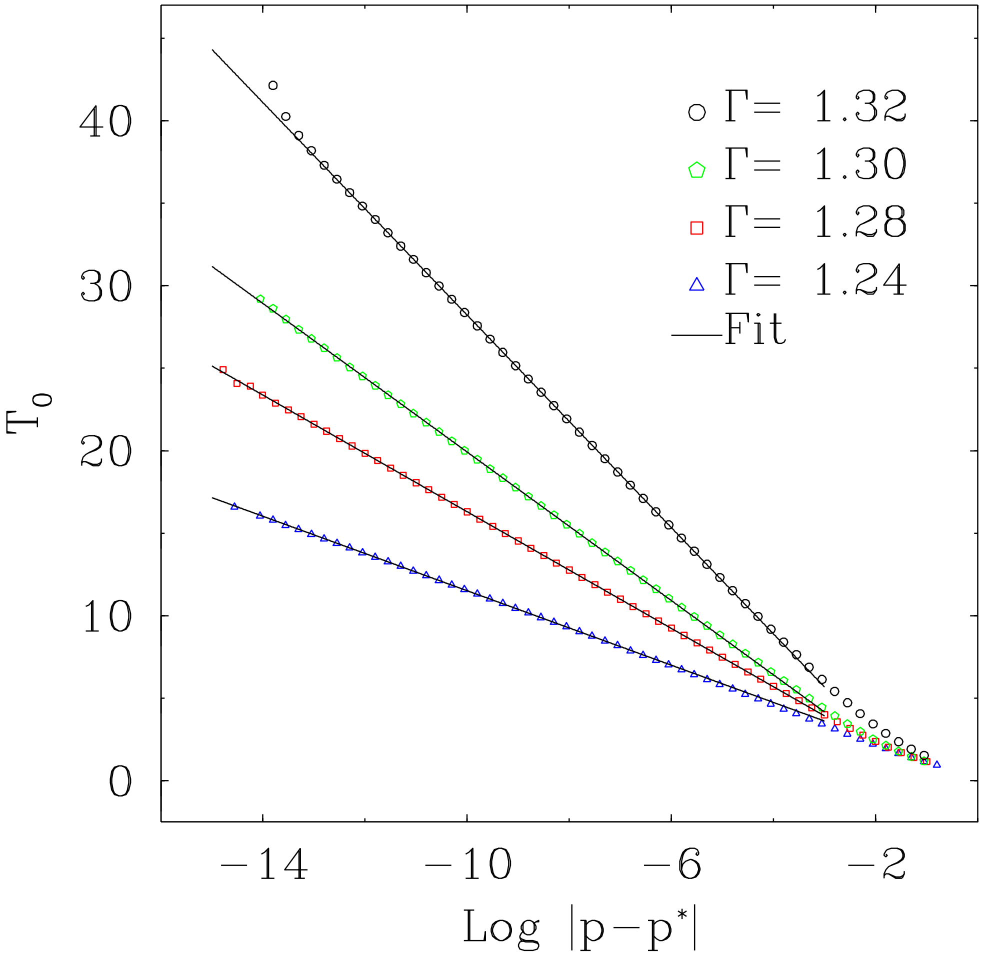

Figure 4.21: Scaling of the critical solution's lifetime (T_0) for various choices of $\Gamma > 6/5$. The lifetime of this intermediate solution scales in a manner that is consistent with the existence of a single unstable mode perturbing the intermediate state. This is evident from its linear relation with $\log|p - p^\star|$, as predicted in Eq. (2.127). The Lyapunov exponent of the unstable mode determines the slope of the linear relationship. Steeper slopes imply smaller Lyapunov exponents which in turn imply more stable solutions. We can then note that as we Γ approaches the 4/3 (the value corresponding to a gas of photons) the critical solution becomes more stable.

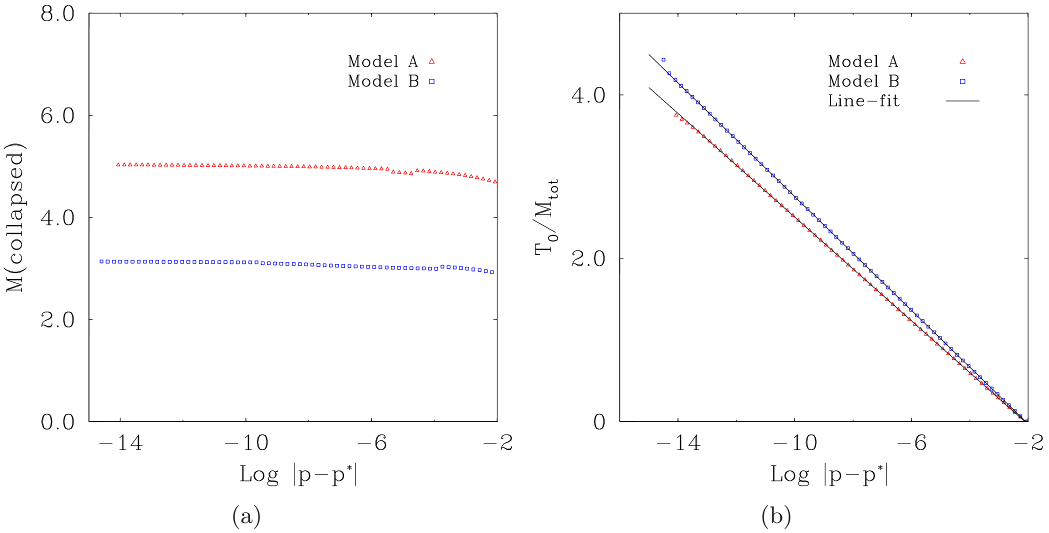

(a) (b)

Figure 4.22: Plots of M(collapsed) (a) and the solution's lifetime divided by the total mass (b) for two distinct 1-parameter families of initial data at $\Gamma = 1.28$. On the left panel we see the scale dependence of the critical solution is made evident by the mass-gap, a characteristic of Type-I critical phenomena. The critical solution is a quasi-static configuration of finite size set by the choice of 1-parameter family of initial data. The lifetime of the critical solutions follows a scaling law, Eq. (2.127) as shown in (b). This scaling is a necessary property of type-I critical phenomena. The two distinct families of data presented follow slightly different scaling. The two 1-parameter families, Models A and B yield different slopes *i.e.* different λ_0s for the linear relationship given by Eq. (2.127). This appears to support the absence of universality for the unstable mode, λ_0.

Chapter 5

Results: Axial Symmetry

The number of numerical studies concerning critical phenomena in gravitational collapse beyond spherical symmetry remain limited. This situation is rather unfortunate given that angular momentum is expected to play a significant role during the late stages of collapse. As the length scale of the gravitation interactions shortens, slow initial rotation will lead to high tangential velocities of the final compact object. In order to investigate the role of angular momentum during critical collapse we adopted axial symmetry for the geometry of the physical system. At the present time the only works which have produced numerical simulations of critical collapse beyond spherical symmetry can be found in, [1, 2, 17, 18, 53, 97]. These pertain to axisymmetric collapse of gravity waves and the scalar field (real and complex).

We have implemented a numerical algorithm to solve the Euler equations of fluid dynamics coupled to Newtonian gravity in axial symmetry. Our aim was to investigate the role of angular momentum near the threshold of gravitational collapse. This work was built upon the results of the spherically symmetric calculations (Chap. 4). We are particularly interested in the addition of slow (infinitesimal) initial rotation to otherwise spherically symmetric initial data near this threshold. The results of the numerical experiments also allowed us to verify the scaling laws predicted in [32], which we have rederived for our Newtonian system in Sec. 2.8.1.

Initial Data

Three distinct 2-parameter families of initial data were chosen for the fluid evolution with axial symmetry. Rotation about the z-axis breaks spherical symmetry, which can be recovered by setting the velocity component $v_\phi = 0$. Otherwise, the three sets of data posses reflection symmetry about the equatorial plane ($x - y$ plane), these are explicitly given in Table 5.1. We have chosen models A and B to coincide with the spherically symmetric 1-parameter sets given in Table 4.4 if $q = 0$ (note that this effectively sets v_ϕ to zero). As we did in spherical symmetry, model A will be the most commonly used set.

In certain cases a fourth 2-parameter family of initial data was used. Similar to what was done in spherical symmetry, this data represents the linear regime near the Hunter-A solution. The initial state is therefore represented by,

$$Z(0, x, \theta) = Z^\star(x) + f_p(x, \theta) + qZ_1(x, \theta). \tag{5.1}$$

As before, $Z^\star(x)$ is the Hunter-A solution. The p-controlled perturbation expressed in cylindrical coordinates (s, ϕ, z) is given by,

$$f_p(s, z) \equiv \begin{pmatrix} pe^{-s^2-z^2} + \varepsilon_\rho(s, z) \\ \varepsilon_{v_s}(s, z) \\ \varepsilon_{v_\phi}(s, z) \\ \varepsilon_{v_z}(s, z) \\ \varepsilon_P(s, z) \end{pmatrix}. \tag{5.2}$$

Once more, the variables such as $\varepsilon_\rho(r, \theta)$ are the cumulative errors generated in approximating the Hunter-A solution. Note that we have introduced a Gaussian perturbation about the background Hunter-A solution of the density profile. Rotation is introduced by initializing the azimuthal component of the velocity field v_ϕ according to the $\ell = 1$ spin-up mode $Z_1(x, \theta)$. In cylindrical coordinates and assuming axial symmetry ($m = 0$), we have

$$qZ_1(s,z) = q \begin{pmatrix} 0 \\ 0 \\ \dfrac{\delta u_\Phi}{x} \dfrac{s}{\sqrt{s^2+z^2}} \\ 0 \\ 0 \end{pmatrix}. \tag{5.3}$$

This expression is equivalent to Eq. (2.90) for $\ell = 1$ and $m = 0$. The function $\delta u_\Phi(x)$ give the radial dependence of the spin-up mode whose formal solution is given in Eq. (2.104). Notice that $x \propto r/t^{2-\Gamma}$ and so, $x \propto \sqrt{s^2+z^2}/t^{2-\Gamma}$.

Table 5.1: Initial data profiles for the primitive variables ρ, v_s, v_ϕ, v_z and P used in the axisymmetric evolutions.

Variable	Model A	Model B	Model C
$\rho(0,s,z)$	$e^{-s^2-z^2}$	$\dfrac{1}{(1+(s^2+z^2)^2)^2}$	$\begin{cases} \cos^3\left(\dfrac{\pi\sqrt{s^2+z^2}}{4}\right) & \text{if } \sqrt{s^2+z^2} < 2 \\ 10^{-12} & \text{if } \sqrt{s^2+z^2} \geq 2 \end{cases}$
$v_s(0,s,z)$	0	0	0
$v_\phi(0,s,z)$	qse^{-s^2}	$\dfrac{qs}{\sqrt{1+s^2}}$	$\begin{cases} q\sin\left(\dfrac{\pi s}{4}\right) & \text{if } \sqrt{s^2+z^2} < 2 \\ 0 & \text{if } \sqrt{s^2+z^2} \geq 2 \end{cases}$
$v_z(0,s,z)$	0	0	0
$P(0,s,z)$	$pe^{-s^2-z^2}$	$\dfrac{p}{(1+(s^2+z^2)^2)^2}$	$\begin{cases} p\cos^3\left(\dfrac{\pi\sqrt{s^2+z^2}}{4}\right) & \text{if } \sqrt{s^2+z^2} < 2 \\ 10^{-12} & \text{if } \sqrt{s^2+z^2} \geq 2 \end{cases}$

5.1 The Unstable Axial (Spin-up) Mode

Section 2.5 highlighted the relevance of the axial perturbation modes. Originally determined in the analysis of Hanawa [38, 40] the axial mode spectrum has a growth rate given by expression (2.103) provided regularity (analyticity) of the similarity solution. As discussed in Sec. 2.5 the $\ell = 1$ axial mode is the only relevant (growing) axial perturbation mode which can be observed through axisymmetric evolution of our fluid model. Recall that for $1 < \Gamma \lessapprox 1.17$ the $\ell = 2$ mode is also unstable, in axial symmetry only the $m = 0$ mode is observable but since our initial data (Table 5.1) is by construction symmetric about the equatorial plane the $\ell = 2$ mode is suppressed during the evolution. Therefore, provided that $1 \leq \Gamma \lessapprox 1.17$ there is only one unstable axial mode that we predicted to be observable, namely the spin-up mode. This mode has a growth rate given by $\lambda_1 = 1/3$. Given its unstable nature and our axisymmetric setup, the spin-up mode is expected to determine the angular momentum of the collapsed core when slowly rotating, supercritical initial conditions are considered. In general, there is no a priori reason to rule out polar perturbations, nevertheless these have been left out of our analysis due to indirect suggestions of their limited relevance, these are mentioned in Sec. 2.5 and Sec. 2.6.3.

We now present our calculations of the spin-up mode for the Hunter-A solution at various values of Γ. Recall that a formal solution is provided by Eq. (2.104) from which it is clear that the spin-up mode couples only to the radial velocity profile of the similarity solution $u(x)$. So we proceeded by solving Eq. (2.100) in simultaneity with Eqs. (2.52) and (2.53). These results are plotted in Fig. 5.1. We plotted the radial part of the spin-up mode given by $\delta u_\Phi / x$. These profiles contain a self-similar "hump", its amplitude decreases with increasing Γ as shown in Fig. 5.1. All of these converge to the same behavior at small x, as illustrated in the inset of Fig. 5.1.

To see the full structure of the spin-up mode in three dimensions we must complement the radial function just described with the mode's angular dependence. This is given by,

$$\delta u_\phi(\tau, x, \phi, \theta) \sim \frac{\delta u_\Phi}{x} \frac{\partial}{\partial \theta} Y_1^0(\theta, \phi) = \frac{1}{2}\sqrt{\frac{3}{\pi}} \frac{\delta u_\Phi}{x} \cos\theta.$$

Note that only the $m = 0$ term is relevant in the context of our axisymmetric fluid model with the symmetry axis aligned with the z-axis. Fig. 5.2 presents the angular

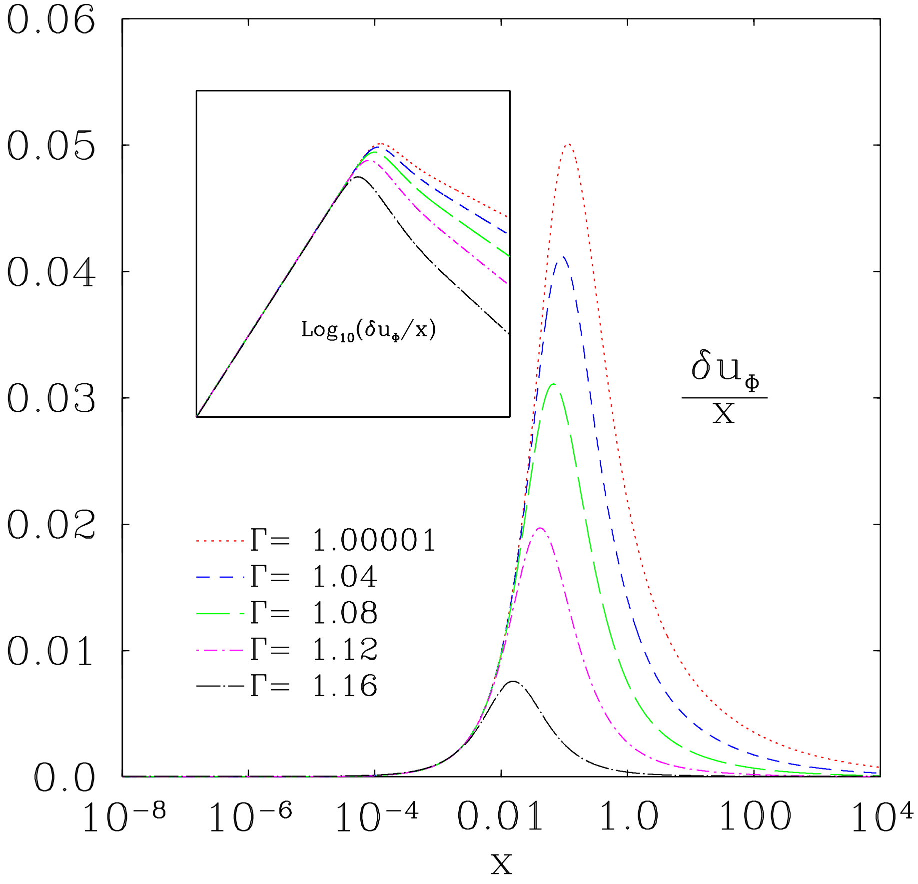

Figure 5.1: Radial function plot of the spin-up mode ($\delta u_\Phi(x)/x$) for the Hunter-A solution at five values of Γ. The angular part can be obtained by the vector spherical harmonics according to Eq. (2.90). All of these functions have a similar profile, with the peak of $\delta u_\Phi/x$ that slightly decreases with increasing Γ. In all these calculations we chose the free parameter $\delta u_{\Phi 0} = 1$. A log-log plot of these profiles is provided in the inset, where we can see that they all have the same behavior near the origin, which follows $\delta u_\Phi(x)/x = \delta u_{\Phi 0} x$.

dependence of the spin-up mode for the Hunter-A solution in the cases, $\Gamma = 1.00001$ and $\Gamma = 1.12$. A similar spatial domain was chosen in both cases. The time prior to singularity formation $(t_0 - t)$ in Eq. (2.91) was chosen independently in each case so that the profiles' maxima are of similar order ($\sim 10^{-2}$). The full $\ell = 1$ axial-mode spatial solutions for $\Gamma = 1.00001, 1.12$ are plotted in Fig. 5.2(a) and Fig. 5.2(b), respectively. The angular dependence is identical for all values of Γ, however due to the small difference in the radial dependence illustrated in Fig. 5.1 the profiles differ slightly with increasing Γ.

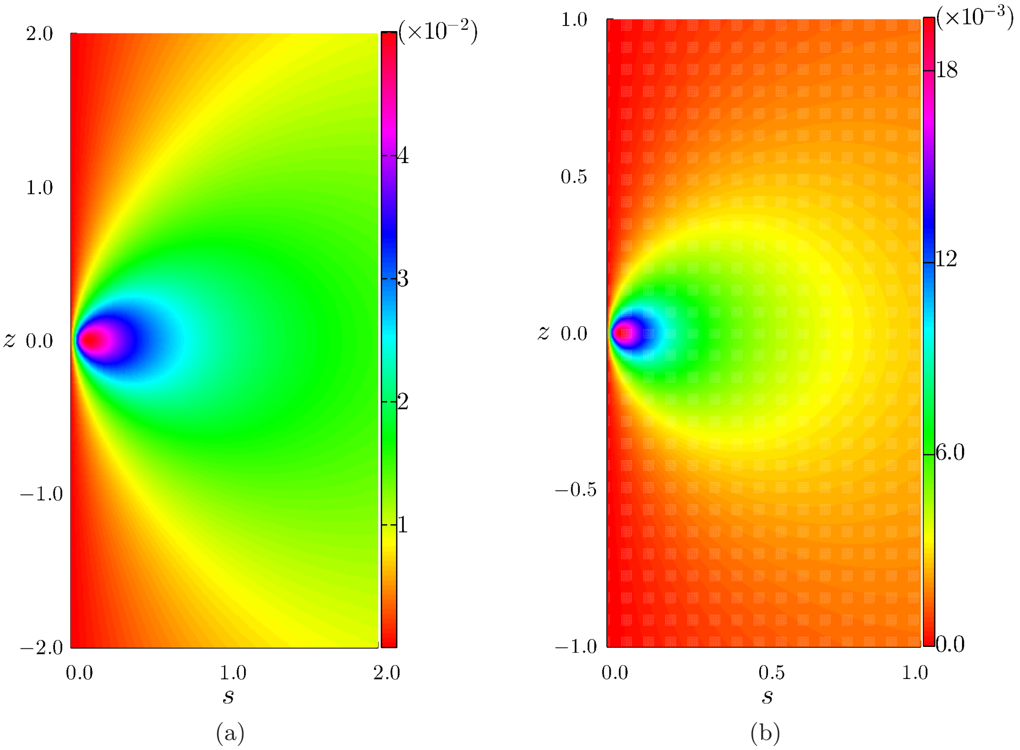

(a) (b)

Figure 5.2: Plots of the spin-up mode's azimuthal-component velocity field v_ϕ for $\Gamma = 1.00001$ and $\Gamma = 1.12$. Panels (a) and (b) present only the $\ell = 1$ contribution of the vector harmonic function $\vec{\Phi}^0_\ell(\theta, \phi)$ at $\Gamma = 1.12$ and $\Gamma = 1.00001$ respectively. Since this is the only observable axial mode which has a positive growth rate as indicated by Eq. (2.103) and the symmetry of our fluid model, slowly rotating initial data near the threshold of gravitational collapse v_ϕ is predicted to resemble this profile at late times.

5.2 Numerical Solutions in Axial Symmetry

The bulk of our calculations in axial symmetry were conducted at $\Gamma = 1.00001$. This value of the adiabatic index (Γ) yielded results which closely resemble previous calculations obtained using the spherically symmetric isothermal gas model [44–48, 64]. The results of the isothermal-gas coupled to Newtonian-gravity are significant since they represent a particular limit ($k \to 0$ in Eq. (1.3)) of the spherically symmetric General Relativistic self-similar perfect fluid solutions [77]. This correspondence between the GR perfect fluid and the Newtonian isothermal gas motivated our choice ($\Gamma = 1.00001$) for the polytropic index. It seems reasonable to suppose that Gundlach's work on non-spherical linear perturbations of the same General Relativistic system [10, 24, 30, 32, 33] also includes the Newtonian isothermal gas limit. From this work we have made the observation that the non-spherical perturbation mode structure is preserved as we look at the Newtonian limit discussed in [77]. More specifically, the unstable axial mode found by [33] whose growth is given by (2.105) becomes the spin-up mode under the Newtonian limit. Based on this observation we predicted that the introduction of nonspherical initial data characterized by slow rotations into our Newtonian axisymmetric model will be analogous to the predicted behavior of the General Relativistic system.

We argue that the situation is exactly analogous in the case of critical collapse. We know of this exact analogy in the cases of spherical symmetry, Chap. 4. In the nonspherical case (slow rotation) the critical solution or more specifically its departure from the Hunter-A solution is governed by two growing modes, thus maintaining its exact analogy with the general relativistic system [30, 32, 33]. In particular the role that non-zero angular momentum plays in both systems should likewise be analogous. It is precisely the effect of non-zero angular momentum on the critical solution that we set out to explore.

5.2.1 Slow Rotation ($q \to 0$)

We solved Euler's equations (2.34)–(2.39) using the finite volume numerical techniques outlined in Chap. 3. We then conducted numerical experiments using the 2-parameter families of initial data given in Table 5.1. The degree of initial rotation is controlled by the parameter q. In the first set of experiments q is set to a very small relative value. Specifically, $q = 10^{-14}$, and since q enters the initial conditions as a factor in v_ϕ, this azimuthal velocity field is many order of magnitude smaller than v_s and v_z after the first time step in the evolution. This scenario is chosen in order to test the prediction that the spherically symmetric results are obtained in the limit $q \to 0$. We prepared critical initial data with parameter p near $p^\star$, where $p^\star$ is a factor of the pressure profile that sets the threshold of gravitational collapse in the absence of rotation ($q = 0$). Turning on the initial rotation by a very small amount for instance by setting $q = 10^{-14}$ does not change the threshold value $p^\star$[12]. In this sense we consider this the addition of infinitesimal rotation.

The first quantity we checked for was the convergence of the collapsing center to the Hunter-A solution. Following what was done in spherical symmetry, we compute the self-similar quantity Q_0 from the dynamical solution for the density at the origin $\rho(t, 0, 0)$. We found precisely the same convergence of $Q_0(t)$ to the Hunter-A solution that we observed in spherical symmetry. All three families exhibit convergence to the same value of Q_0. This fact is presented in Fig. 5.3. As was expected, the discrepancies which characterizes the differences in the initial data sets are "washed away" by their common convergence to the intermediate attractor (the Hunter-A solution), hence the observed universality of the critical solution. Finally, these critical fluid evolutions proceed with their convergence to the Larson-Penston solution. Due to the high computational costs we are unable to follow this convergence to the same degree possible in spherical symmetry. Eventually, this convergence will also

---

[12] There is an inherent uncertainty in the computed value of $p^\star$ due to limitations in numerical precision. Therefore, the change introduced by adding small (infinitesimal) $q = 10^{-14}$ is smaller than this uncertainty.

be interrupted by the spin-up mode of the Larson-Penston solution. Also contained in Fig. 5.3 is the spherically symmetric critical data corresponding to Model A with $\Gamma = 1.00001$.

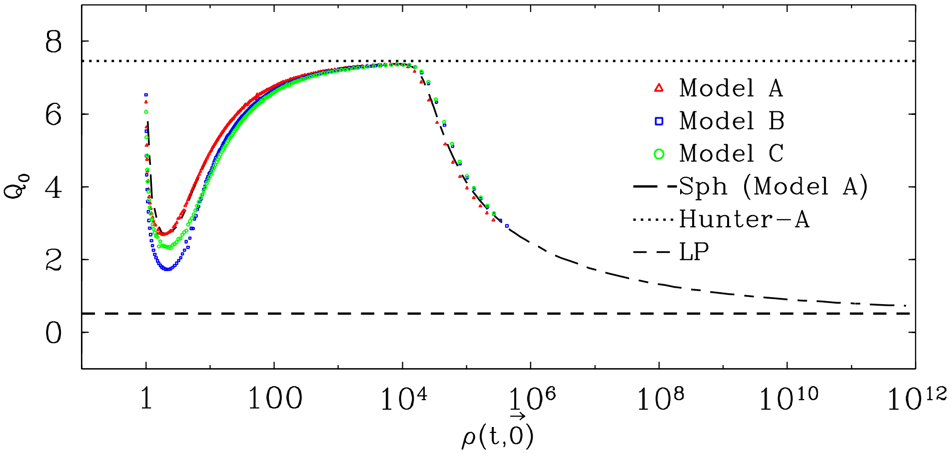

Figure 5.3: Plot of Q_0 versus central density $(\rho(t,0,0))$ for critical initial data. The value of Q_0 was computed from the critical solution using $Q_0(t) = 4\pi G\rho(0,0,t)(t_0 - t)^2$ for the three distinct 2-parameter families of initial data presented in Table 5.1. The degree of initial rotation was controlled by the parameter q which was set to 10^{-14} in all of the three cases. We note that as the central density grows the computed value of Q_0 converges to the value corresponding to the Hunter-A solution, given in Table. 4.2. After some time the convergence to Hunter-A breaks down and the solution begins to approach the Larson-Penston (L-P) solution. The results of the spherically symmetric critical solution are also provided for comparison purposes.

The initial degree of rotation can be made small enough that we reproduced the same spherically symmetry results. Nevertheless, as soon as q is nonzero the linear regime (equation (2.110)) contains an extra unstable mode. From the discussion of Sec. 2.8.1 we should observe an unstable nonspherical axial mode during the evolution of the rotating fluid. This mode enters our formalism through the velocity component v_ϕ, and so it is through monitoring of this velocity field component that we were able to detect it. In essence, if this 2-unstable-mode picture is correct the velocity field v_ϕ should resemble the profiles corresponding to the spin-up mode given in Fig. 5.2.

Indeed, snapshots of v_ϕ at its closest approach to the Hunter-A solution for all three families A-C displayed in Fig. 5.4(a)–Fig. 5.4(c) reproduce the features of the $\ell = 1$ spin-up mode plotted in Fig. 5.4(d) (this is a plot of the azimuthal velocity field computed from the spin-up mode). The time of closest approach is determined by the collapsing center, Fig.5.3. Since the spin-up mode is presumably the only nonspherical growing structure (with all others decaying), the initially distinct profiles are expected to become similar. The differences in the observed scales between the calculation of v_ϕ from the critical evolutions and that computed from the spin-up mode can be accounted by the self-similar radial part, namely $\delta u_\Phi(x)/x$. Fig. 5.4(d) represents a plot of v_ϕ taken at a significantly time before the collapse occurs, so the structures of the spin-up mode are not as "compressed" as they are in panels (a)–(c) of Fig. 5.4. The peak in these profiles is determined by $\delta u_\Phi(x)/x$ and an overall family-dependent scale set by κ as well as $t_0 - t$ (t_0 is the time of collapse), see Eq. (2.91).

The data presented thus far is consistent with the prediction that a growing axial perturbation is solely responsible for the solution's final angular dependence. Critical initial data ($p \approx p^\star$) leads to the known funneling of the solution to the two-mode linear regime described in Sec. 2.5 and given by Eq. (2.110). The interplay of these two modes yields a modified version of Choptuik's mass scaling law Eq. (2.118). The specific angular momentum is also expected to follow similar scaling behavior this is given by Eq. (2.120). The case under current discussion is the limit of infinitesimal initial rotation. The mass and specific angular momentum scaling laws in this limit are respectively given by $M \propto |p - p^\star|^{(4-3\Gamma)/\lambda_0}$ and $a \propto q|p - p^\star|^{(3-2\Gamma-\lambda_1)/\lambda_0}$ (Eqs. (2.123) and (2.124)).

The scaling law for the specific angular momentum in the limit as $q \to 0$ has an explicit dependence on the growth rate of the axial perturbations λ_1, Eq. (2.124). We computed the collapsed mass M and its specific angular momentum a for a series of supercritical runs. First of all, we confirmed that the results are in agreement with spherically symmetric data. This is expected since the mass scaling is independent of q, to leading order, *i.e.* $\partial F(\delta)/\partial q|_{q=0} = 0$. All three 2-parameter families of initial data yielded the same mass scaling behavior as evident in Fig. 5.5. The mass scaling independently computed in spherical symmetry produced the same results. The angular momentum scaling behavior also displays universality for increasingly fine-tuned data ($p \to p^\star$). More importantly, the scaling behavior is consistent the predictions of Eqs. (2.123) and (2.124). Indeed, the measured angular momentum of the intermediate state has the imprint of the axial growing mode. Supplying the known values, $\lambda_0 \approx 9.4643$ (from Table 4.3) and $\lambda_1 = 1/3$, we can compute the perturbation theory prediction. The computed data converges to this prediction as $p \to p^\star$ (Fig. 5.5).

Choosing initial data near the Hunter-A solution allowed us to identify the influence of the two growing modes on the scaling behavior of the collapsed mass and its angular momentum. Plotted in Fig. 5.6 are the measurements of quantities M (collapsed mass) and a (collapsed mass's specific angular momentum) for a series of supercritical evolutions near the collapsed threshold with initial data that approximates the Hunter-A solution, Eqs. (5.1)–(5.3). Notice that with this type of initial data we have already, from the outset "trimmed out" most of the decaying perturbations. We conjectured that a very clear signal of the two growing modes should be observed through the scaling of M and a. Again, we also plotted the predictions from perturbation theory (Fig. 5.6). Clearly, our measurements of M and a closely match the predictions coming from perturbation theory.

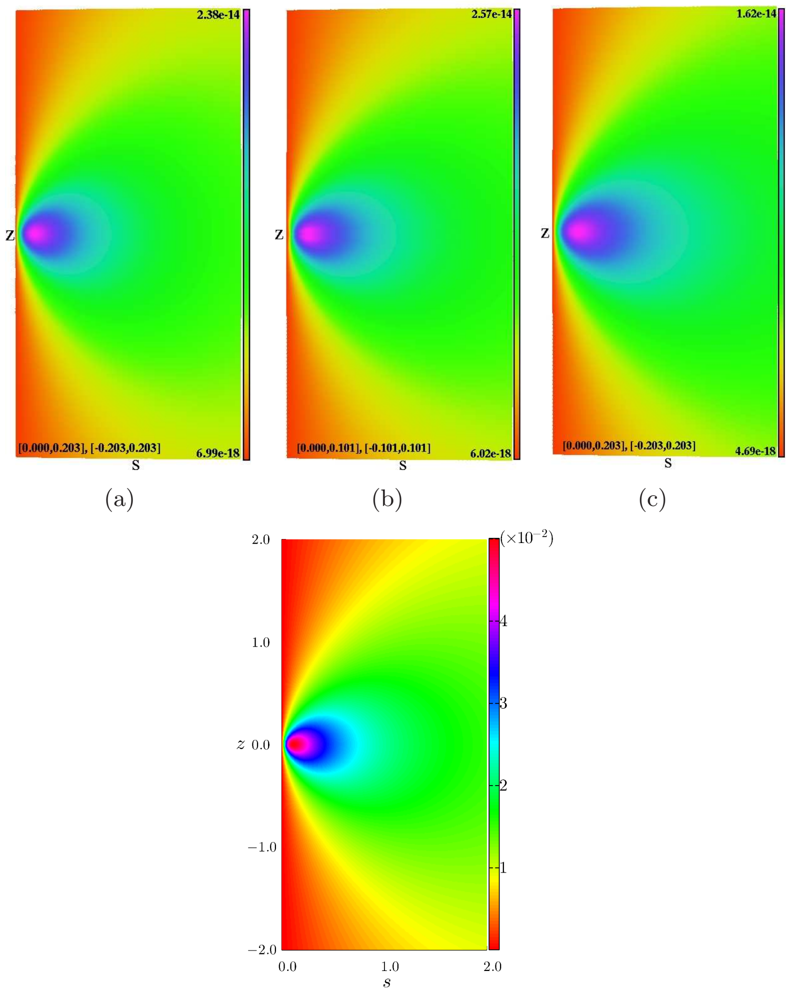

(a) (b) (c)

(d)

Figure 5.4: Critical-evolution measurements of v_ϕ for the spin-up mode, with $\Gamma = 1.00001$. Panels (a) through (c) are the result of critical evolution of initial data corresponding to models A, B and C from Table 5.1 taken at its closest approach the to the Hunter-A solution. The initial rotation is controlled by the parameter q which was set to 10^{-14} in the presented cases. Panel (d) is the result of our explicit computation of the spin-up mode. Recall that the spin-up mode and its angular dependence can be computed explicitly, the angular part is given by the $\ell = 1$ vector harmonic, *i.e.* by $\partial Y_1^0(\theta, \phi)/\partial\theta$. All three initial data sets (A-C) converge to the same profile; one where the only growing structure is described by the spin-up mode (d), thus indicating universality. The scales differences among panels (a-c) and (d) is accounted by the self-similar nature of the radial profile *i.e.* $\delta u_\Phi(x)/x$. Panel (d) is generated at a significant time before the collapse happens. The size and location of the peak is determined by the radial profile $(\delta u_\Phi(x)/x)$ and an overall scale set by the local speed of sound, see Eq.(2.91).

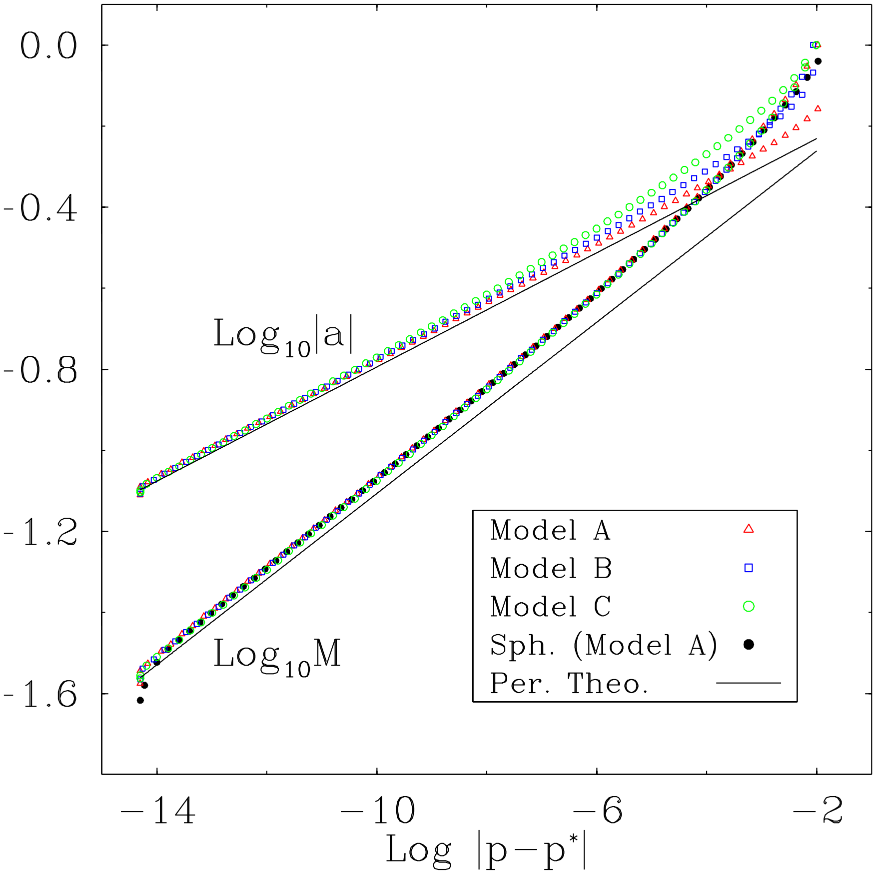

Figure 5.5: The scaling behavior of the collapsed mass (M) and its specific angular momentum (a) for supercritical initial data near the collapse threshold $p^\star$. The cases presented here belong to the three distinct 2-parameter families of initial data given in Table 5.1 with $q = 10^{-14}$. The perturbation analysis developed by Gundlach [32], discussed in Sec. 2.8.1 provided predictions for the scaling behavior of the mass and angular momentum of the compact object near the collapse threshold. Our calculations are in agreement with Gundlach's perturbation theory predictions in this case of slow, initial rotation. All three families converge to the predicted linear relationship suggesting universality. This is explained by convergence to a common scale-invariant state (the Hunter-A solution). Note that in general a should be a vector, but in axisymmetry only the z-component is non-zero.

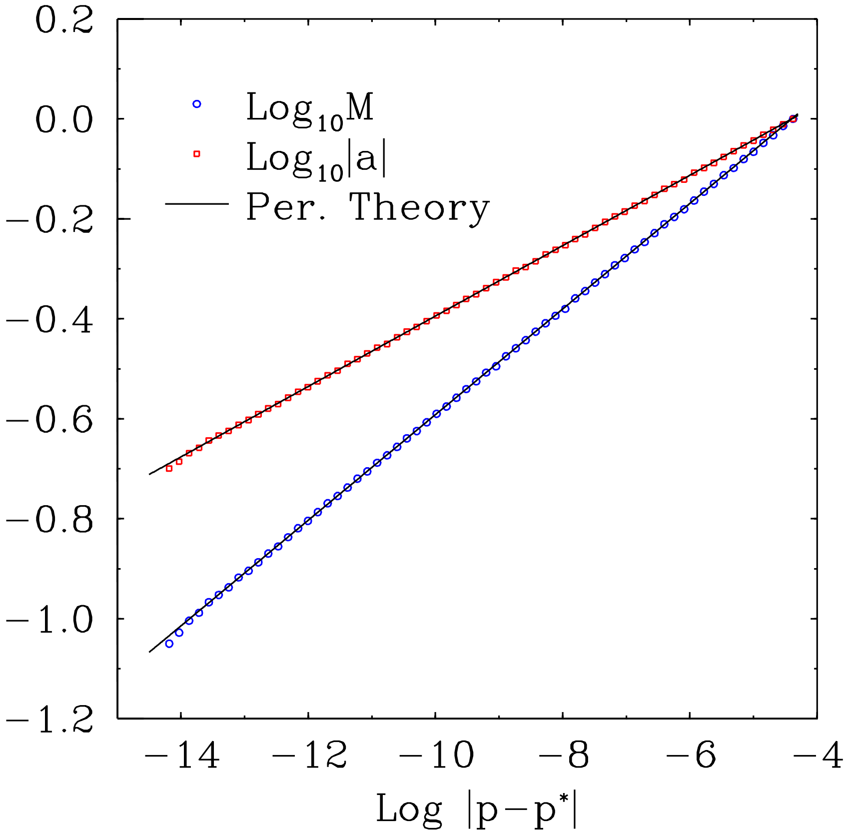

Figure 5.6: Scaling behavior of the collapsed mass M, and the specific angular momentum a, for initial data that closely resembles the Hunter-A solution, Eqs (5.1)–(5.3). The initial data was endowed with an infinitesimal amount of rotation, set by $q = 10^{-14}$. The infinitesimal rotation introduces a non-spherical unstable axial mode (spin-up) with growth rate $\lambda_1 = 1/3$. The existence of this non-spherical growing mode leads to a scaling-law for a, this is given by Eq. (2.124). The scaling of M follows Eq. (2.123). Our calculations of M and a during supercritical evolutions which are now very close to the Hunter-A solutions behave in accordance with the predictions of perturbation theory. More specifically, the slopes of the linear relationships are consistent with the values $\lambda_0 = 9.46430101$ and $\lambda_1 = 1/3$, the growth rates of the spherical and axial modes respectively.

5.2.2 Finite Initial Rotation

In the previous section we considered the evolution of our fluid model subject to infinitesimal initial rotation. The next step in our investigation was to add a finite amount of initial angular momentum to the initial state in order to measure the functions $F(\delta)$ and $G(\delta)$ in Eqs. (2.118) and (2.120), which are presumably universal. The degree of rotation is controlled by q; in this case it is a finite, yet small quantity such that the critical solution still goes through the linear regime given by the expansion (2.113). Prior to presenting our calculations of $F(\delta)$ and $G(\delta)$, we would like to address the question as to what happens to critical initial data when small but finite rotation is included.

We wished to know the fate of initial data near the threshold $p^\star$ upon the addition of a finite amount of initial rotation. In [32] Gundlach discussed two possible results. Initial data, $Z^\star + \delta Z_1$ which teeter on the brink of gravitational collapse, either formed a compact object followed by complete collapse, or it dispersed, leaving behind empty space. In his article [32], he labels these as follows,

- *Possibility* 1: Critical initial data collapses even with the addition of angular momentum through δZ_1.
- *Possibility* 2: Intuitively, the addition of angular momentum should generate an outward "centrifugal" pressure to the critical state that leads to the dispersal of the gas.

The experiment was conducted using our Newtonian model and the results obtained correspond to *Possibility* 2 discussed in Sec. VII of [32]. Possibility-2 as Gundlach pointed out is the more physically intuitive possibility, we expect that the addition of angular momentum promotes the outward dispersal of the fluid. This is indeed what we found in our numerical experiments, adding rotation to already critical data leads unambiguously to fluid dispersal.

The universal functions depend on the initial parameters via $\delta \propto q/|p-p^\star|^{\lambda_1/\lambda_0}$.

We varied δ by fixing p and choosing a series of values for q starting from zero. We chose p in the supercritical regime, so that at $q = 0$, our choice of p yields collapsing data. Nevertheless, p is near the threshold value $p^\star$. Note that $p^\star$ represents the threshold of collapse only if $q = 0$. As we have just discussed, finite q shifts this threshold. We can represent this as $p_{\rm cr}(q)$, with the condition that $p_{\rm cr}(0) \equiv p^\star$ [13]. The calculated values of $F(\delta)$ and $G(\delta)$ are plotted in Fig. 5.7 and Fig. 5.8, respectively. These were calculated from the measured values of M, a and the scaling laws (2.118) 2.120. Three 2-parameter families were tested, with the normalization conditions

$$F(0) = 1, \quad \frac{\partial G(0)}{\partial \delta} = 1, \tag{5.4}$$

which follows from the freedom to normalize the mode functions $Z_0(x)$ and $Z_1(x, \theta, \phi)$. In essence, this amounts to dividing out the family-dependent constants $\bar{C_0}^{(4-3\Gamma)/\lambda_0}$, $C_1\bar{C_0}^{(3-2\Gamma-\lambda_1)/\lambda_0}$ in Eqs. (2.118) (2.120) for $q \to 0$ data. We found evidence to support the universality of these function since all three families yielded nearly identical results.

More detailed measurements of $F(\delta)$ and $G(\delta)$ were generated at the large δ regime. We know already that the addition of initial angular momentum shifts the threshold of gravitational collapse (*Possibility* 2). We began with supercritical data at fixed $p < p^\star$, then we added just enough amount of initial rotation by modulating q until we find the threshold of collapse, we labeled this $q_{\rm max}$. The threshold can be defined in terms of the quantity $\delta_{\rm max}$. Where $\delta_{\rm max} = q_{\rm max}/|p - p^\star|^{\lambda_1/\lambda_0}$. Alternatively, we could start with fixed q and modulate p until $p = p_{\rm cr}$, so that, $\delta_{\rm max} = q/|p_{\rm cr} - p^\star|^{\lambda_1/\lambda_0}$. By definition, both $F(\delta)$ and $G(\delta)$ must vanish for $|\delta| > \delta_{\rm max}$. The universal functions are non-trivial over the region of the p-q plane defined by,

$$\bar{C_0}(p - p^\star) < 0, \quad \text{and} \quad C_1 q < \delta_{\rm max}(\bar{C_0}|p - p^\star|)^{\lambda_1/\lambda_0}. \tag{5.5}$$

---

[13] This definition was also borrowed from Ref. [32]

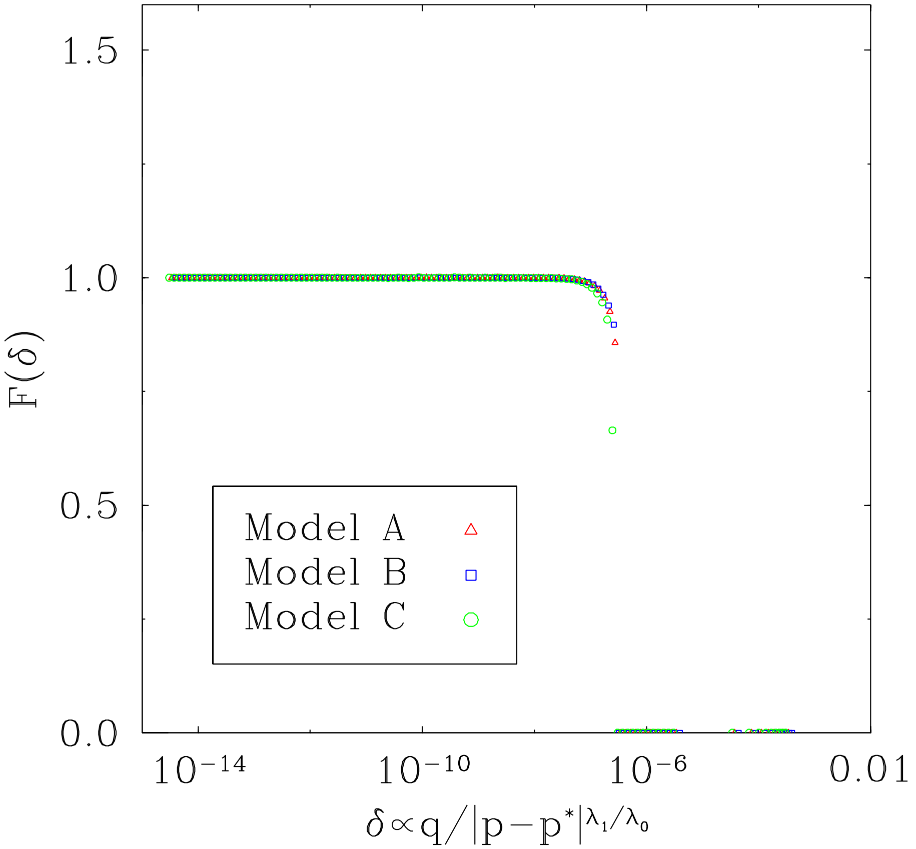

Figure 5.7: Plot of function $F(\delta)$ for three different 2-parameter families of initial data. These 2-parameter families are specified in Table 5.1. This plot confirms speculations concerning the universality of $F(\delta)$ stated in the perturbation theory analysis of [32]. As the initial rotation is turned off ($\delta \to 0$), the function $F(0) \to 1$ for the three families (after appropriate rescaling), a fact which is consistent with the spherically symmetric results. This data belongs to the case where $\Gamma = 1.00001$ in the polytropic EoS (2.18).

Gundlach [32] speculated on the possible nature of these functions near the threshold δ_{max}. Assuming that the situation described by *possibility 2* is realized (as indeed it was in our case), Gundlach provides two subcategories for the behavior of the order-parameters M and a near the collapse threshold given by δ_{max} or p_{cr}. These are,

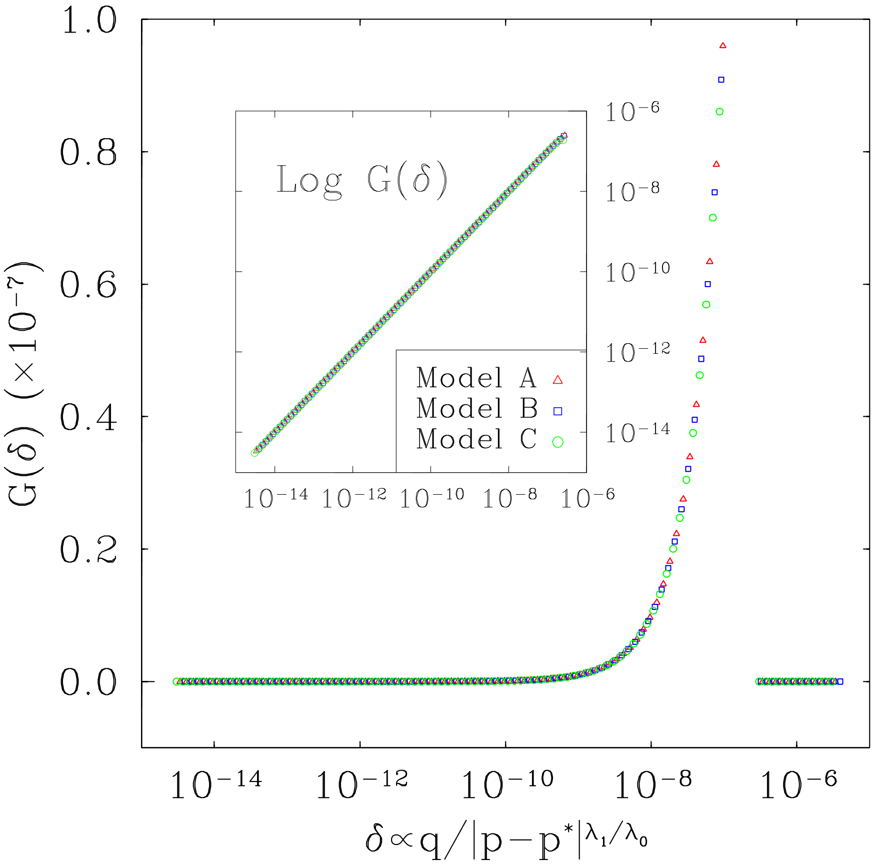

Figure 5.8: Plot of function $G(\delta)$ for three different 2-parameter families of initial data. The three 2-parameter families of initial data can be found in Table 5.1. Our three measurements of $G(\delta)$ corresponding to the initial data families (A-C) are nearly identical; this is in agreement with the predicted universality of $G(\delta)$ [32]. We obtained the expected linear behavior of $G(\delta)$ near $\delta = 0$ (inset).

- *Possibility* $2a$: A mass-gap develops in the collapsed mass spectrum across the $\delta_{\max}$ boundary. This implies a discontinuity in the universal functions.
- *Possibility* $2b$: There is no mass-gap; for this possibility Gundlach proposed a power law behavior for the universal functions which must vanish across the

threshold boundary, *e.g.*,

$$F(\delta) = \begin{cases} K_M(\delta_{\max} - \delta)^{\beta_M} & \delta \lesssim \delta_{\max} \\ 0, & \delta > \delta_{\max} \end{cases} \tag{5.6}$$

where β_M is again a universal exponent and K_M is a family dependent constant. Similarly, for $G(\delta)$,

$$G(\delta) = \begin{cases} K_a(\delta_{\max} - \delta)^{\beta_a} & \delta \lesssim \delta_{\max} \\ 0. & \delta > \delta_{\max} \end{cases} \tag{5.7}$$

Our results indicate continuity of $F(\delta)$ and $G(\delta)$ across the $\delta_{\max}$ boundary, in agreement with Gundlach's *Possibility* $2b$ also discussed in Sec.VII of Ref. [32]. The calculations agree with the proposed behavior near $\delta_{\max}$ as dictated by Eqs. (5.6) and (5.7). These results are plotted in Fig. 5.9. Both $F(\delta)$ and $G(\delta)$ seem to vanish as $\delta \to \delta_{\max}$ according to an power law. The results for the three families appear to be governed by a scaling law whereby the scaling exponents, β_M and β_a are given by,

$$\beta_M = (4 - 3\Gamma)/\lambda_0 \quad \text{and} \quad \beta_a = (3 - 2\Gamma - \lambda_1)/\lambda_0, \tag{5.8}$$

the same as those of scaling laws for M and a given in Eqs. (2.118) and (2.120). This fact is illustrated in Fig. 5.9. If the exponents for the assumed power-laws of $F(\delta)$ and $G(\delta)$ Eqs. (5.6) and (5.7) near $\delta_{\max}$ are indeed those given in Eq. (5.8) then, it is easy to show that the mass M and specific angular momentum a of the collapsed core can be written as,

$$M \propto (q_{\max} - q)^{(4-3\Gamma)/\lambda_0} \quad \text{and} \quad a \propto (q_{\max} - q)^{(3-2\Gamma-\lambda_1)/\lambda_0}, \tag{5.9}$$

provided that $\delta_{\max}$ is found by fine tuning q to $q_{\max}$. If $\delta_{\max}$ is obtained by varying $p \to p_{\text{cr}}$ then in order to see the behavior of M and a near p_{cr} we need to perform an expansion of $F(\delta)$ and $G(\delta)$ in the small quantity $|p_{\text{cr}} - p|$. These requires a bit of algebra to show that,

$$M \underset{\sim}{\propto} (p_{\rm cr} - p)^{(4-3\Gamma)/\lambda_0} \quad \text{and} \quad a \underset{\sim}{\propto} (p_{\rm cr} - p)^{(3-2\Gamma-\lambda_1)/\lambda_0}. \tag{5.10}$$

Where the symbol $\underset{\sim}{\propto}$ indicates the presence of higher order terms of the quantity $|p_{\rm cr} - p|$ that are omitted in Eq. (5.10).

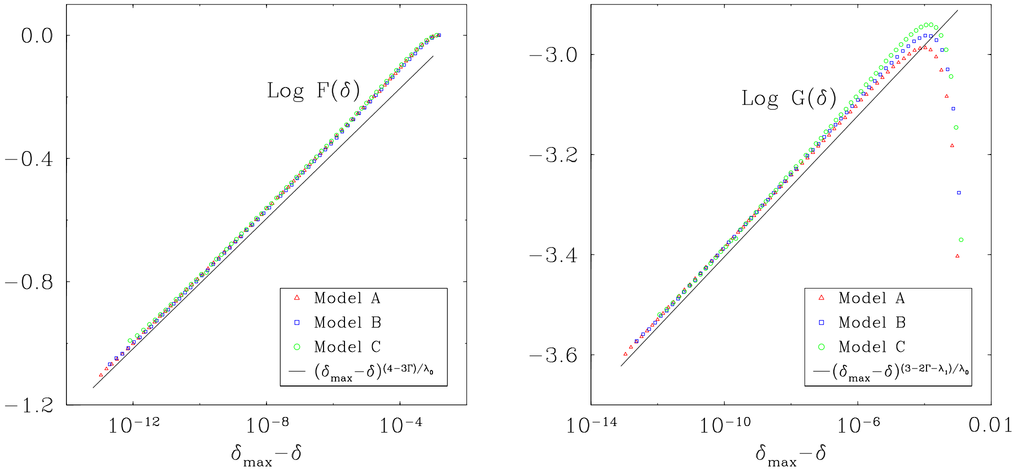

(a) $F(\delta)$ (b) $G(\delta)$

Figure 5.9: Universal functions $F(\delta)$ and $G(\delta)$ near the collapse threshold $\delta_{\rm max}$. Calculations were performed using three distinct 2-parameter families of initial data. The results indicate a vanishing of $F(\delta)$ and $G(\delta)$ as $\delta \to \delta_{\rm max}$ according to a power law $\sim (\delta_{\rm max} - \delta)^{\beta}$. The scaling exponents for $F(\delta)$ and $G(\delta)$, respectively, β_M and β_a seem to be the same as those which govern the scaling of M and a in equations (2.118) and (2.120)

From the above discussion we have learned that, whether we approach the collapse threshold by varying $p \to p_{\rm cr}$ at fixed q or $q \to q_{\rm max}$ at fixed p, M and a have the same scaling behavior that depend only on the "distance" from the collapse threshold. The numerically calculated form of the universal functions F and G indicate continuity of the spectrum of collapsed cores across the threshold boundary. There appears to be no mass gap in the spectrum even with finite initial angular momentum Fig. 5.9.

A parameter survey was conducted over the $p - q$ space. For this survey we selected Model-A from Table 5.1 to define the initial state. The parameter domain was chosen to be a rectangular grid given by $(p,\, q) \in [0.99p^\star,\, 1.01p^\star] \times [-0.1,\, 0.1]$. We then proceeded to find all the p_{cr}s at every q on the grid by way of multiple binary searches [14]. Similarly, we found the $q_{\max}$s at every p value. This procedure allowed us to trace the critical collapse curve $(p_{\mathrm{cr}},\, q_{\max})$. We can clearly establish that the critical curve follows a parabola in the $p-q$ space as displayed in Fig. 5.10. The critical parameters p_{cr} and $q_{\max}$ are modeled by $p_{\mathrm{cr}}(q) = p^\star - Aq^b$, $q_{\max}(p) = \tilde{A}(p-p^\star)^{\tilde{b}}$ respectively. The scalar parameters A or $\tilde{A}$ are dependent on the family of initial data, whereas b or $\tilde{b}$ are universal parameters set by the relative dimensionality of p and q. A least-square curve fit was applied to this data in order to approximate these curve parameters. We discovered that for this data $A \approx 0.114$ and $b \approx 1.99$, a value which is suspiciously close to 2.

Calculations for M and a near the critical curve were generated by approaching the curve along the two independent direction on the $p - q$ plane. From these calculations we were able to ascertain that the behavior of M and a is indeed that given by equations (5.9) and (5.10). Much like the spherically symmetric case arbitrarily small cores can be produced with increased proximity to the critical curve. The survey results are plotted in Figs. 5.11 and 5.12. The quantities M and a seem to be continuous across the critical curve. Furthermore, the scaling of M and a is identical (universal) anywhere near this curve and only seems to depend on its distance (in the $p - q$ plane) from it. The results are also consistent with the symmetry requirements $M(p,-q) = M(p,q)$ and $a(p,-q) = -a(p,q)$ as seen in Figs. 5.11 and 5.12.

We used the results generated by our parameter survey to compare with Gund-

---

[14] A binary search refers to the process of finding the threshold of gravitational collapse by numerically evolving the equations of motion for subcritical and supercritical values of the control parameter. The subcritical-supercritical gap is narrowed until the 'critical' value is identified.

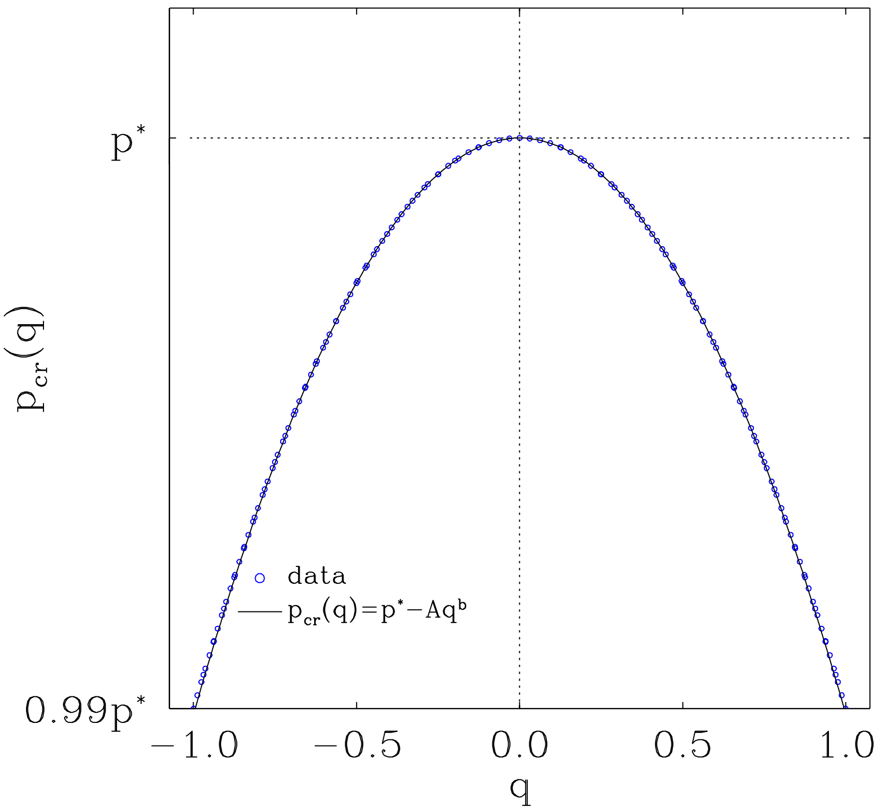

Figure 5.10: Curve of the gravitational collapse threshold on the $p-q$ parameter space for initial data Model-A at $\Gamma = 1.00001$. Binary searches were carried out along the two independent directions over this space to determine the collapse threshold curve. This was done by fixing $p < p^{\star}$ and then fine tuning (via a binary search) q to $q_{\max}$. As expected, we found that for the same value of p another collapse threshold could be identified at $q = q_{\min}$, the value of $q_{\min}$ matches our symmetry expectations *i.e.* $q_{\min} = -q_{\max}$. We plotted the experimentally determined data (p, $q_{\max}$) and (p, $-q_{\max}$). Similarly, at fixed q the binary search (in p) yields p_{cr} for the threshold parameter, naturally, $p_{\mathrm{cr}} = p^{\star}$ in the case where $q = 0$ which corresponds to spherical symmetry. Again, we plotted (p_{cr}, q). A power-law curve of the form, $p_{\mathrm{cr}}(q) = p^{\star} + Aq^{b}$ was fitted to this data using the method of least-squares and determine the parameters A and b. For this data $A \approx 0.114$ and $b \approx 1.99$. The first parameter, A is family dependent, but b is a universal parameter that depends on the relative dimensionality of p and q. The value of b (1.99) is suspiciously close to 2, thus the relation between p and q is a parabola.

lach's schematic plots of M and a found in Fig. 2 of Ref. [32]. The plots presented there are the consequence of considering the form of $F(\delta)$ and $G(\delta)$ to be that of equations (5.6) and (5.7) (*Possibility* 2*b*). These plots have the same general "topology" as our Figs. 5.11 and 5.12. This means continuity of the spectrum of collapsed masses across $p(q_{\max})$. In Gundlach's paper the surface plots of M and a over the $p-q$ space are constructed by assuming the modes' growing rates are $\lambda_0 = 2$ and $\lambda_1 = 1$. However, for our Newtonian model the growing rates are, $\lambda_0 \simeq 9.4643$, and $\lambda_1 = 1/3$.

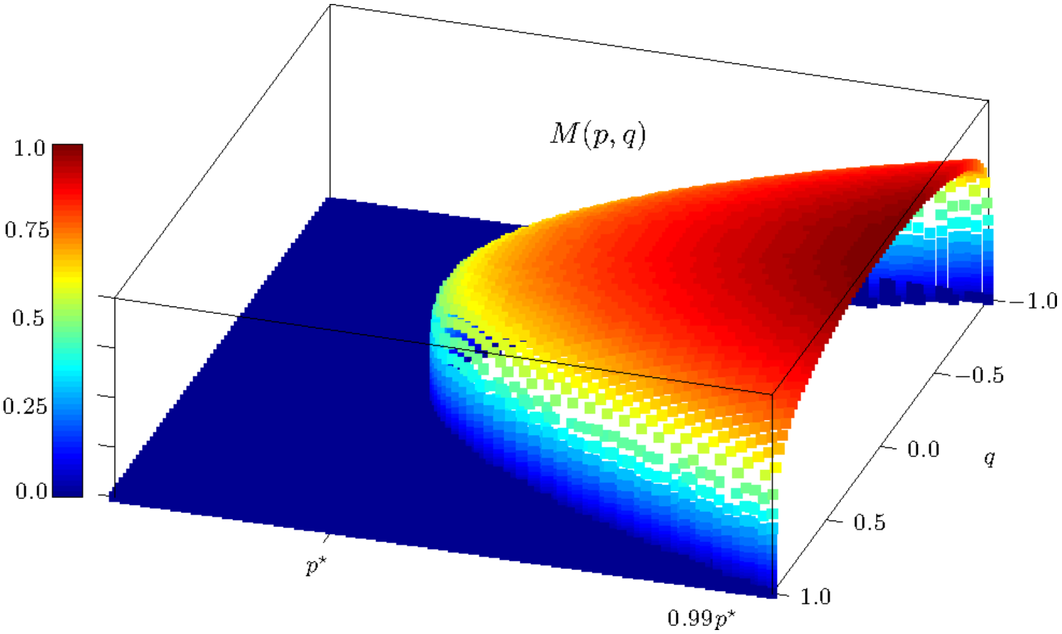

Figure 5.11: Survey of collapsed core masses (M) in the $p-q$ parameter space. These calculations were performed using initial data model A from Table 5.1, and the adiabatic index was set at $\Gamma = 1.00001$. The threshold of gravitational collapsed was found by determining all $q_{\max}$s and $p_{\rm cr}$s; this allowed us to calculate cores' masses near the threshold along the two independent directions in the $p-q$ plane. The evidence indicates that arbitrarily small collapsed cores can be generated across the threshold boundary, *i.e.* the is no mass-gap in the core's spectrum. The behavior near this boundary is the same over the presented parameter ranges and it is given by (5.9) and (5.10). In the $p-q$ plane the collapsed threshold seems to follow a parabolic curve with vertex set ($p = p^\star$, $q = 0$). These results display the expected symmetry about $q = 0$ and they look similar to those plotted in Ref. [32] Fig. 2.

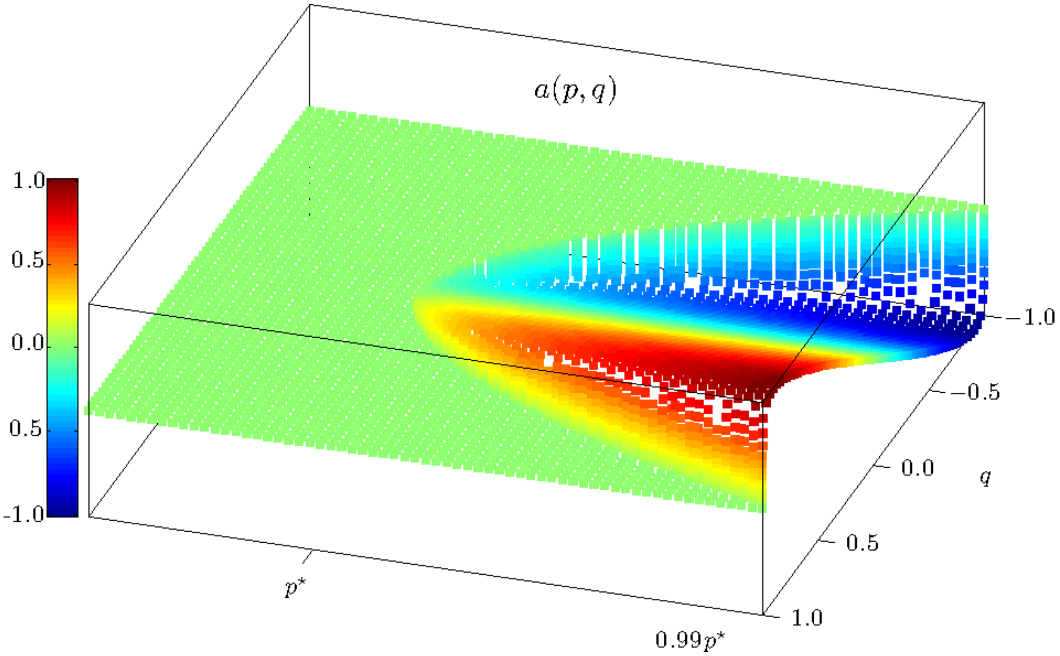

Figure 5.12: Survey of the collapsed core's specific angular momentum a in the $p-q$ parameter space. All the computations were conducted using the initial data set model-A found in Table 5.1, with $\Gamma = 1.00001$. Careful binary searches were carried along the two independent directions in the $p-q$ plane, in order to find the threshold values $p_{\rm cr}$ at every value of q, and $q_{\rm max}$ at every value of p. Once the set $\{p_{\rm cr},\, q_{\rm max}\}$ over the selected part of the $p-q$ plane has been determined we proceeded to compute a near this threshold values. The angular momentum of the collapsed core seems to go continuously to zero in going from the supercritical to the subcritical region. Furthermore, we confirmed that the behavior of a near the curve $(p_{\rm cr},\, q_{\rm max})$ is given by equations (5.9) and (5.10). The collected data for a also displays the expected anti-symmetry $a(p,-q) = -a(p,q)$. These results are similar to those predicted in Ref. [32], Fig. 2.

5.2.3 Rapid Initial Rotation (Large q Regime)

Some of what has been said so far concerning the behavior of M and a near the critical collapse solutions eventually breaks down in the large q regime. For initial data described by Model-A in Table 5.1 the parameter $q \in (0, 0.1]$ yield the results described above. For values $q \gtrsim 0.1$ the critical solutions looks qualitatively different. Concretely, the velocity field component v_ϕ contains features that cannot be accounted for, solely by the $\ell = 1$ spin-up mode. Snapshots of v_ϕ for the critical evolutions of 2-parameter families A, B and C Table. 5.1 at $q = 0.5$ are presented in Fig. 5.13. Clearly, we need to include higher order vectors harmonics to adequately account account for the angular dependence displayed by v_ϕ, as evident in Fig. 5.13. The solution, however, does seem to continue to have features of self-similarity. Albeit, the self-similarity displayed by the velocity field component v_ϕ seems to be of a discrete nature, at least with regard to the field v_ϕ. This is evident in Fig. 5.13. This solution also seems to be a universal critical solution.

Initial data with large values of q does not necessarily go through the linear regime described in Sec. 2.8.1 from which the scaling laws for collapsed mass Eq. (2.118), and specific angular momentum Eq. (2.120) were derived. In fact, the features of the profile for v_ϕ (Fig. 5.13) suggest a departure from the linear regime. Nevertheless, we can calculate the scaling behavior of M and a near the threshold of gravitational collapse. This results in a series of collapsed masses whose scaling behavior near ($p \to p_{\mathrm{cr}}$) remains unchanged, even over this "extreme" regime. However, the specific angular momentum clearly diverts from its slow rotation behavior. The scaling exponent of a near the threshold of collapsed p_{cr} seems to be identical to that of the collapsed mass. These results are plotted in Fig. 5.14. The scaling of a is clearly different from what is predicted by Eq. (5.10). On a speculative note, the observed results are consistent with the scaling exponent $\beta_a = 3 - 2\Gamma$ instead of $\beta_a = 3 - 2\Gamma - \lambda_1$ (Eq. (5.8)) for the $G(\delta)$-ansatz in Eq. (5.7). Interestingly, these results can be derived by assuming a different "linear regime", where the critical solution approaches a one-mode unstable, nonspherical, self-similar solutions (clearly different from Hunter-A). This regime could be represented by,

$$Z(\tau, x, \theta, \phi; \tilde{p}) \simeq Z^{\star}(x, \theta, \phi) + C_0(\tilde{p} - \tilde{p}_{\rm cr}) Z_0(x, \theta, \phi) e^{\lambda_0 \tau}. \tag{5.11}$$

Here $Z^{\star}(x, \theta, \phi)$ is one-mode-unstable similarity solution to the axisymmetric isentropic gas[15] with $Z_0(x, \theta, \phi)$ being its linear unstable mode function. In this case $\tilde{p}$ is the generic parameter with non-trivial critical value $\tilde{p}_{\rm cr}$. Notice that we could use p, q, δ or any other parameter to represent the 1-parameter family of initial data. Repeating the formalism of Sec. 2.8.1 it is easy to show that $e^{\tau_*} \propto (\tilde{p} - \tilde{p}_{\rm cr})^{1/\lambda_0}$, where τ_* represents the sole length scale in the system. From dimensional analysis we know $|\vec{a}| \propto t_*^{2n-1}$ and so,

$$|\vec{a}| \equiv a \propto |\tilde{p} - \tilde{p}_{\rm cr}|^{(3-2\Gamma)/\lambda_0}. \tag{5.12}$$

Our measurements of a near $\tilde{p}_{\rm cr}$ are consistent with Eq. (5.12). This corresponds to the case where $\Gamma = 1.00001$ and $\lambda_0 = 9.4643$ in which case $(4 - 3\Gamma)/\lambda_0 \approx (3 - 2\Gamma)/\lambda_0 \sim 1/\lambda_0$. Thus the scaling of M and a are essentially indistinguishable, see Fig. 5.14.

---

[15] In order to test this assumption we could proceed by assuming a similarity, axisymmetric ansatz to the Euler equations and then show that one of the self-similar solutions has a single unstable mode with growth rate $\sim \lambda_0$. Then, we would need to show that this one-mode solution is the intermediate attractor in critical collapse. This however, is beyond the scope of our current project.

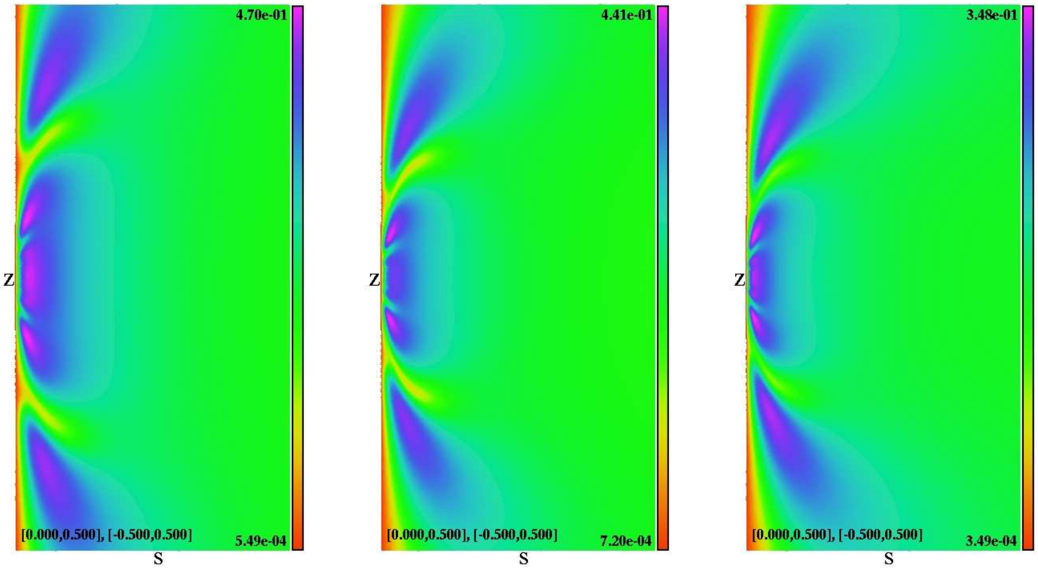

(a) (b) (c)

Figure 5.13: Displays of v_ϕ corresponding to the critical solutions for the case of "large" initial rotation ($q = 0.5$) with $\Gamma = 1.00001$. Panels (a)–(c) correspond to initial data sets A–C respectively. The critical solution appears to be universal as the different initial data sets A, B and C converge to a common solution. Evident in panels (a)–(c) is the appearance of a type of discrete self-similarity in the profile of v_ϕ.

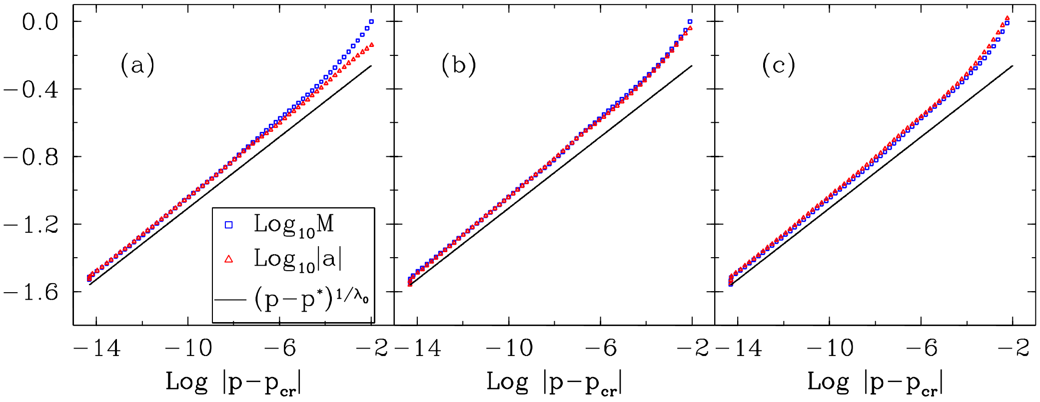

Figure 5.14: Measurements of M and a near the threshold of gravitational collapse $p_{\rm cr}$ for data with "large" initial rotation ($q = 0.5$) with $\Gamma = 1.00001$. Panels (a)–(c) correspond to initial data sets A–C, respectively. The scaling of the mass M remains virtually unchanged compared to the result obtained using slow rotating data. The specific angular momentum a scales differently at large q, its scaling law matches the behavior of the collapsed mass, with scaling exponent, $\sim 1/\lambda_0$. One interpretation of the results is the existence of nonspherical one-mode unstable critical solution with Lyapunov exponent $\sim \lambda_0$. Then, by dimensional analysis, both the specific angular momentum a and the collapsed mass M have very similar scaling when $\Gamma = 1.00001$, since, $(4 - 3\Gamma)/\lambda_0 \approx (3 - 2\Gamma)/\lambda_0 \sim 1/\lambda_0$. This clearly differs from the data presented in Fig. 5.5. The critical solution is clearly universal as all three data sets, A, B and C result in the same scaling near the threshold of gravitational collapse.

5.2.4 Analogy with Statistical Mechanics

Some of the most surprising and interesting elements of critical phenomena in gravitational collapse stem from its analogy with elements of phase transitions in Statistical Mechanics. We will not delve into the nature of statistical mechanical systems; our purpose here is to simply outline the recognized parallels that it shares with the self-gravitating systems. We also would like to describe the extension of this analogy resulting from the present work. For an introduction to phase transitions in Statistical Mechanics see [109]. As pointed out in [10, 32] the formal calculation of critical exponents corresponding to a phase transition in a thermodynamic system is mathematically identical to the linear perturbation analysis that we used to determine the growing mode perturbations. The critical solution is a fixed point of a dynamical system. In statistical mechanics the fixed points contain two growing perturbation modes. One of them is related to temperature T. While the other is connected to a generalized external force *e.g.* an external magnetic field $\vec{B}_{\mathrm{ext}}$.

One example commonly given is the liquid-gas phase transition. Provided other thermodynamic variables are held constant this transition occurs at a critical temperature $T^\star$. Allowing control over one other thermodynamic variable such as the pressure P provides the generalized external force, and thus a second growing mode. For this system the order parameter is the difference in density between the two states *i.e.* $\rho_{\mathrm{liquid}} - \rho_{\mathrm{gas}}$. For T near $T^\star$ the order parameter follows a power-law,

$$\rho_{\mathrm{liquid}} - \rho_{\mathrm{gas}} \propto |T - T^\star|^\gamma, \tag{5.13}$$

where γ is the scaling exponent, related to the growth rates of the perturbation modes. The density interface changes continuously at the critical temperature $T^\star$. This is an example of a *second order phase transition*, thus analogous to type-II critical phenomena in gravitational collapse.

The other example which we have borrowed from [10, 32] follows from consideration of a ferromagnetic material at high temperature. The order parameter is the magnetization $\vec{m}$. The generalized force is the applied/external magnetic field $\vec{B}_{\text{ext}}$. At $\vec{B}_{\text{ext}} = 0$ and $T < T_C$, where T_C is the Curie Temperature, the material assumes spontaneous magnetization $\vec{m}$. As temperature is increased to T_C, $|\vec{m}|$ vanishes according to

$$|\vec{m}| \propto (T_C - T)^{\gamma}. \tag{5.14}$$

However, a finite external magnetic field breaks rotational symmetry above the Curie Temperature; the magnetic moments align themselves with $\vec{B}_{\text{ext}}$. Hence the material becomes *paramagnetic*. This effect is attributed the to second growing mode around the scale-invariant solution at $T = T_C$, $\vec{B}_{\text{ext}} = 0$.

With the confirmed existence of a second growing mode coming from the addition of angular momentum to the initial state in our gravitation collapse scenario, a near exact analogy can be drawn with the ferromagnet plus $\vec{B}_{\text{ext}}$ at high temperature. Gundlach and Goldenfeld [32] pointed out that the second growing mode would make the two systems analogous provided the following associations are made[16]. The vector $\vec{q}$ which specifies the initial angular momentum plays the role of $\vec{B}_{\text{ext}}$. While the specific angular momentum of the collapsed core $\vec{a}$ plays to role of $\vec{m}$. The collapsed mass M is analogous to the correlation length ξ given that $\xi \propto (T_C - T)^{-\gamma}$. Clearly, p is associated with T as is $p^{\star}$ with T_C.

Qualitatively different outcomes follow from initial data that straddle the collapse threshold. In spherical symmetry, $Z^{\star} + \varepsilon Z_0$, and $Z^{\star} - \varepsilon Z_0$ respectively generate the dispersal and collapse outcomes. Beyond spherical symmetry the addition of angular momentum through nonzero $\vec{q}$ adds a second mode to the linear regime *i.e.* $Z^{\star} \pm \varepsilon Z_0 + \vec{\delta} \cdot \vec{Z}_1$. In this case, the outcome (collapse/dispersal) depends solely on the magnitude of the $\vec{\delta}$. Evidence for this can seen in Fig. 5.11 and Fig. 5.12. Similarly, for the ferromagnet $T = T_C - \varepsilon$ and $T = T_C + \varepsilon$ correspond to two qualitatively

---

[16] Their discussion pertained to the general relativistic fluid collapse, however, for reasons made explicit throughout this thesis their conclusions regarding the ferromagnet analogy applies likewise to Newtonian collapse

distinct states. Again, the introduction of the applied magnetic field to the state $T = T_C \pm \varepsilon$ yields an outcome that is dependent on $|\vec{B}_{\rm ext}|$ but independent of its direction. The parameters $\vec{q}$, and $\vec{B}_{\rm ext}$ both set a preferred direction in their respective systems. The final angular momentum of the compact object ($\vec{a}$) is aligned with the direction of $\vec{q}$ from the initial state. Similarly, the spontaneous magnetization $\vec{m}$ which occurs below the Curie temperature T_C has no preferred direction until the $\vec{B}_{\rm ext}$ break this symmetry and $\vec{m}$ always aligns with $\vec{B}_{\rm ext}$. The symmetry breaking occurs at the values $\vec{q} = 0$ and $\vec{B}_{\rm ext} = 0$, hence these are the critical values required to eliminate the second growing mode. The other critical values are, off course, $p^\star$ and T_C. In the latter case, the values cannot be trivially found but depend on other details of the physical model.

5.3 Numerical Solution at Larger Values of Γ

Finally, we present the results for other selected values of the parameter Γ. We chose Γ within the two regimes known from our investigations in spherical symmetry to generate both type-II and type-I critical behavior (Chap. 4). Once more, we investigated the effect of adding an infinitesimal amount of initial rotation on evolution of the fluid at the threshold of gravitational collapse.

5.3.1 Critical Solutions $\Gamma < 6/5$

In spherical symmetry 1-mode unstable solutions (Hunter-A) exist within the range $\Gamma \in [1,\, 6/5)$. We know the mode's Lyapunov exponent grows exponentially as $\Gamma \to 6/5$ (Table 4.3). Due to the this fact it becomes increasingly difficult for the evolution of generic initial data to reach the linear regime. As a result, the initial data used for the dynamical evolutions at $\Gamma = 1.12$ was carefully constructed in accordance to Eqs. (5.1)–(5.3). With infinitesimal amount of rotation ($q = 10^{-14}$) we fine tuned p to the collapse threshold. We observed the same "enhanced" convergence to the Hunter-A solution that we witnessed with $\Gamma \approx 1$. The deviations from the Hunter-A solution are dominated by the two growing modes (spherical and axial). We concluded that for the range of Γ where a Hunter-A solution exists (Sec. 4.1.1) the critical behavior is dominated by the two unstable modes. Thus, for $\Gamma \in [1, 6/5)$ the critical solution is described by linear regime Eq. (2.117).

This linear regime solution dictates the behavior of physical quantities such as M and a. As was done in the case of $\Gamma = 1.00001$ these quantities can be used to identify the unstable modes through calculation of their scaling behavior. Shown in Fig. 5.15(b), the scaling of M and a follow precisely as dictated by the linear regime. Since our solution is already placed in the linear regime at the initial time, the scaling laws follow closely the expectations from perturbation theory. The fine-tuning of this data further shows the "attractor" nature of the Hunter-A solution with only the growing structures of the two unstable modes. The growth of the central density converges to that predicted by the Hunter-A solution. This is evident in Fig. 5.15(a). Lastly, we computed the corresponding universal function $F(\delta)$ and $G(\delta)$ using a series of supercritical data near $p^\star$ with $q = 10^{-14}$. These are plotted in Figs. 5.15(c) and 5.15(d). We found no difference in the behavior of these functions which further supports our conclusion that this 2-mode structure of the critical solutions continues up to but excluding the value of $\Gamma = 6/5$.

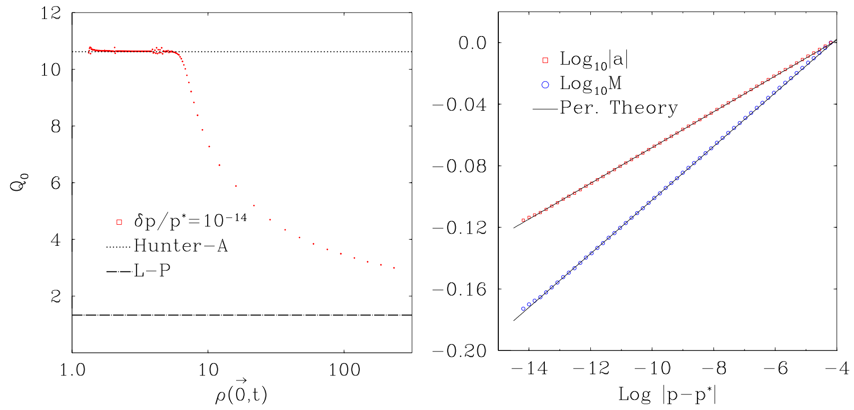

(a) $Q_0(t)$ vs $\rho(t, 0, 0)$ (b) Scaling of M and a

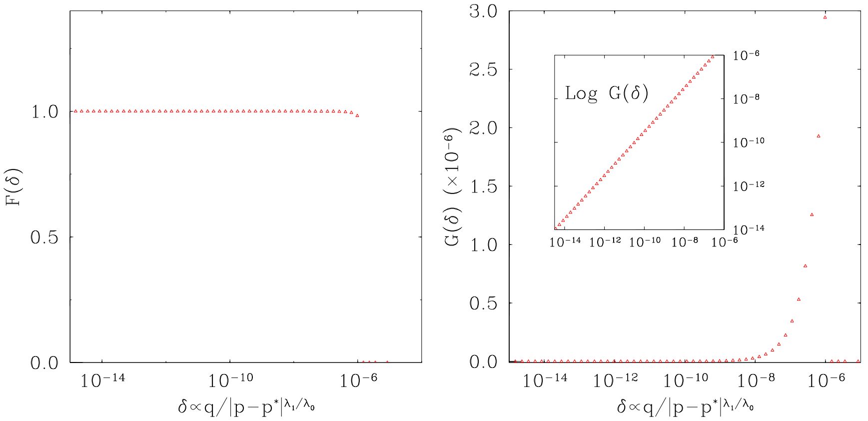

(c) $F(\delta)$ (d) $G(\delta)$

Figure 5.15: Calculations in axi-symmetric critical fluid collapse with $\Gamma = 1.12$ and slow initial rotation ($q = 10^{-14}$). The initial data used here is given by Eqs. (5.2) and (5.3). This data places the initial state near the Hunter-A solution. Therefore, we can see close convergence to appropriate Q_0 value of Hunter-A solution as shown in 5.15(a). Series of calculations of M and a indicate their scaling behavior is governed by the same 2-unstable-mode linear regime. The spin-up mode has the same growth rate $\lambda_1 = 1/3$, but the spherical mode has a much larger growth rate of $\lambda_0 \sim 37$. The scaling laws of M and a are consistent with these exponents as shown in panel 5.15(b). The universal functions $F(\delta)$ and $G(\delta)$ were also computed (panels 5.15(c) and 5.15(d)). The results are formally identical to those obtained in the near isothermal case ($\Gamma = 1.00001$).

Chapter 6

Conclusion and Further Work

This thesis was devoted to the investigation of the critical phenomena generated by a Newtonian self-gravitating fluid at the threshold of gravitational collapse. We extended the previous work on the spherically symmetric isothermal gas model by considering the more general polytropic gas. In the second phase of the our investigation we have relaxed the symmetry restrictions and considered axisymmetric fluid collapse. This allowed us to analyze initially rotating data. We have combined perturbation theory and full nonlinear hydrodynamics in spherical and axial symmetric to construct a more complete picture of the critical phenomena emerging at the threshold of gravitational collapse.

First, we summarize what we've learned from studying our spherically symmetric models. The Euler equation of fluid dynamics with barotropic EoS (2.18) describe a isentropic fluid, which allows self-similar solutions of the first kind. Applying a self-similar ansatz we looked for analytic similarity solutions. We found the spectrum of solutions to be discrete and infinite, with the adiabatic index Γ in EoS (2.18) having an effect on the spectrum of solutions. As a check of consistency we found that the previously known isothermal gas self-similar spectrum is recovered by setting $\Gamma = 1$. Increasing values of the adiabatic index was found to shift the amplitude for the density similarity variable. This pattern persists for $\Gamma \in [1, 6/5)$, where the spectrum of similarity solutions follow the same structure as that of the isothermal gas. This structure is identified as the Hunter-branch of solutions and the Larson-Penston solution. It was discovered that for $\Gamma \geq 6/5$ the discrete but infinite Hunter-branch of solutions vanishes leaving the LP solution as the only similarity solution in this regime. The LP solution persists for $\Gamma \leq 4/3$.

Calculation of the analytic, spherically symmetric linear perturbations about the computed self-similar solutions reveal that the stability properties of the solutions mirror those of the isothermal gas. Again, by setting $\Gamma = 1$ we recovered the known results. More importantly, the first member of the Hunter branch, the so-called Hunter-A solution contains a single unstable mode. All members of the Hunter family contain unstable modes. The Hunter-A is significant given that the formalism of Koike *et. al.* [99] states that the critical solution responsible for critical phenomena must have a single relevant (unstable) mode. As we approached the unexpected transition value of $\Gamma = 6/5$, the Lyapunov exponent corresponding to the unstable mode of the Hunter-A solution diverges. This seems to imply that the Hunter-A solution becomes increasingly unstable as we approach this value for Γ. On the other hand, the LP solution is stable under linear perturbations. Therefore, we expect it to describe generic features of gravitational collapse.

Under conditions of critical gravitational collapse we calculated (numerically) solutions to Euler's equations of fluid dynamics subject to a polytropic EoS (1.4). We found that, similar to the isothermal gas the critical solution converges at intermediate times to the now Γ-dependent Hunter-A solution. At the late stages of the evolution the solution showed converges to the LP solution. This late time convergence to the LP solution was independent of the initial data. The calculation results for $\Gamma \in [1, 6/5)$ are consistent with type-II critical phenomena. However, the non-linear scaling between the time t and radial coordinate r required a modification to the collapsed mass M and specific angular momentum scaling laws which acquired an explicit dependence on the adiabatic index Γ. These results are consistent with those presented in [48] (isothermal gas critical collapse).

Interestingly, in the regime set by $\Gamma \in [6/5, 4/3)$ no Hunter-A solutions exists for the isentropic model. The critical behavior measured is consistent with type-I critical phenomena. The critical solution evolves towards a metastable state whose lifetime T_0 follows a liner scaling law. Following the departure from this state, presumably due to an unstable mode, the solution evolves towards the corresponding LP solution. Therefore, we concluded that the polytropic gas model exhibits both types of critical behavior depending on the parameter Γ. However, the type-I behavior cannot be verified due to the inaccessibility the static solutions resulting from not having enough physical condition to solve the hydrostatic system, see Sec. 4.2.4.

Our axisymmetric work constitutes the first study of critical fluid collapse where the effects of angular momentum were studied dynamically. In spherical symmetry the fluid model plus Newtonian gravity is completely analogous the more realistic GR fluid model. Furthermore, it can be interpreted as an degenerate case of the GR system for $k \to 0$ in EoS (1.3). Therefore, the results obtained hereby directly apply to the GR system for vanishing k[17]. Alternatively, we can view the Newtonian gravity+fluid system as a toy model for studying the effect of slow rotation on the critical solution.

The analogy between the Newtonian and GR fluid models extends beyond spherical symmetry. The GR critical fluid collapse solution, the Evans-Coleman solution is unstable against a nonspherical axial mode. Likewise, we confirmed the presence of an axial unstable mode, the so-called spin-up mode on the Newtonian critical collapse solution (Hunter-A). In this case, the linear regime contains two growing modes, the spherical and the spin-up modes. This linear regime is identical to that discussed by Gundlach in [32]. Grounded on this analogy we borrowed Gundlach's linear-regime-derived scaling behavior of the black-hole mass and its angular momentum. These were used to generated our own predictions for the scaling of the collapsed mass and its specific angular momentum. The results are in agreement with the presence of an extra, axial growing mode.

Our results indicate that all spherically symmetric self-similar solutions in our model are unstable against the axial mode. Of particular interest is the Ori-Piran

---

[17] This can only be correct for the isothermal gas, or for $\Gamma \to 1$ in the polytropic gas.

solution found in [77] which was shown to have a naked singularity in the regime where $0 < k < 0.0105$. The solution being the GR equivalent of the LP solution contains no unstable spherical modes [43, 47]. Thus, it suggests that such a solution should be a global attractor of the evolution. However, according to [31, 32] all such solutions are unstable against nonspherical axial perturbations for $k < 1/9$. Our results are consistent with the instability of the Ori-Piran solution in the limit as $k \to 0$ when rotation effects are included. Therefore, it cannot be a global attractor of the evolution.

The detection of the growing axial mode about the critical collapse solution supports Gundlach's [10, 33] suggested extension to the analogy with statistical mechanics. A ferromagnet at high temperature T subject to an external magnetic field $\vec{B}_{\text{ext}}$ is analogous to the fluid under conditions of critical collapse with initial angular angular momentum. The analogous parameters are $p \to T$ and $\vec{q} \to \vec{B}_{\text{ext}}$. The vector quantity, the specific angular momentum $\vec{a}$ plays the role of the magnetization $\vec{m}$. Both vanish according to a power-law at the critical point $(p = p^\star, \vec{q} = 0)$ for the gravity+fluid model and $(T = T^\star, \vec{B}_{\text{ext}} = 0)$ for the ferromagnet. The collapsed mass, or Newtonian black hole is analogous to the correlation length in the ferromagnet system. Both systems manifest the properties of universality and scale invariance.

6.1 Extensions and Further Work

An obvious extension to the present project is the elimination of all symmetry restrictions in the fluid model and carry out 3-dimensional critical collapse calculations. This would allow us to observe in full generality all the growing nonspherical modes of the critical solution. It is unclear whether the Hunter-A solution is unstable against a polar mode, the so-called bar mode. No evidence of it was found in our axisymmetric simulations. Perturbation theory of the GR critical solution in the Newtonian limit ($k \to 0$) predicts that no other nonspherical modes (besides the axial mode) should be present [33]. Three-dimensional dynamical calculation of critical collapse as well as computation of the linear nonspherical polar perturbations about the Hunter-A solution would allow us to test this prediction.

The polytropic gas model displayed behavior upon critical gravitational collapse that is consistent with both, type-I and type-II critical phenomena. Large values of Γ led to the onset of type-I critical phenomena. These solutions were first discovered in this project. Their role as critical solutions suggests a one-mode linear stability structure, however, an alternative method of computing them needs to be developed which would allow us to study their stability properties. In particular, calculations of the Lyapunov exponent for these solutions are predicted to match their scaling exponent of the T_0 scaling law. Equipped with this knowledge we can generate a more in depth analysis regarding the effects of initial rotation on these solutions. It would be useful to investigate these effects in three dimensions.

Ultimately, we would like to construct a GR hydro code subject EoS (1.3) in axial symmetry. This would allow us to vary the parameter k and test the other perturbation-theory-based predictions made in [31–33]. This is a much more difficult task due to the inherent complexities of solving simultaneously Einstein's equations and the conservation laws for mass, energy and momentum of the fluid in axisymmetry. Such difficulties are exacerbated when one considers extreme conditions of critical gravitational collapse. The Newtonian model presented in this project, although simpler than the GR system provides much of the same insights regarding the nature of critical phenomena in gravitational collapse.

Bibliography

[1] Andrew M. Abrahams and Charles R. Evans. *Phys. Rev. Lett.*, 70:2980–2983, May 1993.

[2] Andrew M. Abrahams and Charles R. Evans. *Phys. Rev. D.*, 49:3998–4003, April 1994.

[3] Nils Andersson. Relativistic fluid dynamics: Physics for many different scales. *Living Rev. Relativity*, 10(1), 2007.

[4] G. I. Barenblatt. *Scaling, self-similarity, and intermediate asymptotics*, volume 14 of Cambridge Texts in Applied Mathematics. Cambridge University Press, 1996.

[5] G. I. Barenblatt and B. Ya Zeldovich. *Ann. Rev. Fluid Mech.*, 4:285–312, 1972.

[6] R. G. Barrera, G. A. Estevez, and J. Giraldo. *Eur. J. Phys.*, 6:287–294, 1985.

[7] Beverly K. Berger. Numerical approaches to spacetime singularities. *Living Rev. Relativity*, 5(1), 2002.

[8] M. J. Berger and P. Colella. *Journal of Computational Physics*, 82:64–84, 1989.

[9] M. Birukou, V. Husain, G. Kunstatter, E. Vaz, and M. Olivier. *Phys. Rev. D*, 65(104036):1–7, 2002.

[10] Gundlach C. *Living Rev. Relativity*, 10(5), 2007.

[11] A. H. Cahill and M. E. Tubb. *Commun. Math. Phys.*, 21:1, 1971.

[12] B. J. Carr and A. A. Coley. *Gen. Relativ. Gravit.*, 16:31–71, 1999.

[13] B. Carter. and R. N. Henriksen. *Ann. Physique. Supp. No. 6*, 14:47, 1989.

[14] B. Carter. and R. N. Henriksen. *J. Math. Phys.*, 32:2580–2597, 1991.

[15] M. W. Choptuik. *Phys. Rev. Lett.*, 70:9, 1993.

[16] Matthew W. Choptuik. Mexican school on gravitation and mathematical physics. VII Mexican School: Lectures. 2006.

[17] M.W. Choptuik, E.W. Hirschmann, S.L. Liebling, and F. Pretorius. *Phys. Rev. D*, 68(044007):1–9, 2003.

[18] M.W. Choptuik, E.W. Hirschmann, S.L. Liebling, and F. Pretorius. *Phys. Rev. Lett.*, 93(131101):1–4, 2004.

[19] C. K. Chu and A. Sereny. *J. Comput. Phys.*, 1974.

[20] Gregory B. Cook. Initial data for numerical relativity. *Living Rev. Relativity*, 3(5), 2000.

[21] W. E. East, F. Pretorius, and B. C. Stephens. *Phys. Rev. D*, 85(124010), 2012.

[22] C. R. Evans and J. S. Coleman. *Phys. Rev. Lett.*, 72:1782, 1994.

[23] J. A. Faber and F. A. Rasio. Binary neutron star merger. *Living Rev. Relativity*, 15(8), 2012.

[24] L. Fernández-Jambrina and L. M. González. *Current Trends in Relativistic Astrophysics*. Springer, Madrid, 2003.

[25] José Font. Numerical hydrodynamics in general relativity. *Living Rev. Relativity*, 6(4), 2003.

[26] José Font. Numerical hydrodynamics and magnetohydrodynamics in general relativity. *Living Rev. Relativity*, 11(7), 2008.

[27] J. B. Goodman and R. J. LeVeque. *Math. Comp.*, 45(171):15–21, 1985.

[28] E. Gourgoulhon. An introduction to relativistic hydrodynamics. *EAS Publ. Ser.*, 21:43–79, 2006.

[29] P. Grandclément and J. Novak. Spectral methods for numerical relativity. *Living Rev. Relativity*, 12(1), 2009.

[30] C. Gundlach and J. M. Martin-Garcia. *Phys. Rev. D*, 61:084024, 2000.

[31] Carsten Gundlach. *Phys. Rev. D*, 57:7080–7083, 1998.

[32] Carsten Gundlach. *Phys. Rev. D*, 65(064019):1–10, 2002.

[33] Carsten Gundlach. *Phys. Rev. D*, 65(084021):1–22, Mar 2002.

[34] Carsten Gundlach. *Phys. Rev.*, 376:339–405, Mar 2003.

[35] B. Gustaffsson, H-O Kreiss, and J. Oliger. *Time Dependent Problems and Difference Methods*. John Wiley & Sons, Inc., New York, 1995.

[36] B. Gustafsson and H. O. Kreiss. *J. Comput. Phys.*, 1979.

[37] Benjamin Gutierrez. *Relativistic Scattering of Solitons in Nonlinear Field Theory*. PhD thesis, The University of British Columbia, Vancouver, 2010.

[38] T. Hanawa and T. Matsumoto. *Astrophys. J.*, 521:703–707, 1999.

[39] T. Hanawa and T. Matsumoto. *Astrophys. J.*, 540:962–968, 2000.

[40] T. Hanawa and T. Matsumoto. *Publ. Astron. Soc. Japan*, 52:241–247, 2000.

[41] T. Hanawa and K. Nakayama. *Astrophys. J.*, 484:238–244, 1997.

[42] T. Hanawa, K. Saigo, and T. Matsumoto. *Astrophys. J.*, 558:753–760, 2001.

[43] T. Harada. *Phys. Rev. D*, 58(104015):1–10, 1998.

[44] T. Harada. *Class. Quantum Grav.*, 18:4549–4567, 2001.

[45] T. Harada. Stability criterion for self-similar solutions with perfect fluids in general relativity, 2001.

[46] T. Harada. Self-Similar Solutions, Critical Behaviour and Convergence to Attractor in Gravitational Collapse, 2003.

[47] T. Harada and H. Maeda. *Phys. Rev. D*, 63:084022, 2001.

[48] T. Harada, H. Maeda, and B. Semelin. *Phys. Rev. D*, 67:084003, 2003.

[49] A. Harten. *J. Comput. Phys.*, 135:260–278, 1997.

[50] A. Harten, P. Lax, and B. van Leer. *SIAM review*, 25(1):35–61, 1983.

[51] J. B. Hartle. *GRAVITY An Introduction to Einstein's General Relativity*. Addison Wesley, San Francisco, 2003.

[52] S. H. Hawley and M. W. Choptuik. *Phys. Rev. D*, 62(104024):1–19, 2000.

[53] James Healy and Pablo Laguna. Critical Collapse of Scalar Fields Beyond Axisymmetry. *Gen. Relativ. Gravit.*, 46:1722, 2014.

[54] G. W. Hedstrom. *J. Comput. Phys.*, 1979.

[55] S. Hod and T. Piran. *Phys. Rev. D*, 55(6):3485–3496, 1996.

[56] C. Hunter. *The Astronomical Journal*, 218:434–845, 1977.

[57] J. D. Anderson Jr. *Modern Compressible Flow: with historical perspective*. New York: McGraw-Hill, second edition, 1990.

[58] R. Kippenhahn, A. Weigert, and A. Weiss. *Stellar Structure and Evolution*. Springer, New York, 2012.

[59] T. Koike, T. Hara, and S. Adachi. *Phys. Rev. D*, 59:104008, 1999.

[60] R. B. Larson. *Mon. Not. R. astr. Soc.*, 145:271–295, 1969.

[61] R. J. LeVeque. *Finite-Volume Methods for Hyperbolic Problems.* Cambridge University Press, Cambridge, 2004.

[62] A. R. Linddle. An introduction to cosmological inflation, 1999.

[63] Y-Q. Lou and W-G Wang. *Mon. Not. R. Astron. Soc*, 372:885–900, 2006.

[64] H. Maeda and T. Harada. *Phys. Rev. D*, 64:124024, 2001.

[65] H. Maeda, T. Harada, H. Iguchi, and N. Okuyama. *Phys. Rev. D*, 66:027501, 2002.

[66] D. Maison. *Phys. Lett. B*, 366:82–84, 1996.

[67] J. M. Martí and E. Müler. Numerical hydrodynamics in special relativity. *Living Rev. Relativity*, 6(7), 2003.

[68] T. Matsumoto and T. Hanawa. *Astrophys. J.*, 521:659–670, 1999.

[69] T. Matsumoto, T. Hanawa, and K. Nakamura. *Astrophys. J.*, 478:569–584, 1997.

[70] C. W. Misner, K. S. Thorne, and J. A. Wheeler. *Gravitation.* W. H. Freeman, San Francisco, 1973.

[71] Bruno Coutinho Mundim. *A Numerical Study of Boson Star Binaries.* PhD thesis, The University of British Columbia, Vancouver, 2010.

[72] David Wayne Neilsen. *Extremely Relativistic Fluids in Strong-Field Gravity.* PhD thesis, The University of Texas, Austin, 1999.

[73] D. H. Nielsen and M. W. Choptuik. *Class. Quantum. Gravit.*, 17:761–782, 2000.

[74] D. H. Nielsen and M. W. Choptuik. *Class. Quantum. Gravit.*, 17:733–759, 2000.

[75] S. C. Noble and M. W. Choptuik. *Phys. Rev. D*, 78:064059, 2008.

[76] Scott Charles Noble. *A Numerical Study of Relativistic Fluid Collapse.* PhD thesis, The University of Texas, Austin, 2003.

[77] A. Ori and T. Piran. *Phys. Rev. D*, 42:1068–1090, 1990.

[78] I. Orlanski. *J. Comput. Phys.*, 1976.

[79] Anninos P. *Living Rev. Relativity*, 4(2), 2001.

[80] T. Padmanabhan. *Theoretical Astrophysics Volume II: Star and Stellar Systems.* Cambridge University Press, Cambridge, 2001.

[81] M. V. Penston. *Mon. Not. R. astr. Soc.*, 144:425–448, 1969.

[82] Max Pettini. Physical cosmology. Lectures. 2010.

[83] W. H. Press, S. A. Teukolsky, W. T. Vetterling, and B. P. Flannery. *Numerical Recipes in FORTRAN.* Cambridge University Press, New York, second edition, 1993.

[84] F. Pretorius and M. W. Choptuik. *J. Comput. Phys.*, 218:246–274, 2006.

[85] Frans Pretorius. *Numerical Simulations of Gravitational Collapse.* PhD thesis, University of British Columbia, Vancouver, 2002.

[86] Dimitrios Psaltis. Probes and tests of strong-field gravity with observations in the electromagnetic spectrum. *Living Rev. Relativity*, 11(9), 2008.

[87] L. F. Richardson. The approximate arithmetical solution by finite differences of physical problems involving differential equations, with and application to the stresses in a masonry dam. *Philosophical Transactions of the Royal Society of London. Series A*, 210:307–357, 1911.

[88] P. L. Roe. *J. Comp. Phys.*, 43:357–372, 1981.

[89] D. H. Rudy and J. C. Strikwerda. *J. Comput. Phys.*, 1980.

[90] D. H. Rudy and J. C. Strikwerda. *J. Comput. Phys.*, 1981.

[91] F. W. Sears and G. L. Salinger. *Thermodynamics, Kinetic Theroy, and Statistical Thermodynamics*. Addison-Wesley Publishing Company, third edition, 1986.

[92] M. Shibata and K. Taniguchi. Coalescence of black hole-neutron star binaries. *Living Rev. Relativity*, 14(6), 2011.

[93] C-W. Shu. *Leture Notes in Mathematics*, 1697:325–432, 1998.

[94] Chi-Wang Shu. Essentially Non-Oscillatory and Weighted Essentially Non-Oscillatory Schemes for Hyperbolic Conservation Laws. Technical report, NASA, November 1997.

[95] F. H. Shu. *The Astronomical Journal*, 214:488–497, 1977.

[96] M. Snajdr. *Class. Quantum. Gravit.*, 23:3333–3352, 2006.

[97] Evgeny Sorkin. On critical collapse of gravitational waves. *Class.Quant.Grav.*, 28:025011, 2011.

[98] Y. Suto and J. Silk. *The Astronomical Journal*, 326:527–538, 1988.

[99] T. Hara T. Koike and S. Adachi. *Phys. Rev. Lett.*, 74:5170, 1995.

[100] Jonathan Thornburg. Event and apparent horizon finders for 3+1 numerical relativity. *Living Rev. Relativity*, 10(3), 2007.

[101] E. F. Toro. *Riemann Solvers and Numerical Methods for Fluid Dynamics.* Springer, New York, 2009.

[102] E. F. Toro, M. Spruce, and W. Speares. Restoration of the contact surface in the hll-riemann solver. Technical Report CoA-9204, Department of Aerospace Science, College of Aeronautics, Cranfield Institute of Technology, UK, March 1993.

[103] J. F. Ventrella and M. W. Choptuik. *Phys. Rev. D*, 68(044020):1–10, 2003.

[104] R. M. Wald. *General Relativity.* The University of Chicago Press, Chicago and London, 1984.

[105] W-G Wang and Y-Q. Lou. *Astrophys. Space Sci.*, 311:363–400, 2007.

[106] S. Weinberg. *Cosmology.* Oxford University Press, Oxford New York, 2008.

[107] Jeffrey Winicour. Characteristic evolution and matching. *Living Rev. Relativity*, 15(2), 2012.

[108] A. Yahil. *The Astronomical Journal*, 265:1047–1055, 1983.

[109] J. M. Yeomans. *Statistical Mechanics of Phase Transitions.* Clarendon Press; Oxford University Press, New York; Oxford, 1992.

[110] N. Yunes and X. Siemens. *Living Rev. Relativity*, 16(9), 2013.

Appendix A

Solution's Behavior Near Sonic Points for $\Gamma = 1$

We assume the solution for the similarity variables $\alpha(x)$ and $u(x)$ in Eqs. (2.52) and (2.53) is analytic. Therefore, at the sonic point the solution can be Taylor expanded. For the isothermal case, $\Gamma = 1$ the coefficients in the expansion can be computed in closed-form in terms x_s. There are two possible expansions at the sonic point, we label these as type 1,

$$\alpha(x) = \frac{2}{x_s} + \frac{2x_s - 6}{x_s^2}(x - x_s) + \frac{x_s^2 - 8x_s + 13}{x_s^3}(x - x_s)^2 + \dots, \tag{A.1}$$

$$u(x) = (x_s - 1) + \frac{x_s - 1}{x_s}(x - x_s) - \frac{x_s - 1}{2x_s^2}(x - x_s)^2 + \dots \tag{A.2}$$

and type 2,

$$\alpha(x) = \frac{2}{x_s} - \frac{2}{x_s^2}(x - x_s) - \frac{x_s^2 - 6x_s + 7}{x_s^3(2x_s - 3)}(x - x_s)^2 + \dots, \tag{A.3}$$

$$u(x) = (x_s - 1) + \frac{1}{x_s}(x - x_s) + \frac{x_s^2 - 5x_s + 5}{2x_s^2(2x_s - 3)}(x - x_s)^2 + \dots \tag{A.4}$$

The free parameter is x_s. Both expansions can be used to set the starting point, (x_s) for the "backward" integration to the matching point x_M, discussed in Sec. 4.1.1.

Appendix B

Polar Perturbations

Generic nonspherical linear perturbations about any spherically symmetric solution to the Eqs. (2.5)–(2.8) have the following general form,

$$\begin{pmatrix} \rho(t,r,\theta,\phi) \\ v_r(t,r,\theta,\phi) \\ v_\theta(t,r,\theta,\phi) \\ v_\phi(t,r,\theta,\phi) \\ P(t,r,\theta,\phi) \\ \varphi(t,r,\theta,\phi) \end{pmatrix} = \begin{pmatrix} \bar{\rho}(t,r) + \delta\rho(t,r,\theta,\phi) \\ \bar{v}_r(t,r) + \delta v_r(t,r,\theta,\phi) \\ \bar{v}_\theta(t,r) + \delta v_\theta(t,r,\theta,\phi) \\ \bar{v}_\phi(t,r) + \delta v_\phi(t,r,\theta,\phi) \\ \bar{P}(t,r) + \delta P(t,r,\theta,\phi) \\ \bar{\varphi}(t,r) + \delta\varphi(t,r,\theta,\phi) \end{pmatrix}, \tag{B.1}$$

when written in spherical coordinates (r, θ, ϕ). The “bar” quantities represent the solution to the spherically symmetric model, Eqs. (2.24)–(2.27). Inserting these ansatz into Eqs. (2.5)–(2.8) we obtain the following system for the linear perturbations,

$$\frac{\partial \delta\rho}{\partial t} + \frac{1}{r^2}\frac{\partial}{\partial r} r^2 (v_r \delta\rho + \rho \delta v_r) + \frac{1}{r\sin\theta}\frac{\partial}{\partial \theta}(\sin\theta \rho \delta v_\theta) + \frac{1}{r\sin\theta}\frac{\partial}{\partial\phi}(\rho\delta v_\phi) = 0, \tag{B.2}$$

$$\begin{aligned}\frac{\partial}{\partial t}(\rho\delta v_r + v_r \delta\rho) + \frac{1}{r^2}\frac{\partial}{\partial r} r^2 (2\rho v_r \delta v_r + v_r^2 \delta\rho) + \frac{\rho v_r}{r}\left(\frac{1}{\sin\theta}\frac{\partial}{\partial\theta}(\sin\theta\delta v_\theta) + \right. \\ \left. \frac{1}{\sin\theta}\frac{\partial \delta v_\phi}{\partial\phi}\right) = -K\Gamma\rho^{\Gamma-1}\left[(\Gamma-1)\frac{\delta\rho}{\rho}\frac{\partial\rho}{\partial r} + \frac{\partial\delta\rho}{\partial r}\right] - \rho\frac{\partial\delta\varphi}{\partial r} - \delta\rho\frac{\partial\varphi}{\partial r},\end{aligned} \tag{B.3}$$

$$\frac{\partial}{\partial t}(\rho\delta v_\theta) + \frac{1}{r^2}\frac{\partial}{\partial r}(r^2\rho v_r \delta v_\theta) + \frac{\rho v_r \delta v_\theta}{r} = -\frac{1}{r}K\Gamma\rho^{\Gamma-1}\frac{\partial\delta\rho}{\partial\theta} - \frac{\rho}{r}\frac{\partial\delta\varphi}{\partial\theta}, \tag{B.4}$$

$$\frac{\partial}{\partial t}(\rho\delta v_\phi) + \frac{1}{r^2}\frac{\partial}{\partial r}(r^2\rho v_r \delta v_\phi) + \frac{\rho v_r \delta v_\phi}{r} = -\frac{1}{r\sin\theta}K\Gamma\rho^{\Gamma-1}\frac{\partial\delta\rho}{\partial\phi} - \frac{\rho}{r\sin\theta}\frac{\partial\delta\varphi}{\partial\phi}, \tag{B.5}$$

$$\frac{1}{r^2}\frac{\partial}{\partial r} r^2 \frac{\partial\delta\varphi}{\partial r} + \frac{1}{r^2\sin\theta}\frac{\partial}{\partial\theta}\sin\theta\frac{\partial\delta\varphi}{\partial\theta} + \frac{1}{r^2\sin^2\theta}\frac{\partial^2\delta\varphi}{\partial\phi^2} = 4\pi G\delta\rho. \tag{B.6}$$

We have assume that the fluid obeys EoS (2.18), thus we can write the δP in terms of $\delta\rho$. It clear that the fluid quantities represent the spherically symmetric solutions, therefore, we omit the bar-notation.

Complementary to the discussion found in Sec. (2.5), we consider polar perturbations about the spherically symmetric self-similar solutions

$$\rho(t,r,\theta,\phi) = \frac{1}{4\pi G t^2}\left(\alpha(x) + \delta\alpha(x)e^{\lambda\tau}Y_\ell^m(\theta,\phi)\right), \tag{B.7}$$

$$\vec{v}(r,\theta,\phi) = \sqrt{\kappa}t^{n-1}\begin{pmatrix} u(x) + \delta u(x)e^{\lambda\tau}Y_\ell^m(\theta,\phi) \\ \delta u_\Psi(x)\dfrac{e^{\lambda\tau}}{\ell+1}\dfrac{\partial}{\partial\theta}Y_\ell^m(\theta,\phi) \\ \delta u_\Psi(x)\dfrac{e^{\lambda\tau}}{(\ell+1)\sin\theta}\dfrac{\partial}{\partial\phi}Y_\ell^m(\theta,\phi)\end{pmatrix}, \tag{B.8}$$

$$\varphi(t,r,\theta,\phi) = \kappa t^{2n-2}\left(\tilde{\varphi}(x) + \delta\tilde{\varphi}(x)e^{\lambda\tau}Y_\ell^m(\theta,\phi)\right). \tag{B.9}$$

Where $\varphi(t,r) \equiv \kappa t^{2n-2}\tilde{\varphi}(x)$ is the similarity variable for the Newtonian potential defined in terms of $m(x)$ via Eq. (2.33) such that,

$$\frac{\partial\tilde{\varphi}(x)}{\partial x} = \frac{1}{3n-2}\frac{m(x)}{x^2}. \tag{B.10}$$

Inserting the polar perturbation ansatz Eqs. (B.7)–(B.9) into the equations for general linear perturbations (B.2)–(B.6) we obtain the following autonomous system,

$$-(\lambda+2)\delta\alpha - nx\frac{\partial\delta\alpha}{\partial x} + \frac{1}{x^2}\frac{\partial}{\partial x}x^2(\alpha\delta u + u\delta\alpha) - \frac{\ell}{x}\alpha\delta u_\Psi = 0, \tag{B.11}$$

$$\begin{aligned}(n-3-\lambda)(\alpha\delta u + u\delta\alpha) - nx\frac{\partial}{\partial x}(\alpha\delta u + u\delta\alpha) + \frac{1}{x^2}\frac{\partial}{\partial x}x^2(2\alpha u\delta u + u^2\delta\alpha)&\\ -\frac{\ell}{x}\alpha u\delta u_\Psi = -\Gamma\frac{\partial}{\partial x}\left(\alpha^{\Gamma-1}\delta\alpha\right) - \alpha\frac{\partial\delta\tilde{\varphi}}{\partial x} - \delta\alpha\frac{\partial\tilde{\varphi}}{\partial x},&\end{aligned} \tag{B.12}$$

$$\begin{aligned}(n-3-\lambda)\alpha\delta u_\Psi - nx\frac{\partial}{\partial x}(\alpha\delta u_\Psi) + \frac{1}{x^2}\frac{\partial}{\partial x}x^2\alpha u\delta u_\Psi + \frac{\alpha u\delta u_\Psi}{x} =&\\ -\frac{\ell+1}{x}\left(\Gamma\alpha^{\Gamma-1}\delta\alpha + \alpha\delta\tilde{\varphi}\right),&\end{aligned} \tag{B.13}$$

$$\frac{1}{x^2}\frac{\partial}{\partial x}x^2\frac{\partial\delta\tilde{\varphi}}{\partial x} - \frac{\ell(\ell+1)}{x^2}\delta\tilde{\varphi} = \delta\alpha. \tag{B.14}$$

Where the parameters $\kappa = K(4\pi G)^{1-\Gamma}$ and $n = 2-\Gamma$.

Again we only consider perturbations which are analytic. Applying the expansions given by Eqs. (2.55) and (2.56) into the autonomous system for the polar perturbations, Eqs. (B.11)–(B.14) yield that the perturbations mush vanish at $x = 0$ according to,

$$\delta\alpha(x) = \delta\alpha_0\alpha_*^{2-\Gamma}x^\ell, \tag{B.15}$$

$$\delta u(x) = \delta u_0\ell x^{\ell-1}, \tag{B.16}$$

$$\delta u_\Psi(x) = \delta u_0(\ell+1)x^{\ell-1}, \tag{B.17}$$

$$\delta\tilde{\varphi}(x) = -\left[\Gamma\delta\alpha_0 - \left(\lambda + 2\Gamma - 3 + \frac{\ell(4-3\Gamma)}{3}\right)\delta u_0\right]x^\ell \tag{B.18}$$

Where $\delta\alpha_0$, and δu_0 are free constant parameters.

It can be shown that at the sonic point $(nx-u) = \sqrt{\Gamma}\alpha^{(\Gamma-1)/2}$ the necessary condition for regularity is,

$$\begin{aligned}\left[(\Gamma-1)\frac{\alpha'}{\alpha}(nx-u)^2 + \left(\frac{2u}{x} - \lambda - 2\right)(nx-u) + (n-1)u + \tilde{\varphi}'\right]\delta\alpha&\\ + \left[3(n-1) - \lambda + 2u'\right]\alpha\delta u - \frac{\ell(nx-u)}{x}\alpha\delta u_\Psi + \alpha\delta\tilde{\varphi}' = 0&\end{aligned} \tag{B.19}$$

Where $\partial(\cdot)/\partial x \equiv (\cdot)'$. The above condition, Eq. (B.19) can be used to solve for either $\delta\alpha$ or δu to be subsequently substituted into Eqs. (B.13) and (B.14) evaluated at the sonic point. The solutions of these equations, *i.e.* $\delta\tilde{\varphi}'$ and δu_Ψ are determined up to and overall constant.